DYNAMIC ANALYSIS AND ALIGNMENT DESIGN OF HIGH-SPEED MAGLEV TRAINS RUNNING ON STRAIGHT, CIRCULAR AND TRANSITIONAL VIADUCTS

WANG ZHILU

PhD

The Hong Kong Polytechnic University

This programme is jointly offered by The Hong Kong Polytechnic University and Tongji University

2019

The Hong Kong Polytechnic University
Department of Civil and Environmental Engineering

Tongji University
Department of Structural Engineering

DYNAMIC ANALYSIS AND ALIGNMENT DESIGN OF HIGH-SPEED MAGLEV TRAINS RUNNING ON STRAIGHT, CIRCULAR AND TRANSITIONAL VIADUCTS

WANG ZHILU

A thesis submitted in partial fulfillment of the requirements for
the Degree of **Doctor of Philosophy**

August 2018

To my family

for their love and support

CERTIFICATE OF ORIGINALITY

I hereby declare that this thesis is my own work and that, to the best of my knowledge and belief, it reproduces no material previously published or written, nor material that has been accepted for the award of any other degree or diploma, except where due acknowledgement has been made in the text.

____________________(Signed)

__WANG Zhilu__(Name of student)

ABSTRACT

In the past two decades, magnetic levitation (maglev) train, a high-efficiency intercity transportation, has attracted the world's attention for its advantages over conventional wheel train systems, such as higher speed, lower risk of derailment, and less energy consumption. Thus far, several maglev train lines, such as the Shanghai Maglev Line (SML), the Changsha Maglev Express, and the Incheon Airport Maglev, have been built in urban areas. The maximum operating speed of the SML is 430 km/h, and the design speed of the Chuo Shinkansen Line (under construction) reaches 500 km/h. In view of the limited space available in urban areas, maglev trains often run on elevated viaducts supported by slender piers. Thus, the dynamic interaction between high-speed maglev trains and viaducts becomes significant and plays a crucial role in the design of the vehicles in the train and the major components of the viaduct. Furthermore, curved tracks/viaducts are inevitable in maglev lines because of land use compatibility in urban areas. Therefore, accurate dynamic analysis and alignment design of high-speed maglev trains running on straight, circular, and transitional viaducts are extremely significant for the safety and comfortability of maglev trains, the safety and functionality of the viaducts, and the construction cost reduction.

This thesis first presents a realistic and detailed high-speed maglev train-viaduct interaction model. It focuses on the accurate simulation of the two subsystems, namely, the train subsystem, including the magnets, and the viaduct subsystem, including the modular function units of the rails. The electromagnet force-air gap model with a proportional-derivative controller is adopted to simulate the interaction between the maglev train via its electromagnets and the viaduct via its modular function units. The flexibility of the rails, girders, piers, and associated elastic bearings are considered in the modeling of the viaduct subsystem to investigate their effects on the interaction between the two subsystems. By applying the proposed model to the SML, the effectiveness and accuracy of the proposed approach are validated through the comparison of the computed dynamic responses and frequencies with the measurement data. This thesis confirms that the proposed model with detailed simulation of the magnets and modular function units can duly account for the dynamic interaction between the train and viaduct subsystems.

Maglev lines are often built in the urban areas; thus, horizontally curved tracks are inevitable because of land use compatibility and socioeconomic consideration, and circular curved tracks are often introduced for this purpose. However, due to high speed of maglev trains, a large cant angle is often required to avoid the use of a large curve radius (CR) and at the same time to counteract the circular curved path-induced centrifugal forces on the vehicle. Accordingly, the issues of curving ride quality of the train and safety performance of the viaduct increase with high train speeds. However, when a vehicle moves on the curved track, the moving direction of the vehicle in the global coordinate system changes. As a result, the direction of the centrifugal force on the vehicle also changes. Meanwhile, the interaction forces between the vehicle and track depend on their relative displacements. The dynamic interaction between the high-speed maglev train and the slender curved viaduct becomes extremely complicated. This thesis proposes a trajectory coordinate-based framework for the analysis of the high-speed maglev train running on the circular curved track. The motion of the maglev train system running on a curved track is defined by a series of trajectory coordinates, and the stiffness and damping matrices of the equations can be reduced into those of the straight track. The curved viaduct system is modeled in the global coordinate system using the finite element method. The electromagnet force–air gap model is also adopted for the maglev vehicle via its electromagnets and rails on the viaduct by appropriate transformation of coordinates. By applying the proposed framework to the SML, curved path-induced dynamic characteristics and responses of the vehicle are explored, which agree well with the measured ones. Moreover, the results of parametric studies show that the track radii and cant deficiencies significantly affect the operational safety and comfortability of the viaduct.

To ensure the ride quality of the train moving from the straight track section to the circular curved track section, a transitional curved track section imbedded between them is also necessary. However, as required by the geometric smoothness of the entire track, the CR and high difference (HD) between the outer and inner rails along the transitional curved track are distance-varying, resulting in a more complicated dynamic interaction than one when trains run on either the straight track or the circular curved track. Thus, the proposed trajectory coordinate-based analysis approach is extended and further developed, in which the origins of the trajectory coordinate systems move along the inner rail of the track, and the Euler angles used to describe the coordinates' orientations are functions of distance-varying CR and HD. By applying this framework to the SML, the dynamic characteristics and responses of the maglev vehicles running on the transitional viaduct are numerically explored, which match the measured data quite well. Moreover, the effect of transitional track length and cant deficiencies on the coupled system are investigated. Results show that the rolling motions of the vehicle are considerable and affect ride quality when the vehicle runs on the transitional track with a high cant angle. Cant deficiency and transitional length significantly affect the vehicle-viaduct interaction.

From a practical perspective, the reduction of construction cost is consistently pursued in the alignment design of a high-speed maglev line. Optimizing the alignment parameters of the curved track is crucial in providing an economical but reliable solution for the construction of new maglev lines because the construction of a curved track is considerably more expensive than a straight track, and the ride comfort is markedly more serious. Hence, a new optimization method is proposed in this thesis for the alignment design of horizontally curved track in a high-speed maglev line, in which the minimum length of the curved track is a major objective function, and the satisfaction of the minimum comfort level of passengers is a boundary condition to constrain the selection of alignment parameters of the curved track. By comparing with the existing solution and the actual curved track of the SML, the solution provided by the proposed optimization method is proven an optimal solution with the minimum length of the curved track and the satisfactory comfort level. The accuracy of the optimal solution provided by the proposed optimization method is further validated by using the coupled maglev train and curved viaduct system established in this thesis. Results demonstrate that with the increase of the vehicle speed, both the radius of the circular track and the length of the transitional track increase. However, the cant remains constant at its upper limit value and the cant deficiency varies slightly around a constant value. The optimal solution provided can be used for the initial alignment design of horizontally curved track in a high-speed maglev line.

PUBLICATIONS ARISING FROM THE THESIS

Journal papers

Li GQ, **Wang ZL**, Chen SW, Xu YL (2016). Field measurements and analyses of environmental vibrations induced by high-speed Maglev. *Science of the Total Environment*, 568, 1295–1307.

Wang ZL, Xu YL, Li GQ, Yang YB, Chen SW, Zhang XL (2018). Modeling and validation of coupled high-speed maglev train-and-viaduct systems considering support flexibility. *Vehicle System Dynamics*, online. DOI: 10.1080/00423114.2018.1450517.

Wang ZL, Xu YL, Li GQ, Chen SW, Zhang XL (2018). Dynamic Analysis of a Coupled System of High-Speed Maglev Train and Curved Viaduct. *International Journal of Structural Stability and Dynamics*. Vol. 18, No. 11.

Xu YL, **Wang ZL**, Li GQ, Chen SW, Yang YB (2018). High-Speed Running Maglev Trains Interacting with Elastic Transitional Viaducts. *Engineering Structures*. (Under review)

Wang ZL, Xu YL, Li GQ, Chen SW (2018). Optimization of horizontally curved track in the alignment design of a high-speed maglev line. *Structure and Infrastructure Engineering.* (Under review)

Conference paper

Wang ZL, Chen SW, Xu YL, Li GQ. (2016). Field measurements of maglev train-induced vibrations. *IABMAS 2016*, pp. 1006–1013, Brazil: Taylor & Francis Group.

ACKNOWLEDGEMENTS

First, I would like to express my sincere gratitude to my chief supervisor, Prof. You-Lin Xu for offering me the opportunity to participate in the Joint Ph.D. Programs Leading to Dual Award between The Hong Kong Polytechnic University (PolyU) and Tongji University (TongjiU). His valuable advice, insightful guidance, and generous support are indispensable in outlining, conducting, and completing the works culminating in this thesis. During the past three years in PolyU, Prof. Xu devoted considerable effort on guiding me how to conduct good research and how to write an excellent journal paper. I learned and achieved more than what constitutes this thesis. I believe that my learnings from Prof. Xu will benefit my entire life moving forward. I truly appreciate his support for ensuring my continuous study in PolyU after the 18-month studentship, without which I cannot finish this thesis.

I would also like to express my profound appreciation to my chief supervisor at TongjiU, Prof. Guo-qiang Li. He always supported me with the best research resources. His serious and responsible attitude, valuable advice, insightful guidance, and generous support kept me moving forward. The guidance and help from my co-supervisor Prof. Suwen Chen are also deeply appreciated.

I am grateful to the members of Board of Examiners, Prof. Wan-Ming ZHAI from Southwest Jiaotong University, Dr. Ilias G. DIMITRAKOPOULOS from Hong Kong University of Science and Technology, and Prof. Yi-Qing NI of PolyU for attending my oral examination and providing insightful comments on my thesis.

Moreover, I would like to express my heartfelt gratitude to Prof. Yeong-bin Yang of Chongqing University for his valuable advice and insightful guidance on my Ph.D. project during his stint as a Distinguished Chair Professor in PolyU, which indeed helped me build confidence in my research work.

I gratefully acknowledge PolyU and the Hong Kong Research Grant Council for financially supporting my Ph.D. study. PolyU also offered me excellent working environment and research facilities. This research work is also financially supported by the National Key Technology R&D Program of 12th Five-Year Plan of China (Project No: 2013BAG 19B00-02-03). The joint PhD scholarship and the collaborative research project with Beijing University of Technology (PolyU:4-ZZGD) provided by The Hong Kong Polytechnic University are appreciated. The field measurements were performed with the help of the staffs from National Maglev Traffic Engineering Technology Research Center and Tongji University, to which the authors are grateful.

My heartfelt gratitude goes to my friends, housemates, and members of the research group at PolyU. They contributed in various ways, such as in guiding me through the highs and lows and inspiring me to continue my research journey. For the works presented here, I extend my gratitude to Mr. Sheng Zhan, Dr. Jia He, Dr. Yue Zheng, Dr. Qing Zhu, Dr. Feng-yang Wang, Dr. Jing-hua Lin, Dr. Yi-xin Peng, Dr. Bin Sun, Mr. Jian-fu Lin, Mr. Rong-pan Hu, and Ms. Zhong-xu Tan for their valuable advice and warm assistance during my study. Getting through my Ph.D. study required more than academic support, and I cannot begin to express my gratitude and appreciation for their friendship and company over the past years.

The same heartfelt gratitude goes to the members of the Research Group for Multi-story and Tall Steel Buildings and Fire-Resistance of Steel Structures of TongjiU. The assistance from Dr. Zeng Qing of The Hong Kong University of Science and Technology is also appreciated.

I am forever indebted to my parents, who indeed cannot be thanked enough, for consistently providing me support and encouragement, which enabled me to achieve every goal in my life. I also thank my elder brother and sister-in-law, who always support my research and my life. I also thank my niece, who gives me happiness during my difficult study. Finally, I thank my partner, Dr. Yi-nan Liu of Fudan University, who has shared me with her happiness and affection and supported me in the years since we met with her love, encouragement, incredible understanding, and sacrifice.

CONTENTS

LIST OF FIGURES

LIST OF TABLES

LIST OF NOTATIONS

${}_{III_i}\boldsymbol{\alpha}_i$	The angular acceleration vector of the i^{th} body defined in the body-fixed coordinate system
A_w	The pole face area
c_{cby}, c_{cbz}	The damping coefficients of the same elements
C_d	The cant deficiency
c, b, t, s, and g	Refers to the car body, bogie, rocker, levitation (suspension) magnet and guidance magnet, respectively
d	The force space
D	The cant
D_{eq}	The equilibrium cant
D_t	The cant of the transitional track
e_w^t	The gap error
$\mathbf{F}_e^i$	The external force vector or the external moment vector acting on the mass center of the i^{th} rigid body
$\mathbf{F}_K^i$, $\mathbf{F}_C^i$	The restoring and damping force or moment vector acting on the i^{th} rigid body due to the stiffness and damping of the linear spring-damper elements connected to the i^{th} rigid body.
F_{ci}^g, F_{tijk}^g , F_{sm}^g	The gravity force acting on the car body, bogie, levitation magnet
$F_{cbr(l)yijk}$, $F_{cbr(l)zijk}$	The lateral and vertical forces generated from the spring-damping elements between the i^{th} car body and the $(jk)^{\text{th}}$ rocker
$F_{str(l)zijkn}$	The connection forces between the bogie and the levitation magnets
$F_{spr(l)zmw}$	The levitation electromagnet force generated from the interaction between the w^{th} pole and the rail track
$F_{gpr(l)ymw}$	The guidance electromagnet force generated from the interaction between the equivalent w^{th} pole and the rail track
$F_{gtr(l)yijkn}$	The connection forces between the bogie and the guidance magnets
$F_{ar(l)zijk}$	The air-spring force between the rocker and bogie

F_{ezijk}	The adjacent rockers on the $(jk)^{\text{th}}$ frame
$F\left(i_w^t, h_w^t\right)$	The current-controlled electromagnetic force between the w^{th} maglev pole and the rail track
${}_{II}\mathbf{F}\left(i_w^t, h_w^t\right)$	The current-controlled electromagnetic force between the w^{th} maglev pole and the rail track, defined in the pertinent trajectory coordinate system
f_i	The driving frequency related to the characteristic length L_i under the vehicle speed v
f_r	The dynamic coefficient defined as the ratio between the response perceived by the passenger and the curved track-induced response
$\mathbf{F}_e^G$	The external force vector, including gravity force, seismic loads, and wind loads
$\mathbf{F}_m^{V\rightarrow G}$	The vector of the electromagnet forces acting on the viaduct
$\mathbf{F}_{G\rightarrow V}^V$	The interaction force vector between the vehicles and guideway rails
$\mathbf{F}_e^V$	The external forces such as gravity forces, seismic loads or wind loads
$\mathbf{F}_{G\rightarrow V}^V$	The interaction force vector between the vehicles and guideway rails
$\mathbf{F}_e^V$	The external forces such as gravity forces, seismic loads or wind loads
${}_{I}\mathbf{F}_{ei}$	The total force acting on the center of mass defined in the global coordinate system
${}_{II_m}\mathbf{F}_{ei}$	The vector of external forces and toques defined in the trajectory coordinate system
${}_{II}\mathbf{F}_V^e$	The external force vector, including the gravity forces, seismic loads or wind loads, defined in the trajectory coordinate system
${}_{II_m}\mathbf{F}_{vi}$	The inertial force vector due to the curved path, defined in the trajectory coordinate system
${}_{II}\mathbf{F}_V^v$	The inertial force vector, including the centrifugal force and Coriolis force, defined in the trajectory coordinate system
${}_{II}\mathbf{F}_V^{G\rightarrow V}$	The interaction force vector between the vehicles and rails, defined in the trajectory coordinate system
${}_{I}\mathbf{F}_G^e$	The external force vector, including the gravity force, seismic loads, and wind loads, defined in the global coordinate system

${}_{I}\mathbf{F}_{G}^{V\to G}$	The vector of the electromagnet forces acting on the viaduct, defined in the global coordinate system
${}_{I}\mathbf{L}^{II_m}$	The velocity transformation matrices, corresponding to the translational motion.
${}_{III_i}\mathbf{H}^{II_m}$	The velocity transformation matrices, corresponding to the rotational motions.
${}_{II}\mathbf{h}_{w}^{t}$	The magnetic air gap for inclusion of the levitation air gap and guidance air gap defined in the pertinent trajectory coordinate system
${}_{III_i}\mathbf{I}_{\theta i}$	The moment of inertia matrix defined in the body-fixed coordinate system
$H(t)$	The unit step function
h_0	The design static gap at the static equilibrium state of the train (10mm for SML)
$h_{cr(l)}$, l_{ckj}, $h_{br(l)1}$,	The dimensions of the vehicle components
$h_{br(l)1}$, $h_{br(l)2}$, $h_{br(l)3}$	The dimensions of the vehicle components
h_w^t	The magnetic air gap
h_g	The horizontal distance between the two rails (the width of the track)
i_0	The required value of the current to balance the train weight and keep the design static gap h_0
i_w^t	The electrical intensity
$\mathbf{I}_3$	The 3×3 identity matrix
$J_{\phi ci}$, $J_{\theta ci}$, $J_{\psi ci}$	The mass moments of inertia of the i^{th} car body about the X-axis, Y-axis, and Z-axis, respectively
$J_{\phi t}$, $J_{\theta t}$, $J_{\psi t}$	The mass moments of inertia of one C-shaped frame about the X-axis, Y-axis, and Z-axis
$J_{\theta s}$	The mass moment of inertia of each levitation magnet about the Y-axis
$J_{\psi g}$	The mass moment of inertia of each guidance magnet about the Z-axis
K_0	The coupling factor related to the cross-sectional area of the core
$\mathbf{K}_N^{tc}$, $\mathbf{K}_N^{bc}$, $\mathbf{K}_N^{bt}$,	The interacting stiffness matrix among the car bodies, bogies,

$\mathbf{K}_N^{sb}$, $\mathbf{K}_N^{gb}$	rockers, levitation magnets, and guidance magnets included in *N* vehicles, respectively
$\mathbf{K}_V$, $\mathbf{C}_V$	The stiffness and damping matrices of the train subsystem
$_{II}\mathbf{K}_V$, $_{II}\mathbf{C}_V$	The stiffness and damping matrices of the train subsystem defined in the trajectory coordinate system
k_{cby}, k_{cbz}	The stiffness coefficients of the spring-damper elements installed between the i^{th} car body and the $(jk)^{th}$ rocker;
k_{az}	The stiffness coefficient of the air-spring element between the rocker and bogie
k_{bbz}	The stiffness coefficient of the adjacent rockers in the *Z*-direction
k_{tsz} , c_{tsz}	The stiffness and damping coefficients of the spring-damper elements between the bogie and levitation magnets, respectively
k_{tgy} , c_{tgy}	The stiffness and damping coefficients of the spring-damping elements between the bogie and guidance magnets, respectively
$k_{tt\phi}$	The relatively rotational stiffness coefficient between the two C-shaped frames
K_p , K_d	The proportional gain and derivative gain, respectively
K_t	The curvature of the transitional track
L	The length of one span of the girder
L_0, L_t	The arc length of the entire transitional curve
l_{tn} , l_{tcn} , $h_{tr(l)1}$	The dimensions of the vehicle components
v_{t1} , v_{t2}	The dimensions of the vehicle components
l_{t1} , l_{t2} , l_{sw} ,	The dimensions of the vehicle components
l_{t1} , l_{t1} , l_{sw}	The dimensions of the vehicle components
L_{total}	The total length of the entire curved track
L_{Vi}	The characteristic length of the train
L_{V1}	The characteristic length of the maglev pole pitch
L_{V2}	The characteristic length of the center distance of adjacent levitation magnets

L_{V3}	The characteristic length of the center distance of adjacent bogies
L_{V4}	The characteristic length of the center distance of two neighboring vehicles,
$\mathbf{M}^i$	The mass matrix or the mass moment matrix of inertia of the ith rigid body
$\mathbf{M}^V$	The mass matrix of the train subsystem
${}_{II}\mathbf{M}_V$	The mass matrix of the train subsystem defined in the trajectory coordinate system
$\mathbf{M}_N^c$, $\mathbf{M}_N^b$, $\mathbf{M}_N^t$, $\mathbf{M}_N^s$, $\mathbf{M}_N^g$	The mass matrices of the car bodies, bogies, rockers, levitation magnets, and guidance magnets included in *N* vehicles, respectively
${}_{II_{m_c}}\mathbf{M}_N^c$, ${}_{II_{m_b}}\mathbf{M}_N^b$, ${}_{II_{m_t}}\mathbf{M}_N^t$, ${}_{II_{m_s}}\mathbf{M}_N^s$, ${}_{II_{m_g}}\mathbf{M}_N^g$	The mass matrices of the car bodies, bogies, rockers, levitation magnets, and guidance magnets included in *N* vehicles, respectively defined in their own trajectory coordinate system
$\mathbf{M}^G$	The global mass matrix of the viaduct
${}_I\mathbf{M}_G$	The global mass matrix of the viaduct in the global coordinate system
${}_I\mathbf{K}_G$	The stiffness matrix for the entire viaduct subsystem in the global coordinate system
${}_{II_m}\mathbf{M}_i$	The mass matrix of the ith body defined in the trajectory coordinate system
m_{ci}, m_t, m_s, m_g	The mass of the ith car body, one C-shaped frame, each levitation magnet, and levitation magnet
N_m	The number of turns in the magnet winding;
p_0	The weight of the maglev train distributed at the wth maglev pole
P_{CT}	The comfort index (Passenger Comfort on Curve Transitions)
P_{CT0}	The limited value of the satisfaction of the comfort level of passengers when the vehicle runs on the curved track
R	The radius of the circular curved track
R_0	The coil resistance of the electronic circuit
${}_I\mathbf{R}^{II_m \to I}$	The transformation matrix defining the orientation of the mth trajectory coordinate system with respect to the global

	coordinate system
${}_{I}\boldsymbol{\gamma}_{R}^{II_m\to I}$	The vectors containing the additional quadratic velocity terms produced by the time-differentiation of the absolute linear velocity vector
${}_{III_i}\boldsymbol{\gamma}_{\boldsymbol{\theta}}^{I\to III_i}$	The vector containing the additional quadratic velocity terms produced by the time-differentiation of the absolute angular velocity vectors
s	The arc length between the calculated point and the starting point
s_w^t	The arc length from the wth maglev pole to the origin of the global coordinate system
$s_r\left(x_w^t\right)$	The track irregularity
t_w	The traveling time of the wth pole since it enters the concerned span of the viaduct
${}_{III_i}\boldsymbol{\tau}$	The total torque about the center of mass of the ith body
Γ_0	The initial inductance of the coil winding of the guidance or levitation magnets
$u_w\left(t\right)$	The motion of the wth magnetic pole
${}_{II}\mathbf{u}_w\left(t\right)$	The motion of the wth magnetic pole defined in the pertinent trajectory coordinate system
$u_G\left(x_w^t\right)$	The track deflection at the wth magnetic pole
${}_{I}\mathbf{u}_G\left(s_w^t\right)$	The deflection of the rail defined in the global coordinate system
${}_{II}\mathbf{u}_G\left(s_w^t\right)$	The rail deflection at the wth magnetic pole with respect to the pertinent trajectory coordinate system
μ_0	The air permeability.
${}_{II_m}\mathbf{U}_i$	The generalized trajectory coordinates
$\mathbf{U}^V$, $\dot{\mathbf{U}}^V$, $\ddot{\mathbf{U}}^V$	The displacement, velocity, and acceleration vectors of the train subsystem
${}_{II}\mathbf{U}_V$, ${}_{II}\dot{\mathbf{U}}_V$, ${}_{II}\ddot{\mathbf{U}}_V$	The displacement, velocity, and acceleration vectors of the train subsystem defined in the trajectory coordinate system
$\mathbf{U}^G$, $\dot{\mathbf{U}}^G$, $\ddot{\mathbf{U}}^G$	The displacement, velocity and acceleration vectors of the viaduct subsystem

${}_{I}\mathbf{U}_{G}$, ${}_{I}\dot{\mathbf{U}}_{G}$, ${}_{I}\ddot{\mathbf{U}}_{G}$	The displacement, velocity and acceleration vectors of the viaduct subsystem defined in the global coordinate system
$\mathbf{U}_{ci}$, $\mathbf{U}_{bij}$, $\mathbf{U}_{tijk}$, $\mathbf{U}_{sm}$, $\mathbf{U}_{gm}$	The vectors of DOFs of the car body, bogie, rocker, levitation magnet and guidance magnet
${}_{II_m}\mathbf{U}_{ci}$, ${}_{II_m}\mathbf{U}_{bij}$, ${}_{II_m}\mathbf{U}_{tijk}$, ${}_{II_m}\mathbf{U}_{tijk}$, ${}_{II_m}\mathbf{U}_{sm}$, ${}_{II_m}\mathbf{U}_{gm}$	The vectors of DOFs of the car body, bogie, rocker, levitation magnet and guidance magnet defined in their own trajectory coordinate system
$\mathbf{U}_N^c , \mathbf{U}_N^b , \mathbf{U}_N^t ,$ $\mathbf{U}_N^s , \mathbf{U}_N^g$	The sub-displacement vectors of the car bodies, bogies, rockers, levitation magnets, and guidance magnets included in *N* vehicles, respectively
${}_{II_{m_c}}\mathbf{U}_N^c$, ${}_{II_{m_b}}\mathbf{U}_N^b$, ${}_{II_{m_t}}\mathbf{U}_N^t$, ${}_{II_{m_s}}\mathbf{U}_N^s$, ${}_{II_{m_g}}\mathbf{U}_N^g$	The sub-displacement vectors of the car bodies, bogies, rockers, levitation magnets, and guidance magnets included in *N* vehicles, respectively defined in their own trajectory coordinate system
${}_{I}\mathbf{u}_{O^I O^{II_m}}$	The position vector of the origin of the *m*th trajectory coordinate system defined in the global coordinate system *I*, which is a function of the arc length ${}_{I}s^{II_m}$
${}_{I}\mathbf{u}_{O^{II_m} O^{III_i}}$	The position vector of the origin of the *m*th trajectory coordinate system to the origin of the *i*th body coordinate system, defined in the global coordinate system *I*
${}_{II_m}\mathbf{u}_{O^{II_m} O^{III_i}}$	The position vector of the origin of the *m*th trajectory coordinate system to the origin of the *i*th body coordinate system, defined in the *m*th trajectory coordinate system
${}_{I}\ddot{\mathbf{u}}_{O^I O^{III_i}}$	The translational acceleration vector of the center of the *i*th body
${}_{II_m}\ddot{\mathbf{U}}_{i}$	The translational and rotational acceleration vector of the *i*th body expressed in terms of the generalized trajectory coordinates
V_w^t	The control voltage of the *w*th maglev pole
v	The operational speed of the train
${}_{III_i}\boldsymbol{\omega}_{i}$	The angular velocity of the body.
$\omega_{\lim}$	The limit of the rate of change of cant
x_w^t	The location of the *w*th maglev pole in the global X-coordinate

y_{ci}, y_{bij}, y_{grm}	Lateral displacement of the car body, bogie and guidance magnet
${}_{II_m}y^{III_{ci}}$, ${}_{II_m}y^{III_{bij}}$, ${}_{II_m}y^{III_{grm}}$	Lateral displacement of the car body, bogie and guidance magnet defined in their own trajectory coordinate system
${}_{II_m}y^{III_i}$, ${}_{II_m}z^{III_i}$	Two translational motions of the i^{th} body defined in the trajectory coordinate system
$\ddot{y}_{1s}$, $\dddot{y}_{1s}$, $\dot{\varphi}_{1s}$	The one-second average of the lateral acceleration, lateral jerk and roll velocity of the vehicle
$\ddot{y}^*_{W_P}(\tau)$, $\dot{\varphi}^*_{W_P}(\tau)$	The lateral acceleration and roll velocity responses of the vehicle running on the curved track
$\ddot{y}_p$	The lateral acceleration response perceived by the passenger
$\dddot{y}_p$	The lateral jerk perceived by the passenger
$\ddot{y}_c$	The vehicle's motion induced lateral acceleration response
$\dddot{y}_c$	The lateral jerk of the vehicle's motion-induced lateral jerk
$\lvert\ddot{y}_{1s}\rvert_{\max}$, $\lvert\dddot{y}_{1s}\rvert_{\max}$, $\lvert\dot{\varphi}_{1s}\rvert_{\max}$	The maximum values of the three one-second averages
z_{ci}, z_{bij}, z_{srm}	Vertical displacement of the car body, bogie and levitation magnet
${}_{II_m}z^{III_{ci}}$, ${}_{II_m}z^{III_{bij}}$, ${}_{II_m}z^{III_{srm}}$	Vertical displacement of the car body, bogie and levitation magnet defined in their own trajectory coordinate system
ϕ_{ci}, ϕ_{bij}, ϕ_{trijk}	Rolling displacement of the car body, bogie and rocker
ψ_{ci}, ψ_{bij}, ψ_{glm}	Yawing displacement of the car body, bogie and guidance magnet
θ_{ci}, θ_{bij}, θ_{srm}	Pitching displacement of the car body, bogie and levitation magnet
${}_{II_m}\phi^{III_{ci}}$, ${}_{II_m}\phi^{III_{bij}}$, ${}_{II_m}\phi^{III_{trijk}}$	Rolling displacement of the car body, bogie and rocker defined in their own trajectory coordinate system
${}_{II_m}\theta^{III_{ci}}$, ${}_{II_m}\theta^{III_{bij}}$, ${}_{II_m}\theta^{III_{srm}}$	Pitching displacement of the car body, bogie and levitation magnet defined in their own trajectory coordinate system
${}_{II_m}\psi^{III_{ci}}$, ${}_{II_m}\psi^{III_{bij}}$,	Yawing displacement of the car body, bogie and guidance

${}_{II_m}\psi^{III_{grm}}$	magnet defined in their own trajectory coordinate system
ϕ_g	The cant angle of the circular curved track
ϕ_{bal}	The balanced cant angle
${}_{II_m}\phi^{III_i}$, ${}_{II_m}\theta^{III_i}$, ${}_{II_m}\psi^{III_i}$	Three rotational motions of the i^{th} body defined in the trajectory coordinate system
$\psi(s)$, $\phi(s)$	The yawing and rolling angles of the track defined in the global coordinate system
${}_I\psi^{II_m}$, ${}_I\theta^{II_m}$ ${}_I\phi^{II_m}$	Three Euler angles about the three axes Z^{II_m}, Y^{II_m}, and X^{II_m}
$\Delta\psi$	The intersection angle of the two straight track sections
$\dot{\varphi}_p$	The roll velocity perceived by the passenger
$\dot{\varphi}_c$	The vehicle's motion-induced roll velocity

LIST OF ABBREVIATIONS

CR	Curve radius
DOF	Degree of freedom
FE	Finite element
HD	Hight difference between the outer rail and inner rail in the track
HGG	Hybrid guideway girder
Maglev	Magnetic levitation
SML	Shanghai Maglev Line
SSB	Simply supported beam

CHAPTER 1

INTRODUCTION

1.1 Research Motivation

High speeds have always been pursued in transportation engineering. In the past two decades, as a high-efficiency intercity transportation, magnetic levitation (maglev) trains have attracted the world's attention for its advantages over conventional wheel train systems, such as higher speed, lower risk of derailment, and less energy consumption (Han & Kim, 2016). Several maglev train lines, such as the Shanghai Maglev Line (SML; Figure 1.1a), Changsha Maglev Express (Figure 1.1b), and Incheon Airport Maglev (Figure 1.1c), have been built in urban areas. The maximum operating speed of the SML is 430 km/h, and the design speed of the Chuo Shinkansen Line (under construction) will reach 500 km/h. In view of the limited space available in urban areas, maglev trains often run on elevated viaducts supported by slender piers. Thus, the dynamic interaction between high-speed maglev trains and viaducts becomes significant and plays a crucial role in the design of the vehicles in the train and the major components of the viaduct. Furthermore, curved tracks/viaducts are inevitable in maglev lines because of land use compatibility in urban areas. Therefore, accurate dynamic analysis and alignment design of high-speed maglev trains running on straight, circular, and transitional viaducts are of extremely significant for the safety and comfortability of maglev trains, the safety and functionality of viaducts, and the construction cost reduction.

(a) Shanghai line (Image from Link 1)
(b) Changsha line (Image from Link 2)
(c) Incheon line (Image from Link 3)
(d) Emsland line (Image from Link 4)

Figure 1.1 Maglev train-based railway systems: (a, b) low- and medium-speed system; (c, d) high-speed system

Partially enhanced by the rapid expansion of high-speed wheel train systems, research on the moving load problems, in general, and vehicle–bridge interactions, in particular, has been booming in the past two decades (Chen & Li, 2000; Guo & Xu, 2001; Ju & Lin, 2003; Nagurka & Wang, 1997; Wu & Yang, 2003; Xia et al., 2000; Xia & Zhang, 2005; Xu et al., 2003, 2003, 2004, 2004, 2010; Xu & Guo, 2004; Yang et al., 2001, 2004; Yang & Yau, 2011; Zhai et al., 2013; Zhang et al., 2008). This interaction effect is critical in high-speed maglev lines because the vehicle mass of the maglev train is large, the maglev guideway is light and flexible, and the pier is tall and slender, as shown in Figure 1. Nonetheless, research on maglev transportation engineer is limited for the few lines available. Thus far, only some simplified dynamic models have been adopted to investigate the interaction effect between the maglev train and guideway system (Cai & Chen, 1996; Ren, 2008; Shi et al., 2007; Yau, 2009a, 2009b; Zhao & Zhai, 2002), most of which modeled the vehicle system by rigid bodies of several degree of freedoms (DOFs), regarded the guideway as a Bernoulli–Euler beam, and simulated the interaction by an equivalent concentrated force for each magnet. The key configurations of the interacting parts (i.e., the magnets of the train system and the modular function units of the viaduct system) have not been exactly considered in the coupled system. Some dynamic characteristics of the coupled system have been overlooked, and the response of the coupled system cannot be realistically revealed and compared with the measurement data (Li et al., 2015). Thus, a realistic and detailed maglev train–viaduct interaction model is of high necessity and significance to enhance the functionality of the numerical model and further advance the maglev transportation.

(a) Incheon line (Image from Link1)

(b) Changsha line (Image from Link2)

(c) Shanghai line (Image from Link3)

(d) Emsland line (Image from Link4)

Figure 1.2 Maglev trains running on curved viaducts: (a, b) low-speed train system; (c, d) high-speed train system

Maglev lines are often built in urban areas; thus, horizontally curved tracks are inevitable because of land use compatibility and socioeconomic consideration, and circular curved tracks are often introduced for this purpose. Accordingly, the issues of curving ride quality of the train and safety performance of the viaduct increase with high train speeds. Many studies have been attempted regarding this aspect (Shabana et al., 2008; Zboifiski, 1998; Zhao & Zeng, 1995; Sadeghi & Shoja, 2013; Dimitrakopoulos & Zeng, 2015; Zeng et al., 2016). The results showed that different from trains that run over straight bridges, the dynamic interaction between trains and curved tracks is three-dimensional (3D), which involves not only the vertical vibration but also the lateral and rolling vibrations. However, the anti-derailment and turning capabilities of the vehicle are highly enhanced in maglev lines compared with traditional ones due to the specific vehicle structure [i.e., a series of independent C-shaped arms (bogies)] that are evenly distributed under the carriage and wrapped around the guideway]. As a result, circular curved tracks with small radii and high cant angles are frequently constructed, as shown in Figure 1.3. For example, the SML is 30 km long, of which 18.5 km (more than 60%) is constructed with curved viaducts of various curvature radii from 2,000 m to 10,000 m and different inclination angles from 1° to 12° (Wu, 2003), as shown in Figure 1.3a. The circular curved section designed with a radius of 3,300 m and inclination angle of 12° for the train running at 300 km/h is marked in Figure 1.3a and shown in Figure 1.3b. The dynamic characteristics of the train running on the circular curved tracks are particular in high-speed maglev lines. Thus, a dynamic analysis of a coupled high-speed maglev train and circular curved viaduct is necessary to provide responsible guidance on the design of curved tracks.

(a) Schematic layout of SML (b) Curved viaduct in SML

Figure 1.3 Schematic layout of the SML and the curved viaduct

However, when the train enters the circular curved track directly from a straight path, the sudden centrifugal forces acting on the train seriously affect the train and bridge in the lateral direction (Dimitrakopoulos & Zeng, 2015). A transitional curved track section imbedded between them is necessary to ensure the ride quality of the train moving from the straight track section to the circular curved track section (Wu, 2003).

However, the curve radius (CR) and high difference (HD) between the outer and inner rails along the transitional curved track are distance-varying as required by the geometric smoothness of the whole track, resulting in a more complicated dynamic interaction than one when trains run on either the straight or circular curved track. Although many transitional curve-related studies have been conducted in the past decades, the majority of the studies solely focus on the alignment design for railway lines. In view of the geometric smoothness requirement, various transitional curves, such as the clothoid, fifth-order parabola (Tari & Baykal, 2005), seventh-order parabola (Woźnica, 2014), and sinusoid (Pirti et al., 2016), were designed. Moreover, many investigations that include vehicle dynamics have been conducted to verify the effectiveness and applicability of the transitional curves on the wheel/rail systems (Droździel & Sowiński, 2006; Kufver, 2000a, 2000b; Woźnica, 2014; Zboinski & Woznica, 2018). Nevertheless, these studies assumed that the track is a rigid body fixed on the rigid ground. They did not consider the dynamics of transitional viaducts on which railway vehicles run or the dynamic interaction between the vehicle and transitional viaduct. Moreover, in comparison with wheel trains, maglev trains are often designed with a higher operational speed even when they run over the curved sections. Therefore, a large cant angle or HD of the track is often required to avoid the use of a large CR and counteract the circular curved path-induced centrifugal acceleration on the vehicle. Accordingly, the requirement on the geometric smoothness of the transitional tracks becomes highly necessary. Therefore, the dynamic interaction between the high-speed maglev train and flexible transitional viaduct becomes considerable and cannot be neglected because of continuously changing and distance-varying CR and HD.

Meanwhile, from a practical perspective, the reduction of construction cost is consistently pursued in the alignment design of a high-speed maglev line. Optimizing the alignment parameters of the curved track is crucial in providing an economical but reliable solution for the construction of new maglev lines because the construction of a curved track is much more expensive than a straight track, and the ride comfort is much more serious. Although many studies on the alignment of horizontally curved track for wheel-based railway lines have been conducted in the past decades, most of them focus on either a circular or transitional track. The radius of a circular track is often determined by the limit value of the lateral acceleration of a train (Zboifiski, 1998; Zhao & Zeng, 1995; Sadeghi & Shoja, 2013). The most important parameter of a transitional track is its length (Kobry, 2017), which is usually determined by the limit of the rate of change of cant (Long & Wei, 2010; Ciotlaus, 2015; Zboinski & Woznica, 2017). To simplify the alignment design of horizontally curved tracks, several standards (CEN, 2010; Chandra & Agarwal, 2007; TB10621, 2014) recommend the limit values of R and L_t based on the allowable comfort level. The alignment parameters of circular and transitional tracks are optimized separately, the curved track-induced lateral and rolling vibrations of the vehicle are not included in the aforementioned studies, and the recommended limit values of the alignment parameters may not be optimal to the entire horizontal curved track. To address this issue, several research works have been conducted on the practical optimal alignment design of a horizontally curved track (Kufver, 1997, 2000; Kufver & Andersson, 1998; Um et al., 2010, 2015). The optimization works aim at finding the optimal alignment parameters for a curved track to ensure that the vehicle operates at the minimum comfort level, which will result in a long curved track required. However, from a practical perspective, the length of the entire curved track is expected to be minimum within a satisfactory comfort level to reduce construction cost and save land space. Thus, the solutions provided by the existing studies are not optimal from a practical viewpoint. Furthermore, in view of the high requirements on maglev-based horizontally curved tracks, the optimization works in the alignment design of high-speed maglev lines are critical (Wilson & Womack, 2004).

Given the aforementioned problems, accurate dynamic analysis and alignment design of high-speed maglev trains that run on straight, circular, and transitional viaducts are extremely significant for the safety and comfortability of maglev trains, the safety and functionality of viaducts, and construction cost reduction.

1.2 Research Objectives

This thesis aims to conduct the dynamic modeling and analysis of high-speed maglev trains that run on straight, circular, and transitional viaducts to reveal and predict the dynamic interaction between the vehicle and viaduct realistically and to optimize further a horizontally curved track in the alignment design of a high-speed maglev line. The major objectives of this research are described as follows.

(1) To propose a realistic and detailed high-speed maglev train-viaduct interaction model considering the modular function units of rails in the viaduct, the maglev poles in the levitation and guidance magnets, and the piers and bridge bearings in the flexible supports.

(2) To explore a trajectory coordinate-based framework for the analysis of high-speed maglev trains that run on a circular curved track and investigate the effects of the curve radii and cants on the dynamic responses of the vehicle and viaduct.

(3) To extend the trajectory coordinate-based analysis approach to the analysis of maglev trains that run on a transitional viaduct and demonstrate the transitional path-induced dynamic characteristics of the coupled systems, as well as the effect of the transitional length.

(4) To propose a minimum length-based optimization method for the alignment design of a horizontally curved track in a high-speed maglev line.

1.3 Assumptions and Limitations

The proposed high-speed maglev train-viaduct interaction model and its development on circular and transitional curved tracks and the optimization method for the alignment design of horizontally curved track are subject to the following assumptions and limitations.

(1) This thesis aims to investigate the dynamic characteristics of vehicle and viaducts with high-speed maglev trains that run on straight, circular, and transitional curved tracks, and further optimize the alignment design of a horizontally curved track. The in the lateral components is neglected in this study. Accordingly, the rigid body assumption can be used to model the major components of the train subsystem, which include car sbodies, rockers, bogies, levitation magnets, and guidance magnets.

(2) The displacements and rotations of vehicle rigid bodies are assumed to remain small throughout the dynamic analysis; thus, the sines of the angles of rotation may be equal to the angles themselves, and the cosines of the angles of rotation may be taken as a whole.

(3) Given that each modular function unit of the rail is installed to the concrete girder through four pairs of rigid brackets with bolts and screws, no relative motion is assumed between the rail and girder at the connection points of the brackets. As a result, the connections between the girders and rails can be simulated by the "Tie Contact" in ABAQUS.

(4) Each column sits on a pile cap foundation of a 10×10 m cross section and 2 m depth based on the study of Wu (2003). Moreover, each cap foundation sits on 20 to 24 piles, each 60 cm in diameter, which are driven down to a fine sand/clay stratum of a depth approximately 30-35 m. As a result, the stiffness of the pile group foundation is considerably larger than that of the piers and guideway girders. Thus, the influence of pile foundation and soil on the pier can be ignored, and the bottom of the pier can be assumed fixed.

(5) In practice, the whole circular curved concrete girder is prefabricated by strictly following a circular curve, while the circular rail track in a standard span is composed of eight straight modular functional units that form a polyline with each unit being 3.096 m. However, to simplify the circular curved rail track modeling, these polyline-composed units are modeled using the ideal circular curve in this research. This is because the maximum difference of the track alignment in the lateral direction based on the two modeling methods is much smaller than the track irregularity. The effect of the former on the system response is relatively weak, which can be covered by the latter. The rational of this assumption can be demonstrated by a typical case used in this study, in which the radius of the circular track is 3300 m. The maximum difference in the track alignment between the two modellings is 0.36 mm, which is much smaller than the track irregularity of a maximum around 1.5 mm. Therefore, the difference in the simulation results by the two modeling methods shall be very small.

(6) In the case studies, the moving speed of the train along the entire track (straight + transitional+ circular track) is assumed constant. Thus, the dynamic interaction effect between the vehicle and viaduct in the longitudinal direction (moving direction of the train) is weak and not discussed in this thesis.

(7) An experimental study is conducted on the train running on the SML to validate the proposed framework and computed results. Only simple measurements are conducted because the the operation of the high-speed maglev train must not be interrupted. Additional complicated field measurements shall be conducted in the future for a throughout validation.

1.4 Outline and Scope

This thesis covers various topics to achieve the above objectives. This thesis is divided into seven chapters. Figure 1.4 presents an overview of the thesis structure. The chapters are organized as follows.

Chapter 1 introduces the problem, motivation, objectives, assumptions, and scope of this work.

Chapter 2 presents an extensive literature review on relevant topics, including the development of maglev trains, dynamic modeling of wheel train-bridge interaction, dynamic modeling of maglev train–guideway interaction, vehicle-bridge interaction on horizontally circular curved track, vehicle-bridge interaction on transitional curved track, and optimization of horizontally curved track in the alignment design of railway lines.

Chapter 3 establishes a realistic and detailed high-speed maglev train-viaduct interaction model. The focus is on the accurate simulation of two subsystems, namely, the train subsystem (including the magnets) and the viaduct subsystem (including the modular function units of the rails). The electromagnet force-air gap model with a proportional-derivative (PD) controller is adopted to simulate the interaction between the maglev train via its electromagnets and the viaduct via its modular function units. The flexibilities of the rails, girders, piers, and associated elastic bearings are considered in the modeling of the viaduct subsystem to investigate their effects on the interaction between the two subsystems. An experimental study is also conducted to validate the effectiveness and accuracy of the proposed approach.

Chapter 4 proposes a trajectory coordinate-based framework for the analysis of high-speed maglev trains that run on a circular curved track. The motion of the maglev train system running on a curved track is defined by a series of trajectory coordinates, and the stiffness and damping matrices of the equations can be reduced into those of the straight track. The curved viaduct system is modeled in the global coordinate system using the finite element method (FEM). The electromagnet force-air gap model is also adopted for the maglev vehicle via its electromagnets and rails on the viaduct by appropriate transformation of coordinates. Moreover, an experimental study is conducted to partially validate the effectiveness and accuracy of the proposed approach. Furthermore, the effects of the curve radii and cants on the dynamic responses of the vehicle and viaduct are investigated in this chapter.

Chapter 5 extends and further develops the proposed trajectory coordinate-based analysis approach to the analysis of the maglev train running on the transitional viaduct, in which the origins of the trajectory coordinate systems move along the inner rail of the track, and the Euler angles used to describe the orientations of the coordinates are the functions of distance-varying CR and HD. By applying this framework to the SML, the dynamic characteristics and responses of the maglev vehicles running on the transitional viaduct are numerically and experimentally demonstrated. Furthermore, the effect of the transitional length on the coupled system is investigated in this chapter.

Chapter 6 proposes a new optimization method for the alignment design of horizontally curved track in a high-speed maglev line, in which the minimum length of the curved track is regarded as a major objective function, and the satisfaction of the minimum comfort level of passengers is considered a boundary condition to constrain the selection of alignment parameters of the curved track. The optimal solution from the proposed method is compared with the optimal solution from the current method and the existing solution for the actual curved track in the SML. The proposed dynamic model of a coupled maglev train and curved viaduct system is also used to validate the accuracy of the optimal solution from the proposed method.

Chapter 7 summarizes the contributions, findings, and conclusions of this thesis. The limitations of this study are discussed, and some recommendations for future study are provided.

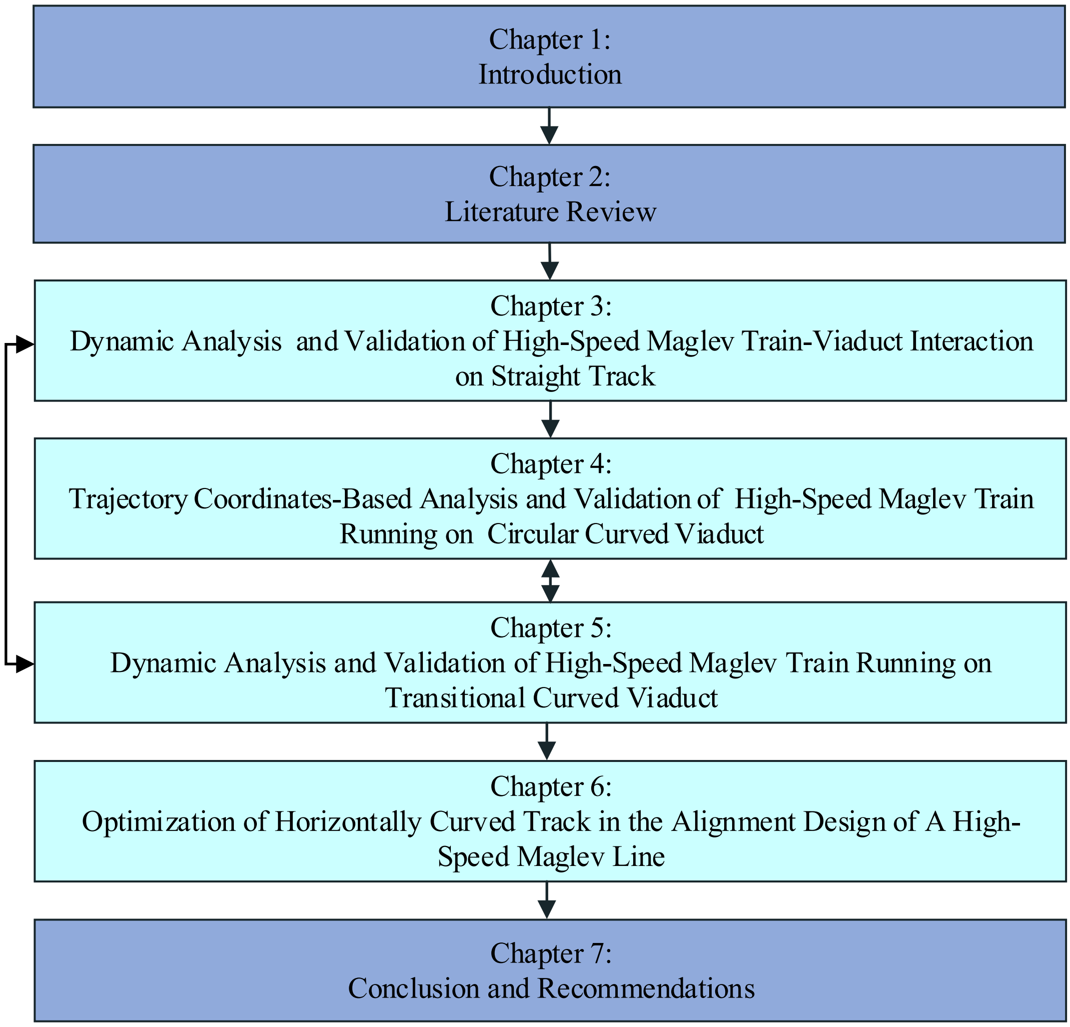

Figure 1.4 Overview of the thesis structure.

CHAPTER 2

LITERATURE REVIEW

As mentioned in Chapter 1, this thesis aims to conduct a dynamic modeling and analysis of a high-speed maglev train that runs on the straight, circular curved, and transitional curved viaducts and further optimize railway alignments at the curved sections. The methodology for the solution of the wheel/rail VBI is used in this thesis for reference. Thus, the current state-of-the-art development of some relevant topics will be reviewed in this chapter, including the development of maglev trains, wheel-based VBI, maglev train-guideway interaction at straight and curved sections, and optimization of the curved railway alignments.

2.1 Development of Maglev Trains

2.1.1 History

During the past four decades, maglev train systems have greatly advanced with the development of electromagnetic levitation technologies. In 1979, the first maglev-based train system with a 908 m track was displayed in Hamburg for the first international transportation exhibition and was opened to the public; it elicited great interest, and more than 50,000 passengers participated in the testing trip (from Wikipedia: maglev). In 1984, the world’s first low-speed commercial maglev system was constructed between the Birmingham International Airport terminal and the nearby Birmingham International railway station. Its track length was 600 m, and the train, which was levitated by electromagnets at an altitude of 15 mm, was propelled with linear induction motors. The first high-speed maglev test line was opened in 1984 in Emsland, Germany, and its total length was 31.5 km. The trains ran between Dörpen and Lathen with turning loops at each end and a maximum speed of 420 km/h. In addition, Japan, South Korea, and China devoted considerable efforts in developing their own maglev systems (from Wikipedia: maglev).

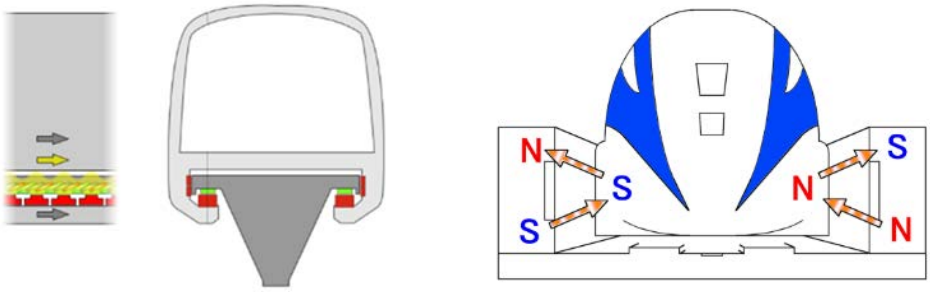

(a) Electromagnetic suspension (EMS) (b) Electrodynamic suspension (EDS)

Figure 2.1 Maglev suspension systems (images from Wikipedia: maglev)

2.1.2 Types of maglev train

With the advances in electromagnetic levitation technology, two main types of suspension systems were developed and applied, as shown in Figure 2.1.

EMS controls electromagnets in the train electronically to attract it to a magnetically conductive rail track. The system is typically arranged in a series of C-shaped arms, with the upper portion of the arm attached to the vehicle and the lower inside the edge that contains the magnets. Magnetic attraction varies inversely with the cube of distance; thus, minor changes in the distance between the magnets and the rail will produce greatly varying forces. These changes in force are dynamically unstable, and slight divergence from the optimum position tends to grow, thereby requiring sophisticated feedback systems to maintain a constant distance from the track (Goodall, 1985; Tsuchiya & Ohsaki, 2000). The major advantage of the suspended maglev systems is that they work at all speeds, unlike electrodynamic systems, which only work at a minimum speed of approximately 30 km/h.

EDS uses superconducting electromagnets or strong permanent magnets to create a magnetic field, which induces currents in nearby metallic conductors in the presence of relative movement, which pushes and pulls the train toward the designed levitation position on the guideway. A major advantage of EDS maglev systems is that they are dynamically stable, and changes in the distance between the track and the magnets create strong forces to return the system to its original position. In addition, the attractive force varies in the opposite manner, thereby providing the same adjustment effects. No active feedback control is needed. However, at slow speed, the current induced in these coils and the resultant magnetic flux are insufficiently large to levitate the train. Thus, the train must have wheels or some other form of landing gear to support the train until it reaches the takeoff speed. The entire track must be able to support low- and high-speed operations because a train may stop at any location due to equipment problems, for instance. Another downside is that the EDS system naturally creates a field in the track in front and to the rear of the lift magnets, which acts against the magnets and creates magnetic drag (He et al., 1994).

2.1.3 Advantages compared with wheel trains


(a) Maglev-based train system (b) Wheel-based train system

Figure 2.2 High-speed train systems

Maglev transport is non-contact and electric-powered and has many outstanding advantages compared with conventional wheel trains (Wu, 2003a). The two systems are shown in Figure 2.2.

Speed: Maglev allows higher speeds than conventional rail. The SML operates at a maximum speed of 430 km/h, whereas the high-speed railway train runs at a top speed of 300 km/h. Moreover, maglev vehicles accelerate and decelerate faster than traditional ones.

Maintenance: Maglev trains currently in operation have demonstrated the need for minimal guideway maintenance. Vehicle maintenance is also minimal (based on hours of operation rather than on speed or distance traveled). Traditional rail is subjected to mechanical wear and tear, which increases exponentially with speed, thereby increasing maintenance.

Efficiency: Given the lack of physical contact between the track and the vehicle, maglev trains experience no rolling resistance but only air resistance and electromagnetic drag, thereby potentially improving power efficiency.

Weight loading: High-speed rail requires more support and construction for its concentrated wheel loading. By contrast, maglev cars are lighter, and its weight is distributed more evenly.

Terrain: Maglev trains can ascend higher grades due to high propulsion power; the maximum gradient can reach 10%, whereas that for the conventional railway trains is only 4%. In addition, the evenly distributed electromagnets underneath the vehicle provide a high capacity of running on curves, together with the guidance system.

Noise: Maglev trains produce less noise than a conventional train at equivalent speeds because their noise comes from displaced air rather than from the wheels that touch the rails.

2.1.4 Operational maglev lines

The SML (see Figure 2.3) is the first EMS high-speed commercial train currently in operation. It has a top speed of 430 km/h and an average of 266 km/h. The line is designed to connect Shanghai Pudong International Airport with Longyang Road Metro Station. It covers a distance of 30.5 km in 8 min and has been in commercial operations since April 2004.

(a) Schematic layout

(b) Shanghai maglev train

Figure 2.3 SML (Images from Link 3)

The Linimo Line (see Figure 2.4) is the first commercial automated maglev system that commenced operation in March 2005 in Aichi, Japan. This line approaches from Banpaku Kaijo Station toward Fujigaoka Station with a top speed of 100 km/h and covers 9 km. It has a minimum operating radius of 75 m and a maximum gradient of 6%.

(a) Schematic layout (b) Linimo maglev train

Figure 2.4 Linimo Maglev System (Images from Link 5)

The Incheon Airport Maglev (see Figure 2.5) is a maglev line in South Korea that opened on February 3, 2016. It is the world's second commercially operating unmanned urban maglev line after Japan's Linimo. It runs at a maximum speed of 110 km/h and links Incheon International Airport to Yongyu Station with a length of 6.1 km. This maglev line specifically utilizes EMS propulsion.

(a) Schematic layout (b) Incheon maglev train

Figure 2.5 Incheon Airport Maglev System (Images from Link 1)

The Changsha Maglev Line (see Figure 2.6) is a medium–low speed maglev line in Changsha, China. It started its trial operations on May 6, 2016. The line stretches over 18.55 km and runs between Changsha Huanghua International Airport and the high-speed Changsha South Railway Station. It is designed for a speed of up to 120 km/h.

(a) Schematic layout (b) Changsha maglev train

Figure 2.6 Changsha Maglev System (Images from Link 2)

Beijing S1 Line (see Figure 2.7), the second medium–low speed maglev line in China, completed its trial operations on June 6, 2017. The entire line is 18.9 km. It starts from the Dinghuiqiao North Number Five Road and goes west toward

Mentougou with a top speed of 110 km/h.

(a) Schematic layout (b) Beijing maglev train

Figure 2.7 Beijing S1 Maglev System (Images from Link 6)

2.2 Wheel/Rail VBI

Enhanced by the rapid increase in the proportion of heavy vehicles on highway- and railway-based train systems on the viaduct, VBI dynamics have remained a crucial topic within the research interests of civil engineering in the past three decades (Yang et al., 2004). Particularly, with the development of the cost-effective construction technology toward bridges, that is, the application of lightweight materials and slender sections, the interaction problems between moving vehicles and bridge structures have become an indispensable factor in bridge design (Chen & Li, 2000; Guo & Xu, 2001; Ju & Lin, 2003; Nagurka & Wang, 1997; Wu & Yang, 2001, 2003; Xia et al., 2000a, 2000b, 2006a; Xia & Zhang, 2005; Xu et al., 2003a, 2003b, 2004a, 2004b, 2010; Xu & Guo, 2004; Yang & Yau, 1997, 2011; Yang et al., 1997, 1999, 2001, 2004; Yau et al., 1999, 2001; Yau, 2009c; Zhai et al., 2013; Zhang et al., 2008). Essentially, VBI indicates that the loads from the upper vehicles influence the lower bridge, resulting in the simultaneous vibration of the bridge, which, in turn, acts as excitation on the vehicle to induce its vibration simultaneously. The two subsystems, namely, the vehicle and the bridge, interact with each other through the contact forces existing between the wheels and track surface (Au et al., 2001). The VBI dynamics reveals fundamental disciplines within the dynamic problems between the vehicle and bridge, such as resonance and cancellation vibration of the vehicle and bridge (Yang et al., 2004), effect of wind on bridge (Xu, 2013), seismic dynamics (He et al., 2011; Zeng & Dimitrakopoulos, 2016a), and damage failure and detection on bridge (Beskhyroun et al., 2011; Shu et al., 2013).

2.2.1 Wheel train modeling

Increasingly high demands are continually placed on railway systems with the large-scale construction of high-speed railway lines across the world. The need for a full-scale and realistic train model has become predominantly demanding to examine the ride quality, running safety, and other dynamic issues of vehicles precisely. Thus far, various numerical models for railway train systems have been presented for different research purposes. Chu et al. (1980) introduced an analytical method for obtaining the dynamic responses of a train of locomotives moving on bridges based on a single-layer suspension system (Figure 2.8a). Yang et al. (2009) studied the pitching effect of the railway vehicle body by using a single-layer suspension system with a full model (Figure 2.8b). Yang and Yau (1997) developed a VBI element for the accurate analysis of railway bridges carrying high-speed trains on the basis of a two-level suspension system with a half model (Figure 2.8c). Yang and Wu (2001) derived a versatile element capable of treating various VBI effects by using a two-level suspension system with a full model (Figure 2.8d). Subsequently, the 3D train model (Figure 2.8e) is widely used in previous studies, of which Wang and Liu (2012) examined the lateral dynamics of the train.

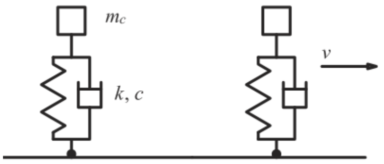

(a) Single-layer suspension system with a half model (Chu et al., 1980)

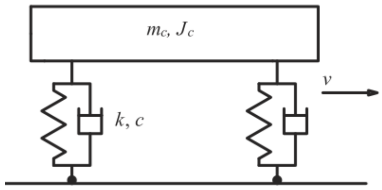

(b) Single-layer suspension system with a full model (Wang et al., 1991)

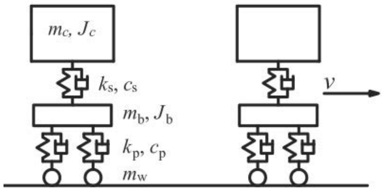

(c) Two-level suspension system with a half model (Yang & Yau, 1997)

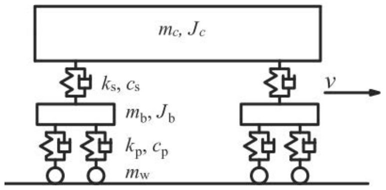

(d) Two-level suspension system with a full model (Yang & Wu, 2001)

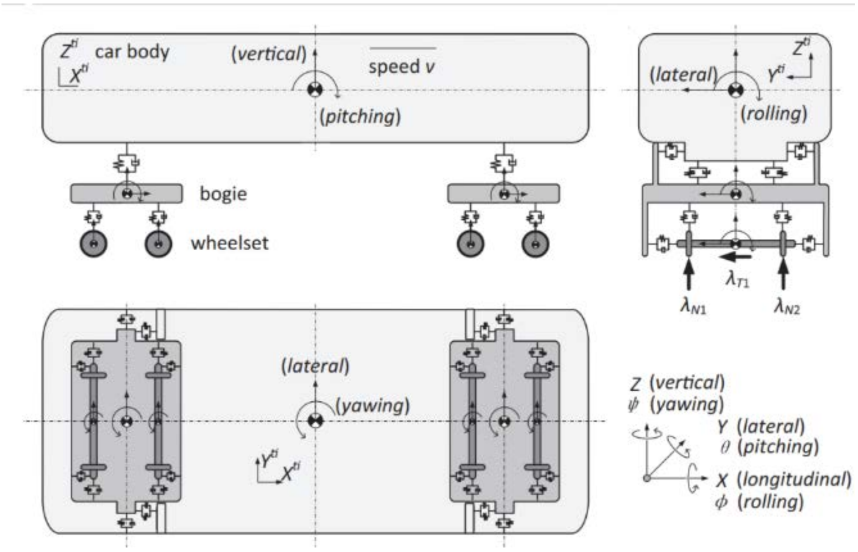

(e) 3D model (Dimitrakopoulos & Zeng, 2015)

Figure 2.8 Various railway train models in previous studies

Most studies have simulated the train vehicle as a multi-rigid-body assembly. Specifically, each vehicle is composed of one car body, two bogies, and four wheelsets. These components are considered rigid bodies, thereby neglecting their elastic deformations, as shown in Figure 2.8e. All components are connected via springs and dashpots, which represent the properties of the suspension systems. The train comprises a series of (usually identical) vehicles independent of each other. The car body has five DOFs; each bogie is designated with five DOFs, and each wheelset has three DOFs (Figure 2.8e). Furthermore, it is extensively applied for the dynamic investigation to assess the running qualities of a train on a curved path (Dimitrakopoulos & Zeng, 2015), track irregularity effect (Xu & Zhai 2017), seismic dynamics (Zeng & Dimitrakopoulos, 2016b), and wheel-rail contact model (Yu & Mao, 2017).

2.2.2 Railway bridge modeling

A simply supported beam is one of the most popular structures with regard to modeling of railway bridge (viaduct). Many analytical solutions toward various VBI problems have been deduced by simulating the bridge as Euler–Bernoulli or Timoshenko beam. Frýba and Steele (1976) derived closed form of a simply supported beam subjected to a moving constant force. Klasztorny and Langer (1990) studied the dynamic response of single-span beam bridges subjected to a series of moving loads. Yang et al. (1997)

investigated the dynamic vibration of simple beams subjected to the passage of high-speed trains. Yau et al. (2001) examined the impact response of the elastic bearing-supported beam to moving loads. Yang et al. (2004) and Xia et al. (2006) investigated the resonance and cancellation mechanism of the VBI dynamics based on Euler–Bernoulli beam theory. Yau and Frýba (2007) evaluated the dynamic response of suspended beams due to moving loads and vertical seismic ground excitations. Overall, the investigations of simply supported beam modeling bridge can provide foundational knowledge in the VBI dynamic problems and further advance the numerical models.

Meanwhile, the rapid developments of FEM and mode superposition method provide important support on the realistic dynamic modeling and analysis of various types of bridges, including truss bridges (Chu et al., 1985), multi-span uniform or non-uniform bridges (Yang et al., 1999), curved girder bridges (Yang et al., 2001), and cable-stayed bridges (Yang et al., 1995; Guo & Xu, 2001). Specifically, when the bridge span is short or the stiffness of the bridge is high, FEM may be the appropriate choice (Yang et al., 2004) to seek the local response for certain members of any type of bridge, which can meet the scale of the matrices and computation cost. Yau (2001) examined the resonance conditions of the continuous bridges under moving loads by utilizing a finite element bridge model. Xu et al. (2004) proposed an FEM-based framework for performing the vibration of cable-stayed bridge under train loading considering wind effect. Furthermore, Xia et al. (2006) investigated the seismic dynamic response of the VBI system using FEM. However, the mode superposition method is usually adopted for a bridge with low stiffness and long span (Zhang et al., 2008). The total DOFs for a bridge system can be greatly reduced by extracting the first few modes to express the global deformations. Xia et al. (2000) investigated the dynamic interaction between long suspension bridges and running trains. In addition, the mode superposition method can also be employed in modeling the multi-span steel truss arch bridge. Du et al. (2012a) presented a framework for the dynamic analysis of VBI effect under non-uniform seismic ground motions.

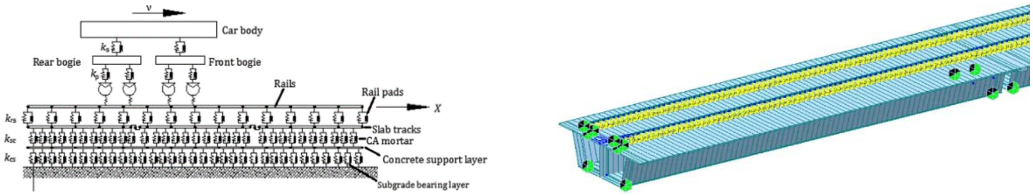

(a) Coupled vehicle–slab track model (b) FE model of railway viaduct

Figure 2.9 Railway viaduct model in previous studies

In terms of the structural design and safety assessment of railway bridges, the realistic dynamic modeling and analysis of the detailed bridge elements are necessary. Therefore, many studies have concluded the detailed configurations of rails, girder decks, and sleepers into the bridge model. Zhai et al. (2013) investigated the train-track-bridge dynamic interactions through numerical simulation and experimental validation based on CRH3 train, as shown in Figure 2.9a. Guo et al. (2012) established a 3D rail–ballast–bridge model using FEM and considering the elasticity and the continuity of the track system, as shown in Figure 2.9b. Moreover, Xu and Zhai (2017) conducted the reliability assessment of the railway vehicle–track dynamics subjected to the limits of track irregularities, including amplitudes and wavelengths, in which the detailed configurations of the bridge, such as rail tracks, rail pads, slab tracks, and concrete support layers, were fully considered. Moreover, the detailed configurations should also be included to analyze the fatigue reliability of the railway bridge comprehensively, such that the stress states of the rail track and girder deck can be used as the damage detecting indicator (Adasooriya, 2016). Eurocode (2003) suggested that the maximum acceleration response of the girder deck should be limited to less than 5 m/s^2; to this end, the verification of the dynamic performance of the girder deck was necessary to ensure the serviceability and safety of the railway bridge subjected to the sudden external forces, such as traffic accidents, seismic loads, and typhoon.

2.2.3 Interaction modeling

In studying the dynamic response of a VBI system, two sets of motion equations should be formulated, that is, one for the bridge and another for the train. The coupling of the two sets of equations can be attributed to the interaction or contact forces existing at the contact points of the two subsystems. Therefore, the interaction modeling is also a key part in duly investigating the dynamic characteristics of the train and bridge subsystems. However, the system matrices become time-dependent and should be updated at each time step in an incremental time–history analysis because the contact points between the wheels and rails change with the movement of vehicle along the bridge. In the rigid contact model, the wheel is assumed rigidly attached to the flexible rail and no separation exists between them. On this basis, the vertical wheel/rail force can thus be determined by the motion status of the wheel and the rail. Yang and Yau (1997) presented a linear relationship between the contact force and wheel/bridge relative displacement/velocity solely in the vertical direction. Zhai et al. (1996) established a nonlinear relationship with the relative displacement between the wheel and rail based on Herz theory, in which the normal contact forces between the wheels and rails were described by Hertzian nonlinear elastic contact theory and the tangential wheel/rail forces were computed by creep theory. The two wheel/rail contact force models have been widely employed by the succeeding research directly or with some modifications (Zhang et al., 2010, 2016; Zhai et al., 2013; Naeimi et al., 2015;Yu & Mao, 2017).

Furthermore, the numerical solution strategies for the VBI problem are included in the interaction modeling and directly determine the computational efficiency (Yang et al., 2004). The numerical solution strategies can generally be summarized into two types. Particularly, the first approach treats the two subsystems as an integrated and condensed system (Yang & Lin, 1995; Xia et al., 2000; Zhang et al., 2001, 2010; Song et al., 2003); consequently, the matrices in the global equations of motion become non-diagonal. This approach exhibits good accuracy, and the iteration between the two subsystems at each time step is avoided. However, the dimensions of the pertinent coupled matrices are considerable, and the matrices vary at each time step along with the position of the wheel on the bridge, resulting in heavy computational work. Under this background, another approach involving the separate integration of the two subsystems is widely utilized (Xia et al., 2003; Majka & Hartnett, 2008; Zhang et al., 2008; Dinh et al., 2009). This method focuses on the computation of the contact forces based on the aforementioned linear or nonlinear interaction force model, in which the adopted displacement and velocity motions are solely extracted from the equations of vehicles and railway bridge structures in terms of the contact displacements. Therefore, the vehicle and bridge equations should initially be discretized in the time domain, and the uncoupled equations of motion of each subsystem are individually solved. The calculated contact forces can then be treated as external loads and transformed as consistent nodal loads onto the wheels of train and rails of the bridge. Finally, the responses of the train and bridge structures can be solved in the next step. Such a procedure has demonstrated high computational efficiency for the reduction of the dimensions of coupled matrices.

2.3 Maglev Train–Guideway Interaction

Partially enhanced by the construction and operation of several maglev commercial lines in the past 12 years (Figures 2.4–2.8), a considerable number of research has been conducted on the problems of the interaction dynamics of maglev vehicles running on viaducts. This section mainly includes the literature review of the modeling of maglev train, guideway, interaction, and track irregularities.

2.3.1 Maglev train modeling

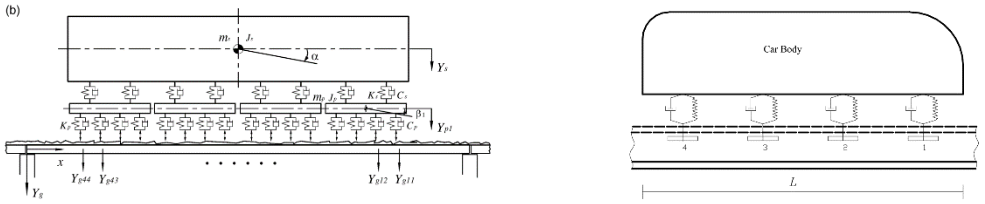

(a) Vehicle model (Zhao et al., 2002) (b) Vehicle model (Dai, 2005)

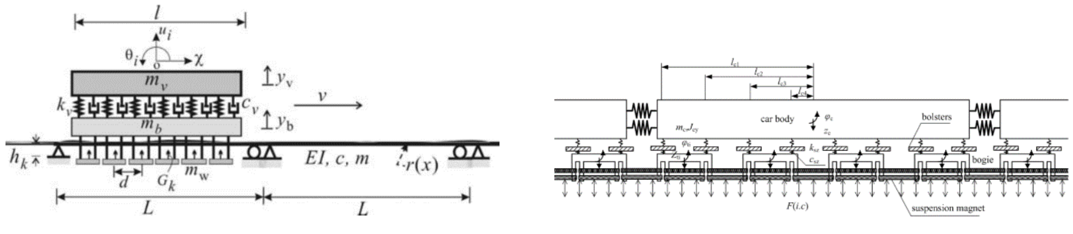

(c) Vehicle model (Yau, 2009b) (d) Vehicle model (Shi et al., 2011)

Figure 2.10 Two-dimension maglev vehicle model presented in previous studies

In the early period before 1990, most studies focused on the investigation of dynamics and control toward the electromagnetic suspension model. Reitz (1970) initially calculated the magnetic lift and drag forces from eddy currents, which was the groundwork for the following research regarding maglev vehicle model. Wilkie (1972) studied the control currents required to obtain suitable dynamic responses of the levitated coils, in which the effects of random track disturbances were initially discussed. The maglev vehicle modeling was not initiated until the particular interest focused on maglev vehicle–guideway effect. Regarding this issue, Cai et al. (1993a) proposed a two-DOF maglev vehicle model, that is, one vertical DOF for the car body and another for the magnet. The vehicle model simulation showed that the rigid maglev car body was supported by the rigid magnet with one linear spring–damper element, which formed the primary and secondary suspensions of the vehicle. Zhao and Zhai (2002) presented a 10-DOF vehicle model for a maglev train, including one car body and four maglev bogies, and each was assigned with 2 DOFs (i.e., vertical motion and pitching rotation, respectively). Similarly, by considering one car body and four magnets into one vehicle, Dai (2005) established a six-DOF train model based on the maglev TR08 system. In this model, the car body mass was assumed with vertical and pitching DOFs, and the four maglev bogies were assigned by only vertical motion to support the upper car body through four springs and dashpots. In addition, an 18-DOF train system comprising three vehicles was established, assuming that no vertical and rotational constraints exist between the adjacent car sections (Dai, 2005). On the basis of a similar 2D maglev vehicle model, several studies have been conducted for the vehicle–guideway interaction (Talukdar & Talukdar, 2016), guideway design (Ren, 2008), ground support settlement-induced vehicle response (Yau, 2009b), aerodynamic response (Yau, 2009a), seismic dynamics (Yau, 2010a), and train–guideway/foundation–soil system (Yang & Yau, 2011).

Various 3D vehicle models have also been developed to reveal the interaction dynamics between the maglev train and guideway systems. Nagurka and Wang (1997) presented a 3D maglev vehicle model by considering the following five DOFs: lateral and vertical translations, yawing, and pitching and rolling rotations; however, the other configurations of maglev bogie and magnets were ignored. On the basis of the UTM-01 train system (urban transit developed by South Korea), Han et al. (2006a) established a 3D FEM for the low-speed maglev vehicle by using LS-DYNA, including one car body and three bogies modeling with beam, solid, and shell elements, and their connections were simulated with discrete elements. A 3D full-vehicle model was also presented based on the UTM-01 train system to model the dynamic interaction between the vehicle and guideway (Kwon et al., 2008; Kim et al., 2015), as shown in Figure 2.11b. Germany TRANSRAPID is one of the most advanced high-speed maglev train systems. On this basis, Shi et al. (2007) and Zhao (2009) introduced a dynamic model of a high-speed maglev vehicle model, including one car body, eight C-shaped frames, detached bolsters, suspension magnets, and guidance magnets (Figure 2.11b). In summary, the key configurations (maglev poles) of the magnets of the train system were not exactly considered in the coupled system in the previous studies, and the magnetic force of each magnet was equivalent to one or several concentrated forces. Consequently, only partial coupling effects were investigated, and some dynamic characteristics of the coupled system were overlooked. Thus, the response of the coupled system could not be realistically predicted and compared against the measurement data (Li et al., 2015).

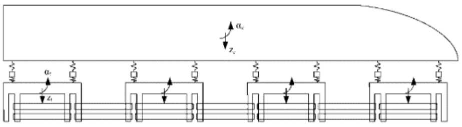

(a.1) Side view

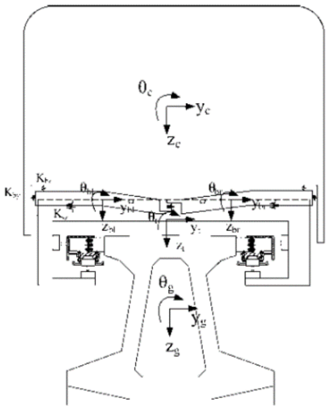

(a.2) Cross view

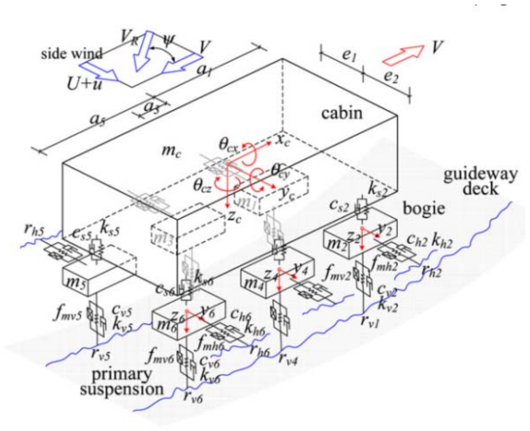

(a) Vehicle model (Shi et al., 2007) (b) Vehicle model (Kwon et al., 2008)

Figure 2.11 3D maglev vehicle model presented in previous studies

2.3.2 Modeling of guideways

Guideways are the supporting structures where the maglev train runs. They are the inseparable parts of the investigation of maglev train–guideway interaction. The hybrid guideway girders built for the maglev train are usually light and flexible (Wu, 2003a). Thus, the guideway effect shall be considered into the dynamic analysis of the upper vehicles; in turn, the dynamic characteristics of the train-induced guideway vibration should also be investigated to provide feedback regarding the design of maglev guideways. In previous studies, Bernoulli–Euler beam has been used extensively in modeling the maglev guideway structure. Katz et al. (1974) derived the flexible guideway effect from the vehicle's performance on the basis of Bernoulli–Euler beam theory, which provided a guideline for the design of guideway flexibility. By assuming that the maglev guideways were freely supported, homogeneous, isotropic, and uniform cross-section, Cai et al. (1993a, 1994) proposed a modal analysis method-based Bernoulli–Euler beam model for guideway modeling; the double-span flexible guideway was also considered (Cai et al., 1996). In recent studies, a Bernoulli–Euler beam modeling guideway has also been preferred because of its simplicity principle in theory and solution (Nagurka & Wang, 1997; Zhao & Zhai, 2002; Dai, 2005; Shi et al., 2007; Ren, 2008; Yau, 2009a, 2009b, 2010a; Zhao, 2009; Shi & Wang, 2011). Although the essential characteristics of the moving train-induced guideway vibration can be detected based on a Bernoulli–Euler beam model, the local dynamics of a certain member cannot be investigated. Yang et al. (2004) indicated that the installation of elastic bearings generally increases the response of the beam. Therefore, high responses of girders and rails shall be induced with the addition of elastic supports. In addition, the modular functional units of the rails installed on both sides of the girder deck directly interact with the magnets of the vehicle. Its flexibility-induced deformation, together with the vibration of its associated girder deck, generally results in a larger rail response compared with that from one-beam modeling girder. This finding may also affect the response of the coupled train–viaduct system due to its influence on the electromagnetic forces generated between the magnets and rails. Thus, formulating the flexibility of the elastic supports, girders, and rails into the viaduct model for an accurate prediction of the response of the coupled maglev train–viaduct system is necessary.

2.3.3 Modeling of electromagnetic forces

Electromagnetic force model used to simulate the interaction between the magnets of the train and rails of the viaduct is also a crucial part for the accurate dynamics analysis of the maglev train and guideway systems. The dynamic behaviors of the upper vehicles and lower guideway structures affect each other through the electromagnetic interaction forces. Furthermore, a control procedure is necessary to adjust the interaction forces constantly, thereby guaranteeing the stability of the maglev train. Hence, the electromagnetic interaction force model in the maglev system is different from the conventional one used in modeling the wheel/rail interaction model.

In 1970, Reitz first calculated the magnetic lift and drag forces from the eddy currents induced in the plate for various coil geometries. On this basis, Sinha (1987) achieved a considerable contribution to the development of control model toward electrodynamic levitation and ferromagnetic suspension. Particularly, the attractive force at any instant of time is calculated by Eq. (2.1), and the electromagnetic track configuration model is shown in Figure 2.12a.

$$F\left(i,h\right)=\frac{\mu_0 N^2 A}{4}\left[\frac{i\left(t\right)}{h\left(t\right)}\right]^2 \tag{2.1}$$

where $i\left(t\right)$ is electrical intensity, $h\left(t\right)$ is the magnetic air gap between the maglev pole and rail; *N* is the number of turns in the magnet winding; *A* is the pole face area; and μ_0 denotes air permeability.

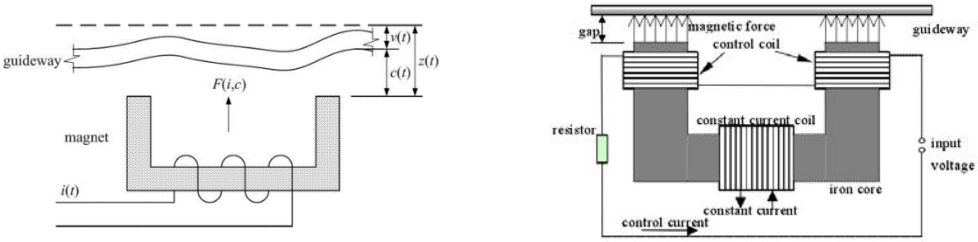

(a) Integrated model (Sinha, 1987) (b) Decoupled model (Teng, 2008)

Figure 2.12 Electromagnetic force model used in previous studies

The electromagnetic force model by Sinha provided an analytical expression for the interactive forces between the magnet and rail. When the train moves on a guideway, the track deflection and vehicle vibration are simultaneously excited with the track random roughness. Consequently, the air gap changes by time and is calculated as follows:

$$h(t)=h_0+u_v(t)+u_G(x_t)+s_r(x_t), \tag{2.2}$$

where h_0 is the design static gap at the static equilibrium state of the train, $u_v(t)$ is the motion of the magnet, $u_G(x_t)$ is the track deflection at x_t location, and $s_r(x_t)$ is the track roughness.

Nagurka and Wang (1997) further revised the electromagnetic force model of Sinha to facilitate its application to the superconducting magnet system, as shown in Figure 2.12b. On this basis, the electromagnetic force is calculated as follows:

$$F(i,h)=\frac{\mu_0 {N_m}^2 A_m}{4h^2}\left(N_{SC}\cdot I_{SC}+N_n\cdot i\right)^2 \tag{2.3}$$

where N_{SC} and N_n are the number of turns in the superconducting coil and the normal coil, respectively; I_{SC} is the current in superconducting coil, which is constant and determined by the gravity of the vehicle in static equilibrium; *i* is the trim current, which is driven by a controlled voltage. The relationship between the trim current and controlled voltage is provided based on Kirchhoff's voltage law, as shown as follows:

$$u=R_c\cdot i+\frac{\mu_0 A_m {N_m}^2}{2h}\cdot\frac{\partial i}{\partial t}-\frac{\mu_0 A_m {N_n}^2\left(N_{SC}\cdot I_{SC}+N_n\cdot i\right)}{2h^2}\cdot\frac{\partial h}{\partial t} \tag{2.4}$$

where *u* is the controlled voltage, and R_c is the resistance of the superconducting coil.

In addition, Lever (1998) presented a linearized electromagnetic force model, in which a small variance is assumed to occur in the air gap between the magnet and rail to facilitate the linearization of the electromagnetic force around the static equilibrium position of (i_0,h_0). On this basis, the electromagnetic force is equivalent to a spring–damper with constant coefficients, as expressed as follows:

$$f=f_0+k(h-h_0)+c\dot{h}, \tag{2.5}$$

where f_0 is the static magnetic force; *k* and *c* are the magnetic stiffness and damping at

(i_0, h_0), respectively; and h and $\dot{h}$ are the air gap and its change rate, respectively.

Subsequently, another linearized magnetic suspension model, including a linearized magnetic force model and a linearized relationship between the control voltage and trim current, was designed by Dai (2005). The attractive magnetic force is linearized at the nominal air gap, as shown as follows:

$$F(h,i) = F(h_0, i_0) + \left.\frac{\partial F}{\partial h}\right|_{\substack{h=h_0 \\ i=i_0}} (h - h_0) + \left.\frac{\partial F}{\partial i}\right|_{\substack{h=h_0 \\ i=i_0}} (i - i_0) \tag{2.6}$$

The voltage law in Eq. (2.6) is also linearized at the nominal air gap, as shown as follows:

$$\begin{aligned} u = {} & u_0\left(h_0, i_0, \dot{h}_0, \dot{i}_0\right) + \left.\frac{\partial u}{\partial h}\right|_{\substack{h=h_0 \\ i=i_0 \\ \dot{h}=\dot{h}_0 \\ \dot{i}=\dot{i}_0}} (h - h_0) + \left.\frac{\partial u}{\partial i}\right|_{\substack{h=h_0 \\ i=i_0 \\ \dot{h}=\dot{h}_0 \\ \dot{i}=\dot{i}_0}} (i - i_0) \\ & + \left.\frac{\partial u}{\partial \dot{h}}\right|_{\substack{h=h_0 \\ i=i_0 \\ \dot{h}=\dot{h}_0 \\ \dot{i}=\dot{i}_0}} \left(\dot{h} - \dot{h}_0\right) + \left.\frac{\partial u}{\partial \dot{i}}\right|_{\substack{h=h_0 \\ i=i_0 \\ \dot{h}=\dot{h}_0 \\ \dot{i}=\dot{i}_0}} \left(\dot{i} - \dot{i}_0\right) \end{aligned} . \tag{2.7}$$

The linearized magnetic suspension model has been widely employed due to its simplicity for the dynamic analysis of the maglev train–guideway interaction on a straight path (Shi et al., 2007; Ren, 2008; Han et al., 2009; Shi & Wang, 2011; Kim et al., 2015). However, in the case of the train moving in a circular or transitional curved track at a high speed, a series of considerable centrifugal forces acting on the vehicles may result in a relatively large lateral variance of the air gap. Therefore, the stability and computational accuracy of the coupled system cannot be maintained with the linearized magnetic suspension model.

In summary, the electromagnetic forces are highly dependent on the air gap and the electrical intensity. However, as shown in Eq. (2.2), the air gap is directly determined by the motion of the magnet, the deflection of the rail, and track irregularities. The electrical intensity should be simultaneously adjusted to maintain the comfort of the ongoing vehicle and avoid the non-derailment of the vehicle from the track. To this end, a series of control designs has been correspondingly utilized. For example, Cai et al., (1993b) designed a hybrid feedback control, which was well tested toward a two-DOF vehicle model. Particularly, a lead–lag regulator (active control) was designed for the primary suspension, and a "skyhook" damper (semi-active control) was constructed for the secondary suspension. On the basis of LQR, an optimal preview control with integral action was then used by Wang and Nagurka (1997), and a good performance of the vehicle under the cross-wind gust was examined. This control system was afterward used by Teng (2008) to assess the performance of high-speed maglev vehicle–guideway interaction. Meanwhile, many optimized control designs have been additionally developed to simulate precisely the interacting electromagnetic forces generated between the magnets and rail tracks from the practical maglev system. Yau (2009b) developed an onboard PI controller with constant tuning gains for the moving maglev vehicle to conduct the dynamic response of maglev vehicle/guideway system subjected to the ground settlement. Furthermore, an onboard hybrid LQR and PID controller with constraint rule base was also designed by Yau et al. (2010a) to keep the operating performance essentially running safely and maintain its satisfactory ride quality for a maglev train traveling over a suspension bridge shaken by horizontal earthquakes. Moreover, because of its efficiency, the PI controller is applied in conducting maglev train-bridge-soil interaction analysis and assessing the safety of maglev trains moving on bridges subject to foundation settlements and earthquakes (Ju et al., 2012, 2014).

2.3.4 Track irregularities

Track irregularities are the main source of vehicle vibration. As the train speed increases, the track irregularities have become an important issue of concern according to Yang et al. (2004). Many investigations have been conducted on the track irregularities of railway system, such as measurements (Qin & Wei, 2012; Shi et al., 2014; Ning et al., 2016), simulations (Haigermoser et al., 2015; Perrin et al., 2013), and the effects on vehicle and bridge (Yang et al., 2015; Sadeghi et al., 2016; Ling et al., 2017). Previous results show that the track irregularities slightly affect the response of bridges but exhibit considerable influence on the running stability and ride quality of trains.

Regarding maglev train system, track irregularities also predominate the vibrations of vehicle through its effect on the air gap, as shown in Eq. (2.2). To this end, several stochastic models for the simulation of track irregularities in the maglev system have been presented. Two approaches have already been taken toward characterizing track irregularities, that is, (1) a deterministic frequency response approach (Wilkie, 1972; Ziyaeifar, 2005) and (2) a power spectral density (PSD) approach (Wilkie, 1972; Perrin et al., 2013). For the former, a sinusoidal function is usually utilized to characterize the track irregularities, which can be expressed as follows:

$$H(x) = F(\lambda)\sin\left(\frac{2\pi x}{\lambda}\right) \tag{2.8}$$

where $H(x)$ denotes the distance-dependent irregularities, λ is the wavelength, and $F(\lambda)$ is a constant function corresponding to wavelength.

The modeling method of PSD-based track irregularities is preferred by many researchers because of its high precision. However, given that no PSD specification in terms of the maglev system was available in the earlier studies, the disturbance PSD for highways, airport runways, and railroads were employed for reference. For example, one parameter-determined PSD function was utilized based on the PSD specification from good-quality railroad welded rails (Wilkie, 1972; Katz et al., 1974; Nagurka & Wang, 1997; Zhao & Zhai, 2002), which can be expressed as follows:

$$S_V(\Omega) = \frac{A}{\Omega^n} \tag{2.9}$$

where A is the roughness amplitude; Ω is the wavenumber; and n is the frequency number, $n = 1.5$–2.5.

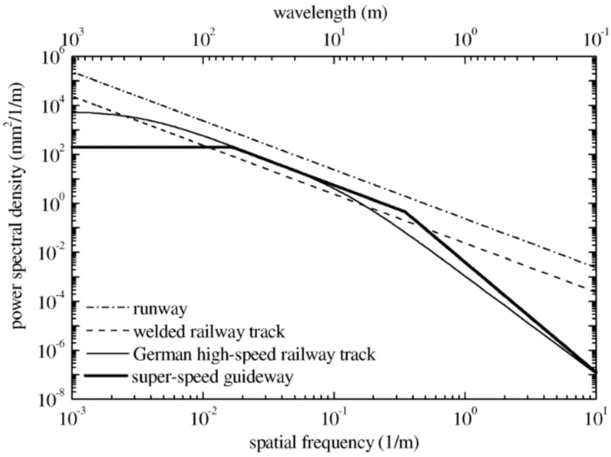

Figure 2.13 Guideway roughness PSD specifications for various road systems

Particularly, the applicability of the super-speed guideway-based PSD specification (Figure 2.13) in modeling the track irregularities of the media and low-speed maglev guideway has been verified through field measurements on the medium- and low-speed maglev systems in Tangshan, China (Zhang et al., 2011). Another PSD function was used by Yau (2009b) and Yang and Yau (2011) to simulate the vertical irregularities of the medium and low-speed maglev systems, which can be expressed as follows:

$$S(\Omega) = \frac{A_v \Omega_c^2}{\left(\Omega^2 + \Omega_r^2\right)\left(\Omega^2 + \Omega_c^2\right)}, \tag{2.10}$$

where Ω is the spatial frequency; $A_v = 1.5 \times 10^{-7}\,\mathrm{m}$ is the roughness amplitude; and Ω_r and Ω_c are relevant parameters, $\Omega_r = 2.06 \times 10^{-6}$ rad/m and $\Omega_c = 0.825$ rad/m.

Furthermore, on the basis of experimental investigation on the medium- and low-speed maglev systems in Tangshan (Zhang et al., 2011), a seven parameter-determined PSD function is used as reference for railway lines in China, as shown as follows:

$$S(\Omega) = \frac{A\left(\Omega^2 + B\Omega + C\right)}{\Omega^4 + D\Omega^3 + E\Omega^2 + F\Omega + G}, \tag{2.11}$$

where $S(\Omega)$ is the PSD $(\mathrm{mm}^2 \times \mathrm{m})$ of line irregularities; Ω is the spatial frequency (rad/m); and A, B, C, D, E, F, and G are seven characteristic parameters. These parameters have been assigned based on the experimental data, as shown in Table 2.1.

Table 2.1 Seven spectral characteristic parameters of PSD function for medium- and low-speed maglev systems

Plane	A	B	C	D	E	F	G
Vertical	0.00378	−0.08751	0.00195	−0.21334	0.01707	−0.00061	8.07×10^{-6}
Lateral	0.00267	−0.15091	0.00662	−0.28928	0.03118	−0.00147	2.60×10^{-5}

The experimental tests conducted on SML by Shi et al. (2014) reveal the features of high-speed maglev guideway irregularities, and the seven parameters used in Eq.(2.11) are revised as shown in Table 2.2.

Table 2.2 Seven spectral characteristic parameters of PSD function for high-speed maglev system

Plane	A	B	C	D	E	F	G
Vertical	0.1099	-2.2498	0.5424	-100.787	30.5318	-0.8974	0.0087
Lateral	0.0339	35.5133	-0.4281	32.4637	1.9028	-0.0321	3.50×10^{-5}

Figure 2.14 shows the PSD model proposed by Shi.

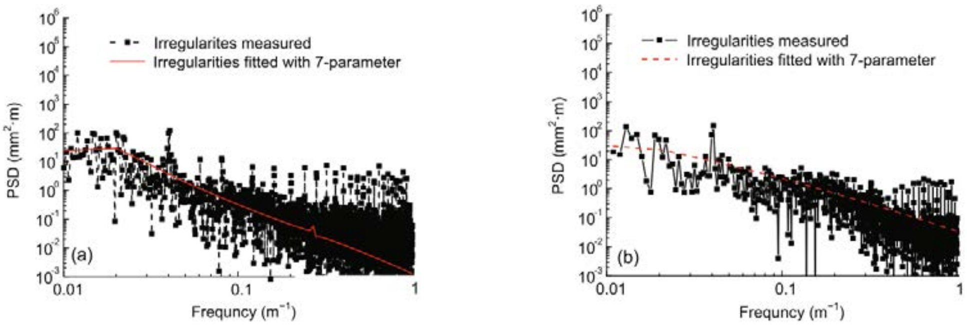

(a) PSD model for vertical irregularity (b) PSD model for lateral irregularity

Figure 2.14 Comparison of the simulated irregularities with measurements (Shi et al., 2014)

The sample function of stochastic process $s_r(x)$ can then be simulated by a trigonometry series as

$$s_r(x)=\sum_{k=1}^{N}\sqrt{2S(\omega_k)\Delta\omega}\,cos(\omega_k x+\phi_k)+\Delta s_x(n) \tag{2.12}$$

where ϕ_k is a random variable with a uniform distribution in $0\sim2\pi$; $\Delta\omega$ is the frequency bandwidth; $\Delta s_x(n)$ is the installment error of stator cores, which is a random variable with a uniform distribution in 0~1 mm; and n is the multiples of characteristic length L_{G1}, which is the interval space of poles. Figure 2.15 shows the vertical and lateral profiles of the track irregularities generated when the train operates at a speed of 430 km/h, which is also used in this thesis.

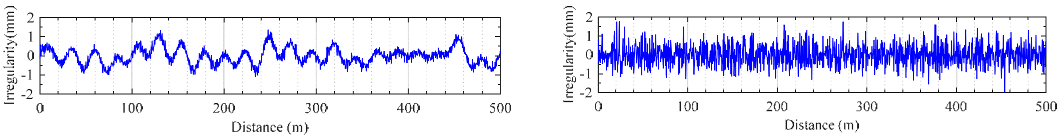

(a) Vertical irregularities (b) Lateral irregularities

Figure 2.15 Time sequence sample of track irregularities at 430 km/h train speed

2.4 VBI on Circular Curved Track

Horizontally curved tracks are inevitable in railway lines in urban areas due to land use compatibility and ride quality requirement, and circular curved tracks are often introduced for this purpose. Conceptually, when a train runs over a curved section, curved path-induced centrifugal force will be imposed on the vehicles. Sizable interaction forces between the vehicle and track are produced to act on the vehicle to avoid the non-derailment of the vehicle from the track. Meanwhile, the interaction forces are also applied on the track, thereby exciting considerable vibration of the track. In turn, the fluctuations of the vehicle are also high due to the coupling effect of the train and track.

Although an abundance of VBI studies have been conducted in the past two decades, the majority of these studies solely focus on the dynamical problem in vertical. Studies on curved bridge are scarce. Initiatively, Yang et al. (2001) derived the closed-form solution for a simply supported beam with a horizontal curvature subjected to a series of lateral and vertical moving loads. Xia et al. (2003, 2008) investigated the lateral dynamics of the train moving over the railway lines supported on straight girders. Shabana et al. (2008) presented a computational approach for vehicles moving on curved paths, in which the trajectory coordinate system was used to solve the VBI problems. Dimitrakopoulos and Zeng (2015) conducted a 3D dynamic analysis on the interaction between trains and curved railway bridges. Subsequently, the dynamic response of the curved bridge under conditions of resonance (Zeng et al., 2016) and frequent earthquakes (Zeng & Dimitrakopoulos, 2016a) has been investigated. The performance of a maglev train running over a curved guideway at a speed of 100 km/h was examined by Yim et al. (2009) by analyzing the air gap response. However, the elevation of guideway and the 3D interaction between the maglev train and curved viaduct were ignored.

In practice, as one of intercity transportation systems, high-speed maglev trains often run on an elevated viaduct. Most viaducts are light and flexible to reduce construction cost while saving the required space. The dynamic interaction between high-speed maglev trains and viaducts, which plays a crucial role in designing the vehicles of the train, including the suspension, and the major components of the viaduct, such as the stiffness, weight, and span length, becomes an important problem. This finding is particularly true for high-speed trains running on curved viaducts; however, this problem has not been thoroughly studied.

2.5 VBI on Transitional Curved Track

As soon as a train commences motion on a circular curve from a straight section, it is subjected to a sudden centrifugal force and gravity component, which not only causes discomfort to the passengers but also distorts and affects the rail tracks and its connected viaducts. Therefore, as the train speed increases, introducing a transitional curved track between the straight track and the circular curved track becomes necessary to ensure ride quality (Wu, 2003). Curved tracks are often defined by two important parameters, that is, CR and HD between the outer and inner rails. CR and HD are constant for circular curved tracks, whereas both parameters vary with distance for transitional curved tracks. Therefore, the dynamic analysis of trains running on a transitional track is more complicated than that when trains run on a straight or circular curved track.

Although an abundance of transitional curve-related studies have been conducted in the past decades, the majority of studies solely focus on the alignment design for railway lines. In view of geometric smoothness requirement, a transitional curve should start tangentially to the straight line and end tangentially to the circular curve, and the change of HD along the transitional track should keep pace with the change of the curvatures along the transitional track (Crandall, 1893). Given these requirements, Higgins (1922) designed a clothoid-formed wheel–railway transitional curve, in which 1/CR and HD linearly increased with the distance from the straight line to the circular curve. However, this curve provides only the first-order smoothness at the connection points between the straight line and transitional curve and between the transitional and circular curves. Moreover, passenger comfort cannot be satisfactorily guaranteed at these connection points. Several other transitional curves of higher-order smoothness, such as fifth-order parabola (Tari & Baykal, 2005), seventh-order parabola (Woźnica, 2014), half-wave sinusoid, and sinusoid (Pirti et al., 2016), have been proposed. Although these transitional curves can satisfy the geometric smoothness requirements, the effectiveness of their practical application should be examined through dynamic analysis or measurement.

In this regard, Kufver (2000a, 2000b) investigated the transitional track-induced vehicle responses and wheel–rail forces, in which the track was assumed to be rigid and geometrically characterized by the clothoid curve, and the vehicle body, bogies, and wheelsets were all modeled as rigid bodies. Droździel and Sowiński (2006a) compared the dynamic responses of the vehicle running on the clothoid, sinusoidal, and parabolic types of transitional curves, and their results showed that the vehicle responses and wheel–rail forces were considerably dependent on the types of transitional curves. Long (2008) studied the effect of transitional curve type on derailment coefficient, focusing on vehicle safety. The results showed that high smoothness of the curve led to low derailment coefficient. Moreover, Zboinski and Woznica (2018) conducted an all-sided literature survey on railway transitional curve optimization and its effects on vehicle dynamics. Nevertheless, the aforementioned studies assumed that the track a rigid body fixed on the rigid ground. They did not consider the dynamics of transitional viaducts, on which railway vehicles run, or the dynamic interaction between the vehicle and transitional viaduct.

Dimitrakopoulos and Zeng (2015) investigated the dynamic interaction between vehicles and a horizontally circular curved girder. They explored a particular case in which the vehicle directly entered the circular curved girder from a straight line. Their results showed the sudden centrifugal forces acting on the vehicle when it entered the connection point seriously affected the vehicle and girder in the lateral direction. Thus, the transitional curved girder between the straight line and circular curved girder was necessary for the dynamic interaction analysis between the vehicles and girders.

(a) Schematic layout of the SML (b) Curved viaduct in SML

Figure 2.16 Schematic layout of the SML and the curved viaduct system

In comparison with wheel trains, maglev trains are often designed with a high operational speed even when they run over curved sections. Therefore, a large cant angle or HD of the track is often required to avoid the use of a large CR and counteract the circular curved path-induced centrifugal acceleration on the vehicle. Accordingly, the requirement on the geometric smoothness of the transitional tracks becomes high. Moreover, when maglev trains run in urban areas, they often run over the viaduct for land use compatibility. The dynamic interaction between the high-speed maglev train and flexible viaduct becomes considerable and cannot be neglected. Figure 2.16 shows the straight-line viaduct, circular curved viaduct, and transitional curved viaduct used in SML. When the maglev train runs over a circular curved viaduct, the responses of the viaduct in the radial and rotational directions improves with the increase in track curvature and cant deficiency. This phenomenon may become crucial for maglev trains that run on transitional curved viaducts because of continuously changing and distance-varying CR and HD.

2.6 Optimization of Horizontally Curved Track in the Alignment Design of Railway Lines

Horizontally curved tracks are inevitable in a high-speed maglev line constructed in an urban area due to land use compatibility. A horizontally curved track is often composed by one circular curved track section and two transitional curved track sections. Each of the transitional track section is used to connect one straight section to the circular track section to ensure that the curvature of track continuously varies between zero and the curvature of the circular track section and the HD between the two rails in the track continuously varies between zero and the HD of the circular curved track section (Kobry, 2017; Lindahl, 2001; Pirti et al., 2016; Yi, 2017). The construction of a curved track is considerably more expensive than a straight track; thus, the length of the curved track is expected to be as short as possible and not cause any safety and comfort problems. Therefore, optimizing the alignment parameters of a curved track to provide an economical but reliable solution for the construction of a high-speed maglev line is crucial.

Although an abundance of studies on the alignment of horizontally curved track for wheel-based railway lines have been conducted in the past decades, most studies focus on either circular or transitional track. Furthermore, the radius (R) of a circular track has been extensively studied because it is the most important alignment parameter. For example, in terms of the limit value of the lateral acceleration of a train, Zboifiski (1998) determined the proper value of R as a function of the track cant. In terms of Vogel's wear index, Zhao and Zeng (1995) investigated the effect of different cant deficiencies on the limit value of R. Sadeghi and Shoja (2013) suggested the minimum value of R for different track cants and vehicle speeds by considering the limit of bending moment in sleepers. Regarding the transitional track utilized to connect the circular track to the straight track, the most important parameter is the transitional length L_t (Kobry, 2017). The limit value of L_t has been recommended based on various indicators. Ciotlaus (2015) determined the minimum value of L_t, by using the cant gradient limit and vehicle derailment boundary condition. Zboinski and Woznica (2017) obtained the minimum value of L_t from the perspective of allowable maximum lateral jerk. Long and Wei (2010) suggested the minimum value of L_t in view of the limit values of lateral acceleration, lateral jerk, and derailment. Several standards (CEN, 2010; Chandra & Agarwal, 2007; JB161, 2012; TB10621, 2014) provided the recommended limit values of R and L_t based on the allowable comfort level to simplify the alignment design of horizontally curved tracks. Nevertheless, the alignment parameters of the circular and transitional tracks have been separately optimized, the curved track-induced lateral and rolling vibrations of the vehicle are not included in the aforementioned studies, and the recommended limit values of the alignment parameters may not be optimal to the entire horizontal curved track.

The practical optimal alignment design of a horizontally curved track began with the introduction of an index P_{CT} (British Standard EN 12299:2009). This index describes the passengers' comfort level when the vehicle is running on a curved track in terms of lateral acceleration, lateral jerk, and roll velocity of the vehicle. Later on, Kufver (1997) explicitly formulated the comfort index P_{CT} as a function of the alignment parameters (i.e., R and L_t) of the curved track, in which the track profile-induced vehicle responses were used. This index was then applied to the alignment design of the curved track to seek the best combination of R and L_t for the minimum value of comfort level (Kufver & Andersson, 1998; Kufver, 2000). By using Kufver's index, Um et al. (2010) also evaluated the comfort level of the vehicle moving on the superimposition of vertical and transitional curves without considering VBI dynamics. The optimization of the superimposition of vertical and transitional curves was also conducted by using the minimum value of the comfort level as an objective function (Um et al., 2015). The aforementioned optimization works aimed at finding the optimal alignment parameters for the curved track to ensure that the vehicle operates at the minimum comfort level. However, from a practical perspective, the length of the entire curved track is expected to be minimum to reduce construction cost and save land space. Furthermore, many uncertainties exist in deciding the comfort level of passengers. The solutions provided by the existing studies may not be optimal from a practical perspective.

In comparison with wheel-based railway lines in rural areas, high-speed maglev lines constructed in urban areas are usually designed with a larger percentage of curved lines with smaller radii of curvature but higher cant angles (Wu, 2003b). For example, the SML is 30 km long (see Figure 2.16), out of which 18.5 km (more than 60%) is constructed with curved viaducts of various curvature radii from 2,000 m to 10,000 m and different cant angles from 1° to 12°. Therefore, the optimization of horizontally curved track is critical in the alignment design of high-speed maglev lines. In this regard, Wilson and Womack (2004) suggested the minimum value of R of the circular track based on the allowable lateral acceleration and the minimum value of L_t of the transitional track based on the limits of the change rate of cant. However, to the best of the author's knowledge, rigorous studies on the optimization of horizontally curved track in the alignment design of high-speed maglev lines are unavailable.

(a) SML (b) Emsland Maglev Line

Figure 2.17 Curved tracks in high-speed maglev lines

CHAPTER 3

MODELING AND VALIDATION OF COUPLED HIGH-SPEED MAGLEV TRAIN-AND-VIADUCT SYSTEMS ON STRAIGHT TRACK

3.1 Introduction

The accuarate modelling of train-viaduct interaction is the most essential part for the dynamics investigation of the maglev vehicle and viaduct, which can not only realistically reveal the dynamic characteristics of the two systems, but also guide the design of the vehicles in the train and the major components of the viaduct. Nonetheless, research on maglev transportation engineer is limited for the very few lines available. So far, only some simplified dynamic models were adopted to investigate the interaction effects between the maglev train and guideway system (Cai & Chen, 1996; Ren, 2008; Shi et al., 2007; Yau, 2009a, 2009b; Zhao & Zhai, 2002), most of which modeled the vehicle system by rigid bodies of several degree of freedoms (DOFs), regarded the guideway as a Bernoulli-Euler beam, and simulated the interaction by an equivalent concentrated force for each magnet. The key configurations of the interacting parts, i.e., the magnets of the train system and the modular function units of the viaduct system, were not exactly considered in the coupled system. As a result, some dynamic characteristics of the coupled system were overlooked, and the response of the coupled system could not be realistically revealed and compared against the measurement data (Li et al., 2015).

To this end, the maglev train-viaduct interaction model within consideration of the key configurations of the interacting parts, the magnets of the train system and the modular function units (rails) of the viaduct system, is established in this chapter. By applying the proposed model on the Shanghai maglev line, the essential characteristics of the coupled system can be obtained from the proposed model. Its accuracy and effectiveness are validated by comparing the simulated system dynamic responses and frequencies with those from the measurement data and Shi’s simulation.

3.2 Dynamic Modeling of Maglev Train Subsystem

3.2.1 Configuration of maglev train subsystem

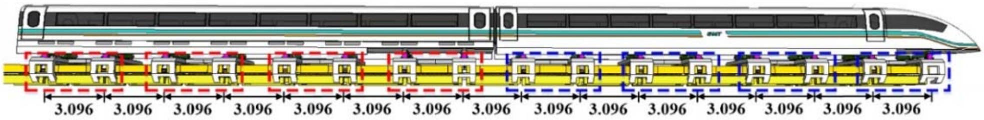

(a) Schematic diagram of maglev train used in SML (unit: m)

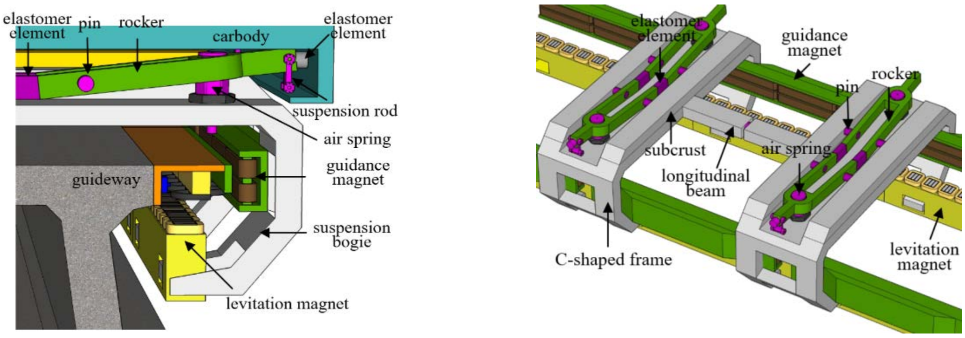

(b) Cross section diagram

(c) Plan diagram

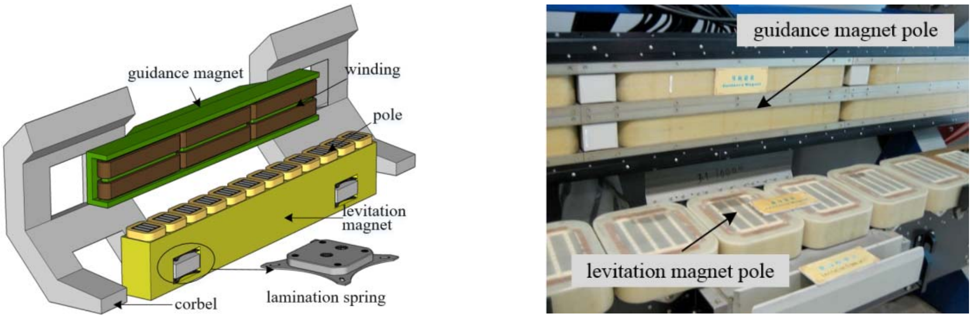

(d) Guidance and levitation magnets

(e) Maglev poles (Wu, 2003a)

Figure 3.1 Schematic diagrams of major components of a maglev train in SML

The high-speed maglev train system used in the SML contains a few vehicles, as shown in Figure 3.1a. Each vehicle contains one car body, four bogies, eight sets of rockeres, fourteen complete and four half sets of electrmagnets, see Figure 3.1b-3.1d. Each bogie is composed of two C-shaped frames, as shown in Figure 3.1c. The two C-shaped frames are conntecd by a longitudinal shaft and thus the two frames can rotate against each other but have no relative translational displacements. Levitation magnets and guidance magnets are installed on the four bogies through lamination springs on each side of the vehicle, and they are arranged with equal distance along the length of the entire vehicle (see Figure 3.1d and Figure 3.1e). The leviation magnets and the guidance magnets intearct with the rails (moduar functional units) of the guideway of the viaduct subsystem through a air gap of 10 mm when the vehicle is running.

3.2.2 Numerical model for maglev train subsystem

Twelve maglev poles with the pole pitch of 0.258m are equidistantly mounted on each levitation magnet, as seen in Figures 3.1d and 3.1e, and they are the foudemantal electromagnetization elements to produce levitation forces. However, in previous studies of modelling the interaction between the maglev train and guideway (Cai et al., 1996; Nagurka & Wang, 1997; Shi et al., 2007; Zhao & Zhai, 2002), one concentrated force model was widely used to represent the set of electromagnetic forces generated from the magnetic field between each magnet and rail. The pole pitch-induced interaction characteristics between the maglev train and guideway cannot be reflected. In this study, with reference to the train model proposed by Shi et al. (2007), a more realistic modeling of the maglev train subsystem with inclusion of maglev poles is presented in Figures 3.2a-3.2e. Since the maglev train subsystem is sizable and complicated. It is practically impossible to model every detail of all the components and connections in either subsystem. The following assumptions are thus adopted in the numerical model.

1. The rigid body assumption is used to model the major components of the train subsystem, which include car bodies, rockers, bogies, levitation magnets, and guidance magnets. The elastic deformation of these components is therefore not considered.
2. The displacements and rotations of the rigid body are assumed to remain small throughout the dynamic analysis so that the sines of the angles of rotation may be taken equal to angles themselves and the cosines of the angles of rotation may be taken unity.
3. Linear spring elements and linear spring-damper elements are used to model the connections between the rigid bodies of the train subsystem.
4. The moving speed of the vehicles in a maglev train is assumed to be constant, and

the guideway or the viaduct is assumed to be straight without curvature and inclination.

5. The interaction between the levitation magnet and the rail is realized through the twelve electromagnetic forces generated from the maglev poles, see Figure 3d. Each force is solely calculated based on the airgap between maglev pole and the displacement of the rail (modular functional unit) in vertical direction.
6. The interaction between the guidance magnet and the rail is also assumed as a three equivalent electromagnetic forces model, see Figure 3e. Each force is solely calculated based on the airgap between the position of the equivalent maglev pole and the displacement of the rail in lateral direction.

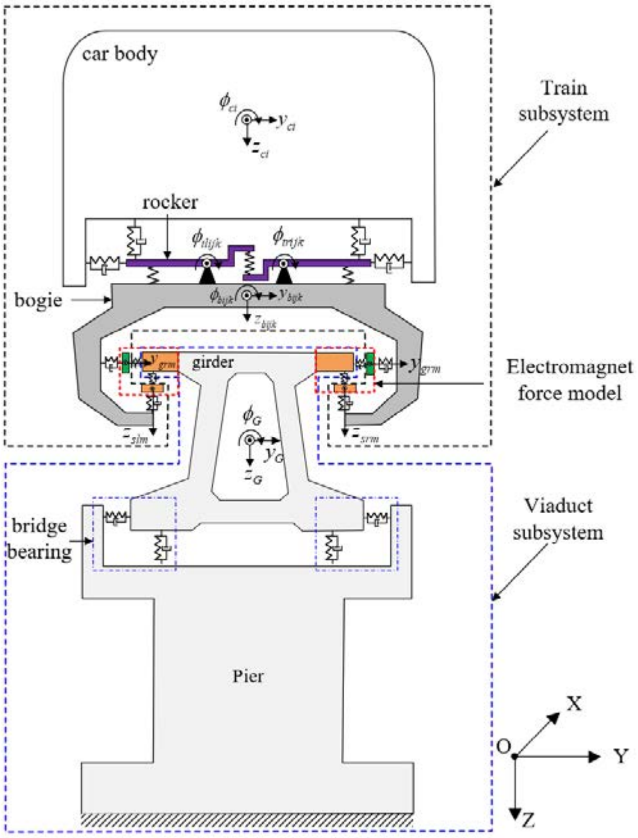

(a) Cross section of the numerical model

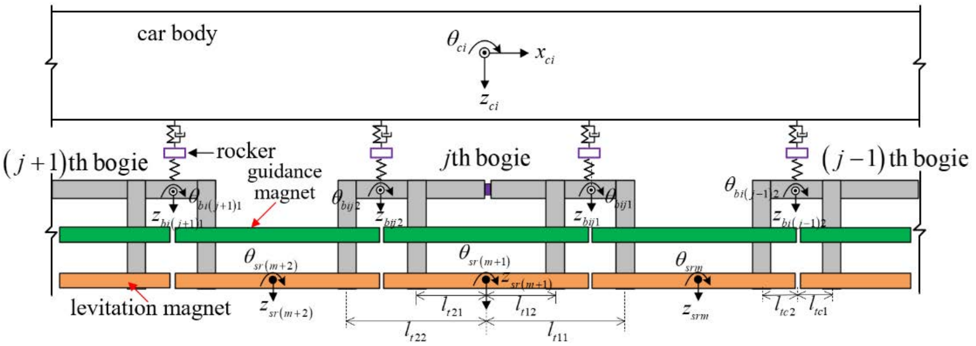

(b) The vertical plan of the train subsystem model

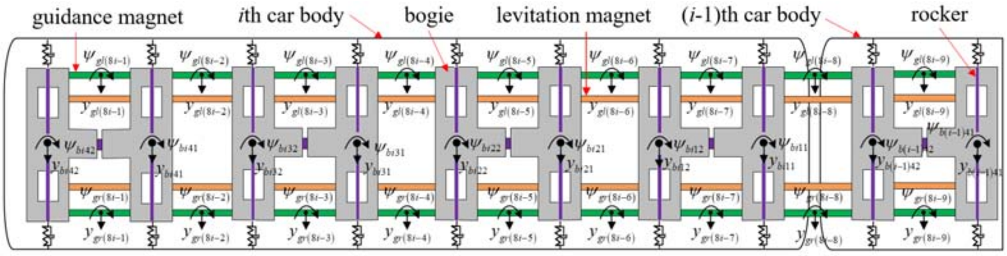

(c) The top plan of the train subsystem model

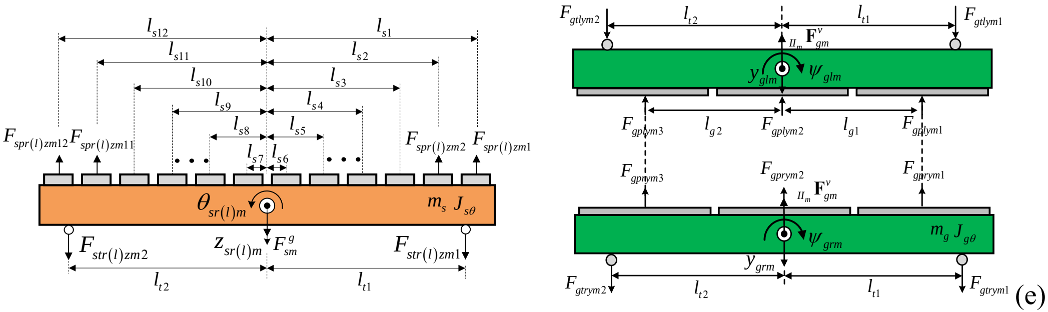

(d) Force diagram of levitation magnet

Force diagram of guidance magnet

Figure 3.2 The schematic numerical model of the maglev train subsystem

3.2.3 Degrees of freedom of the maglev train subsystem

All of the DOFs related to the car body, bogies, guidance magnets, and levitation magnets are shown in Figure 3.2, as well as their definitions of the positive directions. In this study, the i^{th} car body is modelled by five DOFs, i.e. the lateral, vertical, rolling, pitching and yawing, designated by Eq. (3.1a). Each bogie is composed of two C-shaped frames that are conntecd by a longitudinal shaft, and thus the two frames can rotate against each other but have no relative translational displacements. Therefore, the j^{th} bogie under the i^{th} car body has six DOFs: the lateral, vertical, rolling of the front C-shaped frame, rolling of the rear C-shaped frame, pitching and yawing, denoted by Eq. (3.1b). The rockers pinned on each C-shaped frame are composed by two rockers: the left rocker and right rocker (see Figure 3.1c and Figure 3.2c). The independent DOF of each rocker is for its rolling motion only, and the other DOFs are related to the DOFs of the bogie. The rolling rotations symbolized for the left rocker and right rocker are designated by Eq. (3.1c). Each set of levitation (guidance) magnets also consist of one left magnet and right magnet. Each levitation magnet is assigned with two DOFs: the vertical and pitching displacement. The DOFs for the right and left magnets of one set of levitation magnets are denoted by Eq. (3.1d). Similarly, each guidance magnet is also modelled by two DOFs: the lateral and yawing displacement. The DOFs for the right and left magnets of one set of guidance magnets are denoted by Eq. (3.1e). The total number of DOFs for each maglev vehicle is 101.

$$\mathbf{U}_{ci} = \begin{bmatrix} y_{ci} & z_{ci} & \phi_{ci} & \theta_{ci} & \psi_{ci} \end{bmatrix} \tag{3.1a}$$

$$\mathbf{U}_{bij} = \begin{bmatrix} y_{bij} & z_{bij} & \phi_{bij1} & \phi_{bij2} & \theta_{bij} & \psi_{bij} \end{bmatrix} \tag{3.1b}$$

$$\mathbf{U}_{tijk} = \begin{bmatrix} \phi_{trijk} & \phi_{tlijk} \end{bmatrix} \tag{3.1c}$$

$$\mathbf{U}_{sm} = \begin{bmatrix} z_{srm} & \theta_{srm} & z_{slm} & \theta_{slm} \end{bmatrix} \tag{3.1d}$$

$$\mathbf{U}_{gm} = \begin{bmatrix} y_{grm} & \psi_{grm} & y_{glm} & \psi_{glm} \end{bmatrix} \tag{3.1e}$$

where the subscribe c, b, t, s, and g refers to the car body, bogie, rocker, levitation (suspension) magnet and guidance magnet, respectively; the subscribe r or l refers to right or left side; j is the number of the bogie of the i^{th} car body (j =1,2,3,4); k =1,2 represents the front and rear C-shaped frame or the front and rear rocker on the j^{th} bogie; and m is the number of the set of magnets.

3.2.4 Equations of motion for the maglev train subsystem

The train subsystem consists of a few vehicles, and these vehicles are connected by the levitation magnets and guidance magnets. The train subsystem is quite sizable and complicated, and it is difficult to directly establish the equations of motion of the entire train subsystem. Thus, the equations of motion of each rigid body in the train subsystem are first established using the D'Alembert principle, and the equations of motion of all the rigid bodies are then assembled to form the equations of motion of the entire train subsystem. The equations of motion of each rigid body in the train subsystem can be expressed by

$$-\mathbf{M}^i\ddot{\mathbf{U}}^i + \mathbf{F}_e^i - \mathbf{F}_K^i - \mathbf{F}_C^i = \mathbf{0} \tag{3.2}$$

where the first term is the inertial force or the inertial moment and the subscript *i* means the *i*th rigid body; $\mathbf{M}^i$ is the mass matrix or the mass moment matrix of inertia of the *i*th rigid body; $\ddot{\mathbf{U}}^i$ is the translational acceleration response vector or the rotational acceleration response vector of the *i*th rigid body; $\mathbf{F}_e^i$ is the external force vector or the external moment vector acting on the mass center of the *i*th rigid body, which can be the gravity force, wind force or seismic force or the associated moments; $\mathbf{F}_K^i$ and $\mathbf{F}_C^i$ are the restoring and damping force or moment vector acting on the *i*th rigid body due to the stiffness and damping of the linear spring-damper elements connected to the *i*th rigid body.

3.2.4.1 Modeling of car body

The force diagrams of the *i*th car body are shown in Figure 3.3.

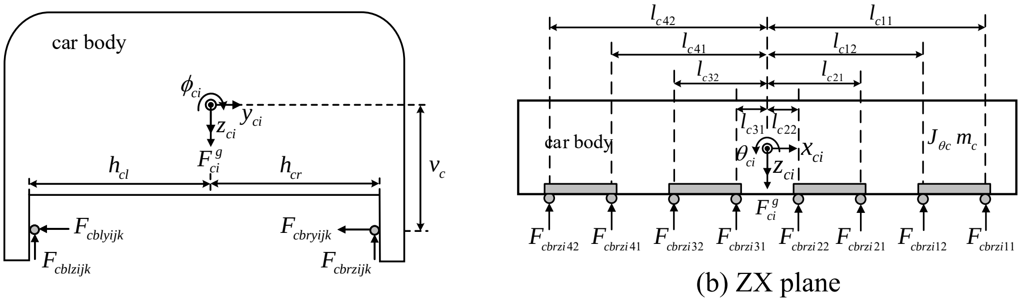

(b) ZX plane

(a) YZ plane

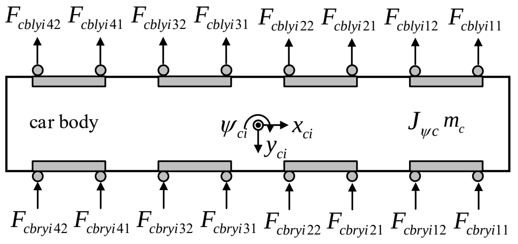

(c) XY plane

Figure 3.3 Force diagrams of the car body

Without considering wind, seismic or other external force, there is only the gravity force F_{ci}^{g} acting on the car body. The lateral forces $F_{cbr(l)yijk}$ and the vertical forces $F_{cbr(l)zijk}$ generated from the spring-damping elements between the i^{th} car body and the $(jk)^{\text{th}}$ rocker can be determined as follows:

$$\begin{aligned} F_{cbr(l)zijk} = & k_{cbz}\left[z_{ci} + h_{cr(l)}\phi_{ci} - l_{cjk}\theta_{ci} - z_{tijk} - h_{br(l)1}\phi_{br(l)ijk} - h_{cr(l)}\phi_{tijk} + l_{tk}\theta_{tijk}\right] \\ & + c_{cbz}\left[\dot{z}_{ci} + h_{cr(l)}\dot{\phi}_{ci} - l_{cjk}\dot{\theta}_{ci} - \dot{z}_{tijk} - h_{br(l)1}\dot{\phi}_{br(l)ijk} - h_{cr(l)}\dot{\phi}_{tijk} + l_{tk}\dot{\theta}_{tijk}\right] \end{aligned} \tag{3.3a}$$

$$\begin{aligned} F_{cbr(l)yijk} = & k_{cby}\left[y_{ci} - \phi_{ci}v_c + \psi_{ci}l_{cjk} - y_{tijk} - \psi_{tijk}l_{tk}\right] \\ & + c_{cby}\left[\dot{y}_{ci} - \dot{\phi}_{ci}v_c + \dot{\psi}_{ci}l_{cjk} - \dot{y}_{tijk} - \dot{\psi}_{tijk}l_{tk}\right] \end{aligned} \tag{3.3b}$$

where k_{cby} and k_{cbz} are the stiffness coefficients of the spring-damper elements installed between the i^{th} car body and the $(jk)^{\text{th}}$ rocker; c_{cby} and c_{cbz} are the damping coefficients of the same elements. The dimensions, $h_{cr(l)}$, l_{ckj}, $h_{br(l)1}$, l_{tk}, and v_c, in Eq. (3.3) are shown in Figure 3.3.

By substituting Eq. (3.3) into Eq. (3.2), the dynamic equations of motion of the i^{th} car body can be obtained as

$$-m_{ci}\ddot{y}_{ci} - \sum_{j=1}^{4}\sum_{k=1}^{2}\left(F_{blyijk} + F_{bryijk}\right) = 0 \tag{3.4a}$$

$$-m_{ci}\ddot{z}_{ci} - \sum_{j=1}^{4}\sum_{k=1}^{2}\left(F_{blzjk} + F_{brzjk}\right) + m_{ci}g = 0 \tag{3.4b}$$

$$-J_{\phi ci}\ddot{\phi}_{ci}-\sum_{j=1}^{4}\sum_{k=1}^{2}\left(F_{blzijk}h_{cl}+F_{brzijk}h_{cr}\right)+\sum_{j=1}^{4}\sum_{k=1}^{2}\left(F_{blyijk}+F_{bryijk}\right)v_{c}=0 \tag{3.4c}$$

$$-J_{\theta ci}\ddot{\theta}_{ci}+\sum_{j=1}^{4}\sum_{k=1}^{2}\left(F_{blzijk}+F_{brzijk}\right)l_{cjk}=0 \tag{3.4d}$$

$$-J_{\psi ci}\ddot{\psi}_{ci}-\sum_{j=1}^{4}\sum_{k=1}^{2}\left(F_{blyijk}+F_{bryijk}\right)l_{cjk}=0 \tag{3.4e}$$

where m_{ci} is the mass of the i^{th} car body; $J_{\phi ci}$, $J_{\theta ci}$, and $J_{\psi ci}$ are the mass moments of inertia of the i^{th} car body about the X-axis, Y-axis, and Z-axis, respectively.

3.2.4.2 Modeling of rocker and bogie

Each bogie is composed of two C-shaped frames, and the two frames are connected by a longitudinal shaft with a considerable rolling stiffness, as shown in Figure 3.1c and Figure 3.4. To facilitate the establishment of the equation of motion of the bogie, the coordinate system is assigned to each frame and the constraint conditions are then introduced. The origin of the coordinate system is fixed on the center of top surface (instead of the mass center) of each C-shaped frame in line with the longitudinal shaft (see Figure 3.4). For the front frame, the following five independent DOFs are assigned. In consideration that the front frame and the rear frame are connected by the longitudinal shaft, only one independent DOF ϕ_{tij2} is assigned to the rear frame.

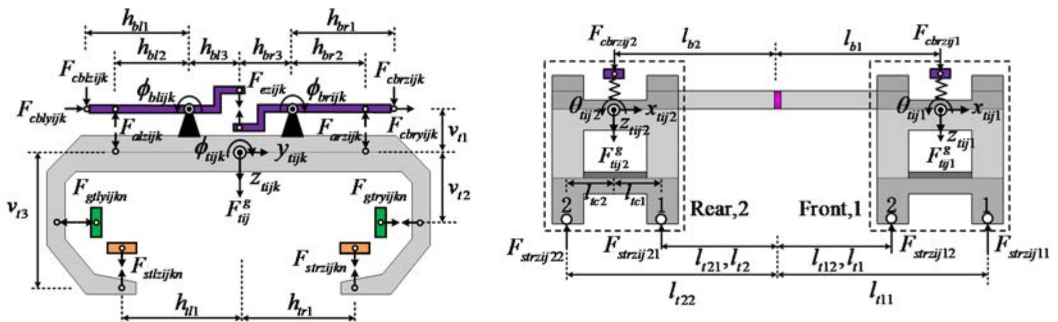

(a) YZ plane

(b) ZX plane

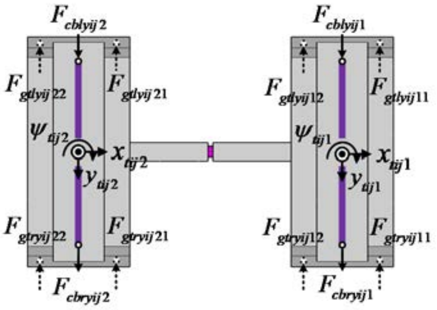

(c) XY plane

Figure 3.4 Force diagrams of the rockers and bogie

$$\mathbf{U}_{tij1} = \begin{bmatrix} y_{tij1} & z_{tij1} & \phi_{tij1} & \theta_{tij1} & \psi_{tij1} \end{bmatrix}^{\mathrm{T}} \tag{3.5a}$$

$$\mathbf{U}_{tij2} = \begin{bmatrix} y_{tij2} & z_{tij2} & \phi_{tij2} & \theta_{tij1} & \psi_{tij1} \end{bmatrix}^{\mathrm{T}} \tag{3.5b}$$

where $y_{tij2} = y_{tij1} - 2\psi_{tij1} l_{t1}$; $z_{tij2} = z_{tij1} + 2\theta_{tij1} l_{t1}$; and l_{t1} is the distance between the center of the shaft and the origin of coordinate system.

Force diagrams of the rockers and bogie are also shown in Figure 3.4, including the gravity force F_{tijk}^{g}, the lateral forces $F_{cbr(l)yijk}$ and the vertical forces $F_{cbr(l)zijk}$ from the spring-damper elements installed between the *i*th car body and the (*jk*)th rocker and calculated by Eq. (3.3), the connection forces $F_{str(l)zijkn}$ between the bogie and the levitation magnets, the connection forces $F_{gtr(l)yijkn}$ between the bogie and the guidance magnets, the air-spring force $F_{ar(l)zijk}$ between the rocker and bogie, and the interaction force F_{ezijk} between the adjacent rockers on the (*jk*)th frame. *n*=1,2 represents the front and the rear corbel of the frame. Except for the gravity force and the forces calculated by Eq. (3.3), the other forces can be determined by the following equations:

$$F_{ar(l)zijk} = k_{az}\phi_{br(l)ijk} h_{br(l)2} \tag{3.6a}$$

$$F_{ezijk} = k_{bbz}\left(\phi_{brijk} h_{br3} - \phi_{blijk} h_{bl3}\right) \tag{3.6b}$$

$$\begin{aligned}F_{str(l)zijkn} = {} & k_{tsz}\left(-z_{sr(l)m} + z_{tijk} - \theta_{sr(l)m}l_{tn} - \theta_{tijk}l_{tcn} + \phi_{tijk}h_{tr(l)1}\right) \\ & + c_{tsz}\left(-\dot{z}_{sr(l)m} + \dot{z}_{tijk} - \dot{\theta}_{sr(l)m}l_{tn} - \dot{\theta}_{tijk}l_{tcn} + \dot{\phi}_{tijk}h_{tr(l)1}\right)\end{aligned} \tag{3.6c}$$

$$\begin{aligned}F_{gtr(l)yijkn} = {} & k_{tgy}\left(-y_{gr(l)m} + y_{tijk} + \psi_{gr(l)m}l_{tn} + \psi_{tijk}l_{tcn} - \phi_{tijk}v_{t2}\right) \\ & + c_{tgy}\left(-\dot{y}_{gr(l)m} + \dot{y}_{tijk} + \dot{\psi}_{gr(l)m}l_{tn} + \dot{\psi}_{tijk}l_{tcn} - \dot{\phi}_{tijk}v_{t2}\right)\end{aligned} \tag{3.6d}$$

where k_{az} is the stiffness coefficient of the air-spring element between the rocker and bogie; k_{bbz} is the stiffness coefficient of the adjacent rockers in the Z-direction; k_{tsz} and c_{tsz} are the stiffness and damping coefficients of the spring-damper elements between the bogie and levitation magnets, respectively; k_{tgy} and c_{tgy} are the stiffness and damping coefficients of the spring-damping elements between the bogie and guidance magnets, respectively; the position number of magnets on the *n*th corbel of the *k*th frame of the *j*th bogie of the *i*th car body can be calculated by *m*=8(*i*-1)+2(*j*-1)+(*k*-1)+(*n*-1) for the entire train. The dimensions, $h_{br(l)1}$, $h_{br(l)2}$, $h_{br(l)3}$, l_{tn}, l_{tcn}, $h_{tr(l)1}$, v_{t1} and v_{t2}, in Eq. (3.6) are shown in Figure 3.4.

By substituting Eq. (3.6) and Eq. (3.3) into Eq. (3.2), the dynamic equations of motion of the rocker with 1 DOF and the bogie with 6 DOFs can be obtained as follows:

$$-J_{\phi b}\ddot{\phi}_{br(l)ijk} + F_{cbr(l)zijk}h_{br(l)1} - F_{ar(l)zijk}h_{br(l)2} \mp F_{ezijk}h_{br(l)3} = 0 \tag{3.7a}$$

$$-2m_t\left(\ddot{y}_{tij1} - l_{b1}\ddot{\psi}_{tij1}\right) + \sum_{k=1}^{2}\left(F_{bryijk} + F_{blyijk}\right) - \sum_{k=1}^{2}\sum_{c=n}^{2}\left(F_{gtryijkn} + F_{gtlyijkn}\right) = 0 \tag{3.7b}$$

$$-2m_t\left(\ddot{z}_{tij1} + l_{b1}\ddot{\theta}_{tij1}\right) + \sum_{k=1}^{2}\left(F_{brzijk} + F_{blzijk}\right) - \sum_{k=1}^{2}\sum_{n=1}^{2}\left(F_{strzijkn} + F_{stlzijkn}\right) + 2m_t g = 0 \tag{3.7c}$$

$$\begin{aligned}& -J_{\phi t}\ddot{\phi}_{tij1} - \sum_{n=1}^{2}\left(F_{strzij1n}h_{tr1} + F_{stlzij1n}h_{tl1}\right) + \sum_{n=1}^{2}\left(F_{gtryij1n} + F_{gtlyij1n}\right)v_{t2} \\ & -\left(F_{bryij1} + F_{blyij1}\right)v_{t1} + F_{brzij1}h_{cr} + F_{blzij1}h_{cl} - k_{tt\phi}\left(\phi_{tij1} - \phi_{tij2}\right) = 0\end{aligned} \tag{3.7d}$$

$$\begin{aligned}&-J_{\phi t}\ddot{\phi}_{tij2}-\sum_{n=1}^{2}\left(F_{strzij2n}h_{tr1}+F_{stlzij2n}h_{tl1}\right)+\sum_{n=1}^{2}\left(F_{gtryij2n}+F_{gtlyij2n}\right)v_{t2}\\&-\left(F_{bryij1}+F_{blyij1}\right)v_{t1}+F_{brzij2}h_{cr}+F_{blzij2}h_{cl}+k_{tt\phi}\left(\phi_{tij1}-\phi_{tij2}\right)=0\end{aligned}\tag{3.7e}$$

$$-2\left(J_{\theta t}+m_{t}l_{b1}{}^{2}\right)\ddot{\theta}_{tij1}+\sum_{k=1}^{2}\sum_{n=1}^{2}\left(F_{strzijkn}+F_{stlzijkn}\right)l_{tkn}-\sum_{k=1}^{2}\left(F_{brzijk}+F_{blzijk}\right)l_{tk}=0\tag{3.7f}$$

$$-2\left(J_{\psi t}+m_{t}l_{b1}{}^{2}\right)\ddot{\psi}_{tij1}-\sum_{k=1}^{2}\sum_{n=1}^{2}\left(F_{gtryijkn}+F_{gtlyijkn}\right)l_{tkn}+\sum_{k=1}^{2}\left(F_{bryijk}+F_{blyijk}\right)l_{bk}=0\tag{3.7g}$$

where m_t is the mass of one C-shaped frame; $J_{\phi t}$, $J_{\theta t}$, and $J_{\psi t}$ are the mass moments of inertia of one C-shaped frame about the X-axis, Y-axis, and Z-axis, respectively; and $k_{tt\phi}$ is the relatively rotational stiffness coefficient between the two C-shaped frames.

3.2.4.3 Modeling of levitation magnet

The force diagram of the m^{th} levitation magnet is shown in Figure 3.5. It includes the gravity F_{sm}^{g}, the connection forces $F_{str(l)zm1}$ and $F_{str(l)zm2}$ in the front end and rear end of the magnet respectively due to the connection of the levitation magnet to the bogie and calculated by Eq. (3.6), and the levitation electromagnet force $F_{spr(l)zmw}$ generated from the interaction between the w^{th} pole and the rail track ($w=1,\cdots,12$). The levitation electromagnet force $F_{spr(l)zmw}$ will be discussed in Section 3.4.

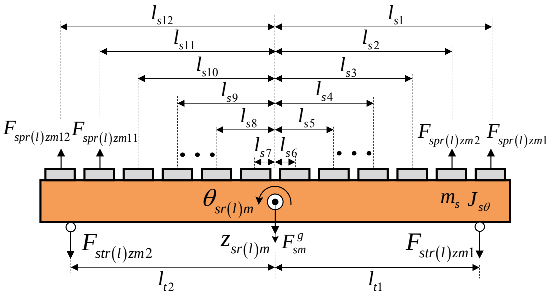

Figure 3.5 Force diagram of the levitation magnet

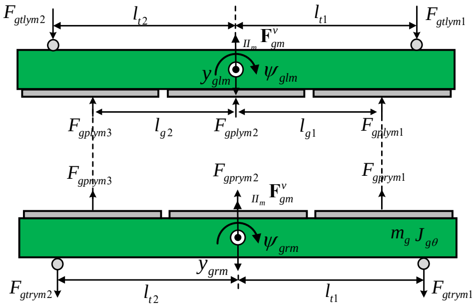

Figure 3.6 Force diagram of the guidance magnet

The dynamic equations of motion of the levitation magnet of 2 DOFs can be expressed as

$$-m_s \ddot{z}_{sr(l)m} + F_{str(l)m1} + F_{str(l)m2} - \sum_{w=1}^{12} F_{spr(l)zmw} + m_s g = 0 \tag{3.8a}$$

$$-J_{\theta s} \ddot{\theta}_{sr(l)m} - F_{str(l)m1} l_{t1} - F_{str(l)m2} l_{t2} + \sum_{w=1}^{12} F_{spr(l)zmw} l_{sw} = 0 \tag{3.8b}$$

where m_s is the mass of each levitation magnet; and $J_{\theta s}$ the mass moment of inertia of each levitation magnet about the Y-axis. The dimensions, l_{t1} , l_{t2}, and l_{sw}, in Eq. (3.8) are shown in Figure 3.5.

3.2.4.4 Modeling of guidance magnet

The force diagram of the m^{th} guidance magnet includes the connection forces $F_{gtr(l)ym1}$ and $F_{gtr(l)ym2}$ in the front end and rear end of the magnet due to the connection between the bogie and the guidance magnet and calculated by Eq. (3.6), and the guidance electromagnet force $F_{gpr(l)ymw}$ generated from the interaction between the equivalent w^{th} pole and the rail track, $w = 1,2,3$. The guidance electromagnet force $F_{gpr(l)ymw}$ will be discussed in Section 3.4. The dynamic equations of motion of the guidance magnet of 2 DOFs can be expressed as

$$-m_g \ddot{y}_{gr(l)m} + F_{tgr(l)m1} + F_{tgr(l)m2} - \sum_{w=1}^{3} F_{gpr(l)ymw} = 0 \tag{3.9a}$$

$$-J_{\psi g} \ddot{\psi}_{gr(l)m} + F_{tgr(l)m1} l_{t1} + F_{tgr(l)m2} l_{t2} - \sum_{w=1}^{3} F_{gpr(l)ymw} l_{sw} = 0 \tag{3.9b}$$

where m_g is the mass of each levitation magnet; and $J_{\psi g}$ the mass moment of inertia of each guidance magnet about the Z-axis. The dimensions, l_{t1}, l_{t2}, and l_{sw}, in Eq. (3.9) are shown in Figure 3.7.

3.2.4.5 Formulation of equation for the whole train subsystem

The equations of motion of all the rigid bodies (car bodies, rockers, bogies, levitation magnets and guidance magnets) are then assembled using MATHEMATICS software to form the equations of motion of the entire train subsystem. It can be written as

$$\mathbf{M}^V\ddot{\mathbf{U}}^V + \mathbf{C}^V\dot{\mathbf{U}}^V + \mathbf{K}^V\mathbf{U}^V = \mathbf{F}_{G\to V}^V + \mathbf{F}_e^V \tag{3.10}$$

where $\mathbf{M}^V$ is the mass matrix of the train subsystem; $\mathbf{K}^V$ and $\mathbf{C}^V$ are the stiffness and damping matrix of the train subsystem, respectively; $\mathbf{U}^V$, $\dot{\mathbf{U}}^V$, and $\ddot{\mathbf{U}}^V$ are the displacement, velocity, and acceleration vectors of the train subsystem; $\mathbf{F}_{G\to V}^V$ is the interaction force vector between the vehicles and guideway rails, which will be further discussed in Section 3.4; and $\mathbf{F}_e^V$ is the external forces such as gravity forces, seismic loads or wind loads.

Suppose that the number of vehicles in one train is *N*. The displacement vector $\mathbf{U}^V$ of the train subsystem can be assembled from the sub-displacement vectors of all vehicle components.

$$\mathbf{U}^V = \begin{bmatrix} \mathbf{U}_N^c & \mathbf{U}_N^b & \mathbf{U}_N^t & \mathbf{U}_N^s & \mathbf{U}_N^g \end{bmatrix}^{\mathrm{T}} \tag{3.10a}$$

where the sub-terms of $\mathbf{U}^V$ represent the sub-displacement vectors of the car bodies, bogies, rockers, levitation magnets, and guidance magnets included in *N* vehicles, respectively. Furthermore, each term in Eq. (3.10a) consists of *N* sets of sub-terms for the car bodies, bogies, and rockers, and *M* sets of sub-terms for the levitation and guidance magnets, in which $M = 8N - 1$.

$$\mathbf{U}_N^{(c,b,t)} = \begin{bmatrix} \mathbf{U}_{(c,b,t)1} & \cdots & \mathbf{U}_{(c,b,t)i} & \cdots & \mathbf{U}_{(c,b,t)N} \end{bmatrix} \tag{3.10b}$$

$$\mathbf{U}_N^{(s,g)} = \begin{bmatrix} \mathbf{U}_{(s,g)1} & \cdots & \mathbf{U}_{(s,g)m} & \cdots & \mathbf{U}_{(s,g)M} \end{bmatrix} \tag{3.10c}$$

where the sub-matrices $\mathbf{U}_{bi}$ and $\mathbf{U}_{ti}$ of the bogies and rockers belonging to the i^{th} vehicle can be expanded as:

$$\mathbf{U}_{bi}=\left[\mathbf{U}_{bi1}\quad \mathbf{U}_{bi2}\quad \mathbf{U}_{bi3}\quad \mathbf{U}_{bi4}\right] \tag{3.10d}$$

$$\mathbf{U}_{ti}=\left[\mathbf{U}_{ti11}\quad \mathbf{U}_{ti12}\quad \cdots\quad \mathbf{U}_{tijk}\quad \cdots\quad \mathbf{U}_{ti41}\quad \mathbf{U}_{ti42}\right] \tag{3.10e}$$

More specially, the sub-displacement vectors in Eq. (3.10a-e) are expressed with respect to the DOFs of the vehicle components as defined in Eq. (3.1).

The mass matrix in Eq. (3.10) can be accordingly assembled from the sub-mass matrices.

$$\mathbf{M}^{V}=\operatorname{diag}\left[\mathbf{M}_{N}^{c}\quad \mathbf{M}_{N}^{b}\quad \mathbf{M}_{N}^{t}\quad \mathbf{M}_{N}^{s}\quad \mathbf{M}_{N}^{g}\right] \tag{3.11a}$$

where the sub-terms of $\mathbf{M}^{V}$ represent the mass matrices of the car bodies, bogies, rockers, levitation magnets, and guidance magnets included in *N* vehicles, respectively. Corresponding to Eq. (3.10b, c), the sub-terms of $\mathbf{M}^{V}$ can be further written as:

$$\mathbf{M}_{N}^{(c,b,t)}=\operatorname{diag}\left[\mathbf{M}_{(c,b,t)1}\quad \cdots\quad \mathbf{M}_{(c,b,t)i}\quad \cdots\quad \mathbf{M}_{(c,b,t)N}\right] \tag{3.11b}$$

$$\mathbf{M}_{N}^{(s,g)}=\operatorname{diag}\left[\mathbf{M}_{(s,g)1}\quad \cdots\quad \mathbf{M}_{(s,g)m}\quad \cdots\quad \mathbf{M}_{(s,g)M}\right] \tag{3.11c}$$

where the mass matrices $\mathbf{M}_{bi}$ and $\mathbf{M}_{ti}$ of the bogies and rockers belonging to the *i*th vehicle are

$$\mathbf{M}_{bi}=\operatorname{diag}\left[\mathbf{M}_{bi1}\quad \mathbf{M}_{bi2}\quad \mathbf{M}_{bi3}\quad \mathbf{M}_{bi4}\right] \tag{3.11d}$$

$$\mathbf{M}_{ti}=\operatorname{diag}\left[\mathbf{M}_{ti11}\quad \mathbf{M}_{ti12}\quad \cdots\quad \mathbf{M}_{tijk}\quad \cdots\quad \mathbf{M}_{ti41}\quad \mathbf{M}_{ti42}\right] \tag{3.11e}$$

More specially, the mass matrices in Eq. (3.11a-e) are further parameterized as follows:

$$\mathbf{M}_{ci}=\operatorname{diag}\left[m_{ci}\quad m_{ci}\quad J_{\phi ci}\quad J_{\theta ci}\quad J_{\psi ci}\right] \tag{3.11f}$$

$$\mathbf{M}_{bij} = \mathrm{diag}\left[m_{bij} \quad m_{bij} \quad J_{\phi bij} \quad J_{\phi bij} \quad J_{\theta bij} \quad J_{\psi bij} \right] \tag{3.11g}$$

$$\mathbf{M}_{tijk} = \mathrm{diag}\left[J_{\phi trijk} \quad J_{\phi tlijk} \right] \tag{3.11h}$$

$$\mathbf{M}_{sm} = \mathrm{diag}\left[m_{srm} \quad J_{\theta srm} \quad m_{slm} \quad J_{\theta slm} \right] \tag{3.11i}$$

$$\mathbf{M}_{gm} = \mathrm{diag}\left[m_{grm} \quad J_{\psi grm} \quad m_{glm} \quad J_{\psi glm} \right] \tag{3.11j}$$

The stiffness and damping matrices of N vehicles in the train subsystem have a similar structure. The stiffness matrix in Eq. (3.10) can be expressed as

$$\mathbf{K}^{V} = \begin{bmatrix} \mathbf{K}_N^{cc} & & & & \mathrm{sym} \\ \mathbf{K}_N^{tc} & \mathbf{K}_N^{tt} & & & \\ \mathbf{K}_N^{bc} & \mathbf{K}_N^{bt} & \mathbf{K}_N^{bb} & & \\ \mathbf{0} & \mathbf{0} & \mathbf{K}_N^{sb} & \mathbf{K}_N^{ss} & \\ \mathbf{0} & \mathbf{0} & \mathbf{K}_N^{gb} & \mathbf{0} & \mathbf{K}_N^{gg} \end{bmatrix} \tag{3.12a}$$

where the sub-matrices are

$$\mathbf{K}_N^{(cc,tt,bb)} = \mathrm{diag}\left[\mathbf{K}_{(cc,tt,bb)1} \quad \cdots \quad \mathbf{K}_{(cc,tt,bb)i} \quad \cdots \quad \mathbf{K}_{(cc,tt,bb)N} \right] \tag{3.12b}$$

$$\mathbf{K}_N^{(ss,gg)} = \mathrm{diag}\left[\mathbf{K}_{(ss,gg)1} \quad \cdots \quad \mathbf{K}_{(ss,gg)m} \quad \cdots \quad \mathbf{K}_{(ss,gg)M} \right] \tag{3.12c}$$

$$\mathbf{K}_N^{(tc,bc,bt)} = \mathrm{diag}\left[\mathbf{K}_{(tc,bc,bt)1} \quad \cdots \quad \mathbf{K}_{(tc,bc,bt)i} \quad \cdots \quad \mathbf{K}_{(tc,bc,bt)N} \right] \tag{3.12d}$$

$$\mathbf{K}_N^{(sb,gb)} = \begin{bmatrix} \mathbf{K}_{(sb,gb)11} & \cdots & \mathbf{K}_{(sb,gb)1i} & \cdots & \mathbf{K}_{(sb,gb)1N} \\ \vdots & \ddots & \vdots & \ddots & \vdots \\ \mathbf{K}_{(sb,gb)m1} & \cdots & \mathbf{K}_{(sb,gb)mi} & \cdots & \mathbf{K}_{(sb,gb)mN} \\ \vdots & \ddots & \vdots & \ddots & \vdots \\ \mathbf{K}_{(sb,gb)M1} & \cdots & \mathbf{K}_{(sb,gb)Mi} & \cdots & \mathbf{K}_{(sb,gb)MN} \end{bmatrix} \tag{3.12e}$$

The detailed expression of each element matrix in Eq. (3.12) is given in Appendix

A. The damping matrix $\mathbf{C}^V$ can be obtained by simply replacing "**K**" by "**C**" in Eq. (3.12).

3.3 Dynamic Modeling of Viaduct Subsystem

The SML shown in Figure 3.7a is taken as an exmaple to demonstrate and establish the numerical model of the maglev viaduct subsystem.

3.3.1 Configuration of viaduct subsystem

The overall view of the maglev viaduct system is shown in Figure 3.7a, which includes rails, concrete girders, concrete piers and bearings. The rail in a standard span consists of eight modular functional units, providing the functions of levitation and guidance for the maglev train (Ren, 2008) (see Figure 3.7d). These functional units with a module length of 3.096m are evenly installed to each side of the concrete girder through four pairs of brackets (see Figure 3.7b). The concrete girder is apt to carry and transfer the loads from vehicles to the concrete piers through the bearings (Figure 3.7 e). Such a combination of rails and concrete girder is also called hybrid guideway girder (HGG) designed specifically for the maglev system (Ren, 2008). The concrete girder is of box-shaped section, and its dimensions are shown in Figure 3.7c.

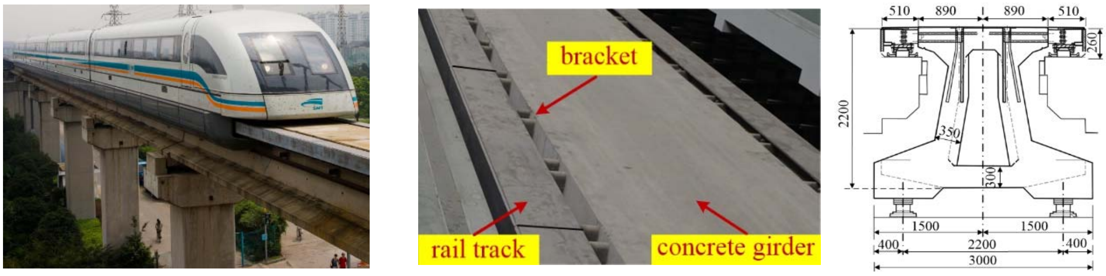

(a) Viaduct with single-column piers

(b) Connections between rails and girder

(c) Cross section (unit: mm)

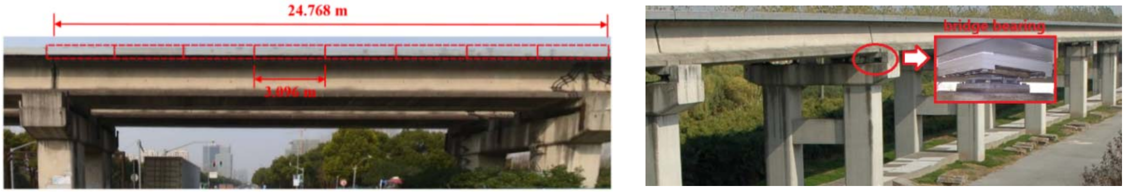

(d) A standard span of the viaduct in SML.

(e) Bridge bearings between the girder and pier

Figure 3.7 Viaduct subsystem used in SML

3.3.2 Viaduct finite element model with rails and supports

Actually, 42% of the Shanghai maglev line is constructed using single-column piers, as seen in Figure 3.7a. For the rest of the line, two-way viaduct is constructed with the double-column piers, as seen in Figure 3.7e. It can be seen that each girder is actually sit right above on its own column. Since this study does not consider the case where the two trains run oppositely and pass the same double-column pier, the viaduct system with single-column pier is adopted and simulated, which can greatly improve the computational efficiency. Having said that, a comparison of simulation results between the double- and single-column pier viaducts for one span has been conducted, and it has been demonstrated that the modeling of the line using single-column pier viaduct is accurate enough.

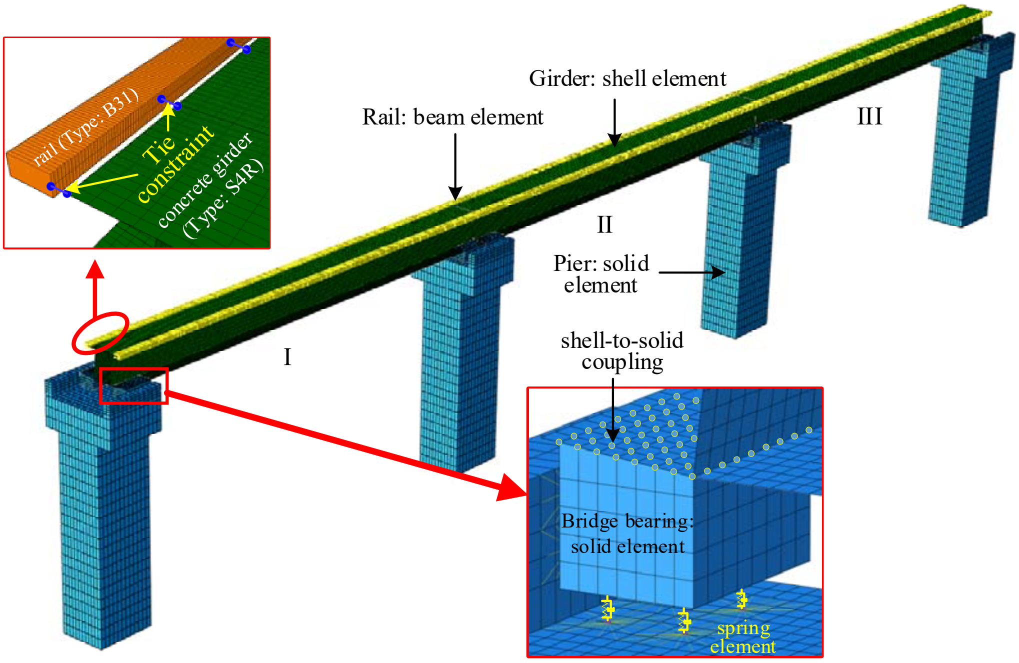

Figure 3.8 Finite element model of maglev viaduct subsystem with reference to SML.

In this study, finite element method is employed to establish the viaduct model referring to the Shanghai maglev line. The flexibilities of rails and its components of modular functional units and brackets are fully considered in the viaduct model (see Figure 3.8). The piers are constructed with a typical dimension of 1.8×1.8 m cross section and 10 m high. According to reference (Wu, 2003a), the stiffness of the pile-group foundation is far larger than that of the piers and guideway girders. Thus, the influence of pile foundation on the pier and on the soil can be ignored and the bottom of the pier can be assumed to be fixed (Malveiro et al., 2014). The steel-laminated elastomeric bearings are designed with a plan dimension of $500 \times 500\,\mathrm{mm}^2$ and 40 mm thick to connect the girder to pier (see Figure 3.7e). The flexibilities of both are thus considered in the viaduct finite element model.

Specifically, the rails of HGG are modeled using 3D 2-node linear Timoshenko beam elements (Type: B31 in ABAQUS), as shown in Figure 3.8. The concrete girder of the box-shaped was modeled using a 4-node, quadrilateral, stress/displacement shell element with reduced integration and a large-strain formulation (Type: S4R in ABAQUS). Six DOFs for each node of one B31 and S4R element are considered, which include three translational DOFs and three rotational DOFs. The upper concrete part of the bearing and the piers are modeled using 8-node linear brick element with reduced integration (1 integration point), and six DOFs of each node in one C3D8R element are considered.

The tie constraint, tying two separate surfaces together so that there is no relative motion between them (Smith, 2019), is implemented to simulate the connections between the rails and girders. Here, the nodes of the shell elements of the concrete girders are taken as master nodes and those of the beam elements of the rails are used as slave nodes for the connections (see Figure 3.8). The shell-to-solid coupling element is utilized to connect the upper concrete part of the bearing to the girder. Besides, 4 linear spring-damper elements parameterized by the equivalent stiffness of the bearing are employed to represent the bearing connected to the single-column pier in both the vertical and lateral directions. More specifically, the stiffness of each spring-damper element in the vertical and lateral direction is assigned with 4×10^{10} N/m and 1.25×10^{10} N/m, respectively. The damping coefficient of each spring-damper element in the vertical and lateral direction is assigned with 1.2×10^{5} N•sec/m and 6×10^{4} N•sec/m, respectively (Malveiro et al., 2014). The pier is modeled by 8-node solid elements (Type: C3D8R in ABAQUS), as shown in Figure 3.8, and six DOFs are considered for each node of one C3D8R element.

3.3.3 Equations of motion of viaduct subsystem

By assembling all the components of the viaduct subsystem, including the rails, concrete girders, bearings and concrete piers, the global mass matrix $\mathbf{M}^G$ and global stiffness matrix $\mathbf{K}^G$ for the entire viaduct subsystem are obtained in the global coordinate system. The equations of motion for the viaduct subsystem can be summarized as:

$$\mathbf{M}^G\ddot{\mathbf{U}}^G + \mathbf{C}^G\dot{\mathbf{U}}^G + \mathbf{K}^G\mathbf{U}^G = \mathbf{F}_m^{V\to G} + \mathbf{F}_e^G \tag{3.13}$$

where $\mathbf{U}^G$, $\dot{\mathbf{U}}^G$ and $\ddot{\mathbf{U}}^G$ are the displacement, velocity and acceleration vectors of the viaduct subsystem; $\mathbf{F}_e^G$ is the external force vector, including gravity force, seismic loads, and wind loads; $\mathbf{F}_m^{V\to G}$ is the vector of the electromagnet forces acting on the viaduct, in which the nonzero parts are actually targeted at the loading rails, and will be discussed in detail in Section 3.4.

In this study, the mass and stiffness matrices of the viaduct system, which includes girders, piers and rails, are firstly established. The damping matrix of the viaduct system is then formed based on the Rayleigh damping assumption that the damping matrix is proportional to a linear combination of the mass matrix and stiffness matrix. In the formulation of the damping matrix of the viaduct subsystem, the two natural frequencies of about 6 Hz and 500 Hz are selected and the two damping ratios are selected as 0.02 for the concrete structure (Li et al., 2015). Accordingly, the damping parameters are α=0.2368 and β=0.000088. The discrete stiffness and damping coefficients of the spring-damper element are finally inserted into the stiffness and damping matrices respectively of the viaduct system to form the global stiffness $\mathbf{K}^G$ and damping matrices $\mathbf{C}^G$ of the entire viaduct system including the bearings (Song & Fujino, 2008; Su et al., 2010; Dimitrakopoulos & Zeng, 2015).

3.4 Interaction Modelling

The interaction between the train subsystem and the viaduct subsystem is realized through levitation and guidance electromagnet forces. This study adopts an interactive electromagnet force-air gap model to simulate the levitation and guidance forces.

3.4.1 Interactive electromagnet force-air gap model

The electromagnetic force-air gap model is established based on the current circuit and the airgap between the electromagnet and rail track (Sinha, 1987).

$$F\left(i_w^t, h_w^t\right) = K_0 \left(\frac{i_w^t}{h_w^t}\right)^2 \tag{3.14}$$

where the superscript (*t*) indicates the current time step and the subscript (*w*) means the *w*th maglev pole; $F\left(i_w^t, h_w^t\right)$ is the current-controlled electromagnetic force between the *w*th maglev pole and the rail track; i_w^t is the electrical intensity; h_w^t is the magnetic air gap; K_0 is a coupling factor related to the cross-sectional area of the core, calculated by $K_0 = \mu_0 {N_m}^2 A_w / 4$; N_m is the number of turns in the magnet winding; A_w is the pole face area; and μ_0 is the air permeability. In Eq. (3.14), the magnetic air gap h_w^t is calculated by

$$h_w^t = h_0 + u_w(t) + u_G\left(x_w^t\right) + s_r\left(x_w^t\right) \tag{3.15}$$

where h_0 is the design static gap at the static equilibrium state of the train (10mm for SML); $u_w(t)$ is the motion of the *w*th magnetic pole; $u_G\left(x_w^t\right)$ is the track deflection at the *w*th magnetic pole; x_w^t is the location of the *w*th maglev pole in the global X-coordinate; and $s_r\left(x_w^t\right)$ is the track irregularity to be discussed in Section 3.4.2.

In Eq. (3.15), $u_w(t)$ and $u_G\left(x_w^t\right)$ are calculated directly from the dynamic analysis of the coupled maglev train and viaduct system. In the static equilibrium, the maglev train is levitated by the electromagnetic levitation force to balance the weight of the maglev train. Such a levitation force is calculated by

$$F\left(i_0,h_0\right)=K_0\left(\frac{i_0}{h_0}\right)^2=p_0 \tag{3.16}$$

where p_0 is the weight of the maglev train distributed at the w^{th} maglev pole; and i_0 is the required value of the current to balance the train weight and keep the design static gap h_0. When Eqs. (3.14-3.16) are used for electromagnet guidance force, p_0 shall set to zero.

To guarantee the smooth running and safety of the train system, two control algorithms were proposed: one controller is to directly regulate the electromagnetic forces to ensure a steady force acting on the vehicles and tracks (Ju et al., 2012, 2014); and the other uses the operation performance of the train to adjust the electromagnetic forces (Yang & Yau, 2011; Yau, 2009b, 2009a, 2010b, 2010a). In the SML, the air gap h_w^t between the maglev pole and rail track is measured and controlled to approach the design static gap h_0 as close as possible so as to avoid the derail. A proportional-derivative (PD) controller is accordingly developed to fulfil this feedback control. This PD controller computes the gap error, the difference between the desired gap and the measured air gap, and then minimizes the gap error by adjusting the current circuit. The gap error e_w^t is expressed as

$$e_w^t=h_0-h_w^t \tag{3.17}$$

Before using the PD controller, the relationship between the control current and the control voltage at time $t+\Delta t$ should be considered since they are essential values in the control of the maglev train system (Ju et al., 2014; Yau, 2010b).

$$\frac{\Gamma_0}{h_w^{t+\Delta t}}\dot{i}_w^{t+\Delta t}-\frac{\Gamma_0 i_w^{t+\Delta t}}{\left(h_w^{t+\Delta t}\right)^2}\dot{h}_w^{t+\Delta t}+R_0 i_w^{t+\Delta t}=V_0+V_w^{t+\Delta t} \tag{3.18a}$$

where $\Gamma_0=2K_0$ is the initial inductance of the coil winding of the guidance or levitation magnets; R_0 is the coil resistance of the electronic circuit; $V_0=R_0 i_0$ is the static voltage; V_w^t is the control voltage of the w^{th} maglev pole, which is determined by minimizing the gap error.

$$V_w^{t+\Delta t} = K_p e_w^{t+\Delta t} + K_d \frac{\mathrm{d}e_w^{t+\Delta t}}{\mathrm{d}t} = K_p\left(h_0 - h_w^{t+\Delta t}\right) - K_d \dot{h}_w^{t+\Delta t} \tag{3.18b}$$

where K_p and K_d are the proportional gain and derivative gain, respectively. By substituting Eq. (3.18b) into Eq. (3.18a) and introducing $\dot{i}_w^{t+\Delta t} \approx \left(i_w^{t+\Delta t} - i_w^t\right)/\Delta t$, the control current can be obtained:

$$i_w^{t+\Delta t} = \left(\frac{1}{\Delta t} - \frac{\dot{h}_w^{t+\Delta t}}{h_w^{t+\Delta t}} + \frac{h_w^{t+\Delta t}}{\Gamma_0} R_0\right)^{-1} \left[V_0 + K_p\left(h_0 - h_w^{t+\Delta t}\right) - K_d \dot{h}_w^{t+\Delta t} + \frac{\Gamma_0}{h_w^{t+\Delta t}\Delta t} i_w^t\right] \frac{h_w^{t+\Delta t}}{\Gamma_0} \tag{3.18c}$$

Since $h_w^{t+\Delta t}$ and $\dot{h}_w^{t+\Delta t}$ can be obtained from Eq. (3.15) in the numerical study and i_w^t is the known current value at time t, the unknown control current $i_w^{t+\Delta t}$ at time $t+\Delta t$ can be determined by Eq. (3.18c). Finally, the levitation or guidance force $F\left(i_w^{t+\Delta t}, h_w^{t+\Delta t}\right)$ at time $t+\Delta t$ can be determined from Eq. (3.14).

3.4.2 Track irregularities

In this study, a 7-parameter power spectrum density (PSD) function is utilized to model track (rail) irregularities (see Section 2.3.4). From the measurement results reported by Shi et al. (2014), the lower and upper limits of wavelength, which define the range of the PSD function, are 0.258 m and 150 m, respectively. Accordingly, the upper and lower spatial frequencies are 24 rad/m and 0.042 rad/m, respectively. The profile of the track irregularities is calculated as suggested in the reference (Ju et al., 2010), in which the total number of terms is 2000.

3.4.3 Equations of motion of coupled system and solution method

The equations of motion of the coupled maglev train-viaduct system can be expressed as

$$\begin{bmatrix} \mathbf{M}^V & \mathbf{0} \\ \mathbf{0} & \mathbf{M}^G \end{bmatrix} \begin{bmatrix} \ddot{\mathbf{U}}^V \\ \ddot{\mathbf{U}}^G \end{bmatrix} + \begin{bmatrix} \mathbf{C}^V & \mathbf{0} \\ \mathbf{0} & \mathbf{C}^G \end{bmatrix} \begin{bmatrix} \dot{\mathbf{U}}^V \\ \dot{\mathbf{U}}^G \end{bmatrix} + \begin{bmatrix} \mathbf{K}^V & \mathbf{0} \\ \mathbf{0} & \mathbf{K}^G \end{bmatrix} \begin{bmatrix} \mathbf{U}^V \\ \mathbf{U}^G \end{bmatrix} = \begin{bmatrix} \mathbf{F}_e^V + \mathbf{F}_m^{G\to V} \\ \mathbf{F}_e^G + \mathbf{F}_m^{V\to G} \end{bmatrix} \tag{3.19}$$

where $\mathbf{F}_m^{G\to V}$ is the vector of the electromagnetic forces acting on the train and its dimension is determined by Eq. (3.10a). The nonzero entries in the vector $\mathbf{F}_m^{G\to V}$ correspond to the levitation and guidance magnets only, and the entries in the vector $\mathbf{F}_m^{G\to V}$ for the car bodies, bogies and rockers are zero. $\mathbf{F}_m^{V\to G}$ is the vector of the electromagnet forces acting on the viaduct, in which the nonzero parts are actually targeted at the loading rails, and they are determined by the position vectors of the moving loads acting on the rails due to the train subsystem. The entries in the vector $\mathbf{F}_m^{V\to G}$ for the girders, piers and foundations are zero.

Suppose that there are *N* vehicles in one train running on the viaduct (see Figure 3.9(a)). The total number of maglev poles arranged on the *M* sets of levitation magnets is then $W = 12M = 12(8N-1)$. Figure 3.9b also shows a concentrated force $F\left(i_w^t, h_w^t\right)$ representing the interactive electromagnetic force generated between the *w*th maglev pole and the rail. For a time increment Δt, all the electromagnetic forces are first computed based on the control algorithm and the feedback of the coupled system at time *t*, as discussed in Section 3.4.1. These electromagnet forces then become the external forces acting on the magnets to form their external resultant forces, such as $-\sum_{w=1}^{12} F_{sprzmw}$ and $\sum_{w=1}^{12} F_{sprzmw} l_{sw}$, which are the external resultant force on and moment around the mass center of the *m*th levitation magnet in the vertical and rotational direction, respectively. The external resultant forces of each magnet are then lumped into the vector $\mathbf{F}_m^{G\to V}$ at the pertinent DOFs of each magnet, and the responses of the train subsystem at the time of $t+\Delta t$ are finally computed. Meanwhile, the electromagnet forces also form the nonzero entries of the vector $\mathbf{F}_m^{V\to G}$, and they are determined by the position vectors of the moving loads acting on the rails. Specifically, the loaded position vector of the electromagnet force from the *w*th magnetic pole can be determined by

$$x_w = v\left(t - t_w\right)\left[H\left(t - t_w\right) - H\left(t - t_w - \frac{nL}{v}\right)\right] \tag{3.20}$$

where v is the operational speed of the train; t_w is the traveling time of the w^{th} pole since it enters the concerned span of the viaduct, $t_w = \left(w-1\right)d/v$; d is the force space; L is the length of one span of the girder; $H\left(t\right)$ is the unit step function; and n is the number of spans. If $x_w = 0$, it means that the w^{th} load is off the n spans, and $u_g\left(x_w^t\right)$ and $s_r\left(x_w^t\right)$ in Eq. (3.11) are assumed to be zero to obtain the air gap h_w^t.

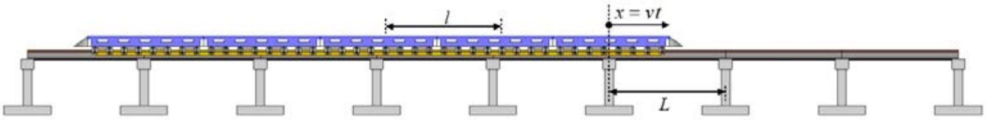

(a) 5 maglev vehicles running on viaduct in SML

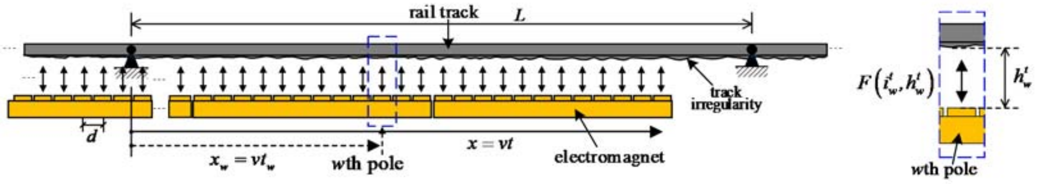

(b) Force diagrams between the electromagnet and rail track

Figure 3.9 The coupled maglev train-viaduct system in SML

To find the solutions for the coupled maglev train-viaduct system, the ABAQUS Explicit Solver is employed in this study for its high computation efficiency. Specifically, the response of the viaduct subsystem at time t is first calculated using the ABAQUS Explicit Solver with the central difference method. At the same time, the response of the train subsystem is computed using the ABAQUS Explicit Solver with a self-developed ABAQUS subroutine, in which the central difference method is also adopted. The above two computations of the two subsystems are linear problems. With the results of responses of both the viaduct and train subsystems at time *t*, the interactive electromagnetic forces at time *t*+Δ*t* can be obtained using Eq. (3.10) to Eq. (14), in which the PD controller is utilized to adjust the interaction forces according to the gap error e_w^t. Accordingly, the two interfaces, VDLOAD for the load application on the rail track by the position vector x_w with $F\left(i_w^t, h_w^t\right)$ and VUFIELD for collection of the response $u_G\left(x_w^t\right)$ and $\dot{u}_G\left(x_w^t\right)$ of the loaded elements of the rail track, are developed for the realization of simultaneous computation of both the train subsystem and the viaduct subsystem. The time interval used in the computation in this study is 4×10^{-6} s after several trial tests to balance the computation time and accuracy. The threshold for the error in the air gap is set as 0.001m. By checking the errors in the air gap, the iteration is performed until the convergence criterion is reached.

Here, the user subroutine VDLOAD is used to define the variation of the distributed load magnitude as a function of position, time, velocity, etc. for a group of points, each of which appears in an element-based or surface-based nonuniform load definition. The user subroutine VUFIELD allows to prescribe predefined field variables at the nodes of a model, a number of field variables at the node can be updated simultaneously whenever a user-subroutine-defined field appears. The flowchart for the realization of the proposed maglev train-viaduct interaction modeling in ABAQUS can be seen in Figure 3.10.

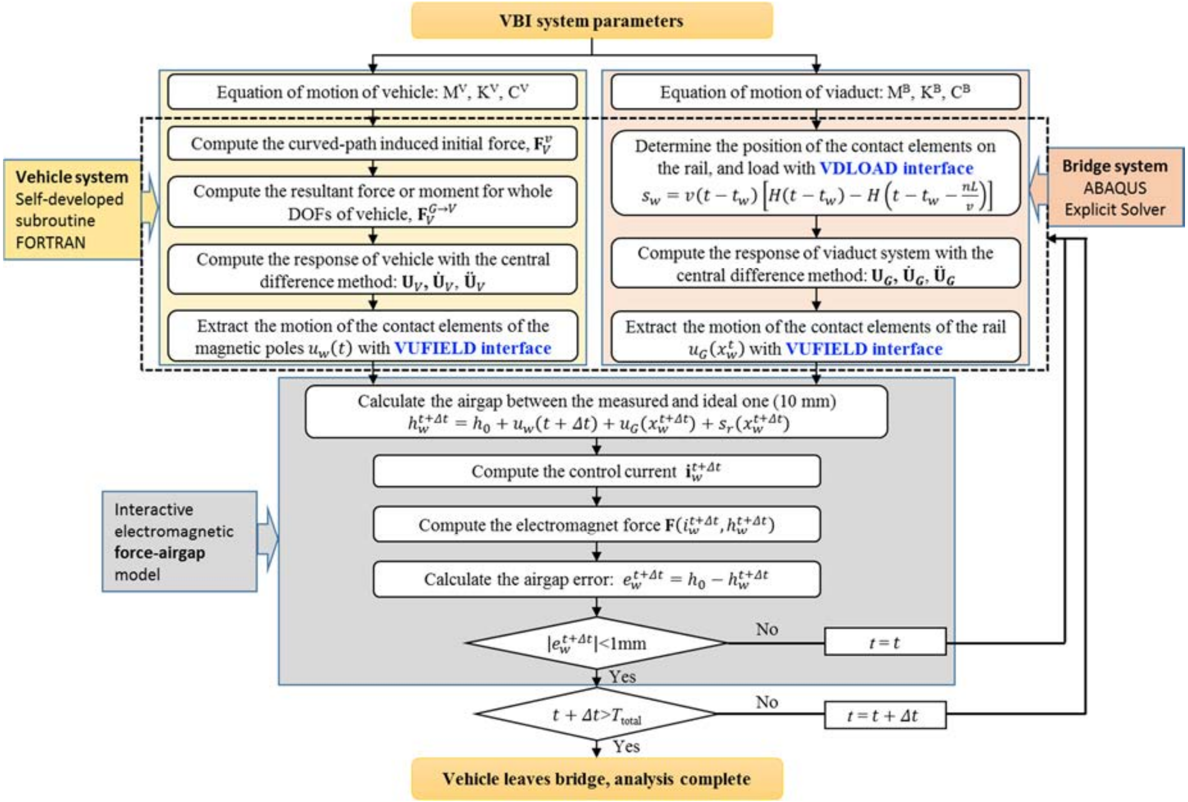

Figure 3.10 The flowchart for the realization of the proposed maglev train-viaduct interaction modeling in ABAQUS

3.5 Validation and Discussion

To validate the effectiveness of the proposed model, the effects of: (a) the inclusion of maglev pole pitch in magnets; (b) the flexible supports; and (c) the flexibility of rails in HGG, are investigated by comparison with the field measurement data and simulation results from Shi et al. (2007). The numerical model of Shi et al. (2007) was developed based on SML, in which one concentrated force model was used to simulate the electromagnetic force generated from the magnetic field between each magnet and rail track without considering the effect of malgev pole pitch; while the maglev guideway was assumed to be a simply supported beam modelled by Euler-Bernoulli beam elements excluding the flexibility of rails and supports. Field measurement was also conducted on the tested section GR0483 of SML, when the train consisting of five vehicles ran on the viaduct with the operational speed of 430 km/h. The major physical parameters of the train subsystem, viaduct subsystem, and electromagnetic force model used in the numerical study are listed in Appendix B.

3.5.1 Characteristic frequencies of coupled maglev train-viaduct system

It has been demonstrated in the previous studies (Ju et al., 2010; Ju et al., 2009; Yang et al., 2004; Yang et al., 2013) that in addition to the girder natural frequencies, the primary frequencies in the girder response are attributed to the so-called driving frequencies that are associated with the duration of a vehicle passing over the girder. Therefore, to comprehensively investigate the dynamic interaction effects of the coupled maglev train-viaduct system, the dominant frequencies, including the natural frequencies of the girder as well as the driving frequencies induced by the vehicle, should be first presented. The dominant frequencies and their definitions of the coupled system are summarized in Table 3.1, in which the driving frequencies are calculated by (Yang et al., 2004):

$$f_i = \frac{v}{L_i} \quad i = 1,2,3,\cdots \tag{3.21}$$

where f_i is the driving frequency related to the characteristic length L_i under the vehicle speed *v*.

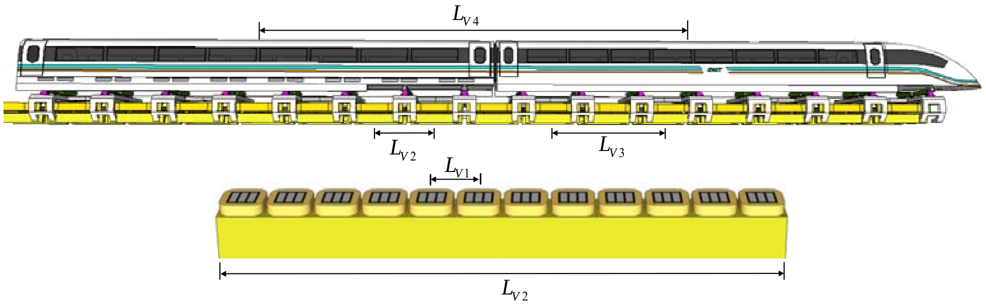

Figure 3.11 The characteristic lengths of the train in SML

Table 3.1 The dominant frequencies of the coupled train-viaduct system for v=430 km/h

Guideway natural frequencies				Vehicle-induced driving frequencies				
Modes	1	2	3	L_{Vi} (m)	0.258	3.096	6.192	24.77
f (Hz)	6.08	15.2	25.83	f_{Vi} (Hz)	463	38.58	19.29	4.82

In Table 3.1, L_{Vi} is the characteristic length of the train shown in Figure 3.11. There are four characteristic lengths L_{Vi} for the train: (1) the maglev pole pitch, L_{V1}; (2) the center distance of adjacent levitation magnets, L_{V2}; (3) the center distance of adjacent bogies, L_{V3}; and (4) the center distance of two neighboring vehicles, L_{V4}.

3.5.2 Maglev pole pith-induced dynamic characteristic on viaduct response

By including the configurations of maglev poles into the presented model, the effect of maglev pole pitch-induced moving loads distribution on the viaduct can be well considered. This effect is then highlighted by comparing the simulated system dynamic responses and frequencies with those from the measurement data and Shi's simulation.

3.5.2.1 Analysis in acceleration time history

Figure 3.12 presents the comparisons of the vertical acceleration time histories of the tested girder at its midspan when the train passed throug it at a speed of 430km/h. The train-induced acceleration response of the girder was recorded for 1.8 seconds. It can be seen from Figure 3.12 that the computed acceleration time history from the present model can well match the measured acceleration time history with the measured data slightly larger than the numerical results. When the tested girder span was fully loaded by the moving vehicles during the period from 0.414 to 1.244s, a steady cluster of periodic acceleration responses can be observed in the curves of presented model and field measurement, as shown in Figure 3.12a. The average of each period is 0.026 s, which approximately equals to the length of one electromagnet (L_{V2}=3.096 m) divided by the train speed (v=119.44 m/s). Figure 3.12b shows a close look at the acceleration time history of the girder at its midspan from 0.726 to 0.933s, when the third (middle) vehicle is passing over the midspan. Seven complete and two half cycles are obviously shown in the curves of presented model and field measurement, while this pattern is roughly observed in the curve of Shi (see Figure 3.12b).

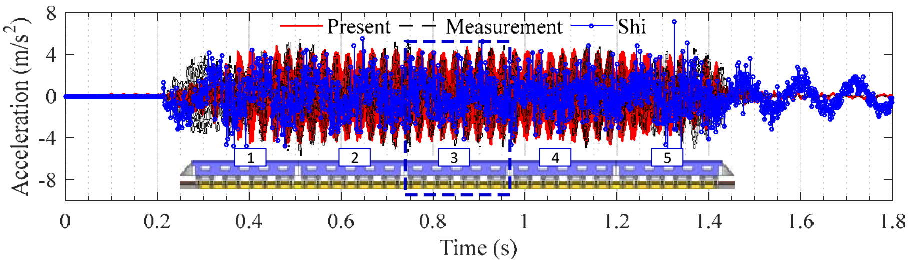

(a) Vertical acceleration time history of the girder at its midpan induced by a train with five vehicles in SML

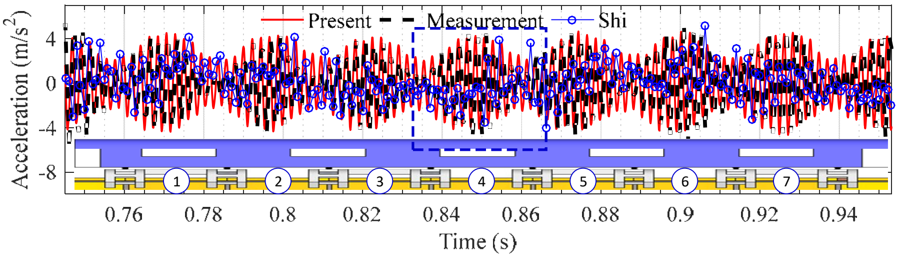

(b) Vertical acceleration time history of the girder at its midpan induced by one vehicle with 7 magnets

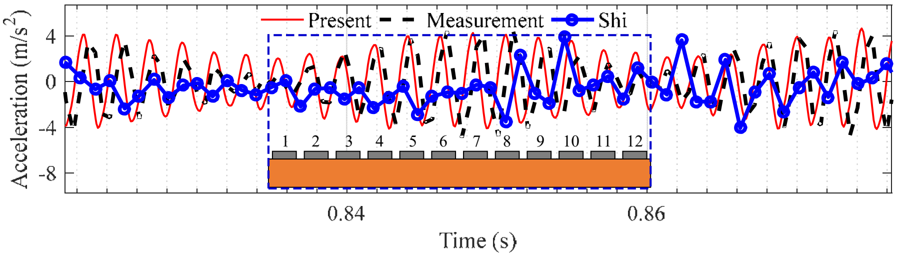

(c) Vertical acceleration time history of the girder at its midpan induced by one magnet with 12 maglev poles

Figure 3.12 Comparisons of vertical acceleration time histories of the tested girder at its midspan for v= 430 km/h.

It is noted that the period of cycles is almost equal to the number of levitation magnets belonging to one vehicle, as introduced in Section 3.2. The time history from 0.72 to 0.76s in Figure 3.12b is further presented in Figure 3.12c, which is induced by one magnet passing over the midspan. From the curves of the measurement and present simulation result in Figure 3.12c, obviously, the number of peak values are quite equal to the number of maglev poles mounted on each magnet. Namely, the average distance of the two adjacent wave peaks is dependent on the pole pitch (L_{V1}=0.258 m). It can be concluded that the present model considering the configuration of maglev poles on the magnet can better reflect the time history response of the viaduct with the measurements, while the simulation result computed based on the model of Shi has a low accuracy in peak values and waveforms. The waveform of the acceleration time history is proved to be highly dependent on the characteristic length of the magnets and pole pitch, which will be further validated in next section.

3.5.2.2 Analysis in frequency domain

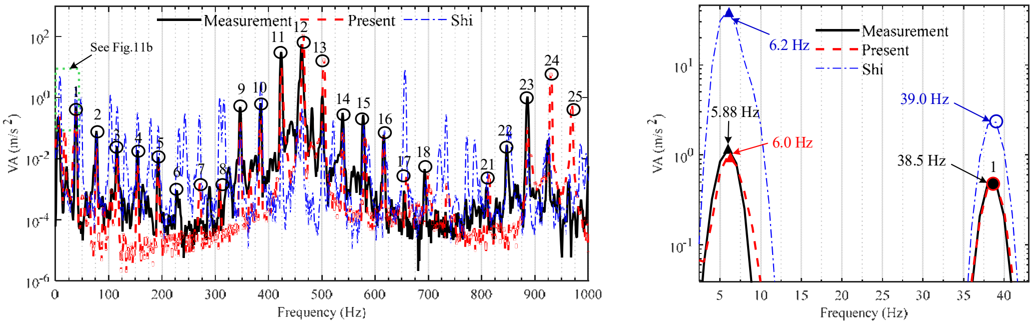

(a) A whole view (b) A close look

Figure 3.13 Comparison of power spectra of vertical acceleration response of the tested girder for v=430km/h

The vertical acceleration response time-histories of the tested girder at its midspan, as shown in Figure 3.12a, are converted to the power spectra to obtain the frequency-domain characteristics of the girder vibration, as shown in Figure 3.13a. It can be observed that there are many dominant frequencies in the vertical acceleration response of the tested girder. The first vertical natural frequency of the girder can be clearly identified from the measurement data, the simulation result of the present model and Shi as 5.88 Hz, 6.0 Hz and 6.2 Hz, respectively, as shown in Figure 3.13b with a close look. Strikingly, some peak values extracted from the measurement and the simulation result of the proposed model are marked by "○", as shown in Figure 13(a). These are actually the multiples of the driving frequency f_{V2} of 38.58 Hz as listed in Table 3.1: $f_1^{\mathrm{O}} = 38.5\,\mathrm{Hz}$; $f_2^{\mathrm{O}} = 77\,\mathrm{Hz}$; $f_3^{\mathrm{O}} = 116\,\mathrm{Hz}$ and $f_4^{\mathrm{O}} = 154\,\mathrm{Hz}$. It is also noted that the maximum peak value recorded in both the measurement and the simulation results from the proposed model appears at the point 12, and the corresponding frequency in the x-axis is about 463 Hz, which is equal to the pole pitch-induced driving frequency f_{V1} as listed in Table 3.1. Besides, the peak value marked by "○" with the number of 24 is also large, and the corresponding frequency is 926 Hz, which is twice of f_{V1}. From the curve of Shi in Figure 3.13a, many peak values with respect to the multiples of the driving frequency f_{V2} of 38.58 Hz are also recorded. However, as the numerical model of Shi is exclusive of the configuration of maglev poles, pole pitch-induced driving frequency f_{V1} and its multiples fail to be identified in the frequency domain result, namely, the maximum peak values around the point 12 are lost. On the other hand, as the magnets are distributed evenly under the five vehicles of the train (see Figure 3.1 and Figure 3.2), the response and gravity of the car bodies, rockers and bogies (all are indirect interacting parts with the rails) are thus evenly transferred into the magnets. Their interaction characteristics such as vehicle-induced driving frequency f_{V4} and bogie-induced driving frequency f_{V3} cannot be clearly reflected in these three curves of Figure 3.13. It can be concluded that the natural frequencies of the girder and the driving frequencies from the vehicles both effectively dominate the dynamic response of the girder. Particularly, the present model with consideration of maglev poles can precisely reveal the dynamic characteristics of the coupled train-viaduct system, and the vertical acceleration response of the girder is mainly attributed by the moving levitation magnets and maglev poles.

3.5.3 Effects of flexible support to girder response

In this section, the vertical displacement of girder at its midspan computed based on the proposed model is first validated through the comparison with the measurement and the simulation result of simply supported beam (SSB) used by Shi et al. (2007). Then, based on the present model, the simulation results of three cases with different supports are conducted and compared with each other.

3.5.3.1 Validation of vertical displacement of girder

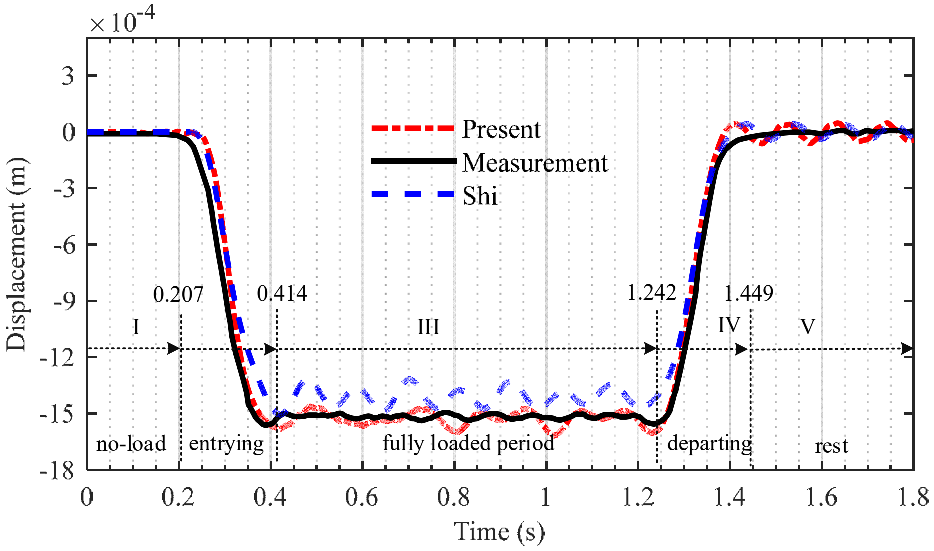

Figure 3.14 Comparison of vertical displacement time history of the tested girder at its midpan for v= 430 km/h.

The vertical displacement time histories of the girder at its midspan, obtained from the field measurement and the numerical simulation results from the present model and Shi, are plotted in Figure 3.14. Overall, the entire displacement time histories can be divided into five segments according to the loading conditions of the tested girder. The first segment refers to the period (I: 0~0.207s) when the first vehicle of the train is moving on the first girder and no loads are acting on the concerned (second) girder. Then, the train begins running on the second girder from 0.207s, and the responses increase quickly and reach to a peak value when the second girder is fully loaded at 0.414s (Period II: 0.207~0.414s). The following is a long period (III: 0.414~1.242s), during which the second girder is continually fully loaded by the passing train. When the last vehicle starts leaving from the second girder during the fourth period (IV:1.242~1.449s), the responses gradually decrease. When the entire train leaves from the second girder, free vibration of the second girder occurs in the fifth period (V:

1.449~1.80 s).

From the view point of displacement time histories occurring in the fully loaded period (III), the simulation result of the present model can well coincide with the measurement data, while a considerable discrepancy is recorded by the simulation result of Shi. Specifically, the displacement time history of the Shi's model vibrates around a slightly smaller value of 1.42 mm, while those of the present model and measurement are 1.54 and 1.53 mm respectively, that is mainly because of the exclusion of the flexibility of the elastic supports in the model of Shi. A further discussion regarding this will be conducted in Section 3.5.3.2. It is also noted that a relatively larger fluctuation is excited by the model of Shi, which is essentially induced by the instability and inaccuracy of the adopted interaction model using one concentrated force to model the interaction between one magnet and rail. In other words, the interaction models of the proposed method with inclusion of the detailed configuration of maglev poles actually employ twelve concentrate forces with independent controller to model the interaction between one magnet and rail, and it does help to suppress the unstable vibration of the viaduct.

3.5.3.2 Comparison of girder response under different supports

The dynamic responses of the girder at its mid-span are computed for three cases: (1) the simply supported girder without considering bearings and piers (HGG); (2) the simply supported girder with bearings but without piers; and (3) the entire viaduct subsystem as investigated in this study.

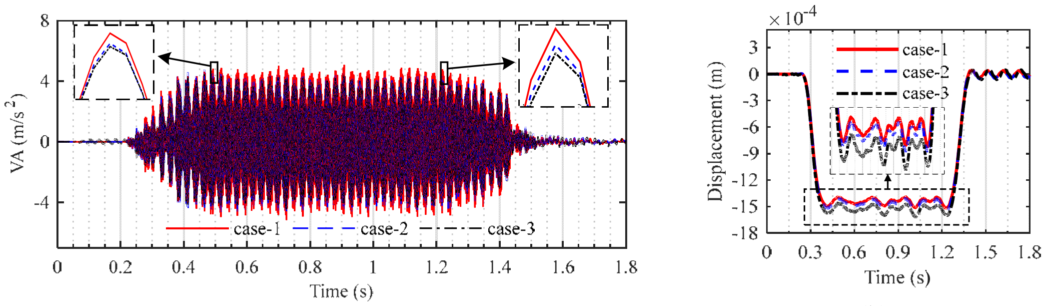

(a) (b)

Figure 3.15 Comparison of dynamic response of girder at its midspan: (a) acceleration time history; (b) displacement time history.

The computed results are plotted in Figure 3.15. It can be seen that with the flexibility of elastic bearings and high column piers introduced, the vertical displacement response of the girder increases but the vertical acceleration response of the girder reduces. The maximum value of vertical displacement response is -1.48 mm, -1.52 mm, and -1.61 mm, respectively, for the three cases. It is also noted that because the vertical stiffness of pier is extremely high, the effect of flexibility of the pier to the girder response including the displacement and acceleration is relatively weaker, and more contributions are induced by the flexibilities of elastic bearings. Moreover, the cushion ability is enhanced within the consideration of bearings and piers, leading to a reduction of the acceleration amplitude from 4.62 m/s^2 to 4.12 m/s^2 and then to 3.93 m/s^2.

3.5.4 Effects of flexibility of rail

The rail is the key part to conduct the interaction between the viaduct and train, and it also influences their responses through its effect on the electromagnetic interaction forces, which are determined by the displacement and velocity of the rail and magnets (see Eq. (3.11) and Eq. (3.14c)). The effects of flexibility of rail are investigated through model of case-1.

3.5.4.1 Effect on viaduct response

The comparison of the vertical responses of the rail and girder at the midspan from the present model with those calculated based on the simply supported beam (SSB) model is shown in Figure 3.16. As the rail is fastened to the girder, the rail track response is simultaneously produced by the combination of its flexibility-induced deformation and the girder response, resulting in a relatively larger response of the rail than the two others, as shown in Figure 3.16. Specifically, during the fully loaded period (III: 0.414~1.242s), the maximum vertical displacement of the rail with a value of 1.61 mm is larger than the two others, as shown in Figure 3.16a. The maximum vertical velocity of the rail is 0.01 m/s, while those of both the girder of the present model and the simply supported beam are recorded with a slightly lower value, as shown in Figure 3.16b. Besides, the girder response of the present model vibrates around the same value with that of the simply supported beam, while the former has a relatively lower fluctuation. This indicates that the coupling effect between the rail and girder constrains the vibration of the girder deck.

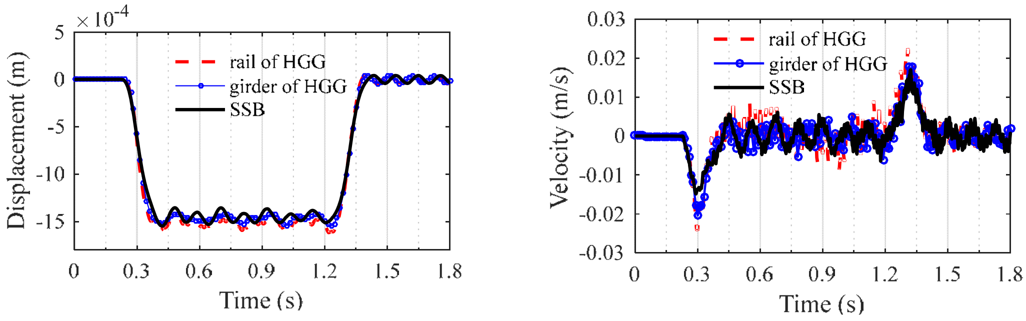

(a) Displacement time history

(b) Velocity time history

Figure 3.16 Comparison of vertical responses of the rail and girder from the present model with simply supported beam model

3.5.4.2 Effect on vehicle response

The accurate control of the air gaps with an ideal value of 10 mm between the electromagnets and rails is important for the safety and functionality of both the train subsystem and the viaduct subsystem. However, the vibration of the rail and the track irregularities simultaneously affect the vehicle response through its effect on the dynamic behavior of electromagnets.

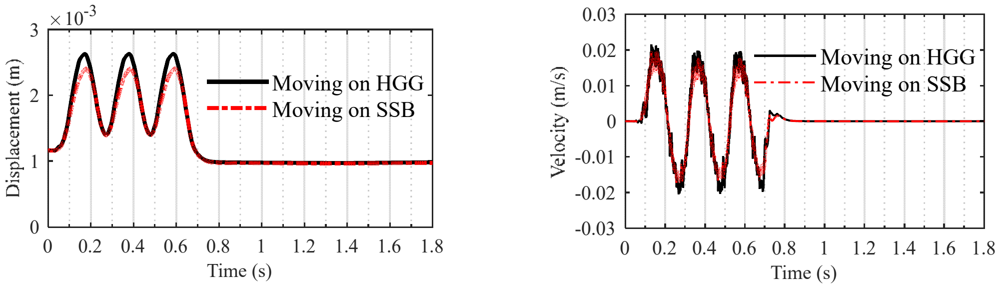

(a) displacement time history

(b) velocity time history

Figure 3.17 Vertical response of the fourth levitation magnet of the first vehicle:

The comparisons of the vertical response of the fourth levitation magnet of the first vehicle respectively moving over the HGG model and the SSB model are presented in Figure 3.17. It can be seen that with the inclusion of the flexibility of the rail, the displacement time history of the magnet moving over the HGG is generally larger than that over the SSB (see Figure 3.17a). This phenomenon keeps consistent with the evolution law of the rail displacement, as shown in Figure 16a. Accordingly, the velocity response of the magnet moving over the HGG is also relatively larger than that moving over the SSB, as shown in Figure 3.17b.

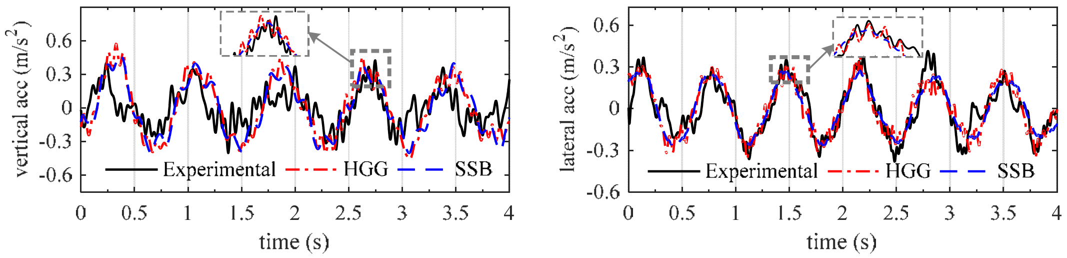

(a) in vertical

(b) in lateral

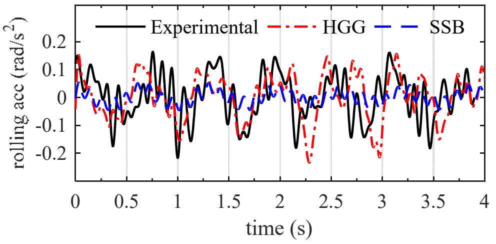

(c) in rotational

Figure 3.18 Acceleration responses of the 2^{ed} car body.

Furthermore, the effect of the flexibility of the rail on the car body response is also conducted, and its simulation result is plotted in Figure 3.18. Overall, the responses in three directions, i.e. vertical, lateral and rotational by the train moving over HGG (the present model) can well match the experimental data. The time history responses in the lateral and vertical directions induced by the train moving over the SSB (Shi's model) is slightly smaller than those of the experiment and the present model. However, because the track irregularities on both the left and right rails are excluded in the SSB model, the SSB-induced rolling acceleration of the vehicle is considerately smaller than the other two. Specifically, the maximum of the roll acceleration of the SSB model is 0.08 rad/s^2, while those are 0.21 rad/s^2 and 0.22 rad/s^2 from the experiment and HGG model, respectively. It can be therefore concluded that the HGG model by proper modeling of the rails, girders, and their connections can provide an accurate prediction of the vehicle response, whereas the SSB model underestimates the vehicle's response, particularly in the roll acceleration.

3.6 Summary

The maglev train-viaduct interaction model within consideration of the key configurations of the interacting parts, the magnets of the train system and the modular function units (rails) of the viaduct system, has been established. By applying the proposed model on the Shanghai maglev line, the essential characteristics of the coupled system can be obtained from the proposed model. Its accuracy and effectiveness are validated by comparing the simulated system dynamic responses and frequencies with those from the measurement data and Shi's simulation. The following conclusions can be drawn from this study.

(1) The computed acceleration and displacement time histories match well with the measured acceleration and displacement time histories of the girder at its midspan. The characteristic frequencies identified from the simulation result are consistent with those from the measured ones. The comparative results show that the developed interaction model is feasible in computation simulation and accurate in response prediction.

(2) The identified characteristic frequencies and spectral analyses manifest that the appropriate modeling of the levitation magnets and the pole pitch is important because they are two key contributors to the dynamic response of the viaduct subsystem.

(3) With the flexibility of elastic bearings and high column piers introduced in the proposed coupled train-viaduct system, the vertical displacement response of the girder increases but the vertical acceleration response of the girder reduces. The effect of flexibility of the pier on the girder response is relatively weaker, and more contributions are induced by the flexibilities of elastic bearings. This effect should be given more attention when the settlements of the pier occur.

(4) The proper modeling of the rails and bracket supports is also important, which not only influences the response of the rails and magnets but also affects the riding comfort of the train, particularly in the roll acceleration.

(5) In general, the present model within full consideration of the maglev poles into the train subsystem and the rails, girders, piers and their connections into the viaduct model, can accurately predict the response of the viaduct and train.

CHAPTER 4

DYNAMIC ANALYSIS OF A COUPLED SYSTEM OF HIGH-SPEED MAGLEV TRAIN AND CIRCULAR CURVED VIADUCT

4.1 Introduction

Chapter 3 has established the realistic and detailed maglev train-straight viaduct interaction model and validated its effectivess and accuracy by comparing with the measurements. This interaction model can be used to predicate the dynamic performance of the train running on the straight track/vaiduct. However, when a vehicle moves on a curved track, the moving direction of the vehicle in the global coordinate system is changing. As a result, the direction of the centrifugal force on the vehicle is also changing. On the other hand, the interaction forces between the vehicle and track depend on their relative displacements. The dynamic interaction between the high-speed maglev train and slender curved viaduct becomes very complicated.

To this end, a trajectory coordinates-based framework for the analysis of the high-speed maglev train running on the circular curved track is proposed in this chapter. The motion of the maglev train system running on a curved track is defined by a series of trajectory coordinates, and the stiffness and damping matrices of the equations can be thus reduced into those of the straight track. The curved viaduct system is modelled in the global coordinate system using the finite element method. The electromagnet force-air gap model is also adopted for the maglev vehicle via its electromagnets and rails on the viaduct, by appropriate transformation of coordinates. And then, the proposed framework is applied to the SML to capture its curved path-induced dynamic characteristics. Moreover, the effect of various curve radii and cant deficiencies on the coupled system are investigated.

4.2 Formulation of a Vehicle Moving over a Horizontally Curved Track

In this section, the trajectory coordinates-based formulation for the equations of motion of a railway vehicle moving on a horizontally curved track is brifely described (Shabana et al., 2008; Dimitrakopoulos & Zeng, 2015).

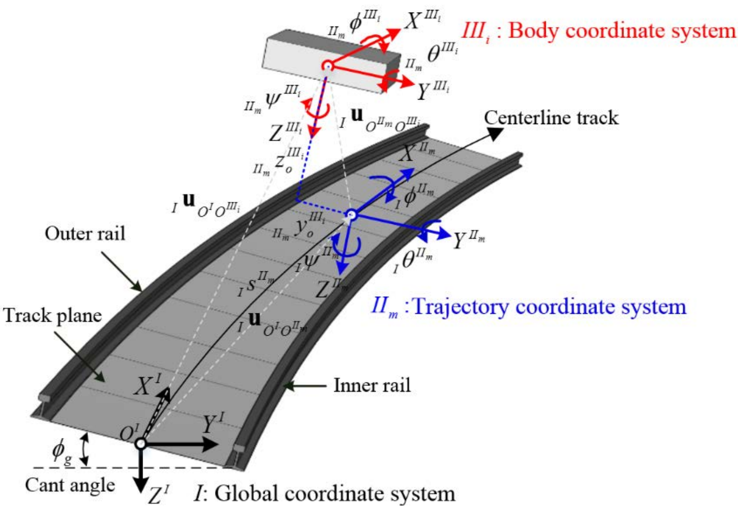

Figure 4.1 Three coordinate systems (Shabana et al., 2008)

4.2.1 Three coordinate systems

As shown in Figure 4.1, three sets of coordinate systems are employed to formulate the equations of motion of a vehicle moving on a horizontally curved track: the global (space-fixed) coordinate system $X^IY^IZ^I$; the trajectory coordinate system $X^{II_m}Y^{II_m}Z^{II_m}$; and the body (vehicle body-fixed) coordinate system $X^{III_i}Y^{III_i}Z^{III_i}$.

The global coordinate system fixed on the earth is used to trace the absolute position of the vehicle body. The trajectory coordinate system is a moving coordinate system with its origin moving on the centerline of the un-deformed curved track, defined in the global coordinate system by one time-dependent coordinate, that is, arc length ${}_Is^{II_m}$. The orientation of the trajectory coordinate system with respect to the global coordinate system can be defined by three sequential Euler angles ${}_I\psi^{II_m}$, ${}_I\theta^{II_m}$, and ${}_I\phi^{II_m}$ about the three axes Z^{II_m} , Y^{II_m} , and X^{II_m} , respectively, which can further be defined in terms of the arc length ${}_I s^{II_m}$. The origin of the trajectory coordinate system always follows the origin of the body coordinate system with zero distance in the longitudinal direction (tangent to the centerline of the track). The motion of the vehicle body with respect to the trajectory coordinate system can be described by only two translational motions ${}_{II_m} y^{III_i}$ and ${}_{II_m} z^{III_i}$, and three rotational motions ${}_{II_m} \phi^{III_i}$, ${}_{II_m} \theta^{III_i}$, and ${}_{II_m} \psi^{III_i}$.

4.2.2 Generalized trajectory coordinates

In this study, the equations of motion of a vehicle body are established in terms of the generalized trajectory coordinates to make it easy to solve the coupled dynamic problem of vehicles and curved tracks (Shabana et al., 2008; Dimitrakopoulos & Zeng, 2015). In this regard, the equations of motion of the vehicle body expressed in the global coordinate system should be established first in terms of coordinate transformation, which are then expressed in terms of the generalized trajectory coordinates.

As shown in Figure 4.1, the absolute position vector ${}_I \mathbf{u}_{O^I O^{III_i}}$ of the origin of the i^{th} body coordinate system for each component of the vehicle defined in the global coordinate system can be deduced by introducing the m^{th} trajectory coordinate system:

$$ {}_I \mathbf{u}_{O^I O^{III_i}} = {}_I \mathbf{u}_{O^I O^{II_m}} + {}_I \mathbf{u}_{O^{II_m} O^{III_i}} = {}_I \mathbf{u}_{O^I O^{II_m}} + {}_I \mathbf{R}^{II_m \to I} \cdot {}_{II_m} \mathbf{u}_{O^{II_m} O^{III_i}} \tag{4.1} $$

where the left subscript of each vector (or matrix) denotes the reference coordinate system, with I indicating the global coordinate system, II_m the m^{th} trajectory coordinate system, and III_i the i^{th} body coordinate system. Hence, ${}_I \mathbf{u}_{O^I O^{II_m}}$ is the position vector of the origin of the m^{th} trajectory coordinate system defined in the global coordinate system I, which is a function of the arc length ${}_I s^{II_m}$; ${}_I \mathbf{u}_{O^{II_m} O^{III_i}}$ is the position vector of the origin of the m^{th} trajectory coordinate system to the origin of the i^{th} body coordinate system, defined in the global coordinate system I; and ${}_{II_m} \mathbf{u}_{O^{II_m} O^{III_i}}$ is the position vector of the origin of the m^{th} trajectory coordinate system to the origin of the i^{th} body coordinate system, defined in the m^{th} trajectory coordinate system. Besides, ${}_{I}\mathbf{R}^{II_m \to I}$ is the transformation matrix defining the orientation of the m^{th} trajectory coordinate system with respect to the global coordinate system.

To express the motions of the i^{th} vehicle body in the global coordinate system in terms of the m^{th} trajectory coordinates, the following generalized trajectory coordinates are defined

$$ {}_{II_m}\mathbf{U}_i = \begin{bmatrix} {}_{I}s^{II_m} & {}_{II_m}y^{III_i} & {}_{II_m}z^{III_i} & {}_{II_m}\phi^{III_i} & {}_{II_m}\theta^{III_i} & {}_{II_m}\psi^{III_i} \end{bmatrix}^T \tag{4.2} $$

Differentiating the absolute position vector ${}_{I}\mathbf{u}_{O^I O^{III_i}}$ with respect to time t yields the translational velocity vector ${}_{I}\dot{\mathbf{u}}_{O^I O^{III_i}}$ in terms of the global coordinate system, which can further be differentiated to yield the translational acceleration vector ${}_{I}\ddot{\mathbf{u}}_{O^I O^{III_i}}$. These two vectors can be expressed with the generalized trajectory coordinates ${}_{II_m}\mathbf{U}_i$. Likewise, the rotational motions of the i^{th} body, including the absolute angular velocity vector ${}_{I}\boldsymbol{\omega}_i$ and absolute angular acceleration vector ${}_{I}\boldsymbol{\alpha}_i$, can be obtained (Shabana et al., 2008).

The absolute acceleration of the center of mass of the ith body can be obtained by differentiating Eq. (4.1) with respect to time t.

$$ {}_{I}\ddot{\mathbf{u}}_{O^I O^{III_i}} = {}_{I}\mathbf{L}^{II_m}\, {}_{II_m}\ddot{\mathbf{u}}_i + {}_{I}\boldsymbol{\gamma}_R^{I \to II_m} \tag{4.3} $$

where ${}_{I}\mathbf{L}^{II_m}$ is the coefficient matrix expressed in the Appendix C; the first part of Eq. (4.3) refers to the acceleration of the vehicle defined in the trajectory coordinate system, which is the relative motion of the vehicle respect to the track; the second part ${}_{I}\gamma_R^{I \to II_m}$ refers to the absolute acceleration of the moving origin of the trajectory coordinate system defined in the global coordinate system, which can be calculated by Eq. (4.4):

$$ {}_{I}\boldsymbol{\gamma}_{R}^{I\rightarrow II_m} = \left(\frac{\partial\, {}_{I}\mathbf{i}^{II_m}}{\partial\, {}_{I}s^{II_m}} + \frac{\partial^2\, {}_{I}\mathbf{R}^{I\rightarrow II_m}}{\partial\left({}_{I}s^{II_m}\right)^2}\, {}_{II_m}\mathbf{u}_{O^{II_m}O^{III_i}} \right) \left({}_{I}\dot{s}^{II_m}\right)^2 + 2\, {}_{I}\dot{\mathbf{R}}^{I\rightarrow II_m}\, {}_{II_m}\dot{\mathbf{u}}_{O^{II_m}O^{III_i}} \tag{4.4} $$

4.2.3 Equations of motion of a vehicle body

The equations of motion of the *i*th vehicle body can now be described by the Newton-Euler equations of motion:

$$ \begin{bmatrix} m_i\mathbf{I}_3 & \mathbf{0} \\ \mathbf{0} & {}_{III_i}\mathbf{I}_{\theta i} \end{bmatrix} \begin{bmatrix} {}_{I}\ddot{\mathbf{u}}_{O^I O^{III_i}} \\ {}_{III_i}\boldsymbol{\alpha}_i \end{bmatrix} = \begin{bmatrix} {}_{I}\mathbf{F}_{ei} \\ {}_{III_i}\boldsymbol{\tau} - {}_{III_i}\boldsymbol{\omega}_i \times \left({}_{III_i}\mathbf{I}_{\theta i}\, {}_{III_i}\boldsymbol{\omega}_i \right) \end{bmatrix} \tag{4.5} $$

where the first line is referred to the global coordinate system, and the second line in the body coordinate system. In Eq. (4.5), m_i is the mass of the *i*th body; $\mathbf{I}_3$ is the 3×3 identity matrix; ${}_{I}\ddot{\mathbf{u}}_{O^I O^{III_i}}$ is the translational acceleration vector of the center of the *i*th body; ${}_{I}\mathbf{F}_{ei}$ is the total force acting on the center of mass; ${}_{III_i}\mathbf{I}_{\theta i}$ is the moment of inertia matrix; ${}_{III_i}\boldsymbol{\alpha}_i$ is the angular acceleration vector of the *i*th body; ${}_{III_i}\boldsymbol{\tau}$ is the total torque about the center of mass of the *i*th body; and ${}_{III_i}\boldsymbol{\omega}_i$ is the angular velocity of the body.

By using Eq. (4.1) and Eq. (4.2), Eq. (4.5) can be re-written in terms of the trajectory coordinates as

$$ {}_{II_m}\mathbf{M}_i\, {}_{II_m}\ddot{\mathbf{U}}_i = {}_{II_m}\mathbf{F}_{ei} + {}_{II_m}\mathbf{F}_{vi} \tag{4.6} $$

where ${}_{II_m}\ddot{\mathbf{U}}_i$ is the translational and rotational acceleration vector of the *i*th body expressed in terms of the generalized trajectory coordinates; ${}_{II_m}\mathbf{M}_i$ is the mass matrix of the *i*th body; ${}_{II_m}\mathbf{F}_{ei}$ is the vector of external forces and toques; and ${}_{II_m}\mathbf{F}_{vi}$ is the inertial force vector due to the curved path. The last three terms are associated with the trajectory coordinate system and given by

$$\begin{cases} {}_{II_m}\mathbf{M}_i = m_i\left({}_I\mathbf{L}^{II_m}\right)^T\left({}_I\mathbf{L}^{II_m}\right)+\left({}_{III_i}\mathbf{H}^{II_m}\right)^T\left({}_{III_i}\mathbf{I}_{\theta i}\right)\left({}_{III_i}\mathbf{H}^{II_m}\right) \\ {}_{II_m}\mathbf{F}_{ei} = \left({}_I\mathbf{L}^{II_m}\right)^T {}_I\mathbf{F}_{ei} + \left({}_{III_i}\mathbf{H}^{II_m}\right)^T {}_{III_i}\boldsymbol{\tau}_{ei} \\ {}_{II_m}\mathbf{F}_{vi} = -m_i\left({}_I\mathbf{L}^{II_m}\right)^T {}_I\boldsymbol{\gamma}_R^{II_m\to I} - \left({}_{III_i}\mathbf{H}^{II_m}\right)^T\left({}_{III_i}\mathbf{I}_{\theta i}\right){}_{III_i}\boldsymbol{\gamma}_{\boldsymbol{\theta}}^{I\to III_i} \\ \qquad\qquad + \left({}_{III_i}\mathbf{H}^{II_m}\right)^T {}_{III_i}\boldsymbol{\omega}_i \times \left({}_{III_i}\mathbf{I}_{\theta i}\, {}_{III_i}\boldsymbol{\omega}_i\right) \end{cases} \tag{4.7}$$

It is noted that the inertial force vector ${}_{II_m}\mathbf{F}_{vi}$ is composed of the centrifugal forces (the first two terms) and the Coriolis forces (the third term) (Shabana et al., 2008; Dimitrakopoulos & Zeng, 2015). The terms ${}_I\mathbf{L}^{II_m}$ and ${}_{III_i}\mathbf{H}^{II_m}$ denote the velocity transformation matrices, corresponding to the translational and rotational motions. Specifically, for curved tracks, both ${}_I\mathbf{L}^{II_m}$ and ${}_{III_i}\mathbf{H}^{II_m}$ vary with time, but they become the identity matrix for straight tracks. ${}_I\boldsymbol{\gamma}_R^{II_m\to I}$ and ${}_{III_i}\boldsymbol{\gamma}_{\boldsymbol{\theta}}^{I\to III_i}$ are the vectors containing the additional quadratic velocity terms produced by the time-differentiation of the absolute linear velocity and the absolute angular velocity vectors, respectively (Shabana et al., 2008; Dimitrakopoulos & Zeng, 2015). Detailed expressions about these transformation matrices or vectors are available in Appendix C.

4.3 Dynamic Modeling of Maglev Train Subsystem

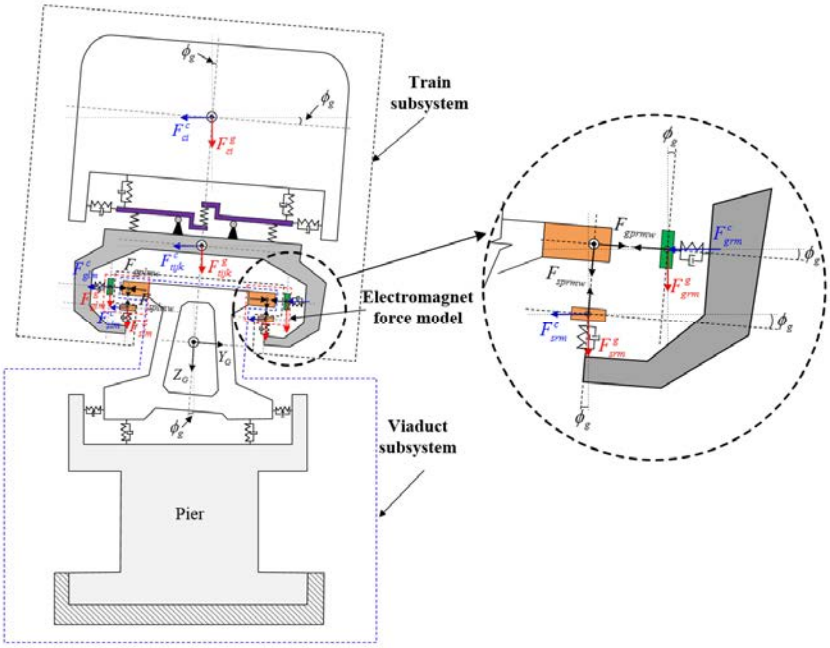

(a) Cross section of the numerical model

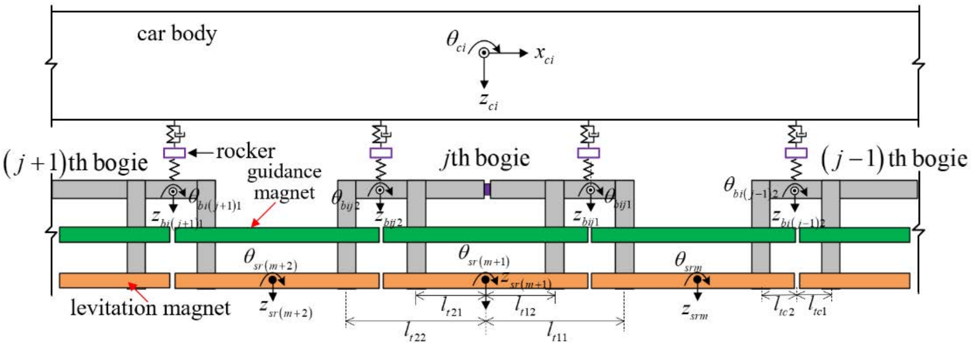

(b) The vertical plan of the train subsystem model

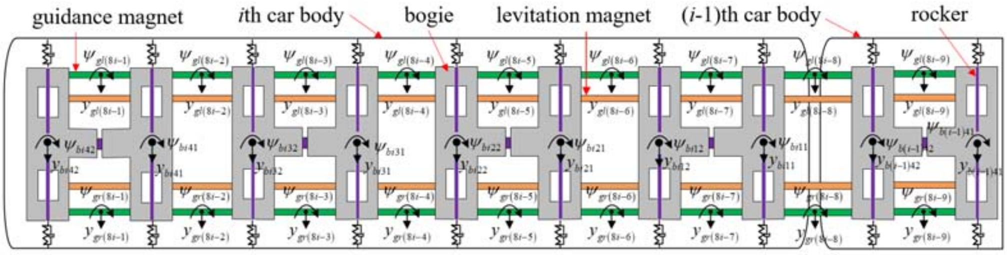

(c) The top plan of the train subsystem model

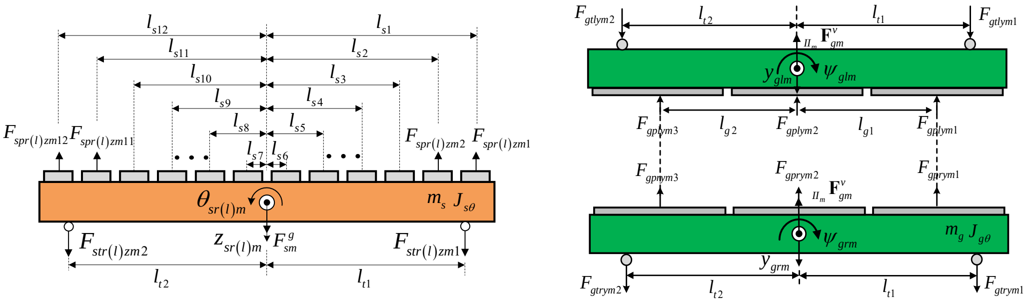

(d) Force diagram of levitation magnet

(e) Force diagram of guidance magnet

Figure 4.2 The schematic numerical model of the maglev train on curved viaduct system

In fact, a train may consist of several vehicles and run over several spans of the curved track. To this end, the equation of motion for each vehicle component is first established and assigned with a unique trajectory coordinate system according to Eq. (4.6). Then the equations of motion for the entire train subsystem is formed by assembling all the equations of motion for the components accoridng to all the trajectory coordinate systems used.

4.3.1 Trajectory coordinate systems used for a maglev train

Suppose that the maglev train has N vehicles. There are 8 sets of the levitation and guidance magnets in each vehicle (see Figure 4.2c), of which each set is assigned a trajectory coordinate system with its origin allocated at the moving point (mass center) on the centerline of the track, as shown in Figure 4.3. Moreover, the mass center of the $(ij)^{\text{th}}$ bogie (including rockers) is at the same position as that of the m^{th} set of electromagnets in the longitudinal direction, where i devotes the i^{th} vehicle, j refers to the j^{th} bogie and m=4(i-1)+2j-1. Therefore, the m^{th} trajectory coordinate system is also assigned to the $(ij)^{\text{th}}$ bogie, as shown in Figure 4.3b. Likewise, the m^{th} trajectory coordinate system is also employed to locate the i^{th} car body (see Figure 4.3a), where m=8(i-1)+4. The total number of the trajectory coordinate systems is therefore M=8N-1. The global coordinate system is fixed on the earth to trace the absolute position of a vehicle component. It is defined with three orthogonal axes: X^I, Y^I, and Z^I, with its origin fixed on the horizontal plane of the track centerline with the X^IY^I plane parallel to the ground. The body coordinate system has three orthogonal axes with its origin fixed to the mass center of the vehicle component.

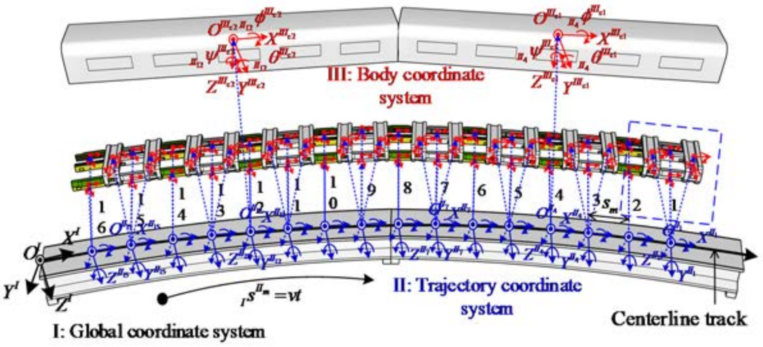

(a) Coordinate systems for vehicles

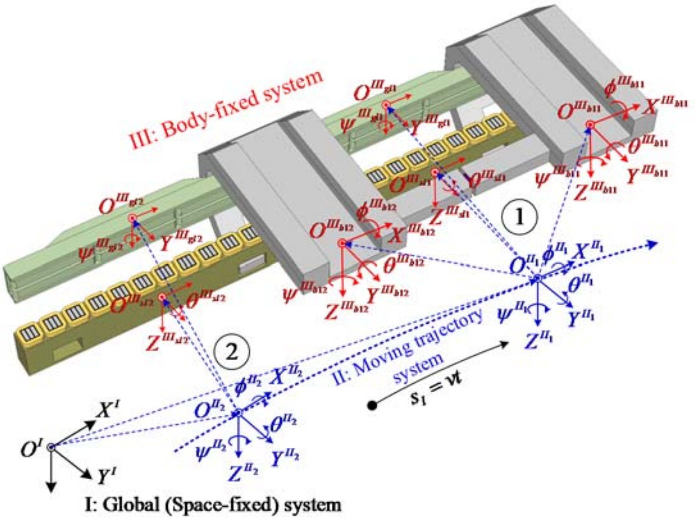

(b) Coordinate systems for components

Figure 4.3 Coordinate systems used for SML

4.3.2 Equations of motion of train subsystem

As expressed in Eq. (4.1), the dynamic motion of each vehicle component is actually described in the global coordinate system via employment of the unique moving trajectory coordinate system. However, the issues of bridge-train dynamics such as ride comfort assessment, interaction force modelling and derailment are generally track path-related rather than space-fixed, particularly for curved tracks. Thus, the dynamic equations of motion of the vehicle components should be transformed from the global coordinates into the generalized moving trajectory coordinates.

By combining the equations of motion for each rigid body (car bodies, rockers, bogies, levitation magnets and guidance magnets) in the train subsystem, the equations of motion of the train subsystem defined in their own trajectory coordinate systems can be written as

$$ {}_{II}\mathbf{M}_V\,{}_{II}\ddot{\mathbf{U}}_V + {}_{II}\mathbf{C}_V\,{}_{II}\dot{\mathbf{U}}_V + {}_{II}\mathbf{K}_V\,{}_{II}\mathbf{U}_V = {}_{II}\mathbf{F}_V^{G\to V} + {}_{II}\mathbf{F}_V^{e} + {}_{II}\mathbf{F}_V^{v} \tag{4.8} $$

where for the train subsystem, ${}_{II}\mathbf{M}_V$ is the mass matrix; ${}_{II}\mathbf{K}_V$ and ${}_{II}\mathbf{C}_V$ are the stiffness and damping matrices, respectively; ${}_{II}\ddot{\mathbf{U}}_V$, ${}_{II}\dot{\mathbf{U}}_V$, and ${}_{II}\mathbf{U}_V$ are the acceleration, velocity and displacement vectors, respectively; ${}_{II}\mathbf{F}_V^{G\to V}$ is the interaction force vector between the vehicles and rails, which will be further discussed in Section 4.5; ${}_{II}\mathbf{F}_V^{e}$ is the external force vector, including the gravity forces, seismic loads or wind loads; and ${}_{II}\mathbf{F}_V^{v}$ is the inertial force vector, including the centrifugal force and Coriolis force. The force vectors ${}_{II}\mathbf{F}_V^{e}$ and ${}_{II}\mathbf{F}_V^{v}$ can be calculated according to Eq. (4.7).

The displacement vector ${}_{II}\mathbf{U}_V$ of the train subsystem can be assembled from the sub-displacement vectors of all the vehicle components as

$$ {}_{II}\mathbf{U}_V = \left[{}_{II_{m_c}}\mathbf{U}_N^{c} \quad {}_{II_{m_b}}\mathbf{U}_N^{b} \quad {}_{II_{m_t}}\mathbf{U}_N^{t} \quad {}_{II_{m_s}}\mathbf{U}_N^{s} \quad {}_{II_{m_g}}\mathbf{U}_N^{g} \right]^{\mathrm{T}} \tag{4.9} $$

in which the entries represent the sub-displacement vectors of the car bodies, bogies, rockers, levitation magnets, and guidance magnets of the train subsystem, respectively. Each sub-displacement vector further consists of *N* sets of sub-terms for the car bodies, bogies, and rockers, and *M* sets of sub-terms for the levitation and guidance magnets, in which $M = 8N - 1$.

Accordingly, the mass matrix in Eq. (4.7) can be assembled from the sub-mass matrices as

$$ {}_{II}\mathbf{M}^{V} = \mathrm{diag}\left[{}_{II_{m_c}}\mathbf{M}_{N}^{c} \quad {}_{II_{m_b}}\mathbf{M}_{N}^{b} \quad {}_{II_{m_t}}\mathbf{M}_{N}^{t} \quad {}_{II_{m_s}}\mathbf{M}_{N}^{s} \quad {}_{II_{m_g}}\mathbf{M}_{N}^{g} \right] \tag{4.10} $$

where the entries represent the sub-mass matrices of the car bodies, bogies, rockers, levitation magnets, and guidance magnets of the train subsystem, respectively, which can be calculated based on Eq. (4.7).

The elements of the vector ${}_{II}\mathbf{K}_{V}$ represent the relative stiffness corresponding to the pre-defined DOFs expressed with respect to their unique trajectory coordinate systems. At any time *t*, it can be assumed that the three orthogonal axes of the body-fixed system for each component are always respectively parallel to those of their unique trajectory coordinate system. That is to say, the motion of each vehicle component on the curved track defined in its unique trajectory coordinate system is similar to that on the straight track in the global coordinate system. Therefore, the vector ${}_{II}\mathbf{K}_{V}$ defined in the trajectory coordinate systems can directly be used for the straight track, which has been fully described in Chapter 3 and Appendix A. Likewise, the vector ${}_{II}\mathbf{C}_{V}$ can be obtained.

4.4 Dynamic Modeling of Circular Curved Viaduct Subsystem

In this section, the SML is taken as an example to illustrate the modeling of a curved viaduct subsystem characterized by an inclination angle and curvature. Specifically, the curved girder is built with a curvature of 1/*R* along the centerline of the track (see Figure 4.4), and a rolling rotation ϕ_g about the centerline is also introduced to the track plane and underlying girder. The details are given in the following subsection.

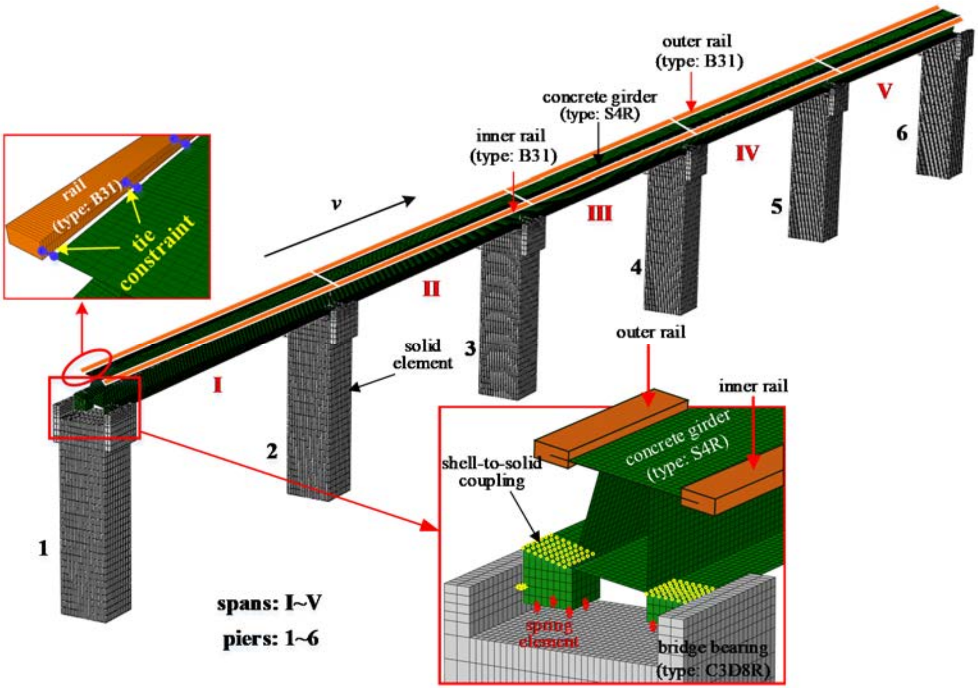

Figure 4.4 Finite element model of curved viaduct subsystem (SML)

4.4.1 Finite element model of circular curved viaduct

The establishment of the finite element model of a circular curved viaduct is similar to that of a straight viaduct, as discussed in Section 3.3, excpet for geometric difference in alignment. The finite element model of the circular curved viaduct is established by considering the two important alignment parameters: curve radius R and cant angle ϕ_g. The cross section of the girder remains unchnaged but its orientation is chnaged.

4.4.2 Equations of motion for circular curved viaduct subsystem

By assembling all the components of the viaduct subsystem, including the rails, concrete girders, bearings, and piers, the global mass matrix ${}_I\mathbf{M}_G$ and stiffness matrix ${}_I\mathbf{K}_G$ for the entire viaduct subsystem are obtained in the global coordinate system. The equations of motion for the curved viaduct subsystem can be summarized as:

$${}_I\mathbf{M}_G\,{}_I\ddot{\mathbf{U}}_G + {}_I\mathbf{C}_G\,{}_I\dot{\mathbf{U}}_G + {}_I\mathbf{K}_G\,{}_I\mathbf{U}_G = {}_I\mathbf{F}_G^{V\to G} + {}_I\mathbf{F}_G^{e} \tag{4.11}$$

where for the subsystem considered, ${}_{I}\mathbf{U}_G$, ${}_{I}\dot{\mathbf{U}}_G$ and ${}_{I}\ddot{\mathbf{U}}_G$ are the displacement, velocity and acceleration vectors; ${}_{I}\mathbf{F}_G^e$ is the external force vector, including the gravity force, seismic loads, and wind loads; and ${}_{I}\mathbf{F}_G^{V\rightarrow G}$ is the vector of the electromagnet forces acting on the viaduct, with the nonzero parts targeted at the loading rails, to be discussed in detail in Section 4.5. The mass, stiffness and damping matrices of the circular curved viaduct subsystem can be formulated in a simlar way as that of the straight viaduct subsystem, as discussed in Section 3.3.3.

4.5 Interaction Modelling

The interaction between the train and curved viaduct subsystems is also simulated by the interactive electromagnet force-air gap model presented in Section 3.4. However, since the magnets of train are continuously and strictly travelling along the curved rails of the viaduct, the interactive electromagnet force vectors are perpendicular to the trajectory coordinate system rather than the global coordinate system. Thus, the interaction between the train and curved viaduct is more conveniently modelled in the trajectory coordinate system.

4.5.1 Interactive electromagnet force-air gap model

The electromagnetic force-air gap model defined in the trajectory coordinate system is also established based on the current circuit and the distance between the electromagnet and rail track (Sinha, 1987).

$$ {}_{II}\mathbf{F}\left(i_w^t, h_w^t\right) = K_0\left(\frac{\mathbf{i}_w^t}{{}_{II}\mathbf{h}_w^t}\right)^2 \tag{4.12a} $$

where ${}_{II}\mathbf{F}\left(i_w^t, h_w^t\right)$ is the current-controlled electromagnetic force between the w^{th} maglev pole and the rail track, defined in the pertinent trajectory coordinate system; the superscript (t) indicates the current time step and the subscript (w) the w^{th} maglev pole; $\mathbf{i}_w^t$ is the electrical circuit; ${}_{II}\mathbf{h}_w^t$ is the magnetic air gap for inclusion of the levitation air gap and guidance air gap, calculated by

$$ {}_{II}\mathbf{h}_w^t = \mathbf{h}_0 + {}_{II}\mathbf{u}_w(t) + {}_{II}\mathbf{u}_G\left(s_w^t\right) + \mathbf{u}_r\left(s_w^t\right) \tag{4.12b} $$

Here $\mathbf{h}_0$ is the design static gap at the static equilibrium state of the train (10 mm for SML); ${}_{II}\mathbf{u}_w(t)$ is the motion of the w^{th} magnetic pole defined in the pertinent trajectory coordinate system, extracted from the response of the train subsystem; s_w^t is the arc length from the w^{th} maglev pole to the origin of the global coordinate system; $\mathbf{u}_r\left(s_w^t\right)$ is the track irregularity referencing Section 3.4.2; and ${}_{II}\mathbf{u}_G\left(s_w^t\right)$ is the rail deflection at the w^{th} magnetic pole with respect to the pertinent trajectory coordinate system, obtained through transformation of the response of the rail at the same location,

$$ {}_{II}\mathbf{u}_G\left(s_w^t\right) = \left({}_{I}\mathbf{R}^{II_m \to I}\right)^T {}_{I}\mathbf{u}_G\left(s_w^t\right) \tag{4.12c} $$

Here ${}_{I}\mathbf{R}^{II_m \to I}$ can be obtained from Eq. (C2); and ${}_{I}\mathbf{u}_G\left(s_w^t\right)$ is the deflection of the rail defined in the global coordinate system.

A proportional-derivative (PD) controller similar with that in Section 3.4.1 is also used to fulfil this feedback control. This PD controller computes the gap error, the difference between the desired gap and the measured air gap, and then minimizes the gap error by adjusting the current circuit:

$$ \begin{aligned} \mathbf{i}_w^{t+\Delta t} = & \left(\frac{1}{\Delta t} - \frac{{}_{II}\dot{\mathbf{h}}_w^{t+\Delta t}}{{}_{II}\mathbf{h}_w^{t+\Delta t}} + \frac{{}_{II}\mathbf{h}_w^{t+\Delta t}}{\Gamma_0} R_0 \right)^{-1} \times \\ & \left[\mathbf{V}_0 + K_p\left({}_{II}\mathbf{h}_0 - {}_{II}\mathbf{h}_w^{t+\Delta t}\right) - K_d\, {}_{II}\dot{\mathbf{h}}_w^{t+\Delta t} + \frac{\Gamma_0}{{}_{II}\mathbf{h}_w^{t+\Delta t}\Delta t} \mathbf{i}_w^t \right] \frac{{}_{II}\mathbf{h}_w^{t+\Delta t}}{\Gamma_0} \end{aligned} \tag{4.12d} $$

where $\Gamma_0 = 2K_0$ is the initial inductance of the coil winding of the guidance or levitation magnets; R_0 is the coil resistance of the electronic circuit; and $\mathbf{V}_0$ is the static voltage. Since ${}_{II}\mathbf{h}_w^{t+\Delta t}$ and ${}_{II}\dot{\mathbf{h}}_w^{t+\Delta t}$ can be obtained from Eq. (4.12b) in the numerical study and $\mathbf{i}_w^t$ is the known current value at time *t*, the unknown control current $\mathbf{i}_w^{t+\Delta t}$ at time $t+\Delta t$ can be determined by Eq. (4.12d). Finally, the levitation or guidance force ${}_{II}\mathbf{F}\left(i_w^{t+\Delta t}, h_w^{t+\Delta t}\right)$ at time $t+\Delta t$ can be determined from Eq. (4.12a).

4.5.2 Equations of motion for the coupled system and solution method

The equations of motion for the coupled maglev train-curved viaduct system are

$$\begin{bmatrix} {}_{II}\mathbf{M}_V & \mathbf{0} \\ \mathbf{0} & {}_{I}\mathbf{M}_G \end{bmatrix}\begin{bmatrix} {}_{II}\ddot{\mathbf{U}}_V \\ {}_{I}\ddot{\mathbf{U}}_G \end{bmatrix}+\begin{bmatrix} {}_{II}\mathbf{C}_V & \mathbf{0} \\ \mathbf{0} & {}_{I}\mathbf{C}_G \end{bmatrix}\begin{bmatrix} {}_{II}\dot{\mathbf{U}}_V \\ {}_{I}\dot{\mathbf{U}}_G \end{bmatrix}+\begin{bmatrix} {}_{II}\mathbf{K}_V & \mathbf{0} \\ \mathbf{0} & {}_{I}\mathbf{K}_G \end{bmatrix}\begin{bmatrix} {}_{II}\mathbf{U}_V \\ {}_{I}\mathbf{U}_G \end{bmatrix}$$

$$=\begin{bmatrix} {}_{II}\mathbf{F}_V^e + {}_{II}\mathbf{F}_V^v + {}_{II}\mathbf{F}_V^{G\to V} \\ {}_{I}\mathbf{F}_G^e + {}_{I}\mathbf{F}_G^{V\to G} \end{bmatrix} \tag{4.13}$$

where the first equation is the one for the train subsystem in the generalized trajectory coordinates; and the second equation for the viaduct subsystem in the global coordinates. The interaction between the two subsystems is realized by the two force vectors ${}_{II}\mathbf{F}_V^{G\to V}$ and ${}_{I}\mathbf{F}_V^{V\to G}$. The dimension of the force vector ${}_{II}\mathbf{F}_V^{G\to V}$ is determined by Eq. (4.9), in which the nonzero entries are associated with the levitation and guidance magnets only, and the entries for the car bodies, bogies and rockers are all zero. Specifically, for a time increment Δt all the electromagnetic forces ${}_{II}\mathbf{F}\left(i_w^t, h_w^t\right)$ are first computed based on Eq. (4.12), and are then combined to determine the external resultant forces on and the external resultant moment around the mass center of the mth magnet in the vertical and pitching rotational directions for the levitation magnets and lateral and yawing rotational directions for the guidance magnets, respectively (see Figures 4.2d and 4.2e). The external resultant forces and moments of each magnet are then placed into the vector ${}_{II}\mathbf{F}_V^{G\to V}$ at the pertinent DOFs, and the responses of the train subsystem at time $t+\Delta t$ are computed. Meanwhile, the calculated electromagnet forces ${}_{II}\mathbf{F}\left(i_w^t, h_w^t\right)$ in the trajectory coordinate system are transformed to the global coordinate system by $\left({}_{I}\mathbf{R}^{II_m\to I}\right)^T {}_{II}\mathbf{F}\left(i_w^t, h_w^t\right)$, which then form the nonzero entries in the vector ${}_{I}\mathbf{F}_V^{V\to G}$. The loaded position of the electromagnet force at the wth magnetic pole to the rail can be determined by:

$$s_w = v\left(t-t_w\right)\left[H\left(t-t_w\right)-H\left(t-t_w-\frac{nL}{v}\right)\right] \tag{4.14}$$

where v is the speed of the train; t_w is the traveling time of the w^{th} pole since it enters the concerned span of the viaduct; $t_w=\left(w-1\right)d/v$; d is the force space; L is the arc length of the centerline of one span; $H\left(t\right)$ is the unit step function; and n is the number of spans. For $s_w=0$, it means that the w^{th} load is off the n spans, and ${}_{II}\mathbf{u}_G\left(s_w^t\right)$ and $\mathbf{u}_r\left(s_w^t\right)$ in Eq. (4.12b) are taken as zero to obtain the air gap ${}_{II}\mathbf{h}_w^t$.

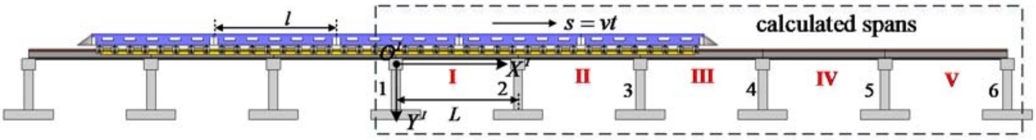

(a) Side view of a train with 5 maglev vehicles running on viaduct in SML

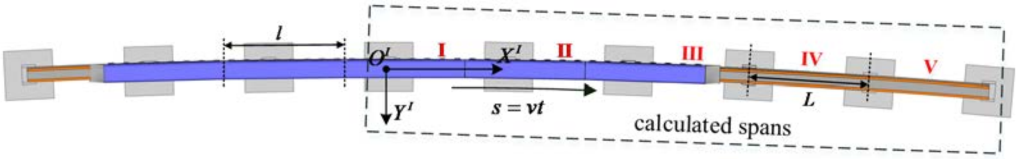

(b) Top view of a train with 5 maglev vehicles running on viaduct in SML

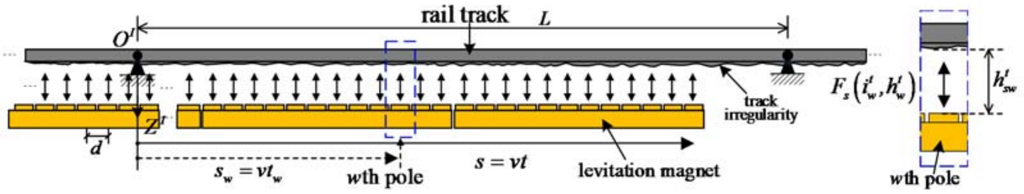

(c) Force diagrams between the levitation magnet and rail track

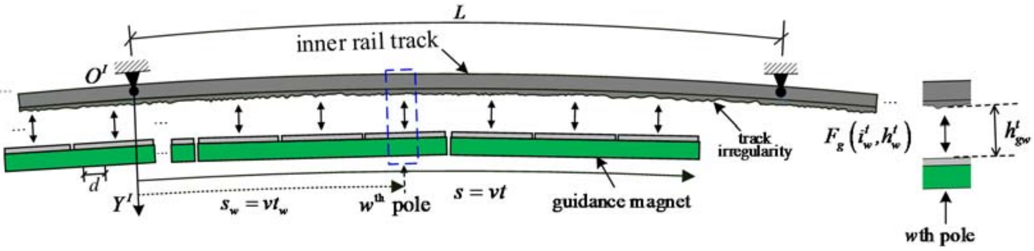

(d) Force diagrams between the guidance magnet and rail track

Figure 4.5 Coupled maglev train-viaduct system in SML

Like the solutions in Section 3.4.3, the ABAQUS Explicit Solver with a self-developed ABAQUS subroutine is used here. Specifically, with the responses of both the viaduct and train subsystems available at time t, the interactive electromagnetic forces at time $t+\Delta t$ can be obtained using Eqs. (4.12a~d), in which the PD controller is used to adjust the interaction forces according to the gap error e_w^t. Accordingly, the two interfaces, VDLOAD for the load application on the rail by the position vector s_w with ${}_{II}\mathbf{F}\left(i_w^t, h_w^t\right)$ and VUFIELD for collection of the response ${}_{II}\mathbf{u}_G\left(s_w^t\right)$ and ${}_{II}\dot{\mathbf{u}}_G\left(s_w^t\right)$ of the loaded elements of the rail, are developed for the simultaneous computation of both the train and viaduct subsystems. The time interval used in the computation is 4×10^{-6} s and the threshold for the error in the air gap is set as 0.001 m.

4.6 Numerical Study and Validation

The proposed procedure is now applied to the SML in the case study. In most of the curved sections of the SML, balanced cant angles are designed to provide a gravitational acceleration component to counteract the curved path-induced centrifugal acceleration. The balanced cant angle can be calculated as:

$$\phi_{bal} = \frac{180^\circ}{\pi}\frac{v^2}{R\cdot g} \tag{4.15}$$

where g is the gravitational acceleration; v is the vehicle speed; and R is the radius of the curved track. The maglev train running over a curved section of R = 3300 m and a balanced cant angle of 12° at v = 300 km/h is first investigated. Since the vehicle speed satisfies Eq. (4.15), it is also called the equilibrium-vehicle speed. The numerical study concerns a maglev train with five vehicles moving on the five-span curved viaduct at v = 300 km/h, as shown in Figure 4.6, the arc length of each span is 24.768 m. The details and major parameters of the viaduct and train subsystems can be found in the Section 3.3. Before the train starts moving on the calculated spans, the vehicles have achieved an equilibrium state by traveling over a long enough curved and rigid track. The initial steady-state vibration has reached a deformed equilibrium configuration with zero radial and vertical accelerations. The computed results are compared with those for the train running over straight viaducts so that the curved path-induced features can be found. The field measurement results of the maglev vehicle response are also used to partially validate the proposed procedure. Then, the effect of curved tracks with different radii and the effect of cant deficiencies on the coupled system are investigated.

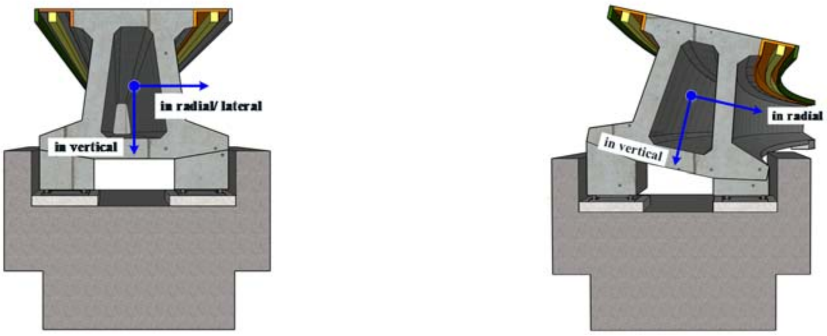

(a) Straight section (b) Curved section

Figure 4.6 Schematic diagrams of straight and curved viaduct sections and definition of directions.

4.6.1 Comparison of vehicle and viaduct responses between curved and straight sections

The schematic diagrams of the straight and curved viaduct sections are shown in Figure 4.6. The vertical and radial/lateral directions are defined to be perpendicular and parallel to the track plane. The responses of the viaduct and the vehicle are compared between the curved and straight sections.

4.6.1.1 Dynamic responses of curved viaduct

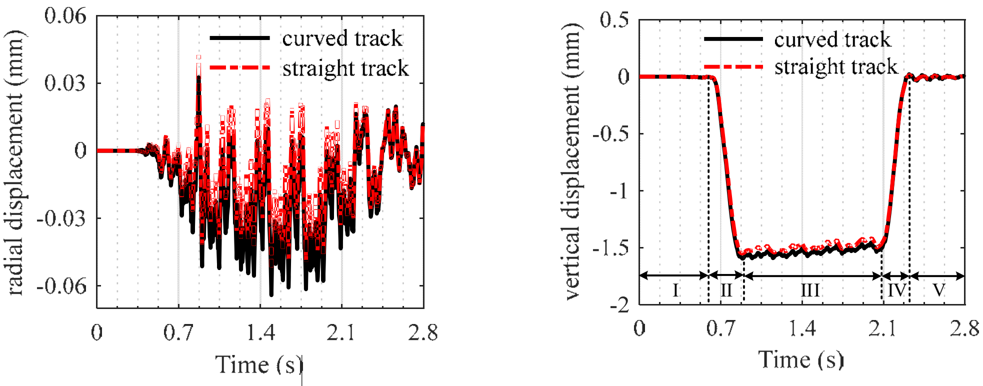

(a) in radial (b) in vertical

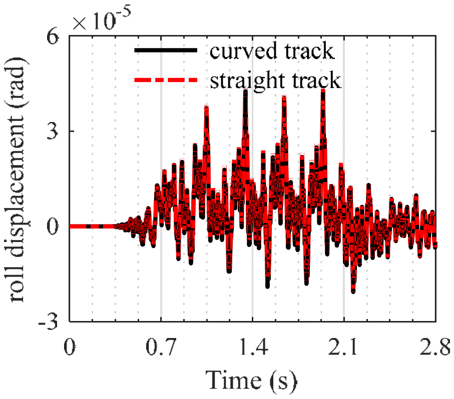

(c) in rotational

Figure 4.7 Comparison of displacement time histories at midspan of the third girder.

Figure 4.7 shows the time-history response computed for the midspan of the third girder in the radial, vertical and rotational directions about the central axis of the girder for the maglev train passing through the curved and straight viaducts for a period of 2.8 seconds. Each time history can be divided into five segments according to the loading conditions of the girder, see Figure 4.7b. The first segment refers to the period (I: 0~0.6 s) when the train is moving on the first two girders. During this period, all the computed responses (see Figure 4.7) are very small, as they are indirectly excited by the vibration of the first two girders through the 3rd pier, see Figure 4.4 and Figure 4.5a. Then, the train begins running on the third (concerned) girder from 0.6 s, the responses increase quickly and reach to a peak when the third girder is fully loaded at 0.89 s (Period II: 0.6~0.89 s). The following is a long period (III: 0.89~2.08 s), during which the third girder is fully loaded by the passing train. When the last vehicle of the train starts leaving the third girder in the fourth period (IV: 2.08~2.38 s), the responses gradually decrease. In this period, the third girder is not directly excited but continuously affected by the loaded fourth girder. Finally, free vibration of the third girder occurs in the fifth period (V: 2.38~2.8 s).

As can be seen from Figure 4.7, for the curved track with balanced radius and cant angle under the train travelling at 300 km/h, the component of centrifugal force in the radial direction is well compensated by that of gravitational force in the same direction. As a result, the response of the curved girder in the radial direction is very small, as shown in Figure 4.7a, close to that of the straight girder, of which the peak values are 0.06 and 0.05 mm, respectively. However, because of the cant angle ϕ_{bal}, the resultant of the gravitational and centrifugal forces in the vertical direction is $g \cdot \cos\left(\phi_{bal}\right) + \frac{v^2}{R} \cdot \sin\left(\phi_{bal}\right)$, which is larger than g for straight girders. Thus, a slightly larger displacement response in the vertical direction is found, compared to that of the straight girder, as can be seen from Figure 4.7b. Besides, similar responses exist for the curved and straight girders in the rotational direction, as shown in Figure 4.7c.

4.6.1.2 Computed and measured results of dynamic responses of maglev vehicle

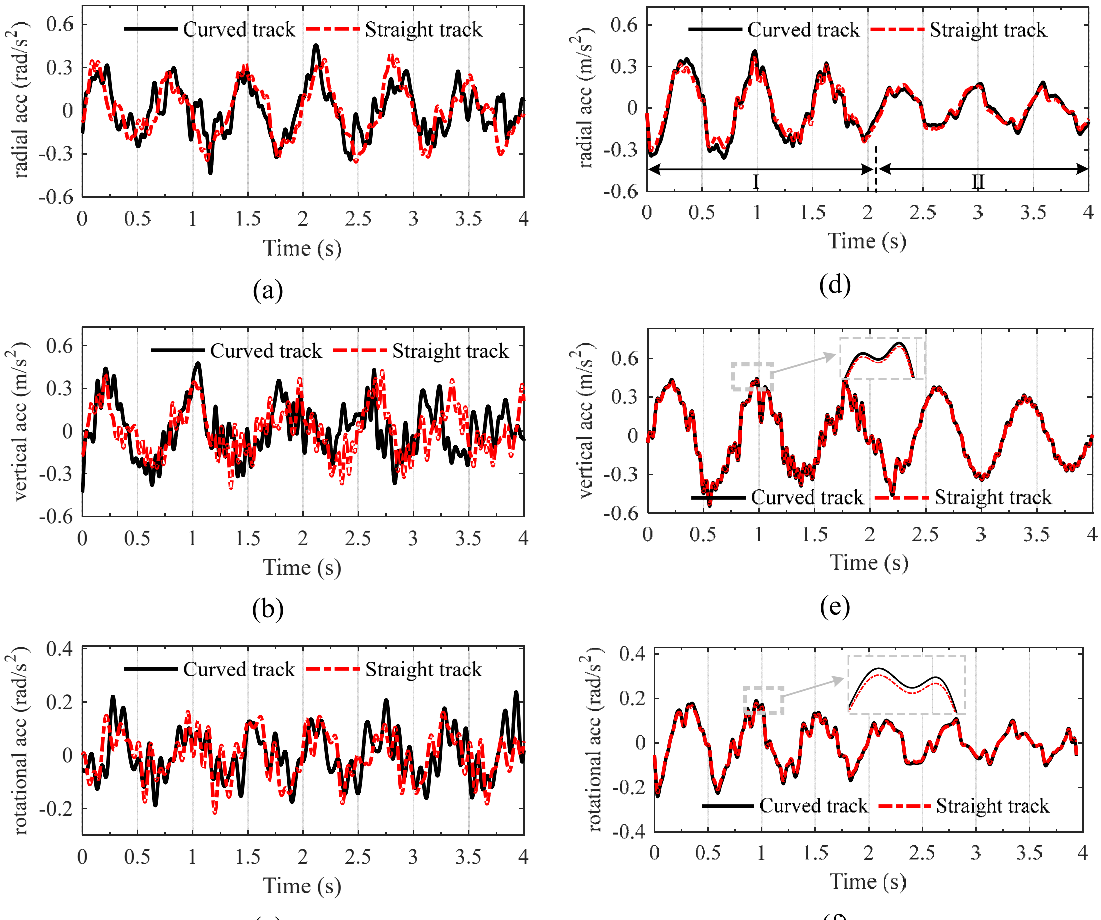

(a) (d)

(b) (e)

(c) (f)

Figure 4.8 Absolute acceleration time histories of the 2nd maglev vehicle body moving over the curved and straight viaducts: (a, b and c) measured results, (d, e and f) numerical results; (a and d) in radial direction, (b and e) in vertical direction, (c and f) in rotational.

Figure 4.8 shows the measured and computed absolute acceleration time histories of the second maglev vehicle moving over the curved and straight viaducts. A phenomenon similar to the girder response is also observed in the vehicle response. That is, the vehicle moving on the curved track with balanced radius and cant angle is similar to that on the straight track. This phenomenon can be seen more clearly from the computed results. Each of the computed results can be divided into two segments according to the operational conditions of the vehicle concerned on and off the five spans, see Figures 4.8d, 4.8e, 4.8f. Specifically, the computed vehicle response in period I (0~2.08 s) has been generated with consideration of the effect of flexibility of the viaducts, while in period II (2.08~4.0 s) the vehicle is set to run on a rigid road. Obviously, the computed response in period I is generally larger than that in period II, as shown in Figures 4.8d, 4.8e, 4.8f. Besides, the computed responses of the vehicle running on the flexible viaducts (period I) can well match the measured ones, respectively, for either curved or straight tracks. Moreover, the absolute accelerations of the vehicle in the three directions increase; however, since the curved track is designed with balanced curve radius and cant, these increases are very small.

4.6.2 Effect of track radius

As shown in Figure 1.3, the tracks of various curvature radii (2000 to 10000 m) and inclination angles (1° to 12°) were used in the SML. Since the viaduct safety and vehicle ride comfort are highly affected by the curved path-induced centrifugal forces, the effect of curved track of various radii on the viaduct and vehicle responses is numerically investigated in this section.

4.6.2.1 Effect of different balanced tracks

In Section 4.6.1, only one balanced track is considered. In this section, the investigation is extended to different balanced tracks. The track radii concerned are 2500, 3000, 5000, 7500, and 10000 m, the corresponding balanced cant angles are 16°, 13°, 8°, 5.4°, and 4°, respectively. The equilibrium vehicle speed is 300 km/h. Before the vehicle enters the circular viaducts, the train is assumed to move along the smooth rigid circular track of the same radius and cant with the established circular viaduct, as a result, the initial response of the vehicle at time $t=0$ in the three directions are zero. The dynamic responses of the maglev vehicle moving over the five curved sections are individually computed and then compared with each other.

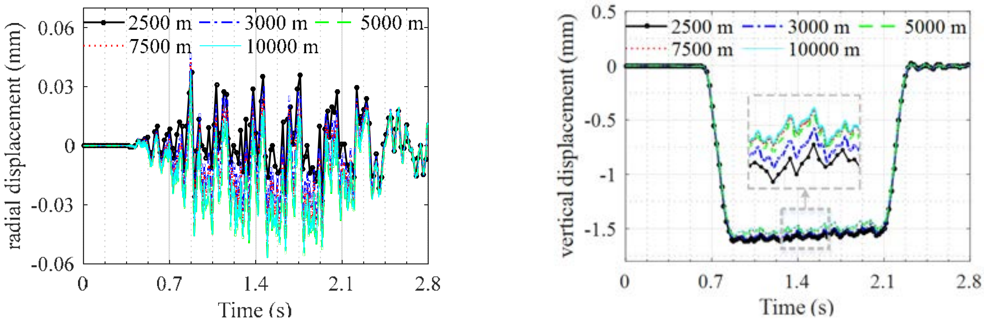

(a) in radial (b) in vertical

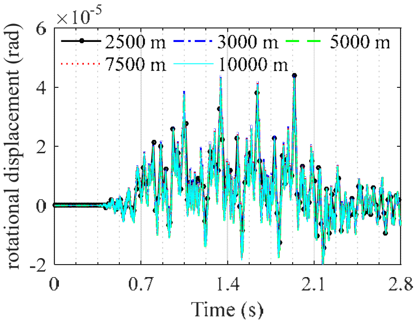

(c) in rotational

Figure 4.9 Displacement time histories at midpoint of the 3rd girder due to the maglev train over five balanced curved tracks.

Figure 4.9 shows the displacement response time histories at the midpoint of the 3rd girder in the radial, vertical and rotational directions due to the maglev train running over the five sets of balanced curved tracks. Because the curved track has a balanced radius and cant angle, the component of centrifugal force in the radial direction is well compensated by that of gravitational force in the same direction. The radial displacements thus fluctuate around zero slightly. However, due to different balanced cant angles for different track radii, the resulting force in the vertical direction, calculated based on the equation $g \cdot \cos(\phi_{bal}) + \frac{v^2}{R} \cdot \sin(\phi_{bal})$, is different. As shown in Figure 4.9b, smaller radius and higher cant angle result in larger vertical displacement. Besides, almost identical response can be observed for the midpoint of the third girder in the rotational direction in Figure 4.9c for the five balanced curved tracks.

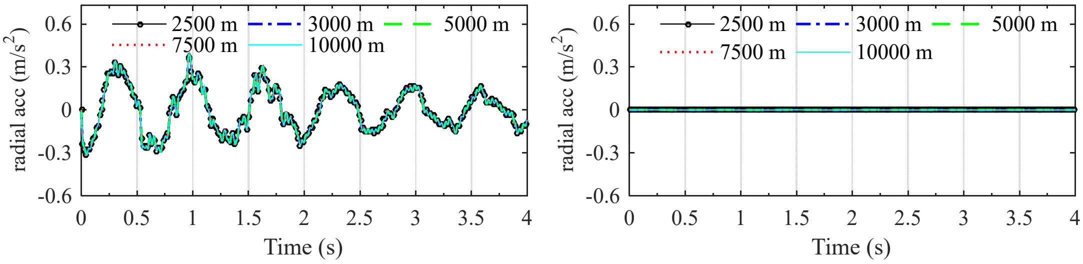

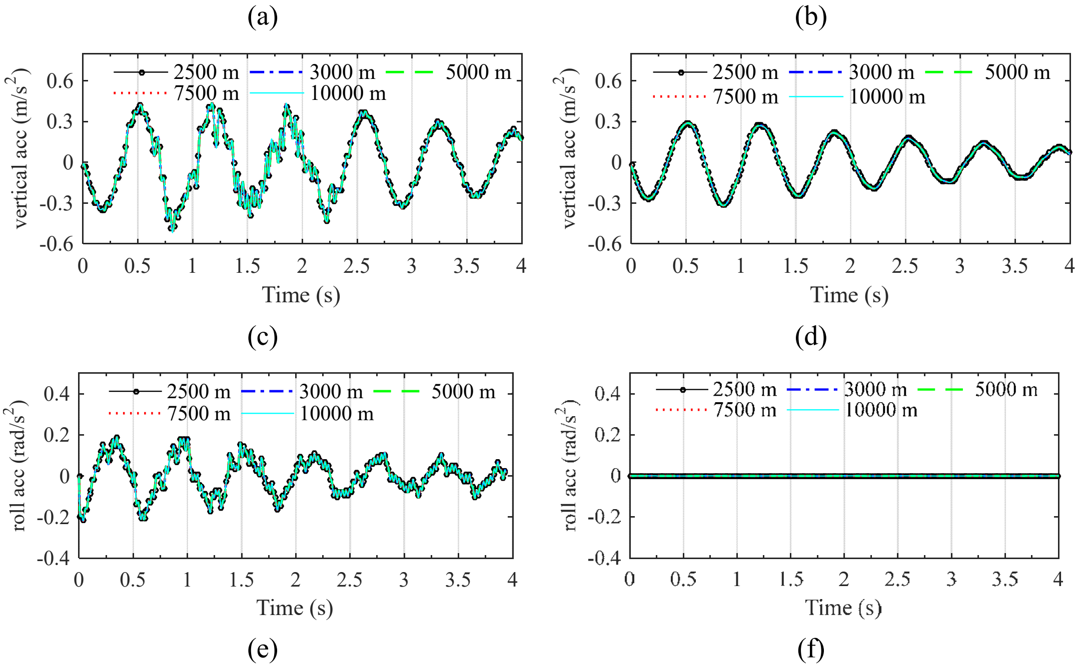

Figure 4.10 Acceleration time histories of the 2^{ed} maglev vehicle *defined in the trajectory coordinate system induced by the train* moving over five balanced curved tracks: (a, b and c) with and (d, e and f) without considering track irregularities; (a and d) in radial direction, (b and e) in vertical direction, and (c and f) in rotational.

The acceleration responses of the second maglev vehicle *defined in the trajectory coordinate system induced by the train* moving over the five balanced curved tracks/viaducts are plotted in Figure 4.10, in which parts (a), (b) and (c) show the responses of the vehicle with track irregularities, and parts (d), (e) and (f) show those without track irregularities. It can be seen that the vehicle responses remain almost the same no matter which set of the balanced curved track and which direction are considered. These responses are also identical to those of the vehicle moving on the straight track. It is noticeable that with consideration of track irregularities, even on the straight or balanced curved track, the radial and rotational responses are comparable with that in the vertical. Nevertheless, when the track irregularities are ignored, the radial and rotational responses of the vehicle turn to be zero, as shown in Figure 4.10d and 4.10f, while the vertical response in Figure 4.10e fluctuates with a peak value varying from 0.45 to 0.30 m/s^2. It can be concluded that track irregularities are the main excitations for the vehicle response in the radial (or lateral) and rotational directions, but not for the vertical response.

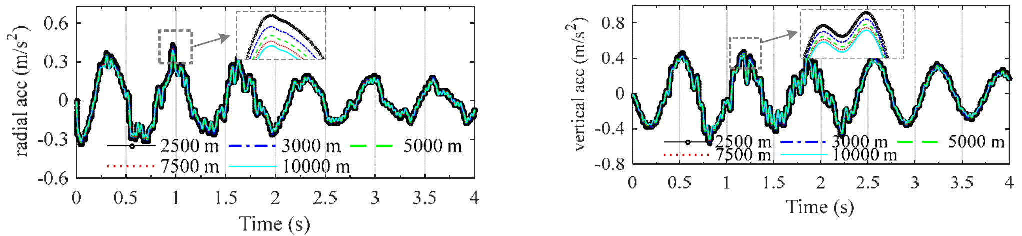

(a) in radial

(b) in vertical

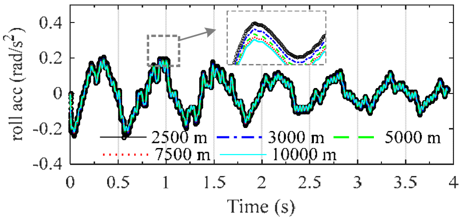

(c) in rotational

Figure 4.11 The absolute acceleration time histories of the 2^{ed} maglev vehicle moving over five balanced curved tracks.

Figure 4.10 shows the relative accelerations of the vehicle respect to the track, however, for the assessment of the passengers' ride quality, the absolute accelerations of the vehicle defined in the global coordinate system should be used instead; they are calculated based on Eq. (4.3) and shown in Figure 4.11. It can be found that with the decrease of the curve radius, the absolute accelerations of the vehicle in the three directions increase; however, since the five sets of curved tracks are designed with balanced curve radii and cants, these increases are slight.

4.6.2.2 Effect of zero cant angle

This section explores what will happen if the unbalanced curved track is used. The cant angles used in Section 4.6.2.1 are now set to zero to yield five unbalanced tracks with five different radii to see what happens with the viaduct and vehicle responses.

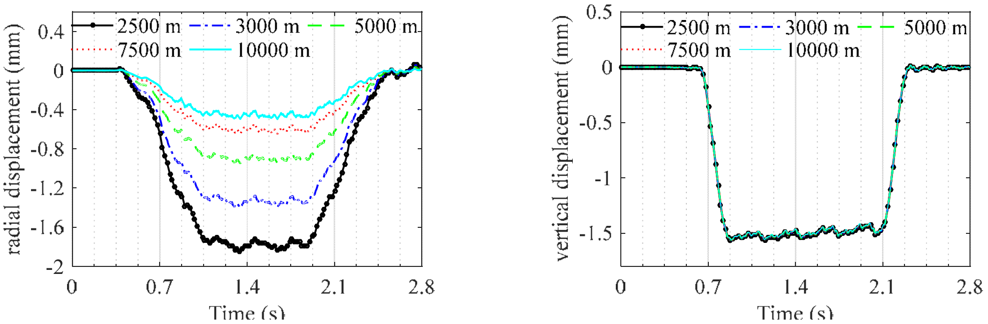

(a) in radial

(b) in vertical

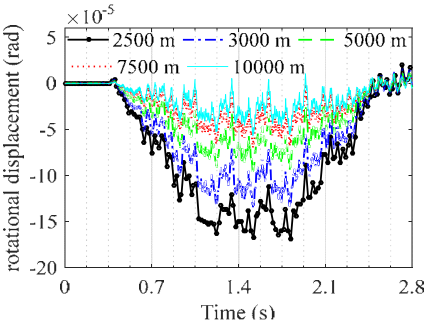

(c) in rotational

Figure 4.12 Displacement time histories at midpoint of the 3rd girder due to moving vehicle on the track with various radii but zero cant angle.

Figure 4.12 shows the displacement time histories at the midpoint of the 3rd girder induced by the maglev train moving over the curved tracks of different radii but zero cant angle. As the cant angle is zero, the curved path-induced centrifugal force on the vehicle shall be counterbalanced by the guidance forces generated between the guidance magnets and rails in the radial direction. Therefore, the guidance forces are highly dependent on v^2/R_i. The smaller is the track radius, the larger the guidance forces act on the girder. As a result, the displacement response of the girder in the radial direction increases as the radius of the curved track decreases. It is noticeable that the radial displacement induced by small curve radii is comparable with the vertical direction. Similar observation can be made for the rotational response of the girder. The rotational response of the girder in Figure 4.12c shows a fluctuation similar to the radial response of the girder in Figure 4.12a. However, for zero cant angle, the gravitational force acting on the girder is equal in the vertical direction. Therefore, the girder responses in the vertical direction are almost the same regardless of the track radius, as shown in Figure 4.12b.

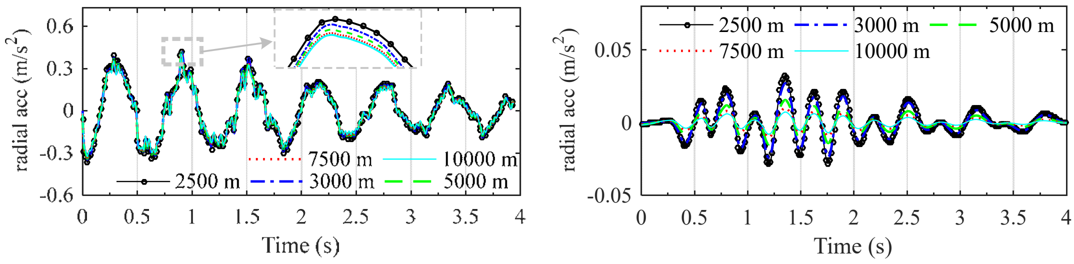

(a)

(b)

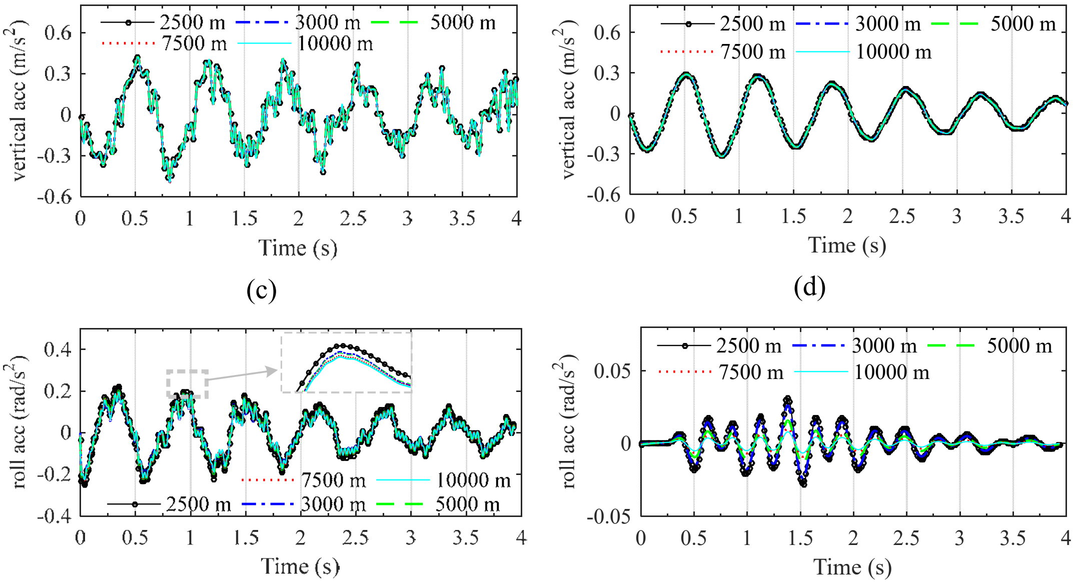

(c) (d)

(e) (f)

Figure 4.13 Acceleration time histories of the 2^{ed} maglev vehicle *defined in the trajectory coordinate system induced by the train* moving over the track of various radii but zero cant angle: (a, b and c) with and (d, e and f) without track irregularities; (a and d) in radial, (b and e) in vertical, (c and f) in rotational.

The acceleration responses of the second maglev vehicle *defined in the trajectory coordinate system induced by the train* moving over the five unbalanced curved tracks/viaducts are plotted in Figure 4.13, in which parts (a), (b) and (c) show the responses of the vehicle with track irregularities, and parts (d), (e) and (f) show those without track irregularities. It can be seen from Figures 4.13a, 4.13b and 4.13c that with consideration of the track irregularities, only slight differences exist in the radial and rotational responses of the vehicle for different radii but with zero cant angle. The vertical responses are almost equal. However, when the track irregularities are absent, sharper reductions appear in the radial (see Figures 4.13a and 4.13d) and rotational (Figures 4.13c and 4.13f) responses of the vehicle, respectively. Besides, it can be observed from Figures 4.13d and 4.13f that the vehicle responses in the radial and rotational directions increase as the radius of track decreases. The reason for this is that the larger responses of the viaduct in the radial and rotational directions are excited for tracks of smaller radii, as revealed by Figures 4.13a and 4.13c. Because of the coupling between the viaduct and train subsystems, the larger response of the maglev vehicle is accordingly induced. However, this observation is not valid for the vertical vehicle response, which is not controlled by track irregularities. It can be concluded that track irregularities are main excitations for the vehicle response in the radial (or lateral) and rotational directions, but not for the vertical response of the vehicle.

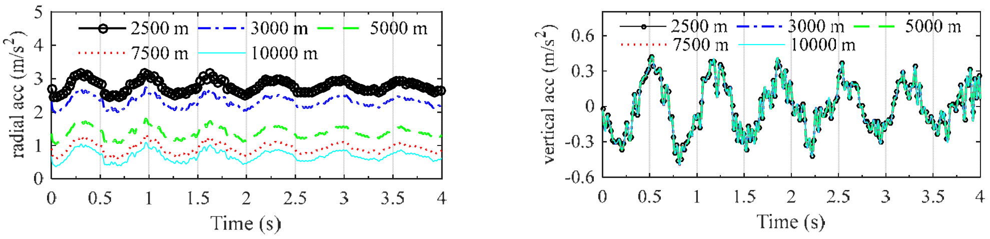

(a) in radial

(b) in vertical

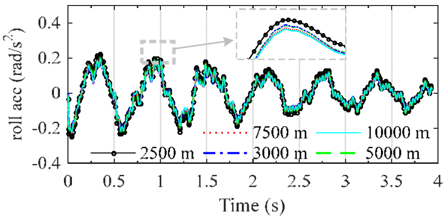

(c) in rotational

Figure 4.14 The absolute acceleration time histories of the second maglev vehicle moving over the tracks of various radii but zero cant angle.

Figure 4.14 shows the absolute accelerations of the vehicle in the three directions defined in the global coordinate system. When the circular track is designed with zero cant, the absolute acceleration of the moving origin of the trajectory coordinate system in the radial direction is approximately equal to the centrifugal acceleration (v^2/R), which is inversely proportional to the curve radius (R). As a result, the absolute acceleration of the vehicle in the radial direction also increases with the decrease of the curve radius, see Figure 4.14(a). However, since the absolute accelerations of the moving origin of the trajectory coordinate system in the vertical and rotational directions are almost zero, the absolute accelerations of the vehicle in the two directions are approximately equal to the relative accelerations of the vehicle respect to the track, (see Figures 4.14(b) and (c)).

4.6.3 Effect of cant deficiency

Cant deficiency occurs when a train runs at a speed more than the equilibrium-speed. It is measured by the difference between the theoretical cant required for such a higher speed and the actual cant provided. In terms of the degree of angle (°), the cant deficiency C_d can be calculated as

$$C_d = C_{bal} - C_{act} \approx \frac{180^\circ}{\pi} \cdot \left(\frac{v^2}{g \cdot R} - \phi_g \right) \qquad (4.16)$$

where C_{bal} is the theoretical cant angle required for the full compensation of the lateral acceleration induced by the centrifugal force; and C_{act} is the actual cant angle used.

To investigate the effect of cant deficiency on the viaduct and train responses, five cases of deficient cant angles 12°, 9°, 6°, 3° and 0° for the train moving over the curved track with a radius of 3300 m at a 300 km/h speed are investigated. The theoretical cant angle C_{bal} is 12°. The viaduct responses computed for various cant deficiencies are plotted in Figure 4.13.

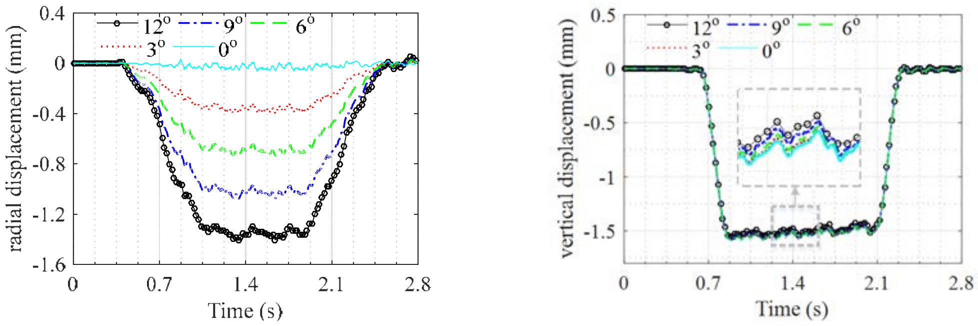

(a) in radial

(b) in vertical

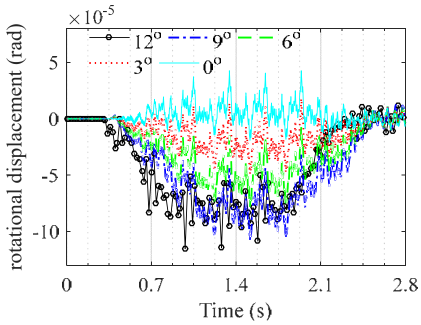

(c) in rotational

Figure 4.15 Displacement time histories at midpoint of the 3rd girder due to maglev train moving on the track of different cant deficiencies.

It is seen from Figures 4.15a and 4.15c that higher responses are excited on the girder in the radial and rotational directions for larger deficient cant angles. This is mainly due to the fact that for a fixed radius, a higher lateral acceleration is induced by a larger deficient cant angle. This in turn results in a larger guidance force on the girder in the radial direction. It is also noticeable from Figure 4.15b that slight difference exists in the vertical response of the girder. The steady vertical force acting on the girder can be calculated as $g \cdot \cos\left(\phi_{bal} - C_d\right) + \frac{v^2}{R} \cdot \sin\left(\phi_{bal} - C_d\right)$, which increases with the decrease of deficient cant angle C_d.

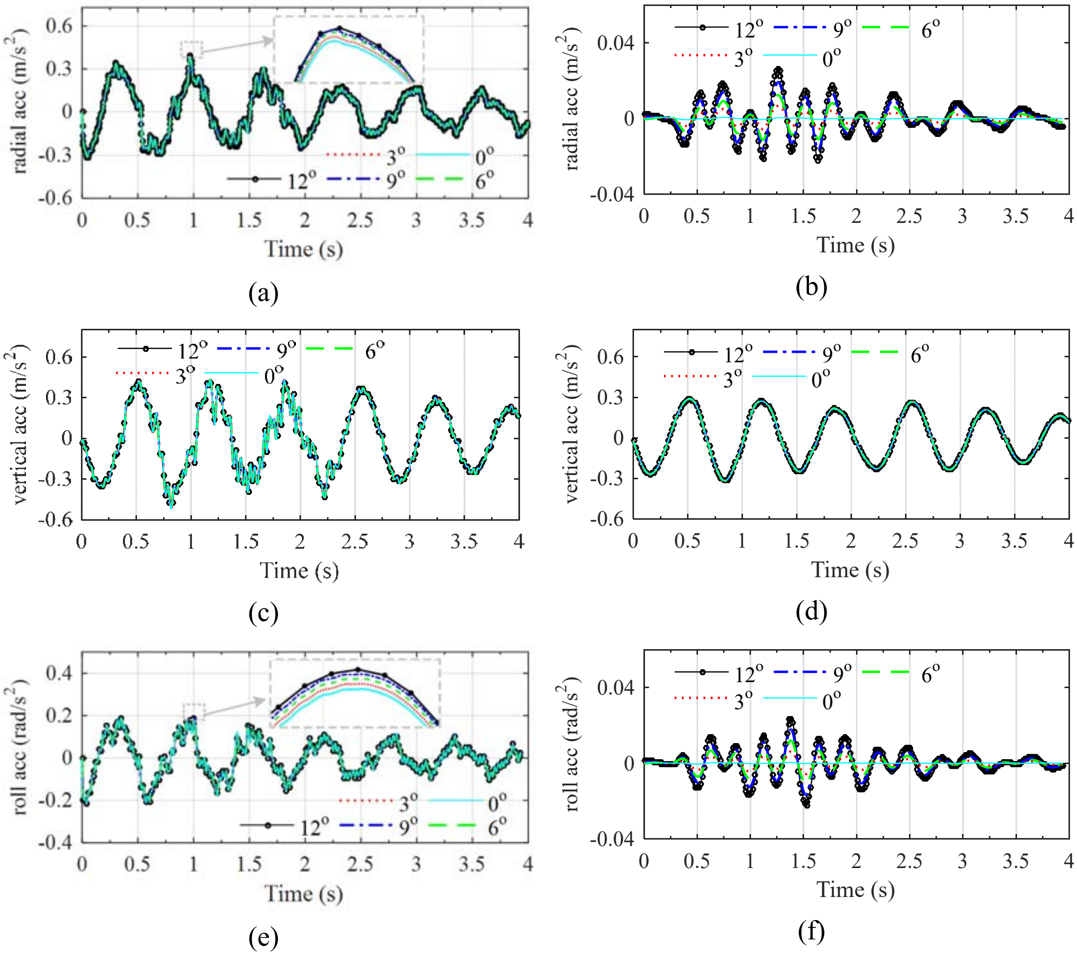

(a) (b)

(c) (d)

(e) (f)

Figure 4.16 Acceleration time histories of the 2nd maglev vehicle *defined in the trajectory coordinate system induced by the train* moving over the track with different deficient cant angles: (a, b and c) with and (d, e and f) without considering track irregularities; (a and d) in radial, (b and e) in vertical, and (c and f) in rotational.

The relative vehicle responses computed for various deficient cant angles are plotted in Figure 4.16. It can be seen from Figures 4.16a, 4.16b and 4.16c that for the case with track irregularities, the vehicle responses are generally independent of the deficient cant angle. However, for the case with no track irregularities, the differences becomes obvious: higher vehicle responses are excited in the radial and rotational directions for increasing deficient cant angles, as shown in Figures 4.16d and 4.16e.

For a fixed radius, a higher lateral acceleration (external force) is induced by a larger deficient cant angle. The vehicle response thus becomes higher in the radial and rotational directions for larger deficient cant angles. It is noticed that for zero deficient cant angle, the vehicle responses in the radial and rotational directions are zero, as shown in Figures 4.16d and 4.16f for the case with no track irregularities. However, this observation is not valid for the vertical vehicle response, which is not controlled by track irregularities. It can be concluded that track irregularities are the main excitations for the vehicle response in the radial (or lateral) and rotational directions, but not for the vertical direction.

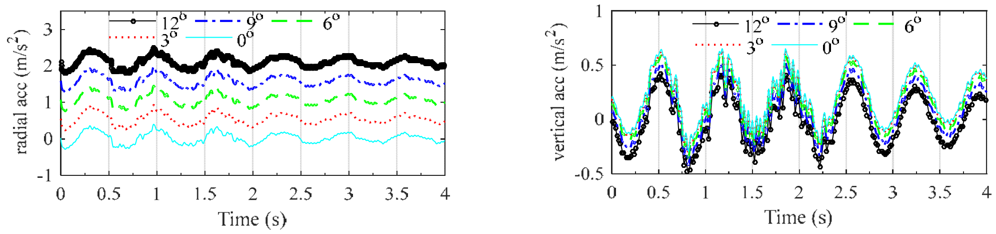

(a) in radial

(b) in vertical

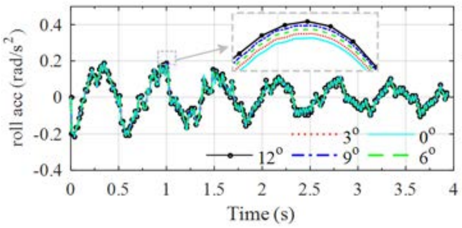

(c) in rotational

Figure 4.17 The absolute acceleration time histories of the second maglev vehicle moving over the tracks with different deficient cant angles.

Figure 4.17 shows the absolute accelerations of the vehicle in the three directions. When the circular track is designed with a deficient cant angle C_d, the absolute acceleration of the moving origin of the trajectory coordinate system in the radial direction can be approximately calculated by $\frac{v^2}{R}\cdot\cos(\phi_{bal}-C_d)-g\cdot\sin(\phi_{bal}-C_d)$, which increases with the deficient cant angle C_d. Accordingly, the absolute acceleration of the vehicle in the radial direction also increases with the deficient cant angle C_d, see Figure 4.17(a). Besides, based on Eq. (4.4), the absolute acceleration of the moving origin of the trajectory coordinate system in the vertical direction can be also calculated, that is approximately equal to $\frac{v^2}{R}\cdot\sin(\phi_{bal}-C_d)+g\cdot\cos(\phi_{bal}-C_d)-g$, which increases with the decrease of deficient cant angle C_d. As a result, the absolute acceleration of the vehicle in the vertical direction also increases with the decrease of the deficient cant angle C_d, as shown in Figure 4.17(b). Also, because the absolute acceleration of the moving origin of the trajectory coordinate system in the rotational direction is zero, the absolute acceleration of the vehicle is equal to the relative acceleration of the vehicle respect to the track, see Figure 4.17(c).

4.6.4 Effect of spiral entry

The above numerical studies were conducted based on the assumption that the initial steady-state vibration of the vehicle has reached a deformed equilibrium configuration with zero radial and vertical acceleration by travelling over a long enough spiral curve. This section investigates the effect of spiral entry on the vehicle response by a theoretical scenario with no entry spiral curve.

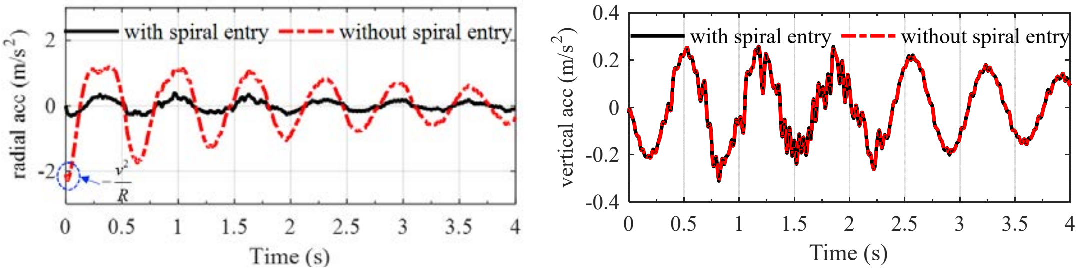

(a) radial

(b) vertical

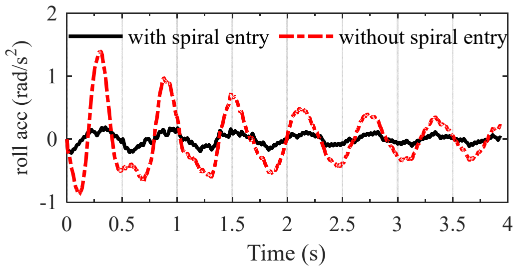

(c) rotational

Figure 4.18 Comparison of acceleration time histories of the 2nd maglev vehicle moving over the track with and without spiral entry.

As shown in Figures 4.18a and 4.18c, seriously larger responses in the radial and rotational directions are excited by the train moving on the curved track without spiral entry. It is also noted that the initial value of the radial acceleration is quite equal to the centrifugal acceleration, defined by $-v^2/R$, as marked in Figure 4.18a. It is therefore concluded that a long enough spiral entry is a must for the maglev train to move from the straight to curved track. Otherwise, issues such as ride comfort and operational safety of the vehicle will become extremely serious. It is important to note that the drawn conclusion is for the spiral entry but not for the exit entry. Further studies will be certainly conducted, based on the current study, on the entire railway including the tangent track section, the transitional curved track section, and the circular curved track section, in which the effects of both exit spiral and entry spiral of different sections will be investigated.

4.7 Summary

An interaction model of the high-speed maglev train and circular curved viaduct has been developed using the trajectory coordinate systems and then applied to the SML to capture its curved path-induced dynamic characteristics. The dynamic behaviors of the maglev train are experimentally and numerically investigated with good agreement. The dynamic responses of the curved viaduct are also examined in the vertical, lateral and rotational directions by comparison with the straight viaduct. Based on the parameteric study, considering particularly the effects of various curve radii and cant deficiencies, the major conclusions drawn from this study are summarized as follows:

(1) The responses of the maglev train moving over curved viaducts of balanced radii and cant angles are almost identical to those of straight viaducts.

(2) For zero cant angle, the responses of the curved viaduct in the radial and rotational directions increase with decreasing track radius.

(3) Cant deficiency is rather significant for the curved viaduct where the increase of deficient cant angle causes a sharp increase in the responses of the radial and rotational directions. The radial displacement induced by a large cant deficiency is comparable with that of the vertical direction.

(4) For the maglev train moving with an initial equilibrium state, track irregularities are the main excitations for the vehicle responses in the radial (or lateral) and rotational directions, but not for the vertical.

(5) For the case with no track irregularity, higher vehicle responses are induced in the radial and rotational directions for decreasing track radius. This increase also appears with the deficient cant angles.

(6) A long enough spiral entry is a must for the maglev train to move from the straight to the curved track. Otherwise, issues such as ride comfort and operational safety of the vehicle will become extremely serious.

CHAPTER 5

DYNAMIC ANALYSIS AND VALIDATION OF HIGH-SPEED MAGLEV TRAIN RUNNING ON TRANSITIONAL VIADUCT

5.1 Introduction

Chapter 4 has presented a trajectory coordinates-based framework for the analysis of high-speed maglev train running on the circular curved track. Based on this, a particular case to investigate the effect of spiral entry on the vehicle response is conducted in Section 4.6.4. The results show that when a vehicle enters the circular curved track directly from a straight path, serious impact on the train in the lateral direction will be induced by the sudden centrifugal forces acting on the vehicle. As a result, to ensure the ride quality, a long enough spiral entry (transitional curved track section) is a must for the maglev train to move from the straight to the curved track. However, required by the geometric smoothness of the whole track, the curve radius (CR) and high difference (HD) between the outer and inner rails along the transitional curved track are both distance-varying, resulting in a more complicated dynamic interaction than one when trains run on either the straight track or the circular curved track.

To this end, this chapter further develops the proposed trajectory coordinates-based analysis approach, in which the origins of the trajectory coordinate systems move along the inner rail of the track, and the Euler angles used to describe the coordinates' orientations are functions of distance-varying CR and HD. By applying this framework to the SML, the dynamic characteristics and responses of the maglev vehicles running on the transitional viaduct are numerically explored, which match the measured data quite well. Besides, the effects of transitional track length and cant deficiency on the coupled system have also been explored.

(a) The schematic layout of the SML (b) Curved viaduct in SML

Figure 5.1 The schematic layout of the SML and the curved viaduct system

5.2 Geometric Characteristics of a Transitional Track

Several transitional curves with different shapes have been proposed in the previous studies (Crandall, 1893; Higgins, 1922; Pirti et al., 2016; Woźnica, 2014) and summarized in Table 5.1. The third-order parabola curve is widely used in wheel train line alignments in some countries for its simplicity in design and construction, while the half-wave sinusoid curve is adopted in Japan. It can be seen from Table 5.1 that two important parameters CR and HD vary with the distance "*s*", the HD function keeps the same form with the curvature function (1/CR), and different curves have different smoothness.

Table 5.1 Typical transition curves

Form	Curvature function (1/CR)	HD function
Third-order parabola	$k=\frac{1}{R}\left(\frac{s}{L_0}\right)$	$h=h_0\left(\frac{s}{L_0}\right)$
Fifth-order parabola	$k=\frac{1}{R}\left[3\left(\frac{s}{L_0}\right)^2-2\left(\frac{s}{L_0}\right)^3\right]$	$h=h_0\left[3\left(\frac{s}{L_0}\right)^2-2\left(\frac{s}{L_0}\right)^3\right]$
Seven-order parabola	$k=\frac{1}{R}\left[6\left(\frac{s}{L_0}\right)^5-15\left(\frac{s}{L_0}\right)^4+10\left(\frac{s}{L_0}\right)^3\right]$	$h=h_0\left[6\left(\frac{s}{L_0}\right)^5-15\left(\frac{s}{L_0}\right)^4+10\left(\frac{s}{L_0}\right)^3\right]$
Half-wave sinusoid	$k=\frac{1}{2R}\left[1-\cos\left(\frac{s}{L_0}\pi\right)\right]$	$h=\frac{1}{2}h_0\left[1-\cos\left(\frac{s}{L_0}\pi\right)\right]$
Sinusoid	$k=\frac{1}{R}\left[\frac{s}{L_0}-\frac{1}{2\pi}\sin\left(\frac{s}{L_0}2\pi\right)\right]$	$h=h_0\left[\frac{s}{L_0}-\frac{1}{2\pi}\sin\left(\frac{s}{L_0}2\pi\right)\right]$

In Table 5.1, R is the radius of the circular curve; h_0 is the HD of the circular curve; s is the arc length between the calculated point and the starting point; and L_0 is the arc length of the entire transitional curve.

Because of the higher-order smoothness at the connection points, the sinusoid curve is preferred in the design of maglev train line such as the SML (Wu, 2003). Therefore, the sinusoid curve will be used in this study as an example for dynamic analysis of the coupled maglev train and transitional viaduct system. Before such a dynamic analysis, the transitional curve shall be converted to the transitional track to provide the coordinates of both inner rail and outer rail. The following explanations and assumptions are adopted for the purpose of conversion.

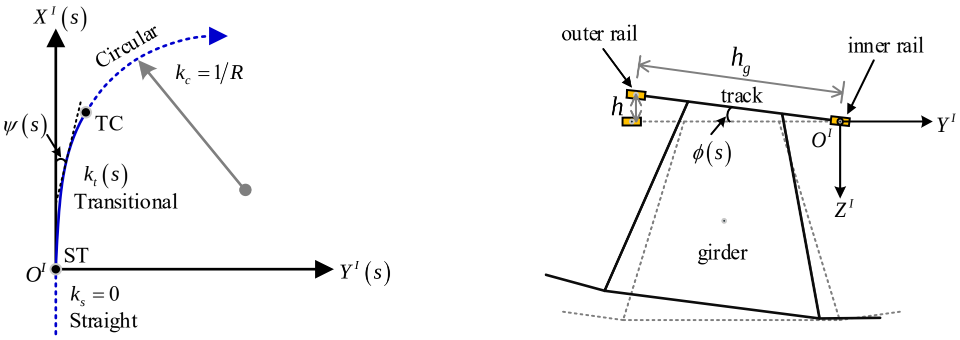

(a) Curvatures of the track

(b) Coordinates of the track

Figure 5.2 Alignment of the transitional track

1) The origin O^I of the global coordinate system $X^I Y^I Z^I$ is fixed on the earth at the centroid of the cross section of the inner rail at the connection point ST, as shown in Figure 5.2.

2) The train continuously travels from the straight track ($s \leq 0$) to the transitional track ($0 < s \leq L_0$), and then to the circular track ($s > L_0$), as shown in Figure 5.2. The curvature and HD of the straight track are zero, while those of the circular track are constant but nonzero.

3) The height of the centroid of inner rail in the vertical direction remains unchanged along the entire track (the straight + transitional+ circular track). The height of the centroid of outer rail is then decided by the HD function with reference to the inner rail.

As a result, the coordinates $\left(x_{inner}, y_{inner}, z_{inner}\right)$ of the centroid of the inner rail can be given by Eq. (5.1a).

$$x_{inner}(s)=\begin{cases} s & , s\le 0 \\ \int_0^s \cos\left[\psi(s)\right]\mathrm{d}s & , 0<s\le L_0 \\ x_{inner}(L_0)+\int_{L_0}^s \cos\left[\psi(s)\right]\mathrm{d}s & , s>L_0 \end{cases}$$

$$y_{inner}(s)=\begin{cases} 0 & , s\le 0 \\ \int_0^s \sin\left[\psi(s)\right]\mathrm{d}s & , 0<s\le L_0 \\ y_{inner}(L_0)+\int_{L_0}^s \sin\left[\psi(s)\right]\mathrm{d}s & , s>L_0 \end{cases} \tag{5.1a}$$

$$z_{inner}(s)=0$$

The coordinates $(x_{outer}, y_{outer}, z_{outer})$ of the centroid of the outer rail are accordingly calculated by Eq. (5.1b).

$$\begin{aligned} x_{outer}(s) &= x_{inner}(s)+h_g\sin\left[\psi(s)\right]\cos\left[\phi(s)\right] \\ y_{outer}(s) &= y_{inner}(s)-h_g\cos\left[\psi(s)\right]\cos\left[\phi(s)\right] \\ z_{outer}(s) &= -h_g\sin\left[\phi(s)\right] \end{aligned} \tag{5.1b}$$

where h_g is the horizontal distance between the two rails (the width of the track), which is constant at any section of the entire track; $\psi(s)$ and $\phi(s)$ are the yawing and rolling angles of the track defined in the global coordinate system (see Figure 5.1), given by Eq. (5.1c) and Eq. (5.1d), respectively.

$$\psi(s)=\begin{cases} 0 & , s\le 0 \\ \int_0^s k(s)\mathrm{d}s & , 0<s\le L_0 \\ \psi(L_0)+\dfrac{s-L_0}{R} & , s>L_0 \end{cases} \tag{5.1c}$$

$$\phi(s)=\begin{cases} 0 & , s\le 0 \\ h/h_g & , 0<s\le L_0 \\ h_0/h_g & , s>L_0 \end{cases} \tag{5.1d}$$

Eq. (5.1) can be used for any transitional curve listed in Table 5.1. Substituting *k*(s) and *h*(s) of the sinusoid curve listed in Table 5.1 into Eq. (5.1) will give the coordinates of the inner and outer rails of the track. These coordinates are the reference coordinates only and after the trains run on the track, the actual deformation or displacement of the rails will be calculated with respect to the reference coordinates.

5.3 Dynamic Modeling of Maglev Train Subsystem

In this study, the global coordinate system used in the track alignment in Section 5.2 remains unchanged. The train is assumed to move along the track at a constant speed v. When a vehicle of the train moves on the straight track (see Figure 5.2a), the motion of the vehicle can be defined in the global coordinate system directly because the moving direction of the vehicle remains unchanged in the X^I axis. However, when a vehicle moves on the curved track (see Figure 5.2a), the moving direction of the vehicle in the global coordinate system is changing. As a result, the direction of the centrifugal force on the vehicle is also changing. On the other hand, the interaction forces between the vehicle and track depend on their relative displacements. Therefore, it will be convenient to introduce a trajectory coordinate system that moves along the track to define the relative motion of the vehicle. In this way, the distance s of the vehicle along the track can be simply calculated by vt. The introduction of the trajectory coordinate system is particularly useful for the transitional curved track that is geometrically characterized by the distance-varying CR and HD. Since a train has a number of vehicles and a vehicle has several components, a series of trajectory coordinate systems will be introduced in this study for dynamic modelling of a train moving on both straight and curved tracks.

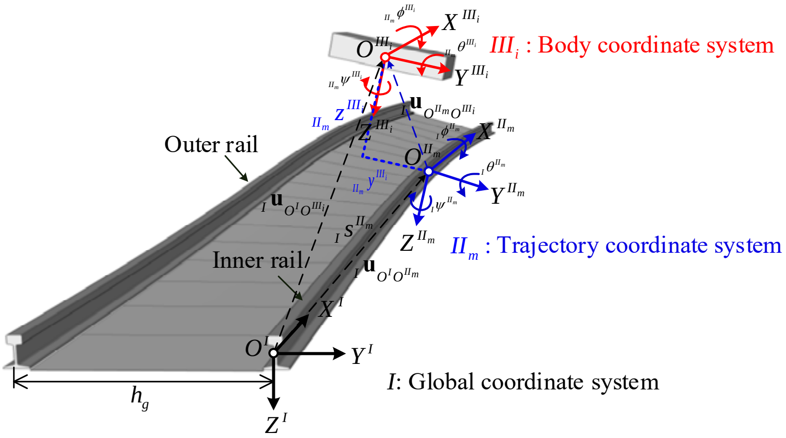

Figure 5.3 Three sets of coordinate systems used.

5.3.1 Three coordinate systems

Figure 5.3 shows three sets of coordinate systems employed to formulate the equations of motion of the *i*th vehicle body moving on a transitional curved track: the global coordinate system $X^I Y^I Z^I$; the trajectory coordinate system $X^{II_m} Y^{II_m} Z^{II_m}$; and the body (vehicle body-fixed) coordinate system $X^{III_i} Y^{III_i} Z^{III_i}$. The global coordinate system is fixed on the earth at the centroid of the cross section of the inner rail at the connection point ST to trace the absolute position of the vehicle body (see Figures 5.2 and 5.3). The global coordinate system is the same as that used in the track alignment discussed in Section 5.2. The trajectory coordinate system is a moving coordinate system with its origin moving on the inner rail of the un-deformed curved track. The origin of the trajectory coordinate system is defined in the global coordinate system by the moving distance of arc length ${}_I s^{II_m}$ only, and its coordinates can then be calculated by Eq. (5.1a). The orientation of the trajectory coordinate system with respect to the global coordinate system is defined by three Euler angles ${}_I\psi^{II_m}$, ${}_I\theta^{II_m}$, and ${}_I\phi^{II_m}$ about the three axes Z^{II_m}, Y^{II_m}, and X^{II_m}, respectively, in which the Z^{II_m}-axis is perpendicular to the track plane, the X^{II_m}-axis is tangent to the inner rail, and the Y^{II_m}-axis is perpendicular to the inner rail. In such a way, ${}_I\psi^{II_m}$ and ${}_I\phi^{II_m}$ are the functions of arc length ${}_I s^{II_m}$ and can be calculated using Eq. (5.1c) and Eq. (5.1d) respectively, while ${}_I\theta^{II_m}$ is zero. It shall be highlighted that the orientation of the trajectory coordinate system changes along the transitional track because the CR and HD of the track varies along the transitional track. The origin of the trajectory coordinate system always follows the origin of the body coordinate system with zero distance in the longitudinal direction (tangent to the inner rail of the track). The motion or degrees of freedom (DOFs) of the vehicle body with respect to the trajectory coordinate system can be described by only two translational motions ${}_{II_m} y^{III_i}$ and ${}_{II_m} z^{III_i}$, and three rotational motions ${}_{II_m}\phi^{III_i}$, ${}_{II_m}\theta^{III_i}$, and ${}_{II_m}\psi^{III_i}$.

5.3.2 Trajectory coordinate systems and DOFs of the maglev train subsystem

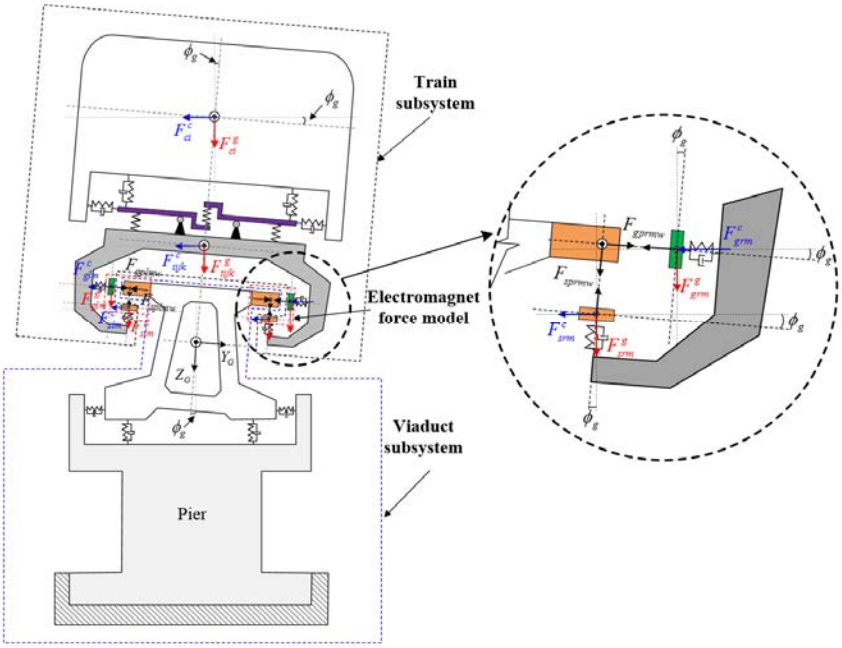

(a) Cross section of the model of the coupled maglev train and viaduct system

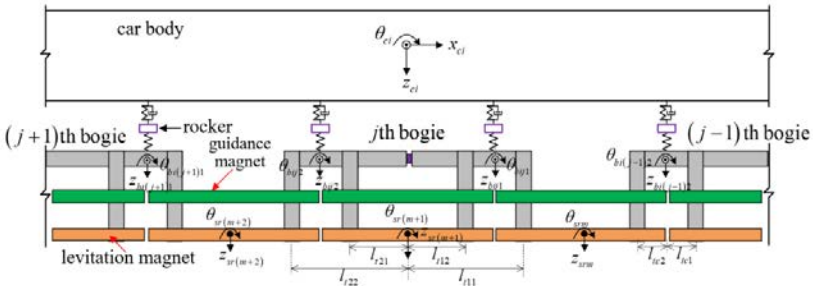

(b) Vertical plan of the train subsystem model

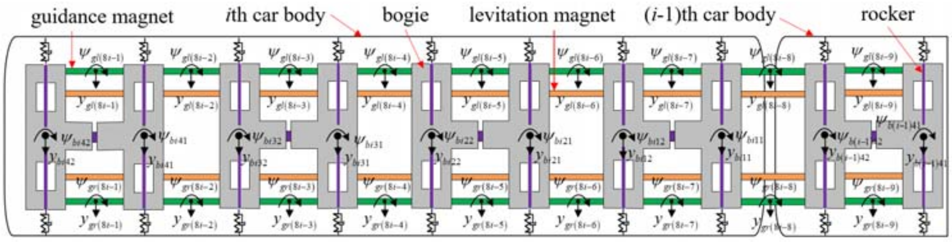

(c) Top plan of the train subsystem model

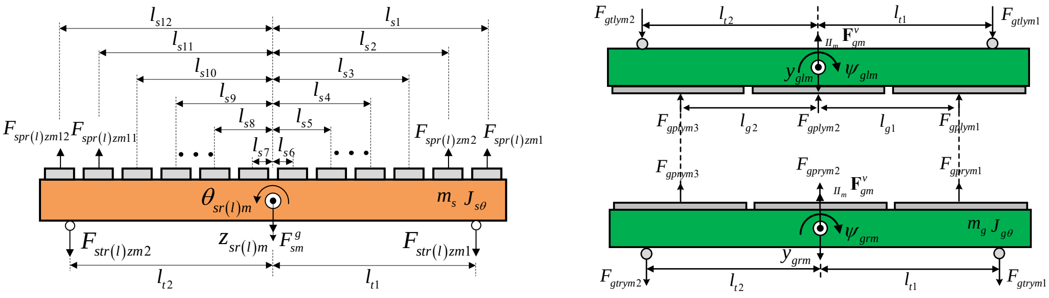

(d) Force diagram of the levitation magnet (e) Force diagram of the guidance magnet

Figure 5.4 Schematic diagram of the maglev train subsystem.

The SML is taken as an example to illustrate the dynamic modelling of a high-speed maglev train running over a transitional viaduct. In the SML, a train consists of several vehicles and each vehicle contains one car body, four bogies, eight sets of rockers, fourteen complete sets of electromagnets and four half sets of electromagnets. The rigid body assumption is used to model the major components of the train subsystem, and the elastic deformation of these components is therefore ignored. The displacements and rotations of the rigid body with respect to the track are assumed to be small. Linear spring elements and linear spring-damper elements are used to model the connections between the rigid bodies of the train subsystem. Figure 5.4a shows the schematic diagram of the coupled maglev train-viaduct system, whereas Figures 5.4b-5.4e show the schematic diagrams of the maglev train subsystem and its vehicle components.

When a maglev vehicle moves on a transitional track, the origins of body-fixed coordinate systems used to define the vehicle components are longitudinally distributed over the section of the track with various CR and HD. As a result, the trajectory coordinate system employed to trace each vehicle component is unique. Suppose that there are N vehicles in a train, the number of sets of levitation and guidance magnets is M=8N-1. Each set of magnets is assigned a trajectory coordinate system, as shown in Figure 5.5. Moreover, because the mass center of the $(ij)^{\text{th}}$ bogie (including rockers) is at the same position as that of the m^{th} set of electromagnets in the longitudinal direction, where m=4(i-1)+2j-1, the m^{th} trajectory coordinate system is also assigned to the $(ij)^{\text{th}}$ bogie. Likewise, the m^{th} trajectory coordinate system is also employed to trace the i^{th} vehicle body, where m=8(i-1)+4.

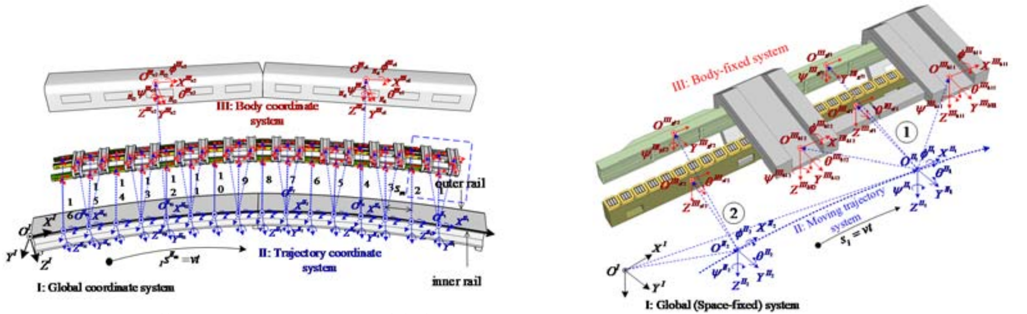

(a) Coordinate systems for vehicles (b) Coordinate systems for components

Figure 5.5 Coordinate systems used for dynamic modelling of the train running on a transitional track.

With each vehicle component assigned a unique trajectory coordinate system, their motions or DOFs can be thus defined. Specifically, the motion of the i^{th} car body is defined by five DOFs: the lateral, vertical, rolling, pitching, and yawing displacement, designated by Eq. (5.2a). Each bogie is composed of two C-shaped frames connected by a longitudinal shaft, and thus the two frames can rotate against each other with no relative translational displacements. Therefore, the j^{th} bogie under the i^{th} car body has six DOFs: the lateral, vertical and rolling displacement of the front C-shaped frame, the rolling of the rear C-shaped frame, the pitching and yawing displacement of the bogie, denoted by Eq. (5.2b). Two rockers are pinned on the left and right sides of each C-shaped frame (see Figure 5.4a). Each rocker is assigned by one DOF to indicate its rolling motion only, as expressed by Eq. (5.2c), and the other DOFs of the rockers comply with the DOFs of the bogie. Each levitation magnet (with left and right units) is assigned with two DOFs for the vertical and pitching displacement, as given in Eq. (5.2d). Similarly, each guidance magnet is also modeled by two DOFs for the lateral and yawing displacement, denoted by Eq. (5.2e). As a result, the total number of DOFs for the train subsystem is 109N-1.

$$ {}_{II_m}\mathbf{U}_{ci} = \left[{}_{II_m}y^{III_{ci}} \quad {}_{II_m}z^{III_{ci}} \quad {}_{II_m}\phi^{III_{ci}} \quad {}_{II_m}\theta^{III_{ci}} \quad {}_{II_m}\psi^{III_{ci}} \right] \tag{5.2a} $$

$$ {}_{II_m}\mathbf{U}_{bij} = \left[{}_{II_m}y^{III_{bij}} \quad {}_{II_m}z^{III_{bij}} \quad {}_{II_m}\phi^{III_{bij1}} \quad {}_{II_m}\phi^{III_{bij2}} \quad {}_{II_m}\theta^{III_{bij}} \quad {}_{II_m}\psi^{III_{bij}} \right] \tag{5.2b} $$

$$ {}_{II_m}\mathbf{U}_{tijk} = \left[{}_{II_m}\phi^{III_{trijk}} \quad {}_{II_m}\phi^{III_{tlijk}} \right] \tag{5.2c} $$

$$ {}_{II_m}\mathbf{U}_{sm} = \left[{}_{II_m} z^{III_{srm}} \quad {}_{II_m}\theta^{III_{srm}} \quad {}_{II_m} z^{III_{slm}} \quad {}_{II_m}\theta^{III_{slm}} \right] \tag{5.2d} $$

$$ {}_{II_m}\mathbf{U}_{gm} = \left[{}_{II_m} y^{III_{grm}} \quad {}_{II_m}\psi^{III_{grm}} \quad {}_{II_m} y^{III_{glm}} \quad {}_{II_m}\psi^{III_{glm}} \right] \tag{5.2e} $$

where the subscripts c, b, t, s, and g denote the car body, bogie, rocker, levitation (suspension) magnet and guidance magnet, respectively; the subscripts r or l refer to right or left side; j is the number of bogies of the i^{th} car body (j =1,2,3,4); k =1,2 represents the front and rear C-shaped frame or the front and rear rocker on the j^{th} bogie; and m is the set number of the magnets and also the corresponding number of trajectory coordinate system.

5.3.3 Equations of motion of train subsystem

The dynamic motion of each vehicle component should be described in the global coordinate system via the employment of the unique moving trajectory coordinate system. However, for transitional curved track, its HD and CR vary along the curved track. The issues of bridge-train dynamics such as ride comfort assessment, interaction force modelling and derailment are generally track path-related rather than space-fixed. Thus, the dynamic equations of motion of the vehicle components should be transformed from the global coordinates into the generalized moving trajectory coordinates. The equations of motion of the train subsystem are then established by combining the equations of motion of all the vehicle components defined in their own trajectory coordinate systems.

The m^{th} generalized moving trajectory coordinates of the i^{th} vehicle body are defined as (Shabana et al., 2008; Dimitrakopoulos & Zeng, 2015):

$$ {}_{II_m}\mathbf{U}_i = \left[{}_{I}s^{II_m} \quad {}_{II_m} y^{III_i} \quad {}_{II_m} z^{III_i} \quad {}_{II_m}\phi^{III_i} \quad {}_{II_m}\theta^{III_i} \quad {}_{II_m}\psi^{III_i} \right]^T \tag{5.3} $$

The Newton-Euler equation of motion describing the motion of the i^{th} vehicle body in terms of the m^{th} generalized trajectory coordinates can be derived as

$$ {}_{II_m}\mathbf{M}_i \cdot {}_{II_m}\ddot{\mathbf{U}}_i = {}_{II_m}\mathbf{F}_i^e + {}_{II_m}\mathbf{F}_i^v \tag{5.4} $$

where ${}_{II_m}\ddot{\mathbf{U}}_i$ is the translational and rotational acceleration vector of the i^{th} vehicle body expressed in terms of the m^{th} generalized trajectory coordinates; ${}_{II_m}\mathbf{M}_i$ is the mass matrix; ${}_{II_m}\mathbf{F}_i^e$ is the vector of external forces and toques; and ${}_{II_m}\mathbf{F}_i^v$ is the inertial force vector due to the curved path. The last three terms are associated with the trajectory coordinate system and given by

$$ \left\{ \begin{aligned} {}_{II_m}\mathbf{M}_i &= m_i \left({}_I\mathbf{L}^{II_m} \right)^T \left({}_I\mathbf{L}^{II_m} \right) + \left({}_{III_i}\mathbf{H}^{II_m} \right)^T \left({}_{III_i}\mathbf{I}_{\theta i} \right) \left({}_{III_i}\mathbf{H}^{II_m} \right) \\ {}_{II_m}\mathbf{F}_i^e &= \left({}_I\mathbf{L}^{II_m} \right)^T {}_I\mathbf{F}_i^e + \left({}_{III_i}\mathbf{H}^{II_m} \right)^T {}_{III_i}\boldsymbol{\tau}_i^e + \left({}_I\mathbf{L}^{II_m} \right)^T {}_I\mathbf{W}_i^g \\ {}_{II_m}\mathbf{F}_i^v &= -m_i \left({}_I\mathbf{L}^{II_m} \right)^T {}_I\boldsymbol{\gamma}_R^{II_m \to I} - \left({}_{III_i}\mathbf{H}^{II_m} \right)^T \left({}_{III_i}\mathbf{I}_{\theta i} \right) {}_{III_i}\boldsymbol{\gamma}_{\boldsymbol{\theta}}^{I \to III_i} \\ &\quad + \left({}_{III_i}\mathbf{H}^{II_m} \right)^T {}_{III_i}\boldsymbol{\omega}_i \times \left({}_{III_i}\mathbf{I}_{\theta i}\, {}_{III_i}\boldsymbol{\omega}_i \right) \end{aligned} \right. \tag{5.5} $$

where ${}_I\mathbf{L}^{II_m}$ and ${}_{III_i}\mathbf{H}^{II_m}$ denote the velocity transformation matrices, corresponding to the translational and rotational motions; ${}_I\boldsymbol{\gamma}_R^{II_m \to I}$ and ${}_{III_i}\boldsymbol{\gamma}_{\boldsymbol{\theta}}^{I \to III_i}$ are the vectors containing the additional quadratic velocity terms produced by the time-differentiation of the absolute linear velocity and the absolute angular velocity vectors, respectively (Shabana et al., 2008; Dimitrakopoulos & Zeng, 2015); ${}_I\mathbf{W}_i^g$ is the gravity force vector, expressed by $\left[0 \quad 0 \quad m_i g \right]^{\mathrm{T}}$; the inertial force vector ${}_{II_m}\mathbf{F}_i^v$ is composed of the centrifugal forces (the first two terms) and the Coriolis forces (the third term). Particularly, the vector $-\left({}_I\mathbf{L}^{II_m} \right)^T {}_I\boldsymbol{\gamma}_R^{II_m \to I}$ is the centrifugal acceleration related with the three translational DOFs, expressed by Eq. (5.6).

$$
\begin{aligned}
\left({}_{I}\mathbf{L}^{II_m}\right)^T {}_{I}\boldsymbol{\gamma}_R^{II_m\rightarrow I} &= k(s)\cdot v^2 \cdot \begin{bmatrix} 0 \\ \mathrm{c}\left({}_{I}\phi^{II_m}\right) + k(s)\cdot\left\{-{}_{II_m}y^{III_i}\cdot \mathrm{c}\left({}_{I}\phi^{II_m}\right)\cdot \mathrm{c}\left({}_{I}\phi^{II_m}\right) + {}_{II_m}z^{III_i}\cdot \mathrm{c}\left({}_{I}\phi^{II_m}\right)\cdot \mathrm{s}\left({}_{I}\phi^{II_m}\right)\right\} \\ -\mathrm{s}\left({}_{I}\phi^{II_m}\right) - k(s)\cdot\left\{-{}_{II_m}y^{III_i}\cdot \mathrm{c}\left({}_{I}\phi^{II_m}\right)\cdot \mathrm{s}\left({}_{I}\phi^{II_m}\right) + {}_{II_m}z^{III_i}\cdot \mathrm{s}\left({}_{I}\phi^{II_m}\right)\cdot \mathrm{s}\left({}_{I}\phi^{II_m}\right)\right\} \\ \mathbf{0}_{3\times 1} \end{bmatrix} \\
&\approx k(s)\cdot v^2 \begin{bmatrix} 0 \\ \cos\left({}_{I}\phi^{II_m}\right) \\ -\sin\left({}_{I}\phi^{II_m}\right) \\ \mathbf{0}_{3\times 1} \end{bmatrix}
\end{aligned}
\tag{5.6}
$$

where $\mathrm{c}\left({}_{I}\phi^{II_m}\right)$ and $\mathrm{s}\left({}_{I}\phi^{II_m}\right)$ are the abbreviations of $\cos\left({}_{I}\phi^{II_m}\right)$ and $\sin\left({}_{I}\phi^{II_m}\right)$, respectively; $k(s)$ is the curvature of the transitional track, as shown in Table 5.1; and ${}_{I}\phi^{II_m}$ is calculated by using Eq. (5.1d).

It should be highlighted that the centrifugal acceleration $-\left({}_{I}\mathbf{L}^{II_m}\right)^T {}_{I}\boldsymbol{\gamma}_R^{II_m\rightarrow I}$ is characterized by the distance-varying CR and HD along the transitional track, while it becomes non-zero constant for the circular track and zero for the straight track. The other vectors, such as ${}_{I}\mathbf{L}^{II_m}$, ${}_{III_i}\mathbf{H}^{II_m}$, ${}_{I}\boldsymbol{\gamma}_R^{II_m\rightarrow I}$, ${}_{III_i}\boldsymbol{\gamma}_{\boldsymbol{\theta}}^{I\rightarrow III_i}$ and ${}_{III_i}\boldsymbol{\omega}_i$ also vary with distance. Detailed expressions of these transformation matrices or vectors can be found in Appendix D.

By combining the equations of motion of all the vehicle components, the equations of motion of the entire train subsystem expressed in terms of the moving trajectory coordinate systems can be written as

$$
{}_{II}\mathbf{M}_V\,{}_{II}\ddot{\mathbf{U}}_V + {}_{II}\mathbf{C}_V\,{}_{II}\dot{\mathbf{U}}_V + {}_{II}\mathbf{K}_V\,{}_{II}\mathbf{U}_V = {}_{II}\mathbf{F}_V^{G\rightarrow V} + {}_{II}\mathbf{F}_V^{e} + {}_{II}\mathbf{F}_V^{v} \tag{5.7}
$$

where ${}_{II}\mathbf{M}_V$ is the mass matrix of the train subsystem; ${}_{II}\mathbf{K}_V$ and ${}_{II}\mathbf{C}_V$ are the stiffness and damping matrices, respectively; ${}_{II}\mathbf{U}_V$, ${}_{II}\dot{\mathbf{U}}_V$, and ${}_{II}\ddot{\mathbf{U}}_V$ are the displacement, velocity, and acceleration vectors, respectively; ${}_{II}\mathbf{F}_V^{G\rightarrow V}$ is the interaction force vector between the vehicles and rails, which will be further discussed in Section 5.5; ${}_{II}\mathbf{F}_V^{e}$ is the external force vector, including the gravity forces, seismic loads or wind loads; and ${}_{II}\mathbf{F}_V^v$ is the inertial force vector, including the centrifugal force and Coriolis force. The force vectors ${}_{II}\mathbf{F}_V^e$ and ${}_{II}\mathbf{F}_V^v$ can be calculated according to Eq. (5.5).

5.4 Modeling of Transitional Viaduct Subsystem

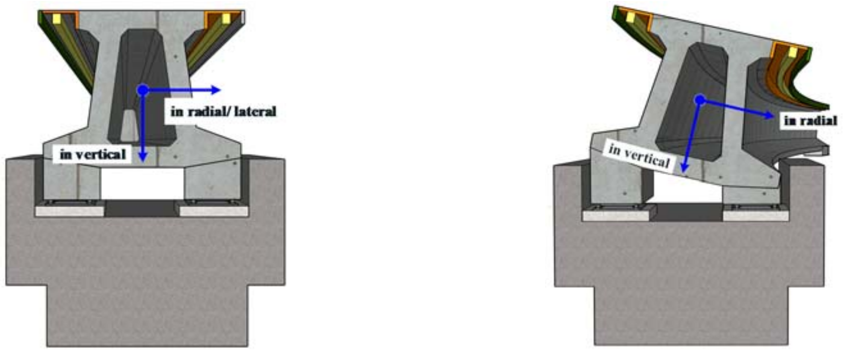

(a) Straight section (b) Curved section

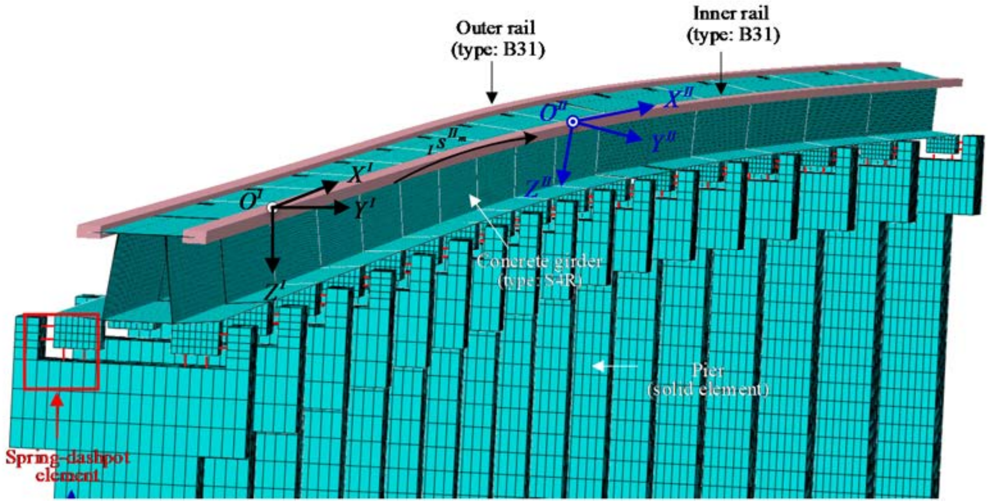

(c) Finite element model

Figure 5.6 Transitional curved viaduct

To completely address the dynamic interactions between the train and transitional curved viaduct, the straight viaduct and the circular curved viaduct connected by the transitional curved viaduct are also modelled to form the entire viaduct subsystem. The dynamic modelling of the straight viaduct and the circular curved viaduct can be found in the Chapters 3 and 4. Different from the straight viaduct and the circular curved viaduct, there are no identical spans in the transitional curved viaduct because of distance-varying CR and HD. Each section of the transitional curved track should be modelled according to the track alignment discussed in Section 5.2. The following section presents the modelling of the transitional curved track only.

5.4.1 Finite element model of transitional curved viaduct

The finite element (FE) model of the transitional curved viaduct is established in ABAQUS software (see Figure 5.6c). The FE models of inner rail and outer rail are first established based on the coordinates calculated by Eq. (5.1a) and Eq. (5.1b), respectively. The model of the girder of unit length is established based on the cross section dimensions of the girder (see Figure 5.6a), and this sectional model is then extended along the inner rail, rotated by the yawing and rolling angles determined by Eq. (5.1c) and Eq. (5.1d) (see Figure 5.6b). Finally, the FE models of the substructures, including the bearings and piers, are established according the design drawings. The element types used to model the components of the transitional curved viaduct include the rails modeled by 3D 2-node linear beam elements, the girders by 4-node shell elements, and each pier by 8-node solid elements. Six DOFs for each node of the above elements are considered, which include three translational DOFs and three rotational DOFs. The influence of pile foundation and soil on the piers is ignored, and the bottom of the piers is assumed to be fixed (Su et al., 2010; Malveiro et al., 2014). The tie constraints are used to simulate the connections between the rails and girder. Besides, 4 linear spring-damper elements parameterized by the equivalent stiffness of the bearing are employed to represent the bearing connecting the girder to the single-column piers in both vertical and lateral directions. The stiffness of each spring-damper element in the vertical and lateral direction is assigned with 4×10^{10} N/m and 1.25×10^{10} N/m, respectively (Malveiro et al., 2014). The damping coefficient of each spring-damper element in the vertical and lateral direction is assigned with 1.2×10^{5} N·sec/m and 6×10^{4} N·sec/m, respectively (Malveiro et al., 2014).

5.4.2 Equations of motion of viaduct subsystem

By assembling all the components of the transitional curved viaduct, the straight viaduct, and the circular curved viaduct, the global mass matrix ${}_{I}\mathbf{M}_{G}$ and stiffness matrix ${}_{I}\mathbf{K}_{G}$ for the entire viaduct subsystem are obtained in the global coordinate system. The equations of motion for the entire viaduct subsystem can be expressed by:

$$ {}_I\mathbf{M}_G\, {}_I\ddot{\mathbf{U}}_G + {}_I\mathbf{C}_G\, {}_I\dot{\mathbf{U}}_G + {}_I\mathbf{K}_G\, {}_I\mathbf{U}_G = {}_I\mathbf{F}_G^{V\to G} + {}_I\mathbf{F}_G^{e} \tag{5.8} $$

where ${}_I\mathbf{U}_G$, ${}_I\dot{\mathbf{U}}_G$ and ${}_I\ddot{\mathbf{U}}_G$ are the displacement, velocity and acceleration vectors of the viaduct subsystem; ${}_I\mathbf{F}_G^{e}$ is the external force vector, including the gravity force, seismic loads, and wind loads; and ${}_I\mathbf{F}_G^{V\to G}$ is the vector of the electromagnet forces acting on the viaduct subsystem, which will be discussed in detail in Section 5.5.

The damping matrix of the viaduct subsystem is formed based on the Rayleigh damping assumption that the damping matrix is proportional to a linear combination of the mass matrix and stiffness matrix. From the experimental and numerical results, the first natural frequency of the viaduct subsystem is near 6 Hz and the upper limit of the frequency concerned is about 500 Hz. Therefore, in the formulation of the damping matrix of the viaduct subsystem, these two frequencies are selected, and the associated two damping ratios are set as 0.02 for concrete structures. As a result, the damping parameters are α=0.2368 and β=0.000088, and the damping matrix of the entire viaduct subsystem is formed. The discrete stiffness and damping coefficients of the spring-damper element are finally inserted into the stiffness and damping matrices of the viaduct subsystem to form the global stiffness matrix ${}_I\mathbf{K}_G$ and damping matrix ${}_I\mathbf{C}_G$, respectively (Dimitrakopoulos & Zeng, 2015; Ju et al., 2014; Kwon et al., 2008; Zeng & Dimitrakopoulos, 2016a).

5.5 Modeling of Interaction between Train and Viaduct Subsystems

This study adopts the interactive electromagnet force-air gap model to simulate the electromagnetic forces including both levitation and guidance forces. Since the electromagnetic forces depend on the relative displacements between the magnets and rails, they are also conveniently defined in the trajectory coordinate system.

5.5.1 Interactive electromagnet force-air gap model

The electromagnetic force-air gap model is established based on the current circuit and the gap between the electromagnet and track rail (Sinha, 1987).

$$ {}_{II_m}\mathbf{F}\left(i_w^t, h_w^t\right) = K_0\left(\frac{\mathbf{i}_w^t}{{}_{II_m}\mathbf{h}_w^t}\right)^2 \tag{5.9a}$$

where ${}_{II_m}\mathbf{F}\left(i_w^t, h_w^t\right)$ is the current-controlled electromagnetic force between the *w*th maglev pole and the track rail, defined in the pertinent trajectory coordinate system; the superscript (*t*) indicates the current time step and the subscript (*w*) for the *w*th maglev pole; $\mathbf{i}_w^t$ is the electrical circuit; K_0 is a coupling factor related to the cross-sectional area of the core; and ${}_{II_m}\mathbf{h}_w^t$ is the magnetic air gap, including both levitation air gap and guidance air gap, calculated by

$$ {}_{II_m}\mathbf{h}_w^t = \mathbf{h}_0 + {}_{II_m}\mathbf{u}_w\left(t\right) + {}_{II_m}\mathbf{u}_G\left(s_w^t\right) + \mathbf{u}_r\left(s_w^t\right) \tag{5.9b}$$

where $\mathbf{h_0}$ is the design static gap at the static equilibrium state of the train (10 mm for SML); ${}_{II_m}\mathbf{u}_w\left(t\right)$ is the motion of the *w*th magnetic pole defined in the pertinent trajectory coordinate system, extracted from the response of the train subsystem; s_w^t is the arc length from the *w*th maglev pole to the origin of the global coordinate system; $\mathbf{u}_r\left(s_w^t\right)$ is the track irregularity, modelled by utilizing a seven-parameter power spectrum density function (Shi et al., 2014); and ${}_{II_m}\mathbf{u}_G\left(s_w^t\right)$ is the rail deflection at the *w*th magnetic pole with respect to the pertinent trajectory coordinate system, obtained through the transformation of response of the rail at the same location,

$$ {}_{II_m}\mathbf{u}_G\left(s_w^t\right) = \left({}_I\mathbf{R}^{II_m\to I}\right)^{\mathrm{T}} {}_I\mathbf{u}_G\left(s_w^t\right) \tag{5.9c}$$

where ${}_I\mathbf{u}_G\left(s_w^t\right)$ is the deflection of the rail defined in the global coordinate system; and ${}_I\mathbf{R}^{II_m\to I}$ is the transformation matrix from the *m*th trajectory coordinate system to the global coordinate system, expressed by Eq. (D.1). Furthermore, the proportional-derivative (PD) controller is used to control the air gap ${}_{II_m}\mathbf{h}_w^t$ between the maglev pole of the train and the inner (outer) rail of the viaduct to approach the design static value $\mathbf{h}_0$ as close as possible.

5.5.2 Coupled equations and solution method

The equations of motion for the coupled maglev train-viaduct system can be expressed as

$$\begin{bmatrix} {}_{II}\mathbf{M}_V & \mathbf{0} \\ \mathbf{0} & {}_{I}\mathbf{M}_G \end{bmatrix}\begin{bmatrix} {}_{II}\ddot{\mathbf{U}}_V \\ {}_{I}\ddot{\mathbf{U}}_G \end{bmatrix}+\begin{bmatrix} {}_{II}\mathbf{C}_V & \mathbf{0} \\ \mathbf{0} & {}_{I}\mathbf{C}_G \end{bmatrix}\begin{bmatrix} {}_{II}\dot{\mathbf{U}}_V \\ {}_{I}\dot{\mathbf{U}}_G \end{bmatrix}+\begin{bmatrix} {}_{II}\mathbf{K}_V & \mathbf{0} \\ \mathbf{0} & {}_{I}\mathbf{K}_G \end{bmatrix}\begin{bmatrix} {}_{II}\mathbf{U}_V \\ {}_{I}\mathbf{U}_G \end{bmatrix} = \begin{bmatrix} {}_{II}\mathbf{F}_V^e + {}_{II}\mathbf{F}_V^v + {}_{II}\mathbf{F}_V^{G\to V} \\ {}_{I}\mathbf{F}_G^e + {}_{I}\mathbf{F}_G^{V\to G} \end{bmatrix} \tag{5.10}$$

The first equation is for the train subsystem in the generalized trajectory coordinate systems, and the second equation is for the viaduct subsystem in the global coordinate system. The interaction between the two subsystems is realized by the two force vectors ${}_{II}\mathbf{F}_V^{G\to V}$ and ${}_{I}\mathbf{F}_G^{V\to G}$. The vector ${}_{II}\mathbf{F}_V^{G\to V}$ is the interaction-induced forces acting on the train subsystem, in which the nonzero entries are associated with the levitation and guidance magnets only and the entries for the car bodies, bogies and rockers are all zero. The interactive forces acting on the train subsystem are determined by the electromagnetic forces ${}_{II}\mathbf{F}\left(i_w^t, h_w^t\right)$ with some mathematical manipulation. Likewise, the vector ${}_{I}\mathbf{F}_G^{V\to G}$ is the interaction-induced forces acting on the viaduct subsystem, in which the non-zero entries appear only at the loaded elements of the inner rail and outer rail. The values of the interactive forces acting on the viaduct subsystem are calculated by $\left({}_{I}\mathbf{R}^{II_m\to I}\right)^{\mathrm{T}}\,{}_{II_m}\mathbf{F}\left(i_w^t, h_w^t\right)$ and the positions of these forces should be on the rails at the magnetic poles of the train, in which the position of the force at the wth magnetic pole can be determined by

$$s_w = v\cdot\left(t-t_w\right)\cdot\left[H\left(t-t_w\right)-H\left(t-t_w-\frac{nL}{v}\right)\right] \tag{5.11}$$

where v is the speed of the train; t_w is the traveling time of the w^{th} pole since it enters the concerned span of the viaduct subsystem, $t_w = (w-1)d/v$; d is the force space, 0.258m for the levitation forces and 1.032m for the guidance forces; L is the arc length of the centerline of each transitional span, 24.768 m; $H(t)$ is the unit step function; and n is the number of spans. When $s_w = 0$, the w^{th} load is off the n spans, and ${}_{II_m}\mathbf{u}_G(s_w^t)$ as well as $\mathbf{u}_r(s_w^t)$ in Eq. (5.9b) are taken as zero to obtain the air gap ${}_{II_m}\mathbf{h}_w^t$.

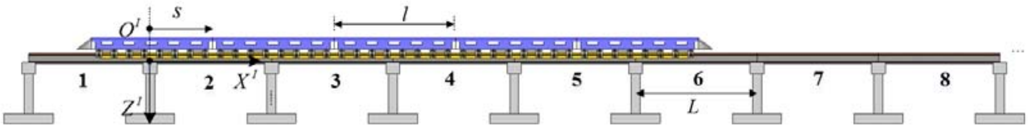

(a) Side view of a train with 5 maglev vehicles running on the curved viaduct

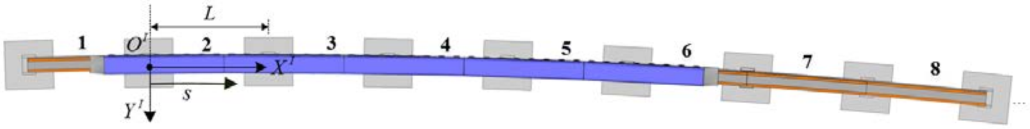

(b) Top view of a train with 5 maglev vehicles running on the curved viaduct

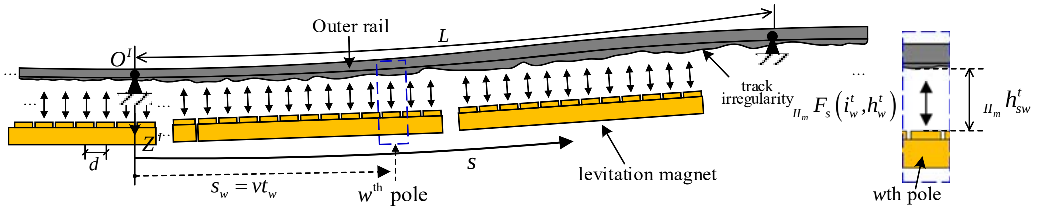

(c) Force diagrams between the levitation magnet and outer rail

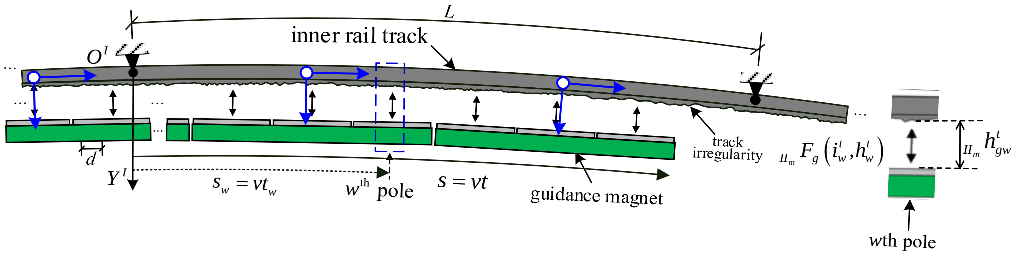

(d) Force diagrams between the guidance magnet and inner rail

Figure 5.7 The schematic diagram of the coupled maglev train and viaduct system in SML.

To find the solutions for the coupled maglev train-viaduct system, the ABAQUS Explicit Solver is employed for its high computation efficiency. Specifically, the response of the viaduct subsystem at time t is first calculated using the ABAQUS Explicit Solver with the central difference method. Meanwhile, the response of the train subsystem is computed using the ABAQUS Explicit Solver with a self-developed ABAQUS subroutine, in which the central difference method is also adopted. The above computations of the two subsystems are linear problems. With the responses of both the viaduct and train subsystems available at time t, the interactive electromagnetic forces at time $t+\Delta t$ can be obtained using Eqs. (5.9a~d), in which the PD controller is used to adjust the interaction forces according to the gap error e_w^t. Accordingly, the two interfaces, VDLOAD for the load application on the rail by the position vector s_w with ${}_{II_m}\mathbf{F}\left(i_w^t, h_w^t\right)$ and VUFIELD for collection of the response ${}_{II_m}\mathbf{u}_G\left(s_w^t\right)$ and ${}_{II_m}\dot{\mathbf{u}}_G\left(s_w^t\right)$ of the loaded elements of the rail, are developed for the simultaneous computation of both the train and viaduct subsystems. The time interval used in the computation is 4×10^{-6} s after several trial tests to balance the computation time and accuracy. The threshold for the error in the air gap is set as 0.001 m.

5.6 Case Study

The proposed framework is now applied to the SML to investigate the dynamic interaction between the maglev train and the transitional curved viaduct. The viaduct subsystem extracted from the SML is of a total arc length of 412.06 m (24.768 m ×17), including one straight span for entrance, 15 transitional curved spans, and one circular curved span for departure. The arc length of each span is 24.768 m. The characteristic parameters for the curved track alignment are L_0 = 371.52 m, R = 3300 m, $\phi_0 = 12°$, h_0=0.47 m, and h_g=2.24 m. The maglev train has five vehicles moving at v = 300 km/h. The details and major parameters of the train subsystem can be found in the Chapters 3 and 4. An experimental study with the maglev train moving over the concerned transitional curved viaduct of the SML is also conducted to partially validate the accuracy of the proposed framework.

5.6.1 Numerical results and experimental validation

From this case study, the electromagnet forces acting on the inner rail and outer rail are found to relate to HD of the transitional curved track closely. Therefore, a discussion on HD of the transitional curved track is given first in this section.

5.6.1.1 Discussion on HD

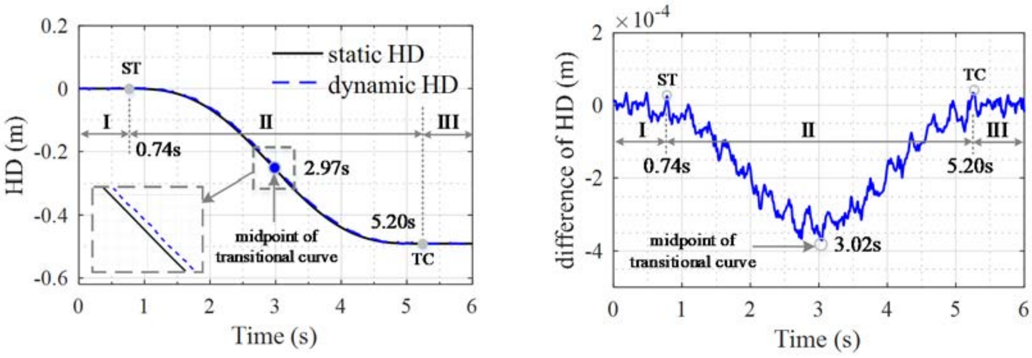

(a) Static and dynamic HD

(b) Difference of the two HD

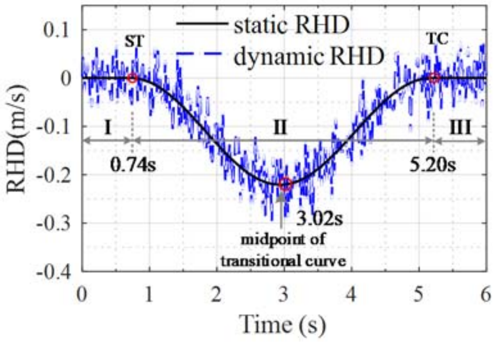

(c) Static and dynamic RHD

Figure 5.8 HD and RHD tracked by the mass center of the 2ed vehicle moving over the whole spans.

The static (reference) HD along the entire track, including the straight, transitional, and circular curved track, can be calculated by substituting the alignment parameters of the SML into the sinusoid function given in Table 5.1, and it is plotted in Figure 5.8a as the function of time (the distance divided by the train speed). Besides, Figure 8a also shows the dynamic HD tracked by the 2ed vehicle moving over the track. The dynamic HD is computed as the difference in the vertical dynamic coordinates between the inner rail and the outer rail without the track irregularities. Figure 5.8b shows the difference between the static HD and the dynamic HD, obtained by subtracting the former from the latter. Furthermore, by differentiating the HD with time, the rate of change of HD (RHD) can be obtained and it is plotted in Figure 5.8c. It can be seen that the entire HD and RHD curve can be divided into three segments. The first segment refers to the period I (0~0.74s) when the mass center of the 2ed vehicle body is moving on the straight span. The second segment corresponds to the period II (0.74s~5.20s) when the 2nd vehicle body is moving on the transitional curved spans, while the 3rd segment conforms the period III, during which the 2nd vehicle body is moving on the circular curved span. It is noticed from Figure 5.8a that the dynamic HD is very close to the static HD, which means that the vertical dynamic displacement of the track is small. Nevertheless, it is also noticed from Figure 5.8b that although the dynamic HD in the straight span and the circular curved span is almost equal to their static HD with some small fluctuations, there is considerable difference between the static HD and dynamic HD in the transitional curved span. The HD difference contains one slowly-varying component and one high-frequency component. By comparing Figure 5.8b with Figure 5.8c, it is interesting to see that the slowly-changing pattern of the HD difference is similar to the slowly-changing RHD curve and that the slowly-changing HD difference has a good correlation with the slowly-changing RHD. The maximum HD difference appears at the middle point of the transitional curved track where it is also the point for the maximum RHD. The subsequent study reveals that the maximum difference of the levitation forces applied on the outer rail and inner rail occurs when the RHD reaches its maximum value, and that the maximum HD difference is mainly induced by the difference of levitation forces applied on the outer rail and the inner rail, as shown in Figure 5.9a. The high frequency component of the HD difference is due to the difference in high frequency displacement response of the inner and outer rails.

5.6.1.2 Computed electromagnetic forces

Electromagnetic forces are highly influenced by the air gap between the magnets of the vehicle and the rails of the viaduct, as shown in Eq. (5.9a). It has been demonstrated in the previous studies (Han & Kim, 2016; Han et al., 2009; Ju et al., 2012; Ren, 2008; Shi et al., 2007; Song & Fujino, 2008; Zhao & Zhai, 2002) that the levitation force has a strong positive correlation with the value of air gap: larger force is induced by higher air gap.

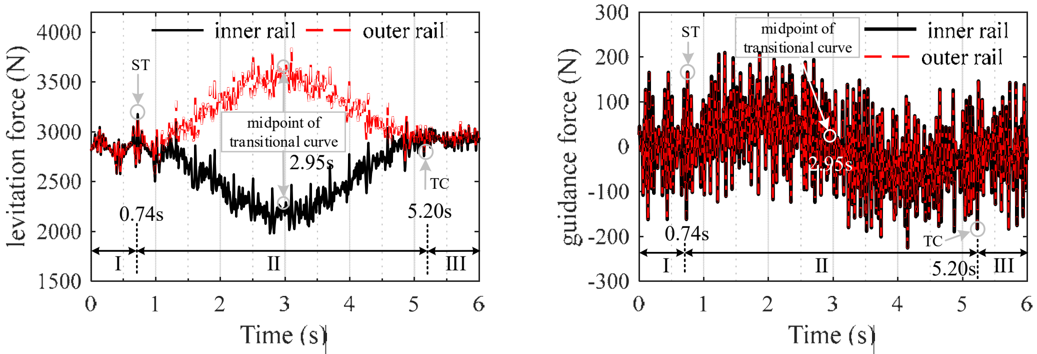

(a) levitation forces (b) guidance forces

Figure 5.9 Time history of one set of electromagnetic forces applied on the inner rail and outer rail, respectively.

Figure 5.9 shows the time history of one set of electromagnetic forces applied on the inner rail and outer rail. They are generated from the 6th maglev levitation pole and the 2nd maglev guidance pole of the 4th set of magnets under the 2ed vehicle body. As described in Section 5.5.1, the airgap between the magnet and the rail is continuously adjusted by the PD controller to approach the design static value $\mathbf{h_0}$ as close as possible. When the vehicle moves on the straight and circular track, the airgap between the levitation magnet and the rail is almost constant with a slight fluctuation only. As a result, the levitation forces applied on the inner rail and the outer rail of the straight track and circular track fluctuates around the constant value of 2810N, which is actually the gravity-induced steady levitation force, as shown in Figure 5.9a in the 1st and 3rd segments. However, when the vehicle is running on the transitional curved track, the outer rail is lifted with respect to the inner rail by following the static HD presented in Figure 5.8a. To make sure the airgap approaches $\mathbf{h_0}$ as close as possible, the levitation magnet moving under the outer rail is accordingly lifted by increasing the levitation forces through the interactive electromagnet-airgap force model. Since the increase of airgap, when the vehicle moves into the transitional curved track, is in directly proportional to the RHD, as shown in Figure 5.7c and Figure 5.8c, the levitation forces applied on the outer rail keep pace with the RHD, as shown in Figure 5.9a. The maximum levitation force on the outer rail occurs around the middle point of the transitional curved track (t=2.95 s), where is also the point the maximum RHD locates (t=2.97 s). Moreover, to ensure a relative balance of the vehicle in the vertical direction, the levitation forces acting on the inner rail are accordingly in inversely proportional to those on the outer rail, as shown in Figure 5.9a. However, the guidance forces acting on the inner rail and outer rail are approximately equal and both fluctuate around zero, as shown in Figure 5.9b. The main reason is because along the entire track including the transitional curved track, each section of the track is assigned with a balanced radius and cant angle with the train travelling at 300 km/h. In such a way, the component of centrifugal force in the radial direction is well compensated by that of gravitational force in the same direction. As a result, the guidance forces are mainly induced by the track irregularities. Besides, it can be also observed from Figure 5.9b that the guidance forces induced by the vehicle running on the transitional track (Period II) are slightly larger than those on the straight track (Period I) and circular curved track (Period III).

5.6.1.3 Computed vehicle dynamic responses

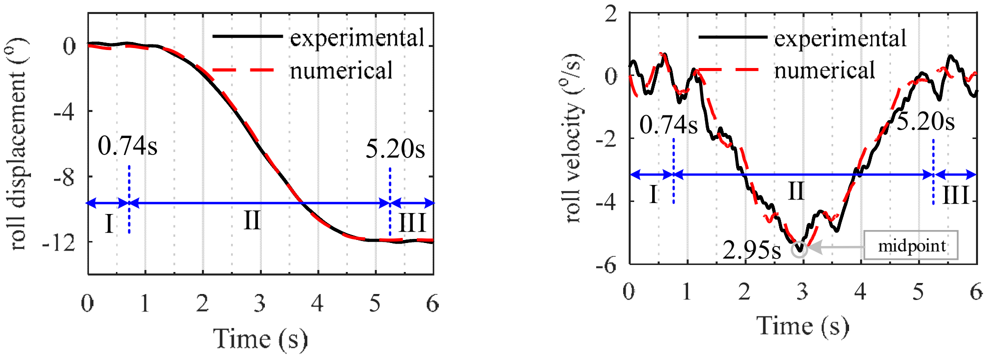

(a) displacement

(b) velocity

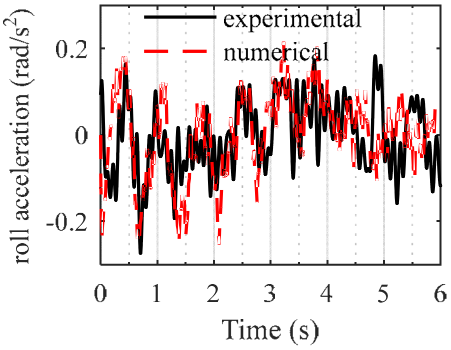

(c) acceleration

Figure 5.10 Rolling motion of the 2ed vehicle recorded from the numerical study and experimental result.

Figure 5.10 shows the rolling motions of the 2nd vehicle, including rolling displacement, velocity and acceleration. They are induced mainly due to the distance-varying HD. Since the air gap between the magnet of train and the rail of the viaduct is controlled around an ideal value of 10 mm, the rolling angle of the vehicle approximately follows that of cant angle of track, as shown in Figure 5.10a. The cant angle of the circular span is designed with 12°, and the maximum rolling angle of the vehicle is computed as 11.94° accordingly. Figure 5.10b shows the vehicle angular velocity. When the vehicle is running on the straight span (Period I), the vehicle rolls around zero with a maximum value about 0.92°/s. A rapid increase in angular velocity appears during the period from 0.74 to 2.95s. By the time of 2.95s, the angular velocity is up to a peak value about -5.61°/s. After that, the angular velocity falls off rapidly until the vehicle runs on the circular curved span at the time of 5.20 s. Only a slight fluctuation occurs when the vehicle moves on the circular span. However, no obvious response increase in angular acceleration is found when the vehicle moves on the transitional span compared with the straight and circular spans, as shown in Figure 5.10c. By comparing Figure 5.10b with Figure 5.8, it is obvious that the angular velocity of the vehicle varies in a similar way as RHD shown in Figure 5.8c. This indicates that the vehicle angular velocity is mainly induced by the rate of change of HD. It can be concluded that the rolling displacement and velocity of the vehicle are highly related to the HD and RHD of the track, respectively. The maximum value of the vehicle angular velocity appears when the peak RHD occurs.

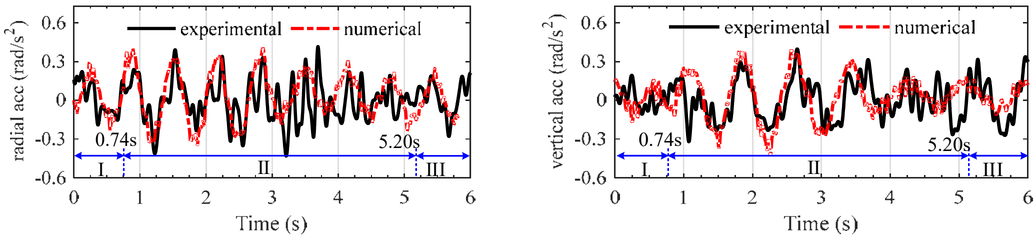

(a) lateral (b) vertical

Figure 5.11 Acceleration time histories of the 2nd vehicle recorded from the experimental and numerical studies

Figure 5.11 shows the acceleration responses of the 2nd vehicle in the lateral and vertical directions of the track plan. It is recalled that the guidance forces (see Figure 5.9b) generated by the vehicle moving over the transitional spans are slightly larger than those over the straight span and circular span. As a result, the lateral acceleration response of the vehicle in Period II is slightly larger than that in Period I and Period III, as shown in Figure 5.11a. When the vehicle is running on the transitional spans, the levitation forces acting on the electromagnets at the inner side and outer side of the vehicle are considerably different, but their resultant is only slightly larger than that when the vehicle moves on the straight track and circular track. As a result, the total external forces acting on the vehicle body in the vertical direction when the vehicle moves on the transitional track is almost equal to those when the vehicle moves on the straight track and circular track. Therefore, the vertical responses of the vehicle when the vehicle moves on the transitional track is only slightly larger than those when the vehicle moves on the straight track and circular track, as shown in Figure 5.11b.

5.6.1.4 Experimental validation of vehicle dynamic responses

(a) experimental scene (b) accelerometer (c) angular velocity transducer

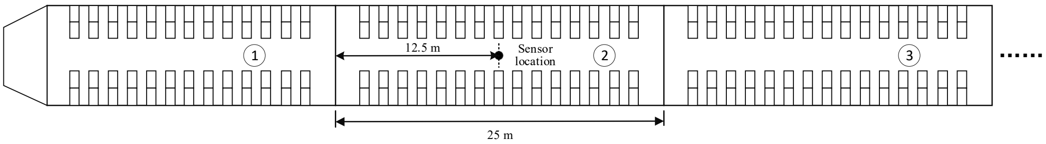

(d) schematic diagram of sensor arrangement

Figure 5.12 Sensor arrangement on the 2nd carriage of the Shanghai maglev train.

To validate the proposed framework and computed results, an experimental study was carried out on the train running on the SML. Since it was not allowed to interrupt the operation of the high-speed maglev train, only simple measurements were conducted. Two sensors, including one three-direction accelerometer (see Figure 5.12b) and one angular velocity transducer (see Figure 5.12c), were installed on the midpoint of the floor of the 2nd vehicle of the maglev train to respectively measure the acceleration responses and rolling angular velocity of the vehicle (see Figure 5.12a). The responses of the vehicle were recorded for the whole SML of a total length of 30 km. The measurement data were then extracted for the vehicle running over the concerned section (see marked in Figure 5.1) and plotted in Figures 5.10 and 5.11 together with the computed results. The comparative results show that the simulated responses of the 2nd vehicle body, including the rolling motions, lateral acceleration, and vertical acceleration, can match with the measurement data relatively well. Nevertheless, for a throughout validation, the more complicated field measurement shall be conducted.

5.6.1.5 Computed dynamic responses of transitional curved viaduct

Table 5.2 lists the radii and cant angles of the middle sections of the girder spans. Only the responses of the girder in the straight, 6th, 8th, 10th and circular spans are presented in this subsection. The rails are the key component for the interaction between the vehicle and viaduct. Therefore, the responses of the inner and outer rails are also presented in addition to the girder responses.

Table 5.2 The radii and cant angles of the middle sections of the girder spans

No.	Straight	2	4	6	8	10	12	14	Circular
Radius (m)	+∞	511542	43970	13285	6600	4390	3568	3321	3300
Cant (°)	0	0.08	0.90	2.98	6.00	9.02	11.10	11.92	12

Figure 5.13 shows the vertical displacement responses of the girder and the rails at the designated middle spans. The duration of the response time histories is 1.75 seconds, beginning when the 1st vehicle of the train is going to move on the concerned span and ending when the 5th (last) vehicle of the train is leaving from the concerned span. Because of the distance-varying difference of the levitation forces acting on the inner rail and outer rail (see Figure 5.9a), the vertical displacement responses of the girder and rails of the designated spans change span by span.

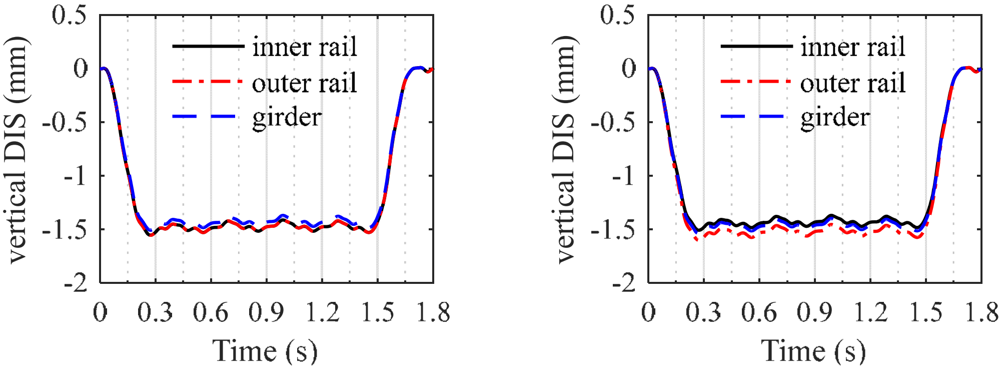

(a) The straight span

(b) The 6th span

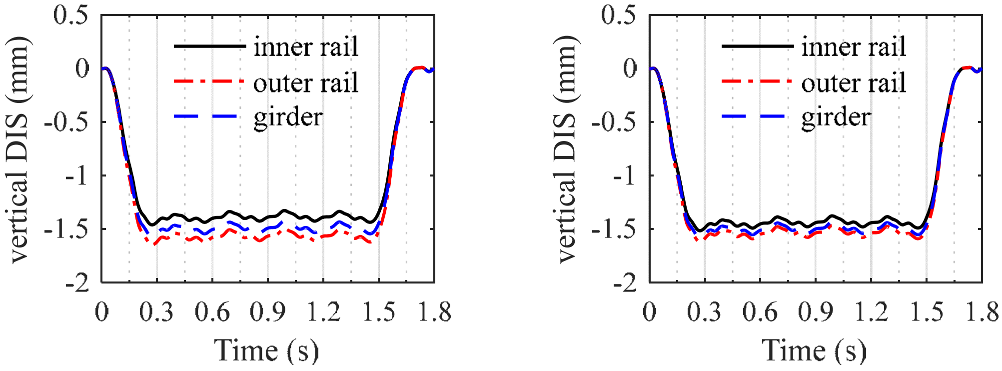

(c) The 8th span (d) The 10th span

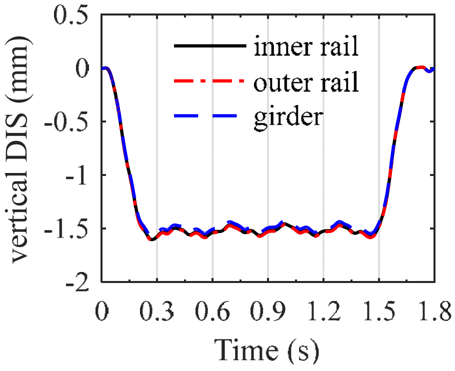

(e) The circular span

Figure 5.13 The computed vertical displacement responses of the inner rails, outer rails and girders of the designated spans.

The displacement responses of the inner rail, outer rail and girder of the straight span are almost equal, as shown in Figure 5.13a, because the levitation forces acting on the inner rail and outer rail are almost equal. Nevertheless, slight differences appear in the displacement responses of the inner rail, outer rail and girder of the 6th span, as shown in Figure 5.13b. The differences become more obvious in the displacement responses of the inner rail, outer rail and girder of the 8th span (see Figure 5.13c), where the lowest and largest levitation forces are respectively loaded on the inner rail and outer rail, as presented in Figure 5.9a. It is also noticeable that the maximum displacement of the girder is slightly smaller than that of the outer rail but slightly larger than that of the inner rail. Nevertheless, such differences are reduced for the 10th span (see Figure 5.13d) and become almost zero for the circular curved span (see Figure 5.13e). The displacement response of the circular span is slightly larger than that of the straight span. This is because of the resultant of the gravitational and centrifugal forces in the vertical direction of the circular track plane is $g \cdot \cos\left(\phi_{bal}\right) + \frac{v^2}{R} \cdot \sin\left(\phi_{bal}\right)$, which is larger than g for straight span.

However, as the entire track is designed with balanced radii and cant angles for the train running at 300 km/h, the component of centrifugal force in the lateral direction is well compensated by that of the gravitational force in the same direction, as indicated in Figure 5.9b. As a result, the lateral responses of the inner rails, outer rails, and girders of all the concerned spans are very small, as shown in Figure 5.14. The lateral responses of the rails and girders are almost equal with very small difference.

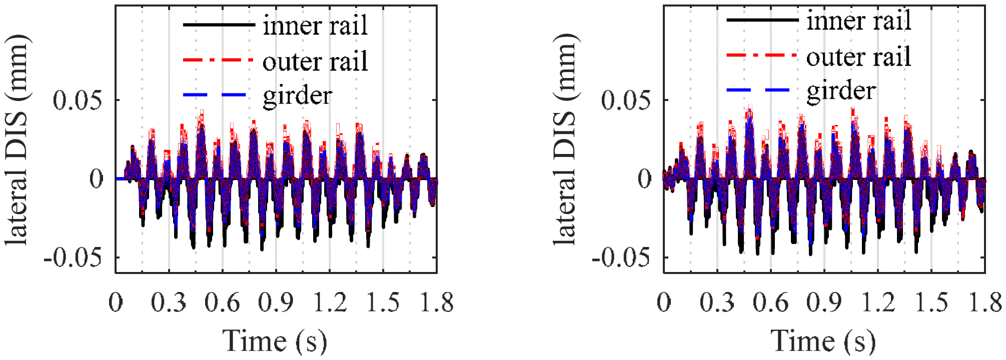

(a) The straight span

(b) The 6th span

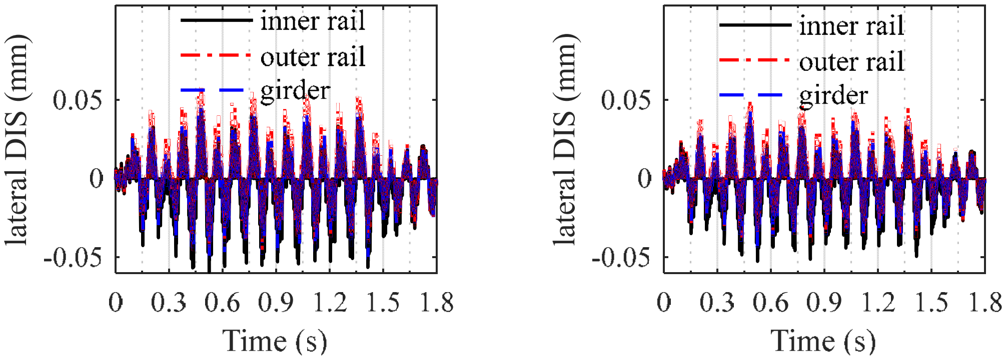

(c) The 8th span

(d) The 10th span

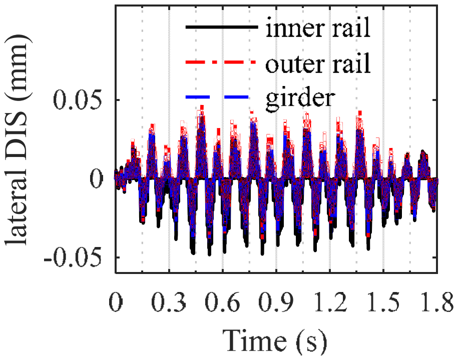

(e) The circular span

Figure 5.14 The computed lateral displacement responses of the inner rails, outer rails, and girders of the designated spans

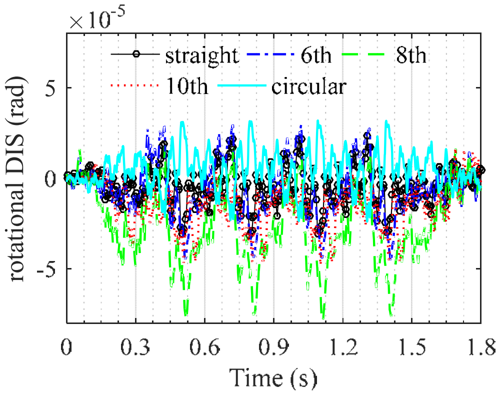

Figure 5.15 The computed rotational displacement responses of the girders at the middle sections of the designated spans

Nevertheless, with the unsymmetrical electromagnetic forces on the inner rail and outer rail (see Figure 5.9), the rotational displacement responses of some of the spans are induced. Figure 5.15 shows the rotational displacement responses of the girders at the middle sections of the selected spans. For the straight and circular spans, since almost the same forces loaded on the inner rail and outer rail, the rotational displacement responses slightly fluctuate around zero. However, with the difference in the levitation forces between the inner rail and outer rail, the rotational displacement responses of the girders in the transitional spans are nonzero and vary span by span. The maximum rotational displacement response occurs in the 8^{th} span, where the maximum difference in the levitation forces between the inner rail and outer rail appears.

5.6.2 Effect of transitional length

The length of transitional viaduct has a direct association with construction cost, vehicle ride comfort, and guideway safety. To this end, the effect of transitional length on dynamic responses of vehicle and viaduct is investigated in this section. The number of spans in the transitional viaduct considered in this study is 5, 10, 15 and 20. It is important to highlight that for each section of the transitional track of different lengths, it is designed with balanced cant angle and radius by following Table 5.1 and Eq. (5.1).

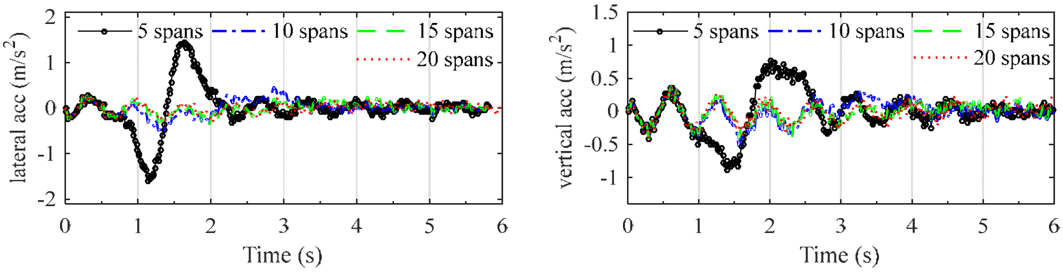

(a) lateral acceleration (b) vertical acceleration

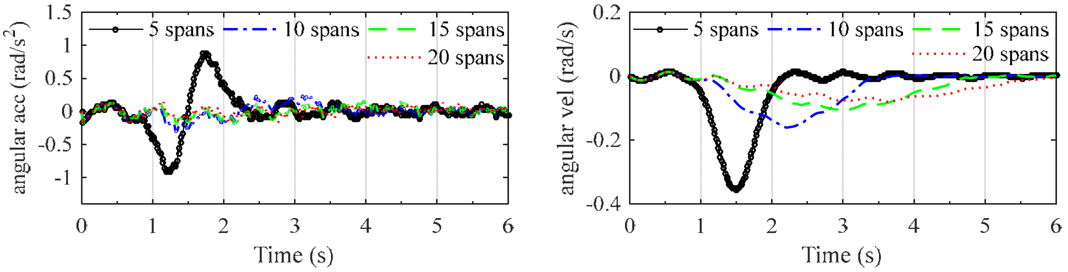

(c) angular acceleration (d) angular velocity

Figure 5.16 Vehicle dynamic responses induced by the train moving over different length of transitional spans.

Figure 5.16 shows the dynamic responses of the 2nd vehicle when the maglev train of five vehicles move over transitional spans of different lengths. It can be observed that the length of transitional viaduct has a significant effect on all types of vehicle response. The shorter the transitional length, the higher response of the vehicle is. More than double peak responses are recorded in Figures 5.16a-d when the number of spans is reduced from 10 to 5. Nonetheless, when the number of spans is reduced from 20 to 10, apart from a moderate increase in vehicle angular velocity (see Figure 5.16d), all other dynamic responses (see Figures 5.16a-c) change slightly. It is interesting to note that the number of spans of the concerned transitional viaduct in the SML is 15, by which all the dynamic responses of the vehicle are small enough.

The dynamic response of the girder at the middle section of the transitional viaduct is used to investigate the effect of transitional length on the viaduct. The three displacement responses of the girder are plotted in Figure 5.17. It can be seen that despite of the track with balanced curve radius and cant angle, considerable dynamic responses of the girder are excited in the vertical and rotational directions, as shown in Figures 5.17b and c. For the lateral and rotational responses, the shorter the transitional length, the higher response of the girder is. With the transitional length reduced from 20 spans to 5 spans, the responses increase many times. However, the increase in the vertical direction is moderate, as shown in Figure 5.17b, and only higher fluctuation is induced by the shortest transitional length.

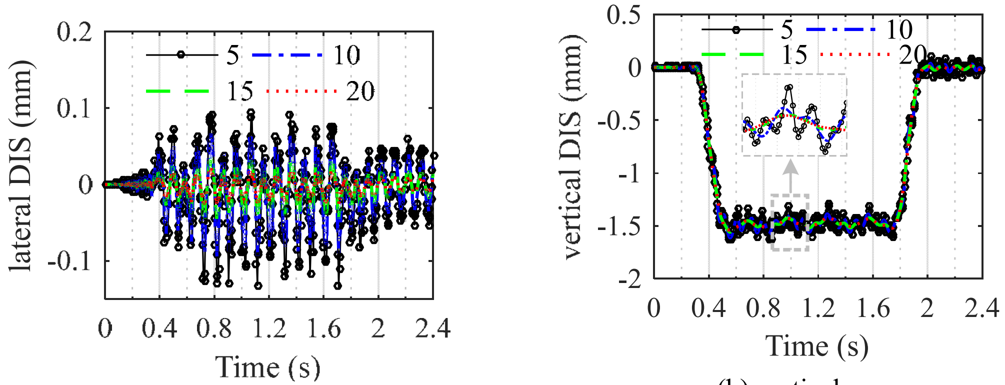

(a) lateral

(b) vertical

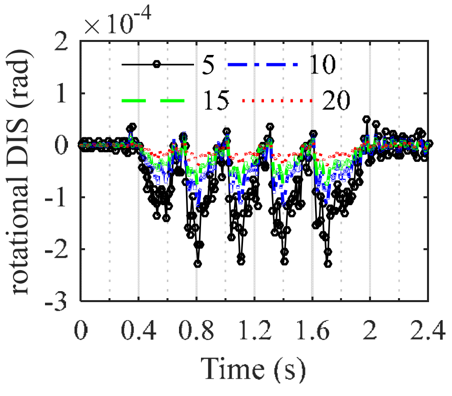

(c) rotational

Figure 5.17 Displacement responses of the girder at the middle section of the transitional viaduct of different lengths.

5.6.3 Effect of cant deficiency

In this case study, the train runs at the circular curved viaduct of the SML at an equilibrium speed of 300km/h. The cant deficiency is measured by the difference between the theoretical cant required for such an equilibrium speed and the actual cant designed. In terms of the degree of angle (°), the cant deficiency C_{d0} can be calculated as

$$C_{d0} = D_{bal0} - D_{act0} \approx \frac{180^\circ}{\pi} \cdot \left(\frac{v^2}{g \cdot R} - \frac{h_0}{h_g} \right) \tag{5.12}$$

where D_{bal0} is the theoretical cant angle required for the full compensation of the lateral acceleration induced by the centrifugal force; and D_{act0} is the actual cant angle used. Once the cant deficiency of the circular curved track is determined, the cant deficiency C_d of the section of the transitional curved track at a distance s from the connection point ST can be calculated by

$$C_d\left(s\right)=C_{d0}\cdot\left[\frac{s}{L_0}-\frac{1}{2\pi}\sin\left(\frac{s}{L_0}2\pi\right)\right] \tag{5.13}$$

Clearly, the cant deficiency of the transitional curved track varies with distance s. To investigate the effect of cant deficiency on the transitional viaduct and vehicle responses, the theoretical cant of the circular curved track remains unchanged but the deficient cant angles of the circular span are taken as 0°, 3°, 6°, 9°, and 12° respectively.

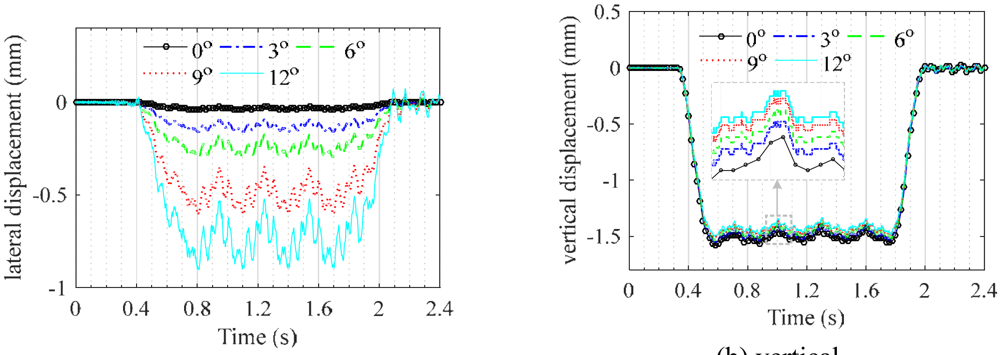

(a) radial

(b) vertical

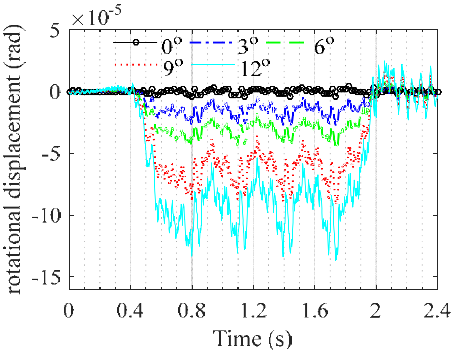

(c) rotational

Figure 5.18 Effects of cant deficiency on displacement responses of the girder at the middle section of the 8th transitional curved span.

The dynamic responses of the girder at the middle section of the 8th transitional curved span are plotted in Figure 5.18 to demonstrate the effect of cant deficiencies on viaduct dynamic responses. It is seen from Figures 5.18a and 5.18c that higher responses of the girder are excited with larger deficient cant angles in the radial and rotational directions. This is mainly due to the fact that for a fixed radius, larger deficient cant angle results in larger guidance forces and larger unbalanced levitation forces which act on the girder and cause larger lateral and rotational displacement responses of the girder. It is also noticeable from Figure 5.18b that only slight decrease in the vertical displacement response of the girder appears as deficient cant angle increases. The steady vertical force acting on the girder can be calculated as $g \cdot \cos\left(D_{bal} - C_d\right) + k \cdot v^2 \cdot \sin\left(D_{bal} - C_d\right)$, where D_{bal} is the balanced cant required for the full compensation of the lateral acceleration induced by the centrifugal force. As a result, the vertical force decreases with the increase of deficient cant angle C_d .

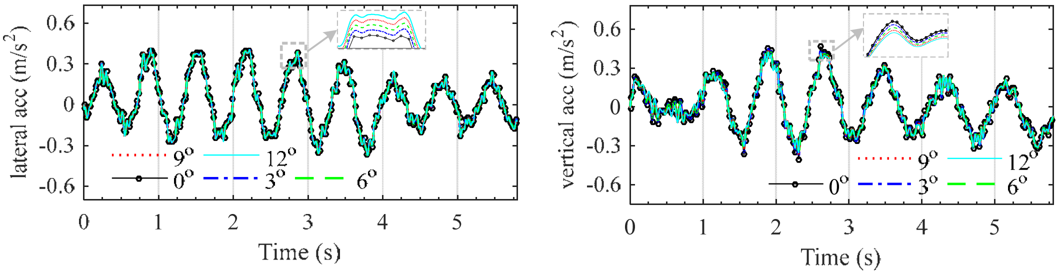

(a) lateral acceleration

(b) vertical acceleration

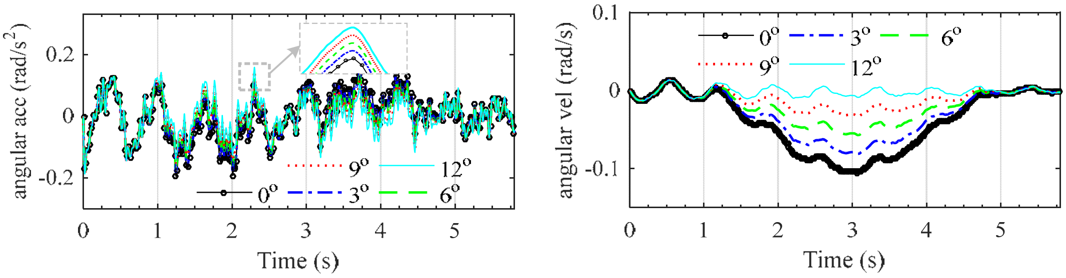

(c) angular acceleration

(d) angular velocity

Figure 5.19 Time histories of the 2nd maglev vehicle moving over the track with different deficient cant angles.

Figure 5.19 shows the dynamic responses of the 2nd vehicle moving over the track with different deficient cant angles. It can be seen from Figures 5.19a and 5.19c that the lateral acceleration and angular acceleration of the vehicle increases slightly as the deficient cant angle increases. This is consistent with the observation from the girder response in consideration of the optimal controller used in the train. Because higher vibration of the viaduct is excited by higher deficient cant angle (see Figures 5.19a and 5.19c), the fluctuations of the vehicle in the lateral acceleration and angular acceleration are also larger. Likewise, because the vertical response of the viaduct decreases with the increase of the deficient cant angle, the vertical acceleration of the vehicle has also a slight decrease, as shown in Figure 5.19b. Nonetheless, it is evident from Figure 5.19d that the vehicle angular velocity has a significant negative correlation with the deficient cant angle. The main reason is that with the increase of deficient cant angle, both HD and RHD decrease (see Figure 5.19). For the 12° cant deficiency, both HD and RHD fluctuate around zero. As a result, the vehicle angular velocity vibrates around zero.

5.7 Summary

A framework for accurate dynamic analysis of high-speed maglev trains running over transitional curved viaducts has been presented in this paper. By applying this framework to the Shanghai Maglev Line (SML), the dynamic characteristics and responses of the maglev vehicles and the transitional curved viaduct have been investigated. Besides, the effects of transitional track length and cant deficiency on the coupled system have also been explored. The major conclusions drawn from this study are summarized as follows:

1) The dynamic height difference (HD) of the track in the straight span and the circular curved span is almost equal to their static HD with some small fluctuations, while there is considerable difference between the dynamic and static HDs in the transitional curved spans. The slowly-varying component of the HD difference has a good correlation with the slowly-changing the change rate of HD (RHD) and its maximum value appears at the middle section of the transitional curved track where it is also the section for the maximum RHD.

2) When the vehicle is running on the transitional curved track, the levitation forces applied on the outer rail keep pace with the RHD, and the maximum levitation force occurs at the location where the maximum RHD occurs.

3) Since the air gap between the magnet of the vehicle and the rail of the viaduct is controlled to approach an ideal value, the rolling displacement and velocity of the

vehicle are highly related to the HD and RHD of the track. The maximum value of the vehicle angular velocity appears when the peak RHD occurs.

4) When the vehicle is moving on the straight track or circular track, the vertical displacement responses of the outer rail and inner rail are almost equal. However, when the vehicle is running on the transitional curved track, the differences occurs, and the maximum value of such difference appears at the middle section of the transitional track. Similar phenomenon also occurs in the rotational displacement response of the viaduct.

5) The length of transitional viaduct has a significant effect on all types of vehicle responses. The shorter the transitional length, the higher responses of the vehicle are. The transitional length also affects the lateral and rotational responses of the viaduct, while its effect on the vertical response is moderate.

6) The increase of deficient cant angle causes a sharp increase in the responses of the transitional curved viaduct in the radial and rotational directions. Besides, the cant deficiency has a considerable effect on the angular velocity response of the vehicle moving on the transitional curved viaduct.

7) The proposed framework is demonstrated feasible and accurate, providing a powerful tool for the dynamic analysis of high-speed maglev trains on straight, transitional and circular viaducts.

CHAPTER 6

OPTIMIZATION OF HORIZONTALLY CURVED TRACK IN THE ALIGNMENT DESIGN OF A HIGH-SPEED MAGLEV LINE

6.1 Introduction

The proposed framework in Chapter 5 has been demonstrated feasible and accurate, providing a powerful tool for the dynamic analysis of high-speed maglev trains running on the horizontally curved track composed by the straight, transitional and circular curved track sections. Besides, the effect of alignment parameters of the horizontally curved track, i.e., the curve radii and cants of the circular curved track and the lengths of the transitional curved track, on the dynamic responses of the coupled train and viaduct have also been individually investigated in Chapters 4 and 5. The results showed that these three alignment parameters significantly affected the ride quality of vehicle. Therefore, it is necessary and important to optimize the alignment parameters of the horizontally curved track to ensure the ride quality of high-speed maglev trains. Regarding this aspect, considerable efforts have been made by the previous studies (Kufver, 1997; Kufver & Andersson, 1998; Kufver, 2000; Um et al., 2010; Um et al., 2015). These optimization works aimed at finding the optimal alignment parameters for the curved track to ensure that the vehicle operates at a comfort level, as a result, leading to a longer curved track required.

However, from a practical point of view, the reduction of construction cost is always pursued in the alignment design of a high-speed maglev line. That is truly significant and necessary for the horizontally curved track, because its construction is much more expensive than a straight track and the ride comfort is much more serious. With this concern, this chapter proposes a new optimization method for the alignment design of horizontally curved track in a high-speed maglev line, in which the minimum length of the curved track is regarded as a major objective function and the satisfaction of the minimum comfort level of passengers is taken as a boundary condition to constrain the selection of alignment parameters of the curved track. The optimal solution from the proposed optimization method has been compared with the optimal solution from the current (Kufver's) method and the existing solution for the actual curved track in the SML. Furthermore, the dynamic model of a coupled maglev train and curved viaduct system presented in Chapter 5 is also used in this chapter to validate the accuracy of the optimal solution from the proposed optimization method.

(a) Shanghai maglev line (b) Emsland maglev line

Figure 6.1 The curved tracks in high-speed maglev lines

6.2 Minimum Length-Based Optimization of Horizontally Curved Track

In general, the alignment of a horizontally curved track in a high-speed maglev line is similar to that in a wheel-based railway line, but there are certain differences in transitional curves between the two because of high speed of the maglev train. In this study, the optimization of horizontally curved track alignment is addressed for high-speed maglev line only.

6.2.1 Features of horizontally curved track

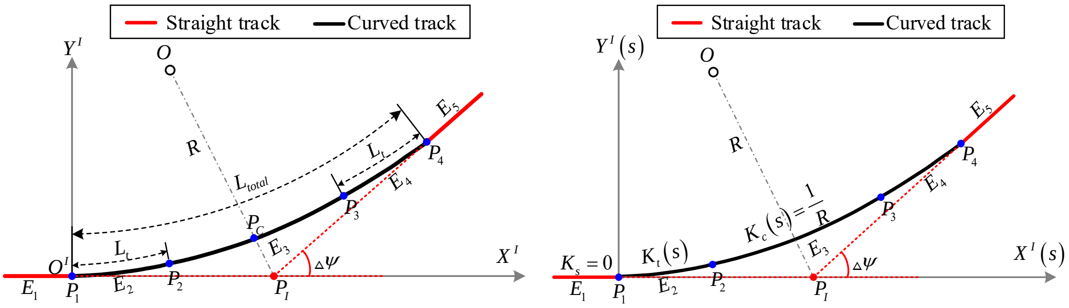

(a) Alignment of curved track (b) Curvature of radius along curved track

Figure 6.2 Schematic diagram of curved track alignment.

Figure 6.2 shows the schematic diagram of the alignment of the curved track between two straight track sections (Yi, 2017). The lines E_1 and E_5 are the two straight track sections. Their orientations are often pre-determined, and their intersection point P_I and the intersection angle $\Delta\psi$ are also pre-determined. On the other hand, the curved track is often composed by three sections (Kobry, 2017; Lindahl, 2001; Pirti et al., 2016; Yi, 2017; Kufver, 1997; Kufver & Andersson, 1998; Kufver, 2000): two transitional track sections marked by E_2 and E_4 and one circular track section marked by E_3 in Figure 6.2. The circular track is embedded between the two transitional tracks which are deployed to connect with the lines E_1 and E_5, respectively. P_1 and P_4 are the connection points between the transitional tracks and the straight track. P_2 and P_3 are the connection points between the transitional tracks and the circular track. P_C is the center point of the circular track. In general, the lengths of the two transitional tracks are equal. As thus, the entire curved track is symmetric about the line P_IP_C, the origin of the radius of the circular track is on the line P_IP_C, and the alignment design of the curved track can be considered on the line E_1+E_2+half E_3 only.

To ensure the ride comfort when the train runs on the curved track, there are some requirements on the geometry of the transitional tracks and the circular track. Each of the transitional track should be designed to ensure that its curvature and HD varies continuously between zero and the curvature and HD of the circular curved track (see Figure 6.2b) respectively. Sometime, the HD is replaced by the cant which is equal to HD/h_g, where h_g is the distance of the two rails, with a unit of radian. To high-speed maglev train, both curvature and cant of the transitional track are often the sinusoidal functions of the distance of arc length s, defined by Eq. (6.1).

$$K_t(s) = \frac{1}{R}\cdot\left[\frac{s}{L_t} - \frac{1}{2\pi}\sin\left(\frac{s}{L_t}2\pi\right)\right] \tag{6.1a}$$

$$D_t(s) = D\cdot\left[\frac{s}{L_t} - \frac{1}{2\pi}\sin\left(\frac{s}{L_t}2\pi\right)\right] \tag{6.1b}$$

where s is the arc length of the concerned point with reference to the connection point P_1, as shown in Figure 6.2; K_t and D_t are the curvature and the cant of the transitional track, respectively, and they are the function of arc distance s; R and D are the radius and cant of the circular track, respectively; L_t is the arc length of the entire transitional track, as shown in Figure 6.2a. Obviously, both K_t and D_t are zero at the connection point P_1, which are also equal to those of the straight track (see Figure 6.2b). At the point P_2, K_t is $1/R$ and D_t is D, and they are equal to those of the circular track section, respectively (see Figure 6.2b). In some cases, the term cant deficiency is used and expressed by

$$C_d = D_{eq} - D = \frac{v^2}{g \cdot R} - D \tag{6.2}$$

where D_{eq} is the equilibrium cant; v is the train speed (unit: m/s); and g is the gravitational acceleration of 9.80 m/s^2.

From Eq. (6.1) and Eq. (6.2), it is obvious that R, L_t and D (or C_d) are the prerequisite alignment parameters used in the alignment design of curved track. Among them, R and L_t are the two parameters related to the curved track length. The total length of the entire curved track, L_{total}, can be derived as

$$L_{total} = L_t + R \cdot \triangle\Psi \tag{6.3}$$

6.2.2 Comfort level of passengers on transitional track (P_{CT})

The ride comfort for passengers is the complex sensation. When a train is moving on the straight track, a long time-based average sensation is often used to define the ride comfort for passengers (Lauriks et al., 2003). However, when the train starts moving on the transitional curved track, a sudden change of the average sensation will be perceived by the passengers. This instantaneous sensation is mainly induced by the lateral acceleration, lateral jerk, and roll velocity of the vehicle. As a result, these three quantities should be integrally included in the assessment of ride quality of the vehicle moving on the transitional curved track. Accordingly, the comfort index P_{CT} (Passenger Comfort on Curve Transitions) was introduced in the British Standard (EN 12299:2009) and expressed by

$$P_{CT} = \underbrace{\max\left\lfloor \left(a\cdot\left|\ddot{y}_{1s}\right|_{\max} + b\cdot\left|\dddot{y}_{1s}\right|_{\max} - c\right);\, 0\right\rfloor}_{P_{CT1}} + \underbrace{\left(d\cdot\left|\dot{\varphi}_{1s}\right|_{\max}\right)^{h}}_{P_{CT2}} \tag{6.4}$$

where a, b, and c are the constants in relation to lateral responses of the vehicle; d and h are the constants in relation to rolling response of the vehicle. Table 6.1 lists the recommended values for these constants.

Table 6.1 Constants for P_{CT} comfort index (British Standard EN 12299:2009)

Condition	a [s^2/m]	b [s^3/m]	c [-]	d [s/rad]	h [-]
In rest-standing	0.2854	0.2069	0.111	3.64	2.283
In rest-seated	0.0897	0.0968	0.059	0.916	1.626

In Eq. (6.4), $\ddot{y}_{1s}$, $\dddot{y}_{1s}$, and $\dot{\varphi}_{1s}$ are the one-second average of the lateral acceleration, lateral jerk and roll velocity of the vehicle, and they can be estimated by using Eq. (6.5). $\left|\ddot{y}_{1s}\right|_{\max}$, $\left|\dddot{y}_{1s}\right|_{\max}$, and $\left|\dot{\varphi}_{1s}\right|_{\max}$ are the maximum values of the three one-second averages, called intermediate quantities (British Standard EN 12299:2009), and they can be found from the one-second average responses calculated by Eq. (6.5).

$$\ddot{y}_{1s}\left(t\right) = \frac{1}{T}\cdot\int_{t-\frac{T}{2}}^{t+\frac{T}{2}} \ddot{y}^{*}_{W_P}\left(\tau\right)\mathrm{d}\tau \tag{6.5a}$$

$$\dddot{y}_{1s}\left(t\right) = \frac{1}{T}\cdot\left[\ddot{y}_{1s}\left(t+\frac{T}{2}\right) - \ddot{y}_{1s}\left(t-\frac{T}{2}\right)\right] \tag{6.5b}$$

$$\dot{\varphi}_{1s}\left(t\right) = \frac{1}{T}\cdot\int_{t-\frac{T}{2}}^{t+\frac{T}{2}} \dot{\varphi}^{*}_{W_P}\left(\tau\right)\mathrm{d}\tau \tag{6.5c}$$

where $T = 1$ second; $\ddot{y}^{*}_{W_P}\left(\tau\right)$ and $\dot{\varphi}^{*}_{W_P}\left(\tau\right)$ are the lateral acceleration and roll velocity responses of the vehicle running on the curved track.

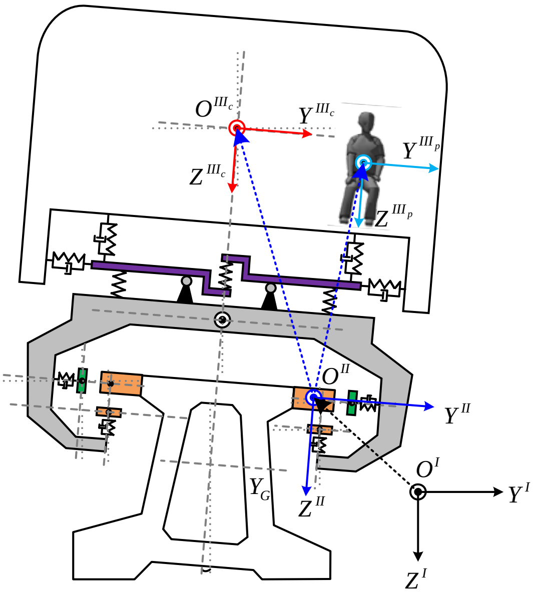

Figure 6.3 Schematic diagram of the passenger and the vehicle moving on the curved track.

It is assumed in this study that the train runs at a constant speed *v* along the entire track, and the passengers have no relative motion to the vehicle. With these assumptions, the external forces acting on the passenger can be seen as composed by two parts (Kufver, 1997; Kufver, 2000b; Lauriks et al., 2003; Um et al., 2010): (a) the curved track-induced centrifugal and gravitational forces in the vertical and horizontal directions of the track plane (see the entire vehicle as a rigid body moving on the perfect curved track) and (b) the vehicle's motion-induced forces (the forces induced by vehicle motions relative to the track). As a result, the lateral acceleration response of the passenger can be expressed by

$$\begin{aligned}\ddot{y}_p(t) &= \left\{K_t(s)\cdot v^2\cdot\cos\left[D_t(s)\right]-g\cdot\sin\left[D_t(s)\right]\right\}+\ddot{y}_c(t)\\ &\approx g\cdot C_d\cdot\left[\frac{s}{L_t}-\frac{1}{2\pi}\sin\left(\frac{s}{L_t}2\pi\right)\right]+\ddot{y}_c(t)\end{aligned} \tag{6.6a}$$

where *t* is the running time of the vehicle on the transitional track; $s=vt$; K_t, D_t, and C_{dt} are the curvature, cant, and cant deficiency of the transitional track, respectively; $\ddot{y}_p$ is the lateral acceleration response perceived by the passenger; $\ddot{y}_c$ is the vehicle's motion induced lateral acceleration response; and the first item on the right side of Eq. (6.6a) is the curved track profile-induced lateral acceleration response. It is noted that the approximation of Eq. (6.6a) is obtained based on the assumption that D_t is so small that $\cos\left(D_t\right) \approx 1$ and $\sin\left(D_t\right) \approx D_t$.

Lateral jerk is defined as the changing rate of lateral acceleration per unit time. Therefore, it can be obtained by differentiating Eq. (6.6a) with time.

$$\dddot{y}_p\left(t\right) = g \cdot \frac{v}{L_t} \cdot C_d \cdot \left[1 - \cos\left(\frac{s}{L_t} 2\pi\right)\right] + \dddot{y}_c\left(t\right) \tag{6.6b}$$

where $\dddot{y}_p$ is the lateral jerk perceived by the passenger; and $\dddot{y}_c$ is the vehicle's motion-induced lateral jerk.

Roll velocity is the changing rate of the roll angle with time about the longitudinal axis of the vehicle. It is mainly induced by the changing rate of track cant and it can be written as

$$\dot{\varphi}_p\left(t\right) = \frac{\mathrm{d}D_t\left(s\right)}{\mathrm{d}s} \cdot \frac{\mathrm{d}s}{\mathrm{d}t} + \dot{\varphi}_c\left(t\right) = \frac{D \cdot v}{L_t}\left[1 - \cos\left(\frac{s}{L_t} 2\pi\right)\right] + \dot{\varphi}_c\left(t\right) \tag{6.6c}$$

where $\dot{\varphi}_p$ is the roll velocity perceived by the passenger; $\dot{\varphi}_c$ is the vehicle's motion-induced roll velocity; and the first term on the right side of Eq. (6.6c) is the curved track-induced roll velocity.

The previous studies (Kufver, 1997; Kufver, 2000b; Lauriks et al., 2003; Um et al., 2010) revealed that in the case of non-derailment, the vehicle's motion-induced responses of the passengers in terms of one second average are small compared with the curved track-induced responses. As a result, the intermediate quantities used in the P_{CT} formula were approximately estimated by considering the curved track-induced response multiplied by a dynamic coefficient f_r (Kufver, 1997; Kufver, 2000b; Lauriks et al., 2003; Um et al., 2010). The dynamic coefficient is defined as the ratio between the response perceived by the passenger and the curved track-induced response. Consequently, based on Eq. (6.6), the intermediate quantities used in the P_{CT} formula can be approximately calculated by

$$\left|\ddot{y}(t)\right|_{\max} = \left|\ddot{y}\left(\frac{L_t}{v}\right)\right| = g \cdot f_r \cdot C_d \tag{6.7a}$$

$$\left|\dddot{y}(t)\right|_{\max} = \left|\dddot{y}\left(\frac{L_t}{2v}\right)\right| = \mathrm{g} \cdot f_r \cdot C_d \cdot \frac{2v}{L_t} \tag{6.7b}$$

$$\left|\dot{\varphi}(t)\right|_{\max} = \left|\dot{\varphi}\left(\frac{L_t}{2v}\right)\right| = \left(\frac{v^2}{g \cdot R} - f_r \cdot C_d\right) \cdot \frac{2v}{L_t} \tag{6.7c}$$

Since the train considered here is one of the non-tilting train systems, f_r is recommended to be 1.2 (Kufver, 1997; Lauriks et al., 2003). Then, by substituting Eq. (6.7) into Eq. (6.4), the comfort index P_{CT} can be explicitly formulized by the alignment parameters R, L_t, and C_d of the curved track as

$$P_{CT} = \underbrace{\max\left[\left(a \cdot g \cdot f_r \cdot C_d + b \cdot \mathrm{g} \cdot f_r \cdot \frac{2v}{L_t} \cdot C_d - c\right); 0\right]}_{P_{CT1}} + \underbrace{\left[d \cdot \left(\frac{v^2}{g \cdot R} - f_r \cdot C_d\right) \cdot \frac{2v}{L_t}\right]^h}_{P_{CT2}} \tag{6.8}$$

It can be seen from Eq. (6.8) that the P_{CT} is composed of two terms: the first term, called P_{CT1}, considers lateral acceleration and lateral jerk, while the second term, called P_{CT2}, considers roll velocity. For the first term, if the value in the round bracket is smaller than zero, the first term is taken zero. Otherwise, the first term takes the value in the round bracket.

6.2.3 Objective function

An objective function describes the output target corresponding to its maximization or minimization based on a set of constraints or the relationship between one or more decision variables. Different objective functions lead to different optimization results. In this subsection, the current optimization method (the Kufver's method) for horizontally curved track in the alignment design of railway lines is briefly introduced. The new optimization method and solution proposed in this study is then described in detail.

6.2.3.1 The current optimization method

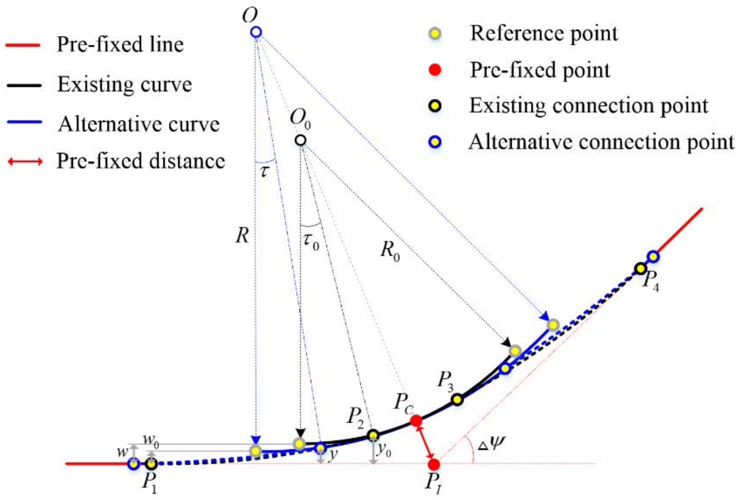

Figure 6.4 Schematic diagram of the alignment design of horizontally curved track (the current method)

The Kufver's method was proposed under the background that reconstruction works on existing railway lines were extensively performed to meet the demand of the increase of operating train speed and that the improvement and optimization of the existing curved track alignment to guarantee the ride quality of the vehicle operating at a higher speed was particularly necessary and important. In this regard, the objective of the optimization of the existing curved track alignment was set to seek the optimal solution for the train operating at the minimum discomfort level (Kufver, 1997). Based on this, the objective function of the Kufver's method was written as

$$\text{minimum } P_{CT} = \text{minimum}\left\langle \max\left[\left(a \cdot g \cdot f_r \cdot C_d + b \cdot \text{g} \cdot f_r \cdot \frac{2v}{L_t} \cdot C_d - c\right);\ 0\right] + \left[d \cdot \left(\frac{v^2}{g \cdot R} - f_r \cdot C_d\right) \cdot \frac{2v}{L_t}\right]^h \right\rangle \tag{6.9a}$$

On the other hand, the reduction of construction cost was also moderately considered in the Kufver's method. It has been reported (Kufver, 1997; Kufver, 2000b; Lauriks et al., 2003; Um et al., 2010) that when the center of the existing circular curved track (see the point P_C in Figure 6.4) was selected as the setting-out point for the alternative curved track to pass through, the smallest radius compensation could be obtained by changing the length of the transitional track, which to some extent could reduce the length of the entire curved track (construction cost) under the demand of the minimum discomfort level. Therefore, a boundary condition was subjoined to constrain the alignment parameters R and L_t. When the center (P_C) of the existing circular curve was pre-fixed, the distance $L_{P_C P_I}$ between the point P_C and the point P_I was thus determined as a constant. Accordingly, the geometrical relationship between R and L_t could be worked out by

$$\frac{R+w}{\cos\left(\frac{\Delta\,\psi}{2}\right)} - R = \frac{R_0 + w_0}{\cos\left(\frac{\Delta\,\psi}{2}\right)} - R_0 = \text{constant} \qquad (6.9b)$$

where R_0 and R were the radius of the existing and alternative circular curved track, respectively; L_t and L_{t0} (used in Eq. (6.9c)) were the length of the existing and alternative transitional curved track, respectively; w_0, y_0 and τ_0 were the geometrical parameters related with R_0 and L_{t0}; Likewise, w, y and τ were the geometrical parameters related with R and L_t. These parameters could be calculated by Eq. (6.9c).

$$w = y - R(1-\cos\,\tau) = \frac{L_t^2}{6R}\left(1-\frac{3}{2\pi^2}\right) - R\left[1-\cos\left(\frac{L_t}{2R}\right)\right] \qquad (6.9c)$$

The detail way to determine the optimal cant deficiency C_d used in Eq. (6.9a) and the detail way to find the optimal solution of R and L_t for the minimum value of P_{CT} in terms of Eq. (6.9) can be found in the references (Kufver, 1997; Kufver, 2000a; Kufver, 2000b). It is noted from Eq. (6.9a) that the value of comfort index P_{CT} is inversely proportional to the parameters of R and L_t. Thus, to seek the optimal solution for the minimum of P_{CT}, both R and L_t would be duly increased. As a result, the entire length of the curved track offered by the current method is certainly longer than the existing one.

6.2.3.2 The new optimization method

From a practical point of view, if the comfort level of passengers can be satisfied, the length of the entire curved track is expected to be minimum in order to reduce construction cost and save land space (Kobry, 2017; Lindahl, 2001; Pirti et al., 2016; Yi, 2017). Under this demand, this study takes the minimum length of the entire curved track as the objective function which can be expressed by

$$\text{minimum } L_{total} = \text{minimum}\left\langle L_t + R\cdot\Delta\,\psi\right\rangle \qquad (6.10a)$$

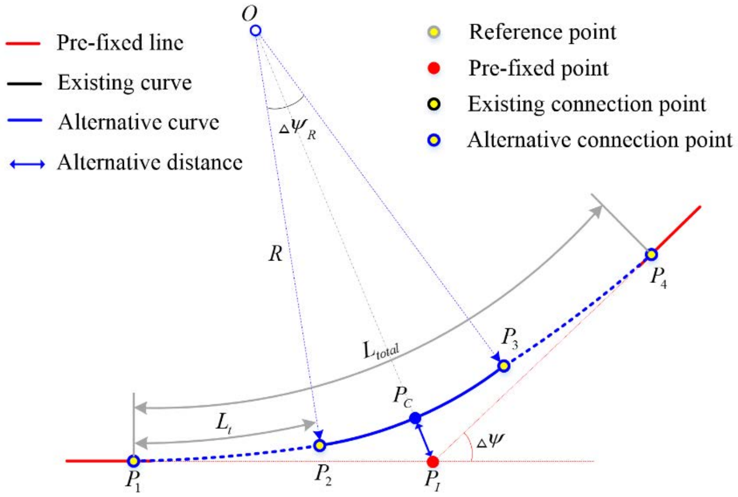

Figure 6.5 Schematic diagram of the alignment design of horizontally curved track (the proposed method)

Meantime, the solution of alignment parameters of R and L_t in Eq. (6.10a) should also meet the requirement of the satisfaction of comfort level, which is often determined by the limit (minimum) value of the comfort level of passengers suggested by the standard or empirical criterion. As a result, a boundary condition to constrain the alignment parameters of R and L_t of the curved track should be subjoined and can be expressed by

$$\max\left\lfloor\left(a\cdot g\cdot f_r\cdot C_d+b\cdot \mathrm{g}\cdot f_r\cdot\frac{2v}{L_t}\cdot C_d-c\right);0\right\rfloor+\left[d\cdot\left(\frac{v^2}{g\cdot R}-f_r\cdot C_d\right)\cdot\frac{2v}{L_t}\right]^h\leq P_{CT0}\quad(6.10\text{b})$$

where P_{CT0} is the limited value of the satisfaction of the comfort level of passengers when the vehicle runs on the curved track.

The comparison between Figure 6.4 and Figure 6.5 shows that the pre-fixed setting-out point (P_C) and the parameters of w_0, y_0 and τ_0 of the exiting curve required in the Kufver's method are excluded in the proposed method. That is to say, the present method is independent of the existing solution, leading to a different optimal solution. Besides, by given a limited value of comfort level P_{CT0}, the proposed method can be not only suitable to improve an existing curved track but also used to design a new curved track. Furthermore, it is noted from Eq. (6.10a) that the length of the entire curved track is proportional to R and L_t. To achieve the goal of minimizing L_{total}, both R and L_t shall be duly decreased but shall meet the boundary condition of Eq. (6.10b).

As a result, the entire length of the optimal curved track offered by the proposed method is shorter than the existing one and meantime meets the satisfaction of comfort level.

In summary, because of the different objective functions taken in the two methods, the optimal solutions offered are thus different: the Kufver's method offers the optimal solution for the best comfort level of passengers by enlarging the length of the entire curved track, whereas the proposed method provides the optimal solution for the minimum length of the entire curved track with a satisfaction of the comfort level of passengers.

6.2.4 Optimal cant deficiency

Eq. (6.10b) shows that in addition to the alignment parameters R and L_t, the variable of C_d also influences the minimum value of L_{total}. As a result, to obtain the optimal solution for the minimum value of L_{total}, the value of C_d should also be optimal. Moreover, given that the first-order differential of Eq. (6.10b) is discontinuous with C_d, two cases are discussed in the following to obtain the optimal C_d.

Case A: $P_{CT1}=0$

In this case, C_d should satisfy the following constraint condition:

$$C_d \le \frac{c \cdot L_t}{g \cdot f_r \cdot (a \cdot L_t + 2b \cdot v)} \tag{6.11}$$

Hence, Eq. (6.10b) can be rewritten as

$$\left(\frac{2d \cdot v}{L_t}\right)^h \cdot \left(\frac{v^2}{g \cdot R} - f_r \cdot C_d\right)^h = P_{CT2} = P_{CT0} \tag{6.12}$$

By combining Eq. (6.3) with Eq. (6.12), the relationship between L_{total} and C_d can be established.

$$L_{total} = \frac{d \cdot v^3 \cdot \Delta\,\Psi}{g \cdot L_t \cdot \sqrt[h]{P_{CT0}} + g \cdot d \cdot v \cdot f_r \cdot C_d} + L_t \tag{6.13}$$

It is clear that L_{total} decreases with the increase of C_d. Therefore, to minimize L_{total}, C_d should be maximized. Thus, the optimal cant deficiency C_d^* can be calculated by

$$C_d{}^* = \frac{c \cdot L_t}{g \cdot f_r \cdot \left(a \cdot L_t + 2b \cdot v\right)} \tag{6.14}$$

Case B: $P_{CT1}>0$

In this case, C_d should satisfy the following constraint condition:

$$C_d > \frac{C \cdot L_t}{g \cdot f_r \cdot \left(A \cdot L_t + 2B \cdot v\right)} \tag{6.15}$$

Here, Eq. (6.10b) can be rewritten as

$$a \cdot g \cdot f_r \cdot C_d + b \cdot \mathrm{g} \cdot f_r \cdot \frac{2v}{L_t} \cdot C_d - c + \left(\frac{2d \cdot v}{L_t}\right)^h \cdot \left(\frac{v^2}{g \cdot R} - f_r \cdot C_d\right)^h = P_{CT0} \tag{6.16}$$

By combining Eq. (6.3) with Eq. (6.16), the relationship between L_{total} and C_d can be obtained as

$$L_{total} = \frac{2d \cdot \triangle\Psi \cdot v^3}{2d \cdot g \cdot f_r \cdot C_d \cdot v + g \cdot L_t \cdot \sqrt[h]{P_{CT0} - a \cdot g \cdot f_r \cdot C_d - b \cdot \mathrm{g} \cdot f_r \cdot \frac{2v}{L_t} \cdot C_d + c}} + L_t \tag{6.17}$$

The optimal cant deficiency occurs where $\frac{\mathrm{d}L_{total}}{\mathrm{d}C_d} = 0$, and it can be calculated by

$$C_d{}^* = \frac{P_{CT0} \cdot L_t}{a \cdot g \cdot f_r \cdot L_t + 2v \cdot b \cdot \mathrm{g} \cdot f_r} - \left(2d \cdot f_r \cdot v\right)^{\frac{h}{1-h}} \cdot \left(a \cdot g \cdot f_r \cdot L_t + 2v \cdot b \cdot \mathrm{g} \cdot f_r\right)^{-\frac{1}{1-h}} \cdot L_t \tag{6.18}$$

6.2.5 Optimization solution

The flowchart for finding the optimal solution for the minimum curve length is shown in Figure 6.6. To ensure the safety of the vehicles and passengers, the maximum cant of the curved track should be limited to less than or equal to 12° (Wilson & Womack, 2004). Accordingly, the calculated cant *D* should be checked by using Step 8 in the flowchart. When the value of *D* exceeds the stipulated limit, the limit value of 12º is used instead. Besides, the rate of change of cant should also be checked using Step 9 in the flowchart, and it shall not exceed the limit value of 0.10 rad/s (Wilson & Womack, 2004). When the rate of change of cant exceeds the stipulated limit, the limit value of 0.10 rad/s should be used instead.

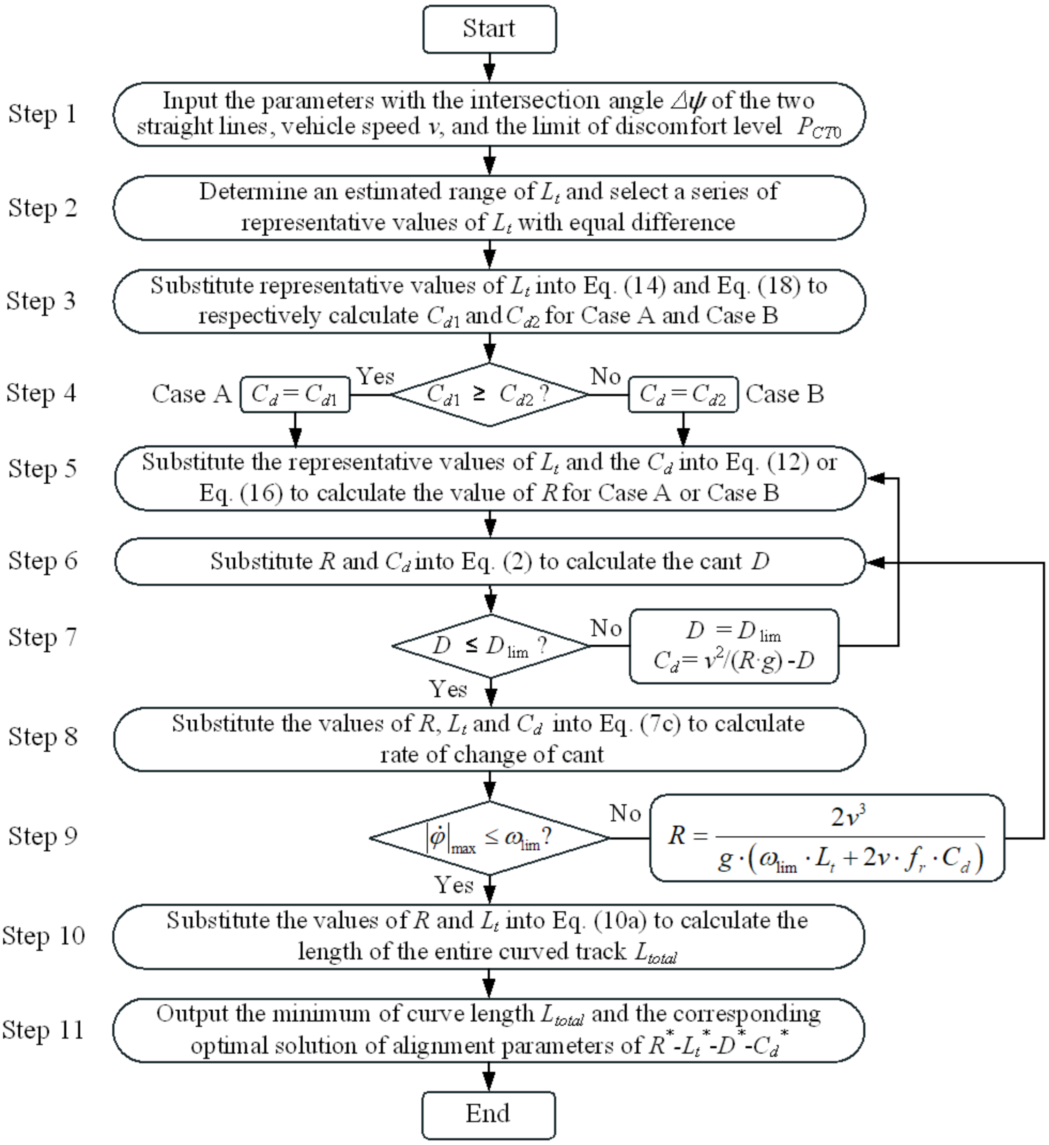

Figure 6.6 Flowchart for finding optimal solution in the proposed method.

6.3 Comparison between Kufver's Solution and Present Solution

This subsection mainly focuses on the comparison between the Kufver's solution and the present solution by using the actual curved track in the SML as a reference.

6.3.1 The actual curved track

The actual curved track of the SML used in this study is imbedded between the two intersecting straight tracks with a deflection angle $\Delta\psi$ is 0.255 rad. The alignment parameter *R* of the circular curved track section and the alignment parameter L_t of the transitional curved track section are separately optimized based on some considerations. For example, the two alignment parameters *R* and *D* of the circular track section are synergistically designed to guarantee that the circular track-induced centrifugal acceleration of the vehicle is fully counteracted by the cant-induced gravitational acceleration component (Wilson & Womack, 2004). Based on this consideration, the cant deficiency C_d is 0° and the radius of the circular track can be calculated by Eq. (6.19).

$$R = \frac{v^2}{g \cdot \tan(D)} \tag{6.19}$$

where *v* is the design speed of the train moving over the actual curved track, which is 300 km/h; and *D* is the cant of the actual circular track section, designed with 12°. By using Eq. (6.19), the radius of the actual circular track, *R,* is 3300 m.

The minimum length of the transitional track section can be calculated based on the limit of the rate of change of the cant (Wilson & Womack, 2004) by Eq. (6.20).

$$L_t = \frac{2v}{\omega_{\lim}} \cdot \left(\frac{v^2}{R \cdot g} - C_d \right) \tag{6.20}$$

where $\omega_{\lim}$ is the limit of the rate of change of cant, which is 0.10 rad/s (Wilson & Womack, 2004). In view of the limit design by Eq. (6.20), L_t should be 358 m, but the length of the actual transitional track section is designed with a relatively conservative value of 371.52 m, which is equal to the entire length of 15 spans (24.768 × 15).

In summary, the alignment parameters *R*, L_t, *D*, and C_d of the actual curved track in the SML are 3300 m, 375 m, 12° and 0° respectively. By substituting the alignment parameters into Eq. (6.8) and (6.3), the comfort level P_{CT} is calculated as 9.14% and the length of the entire curved track is 1213 m.

6.3.2 Optimal solution based on the Kufver's method

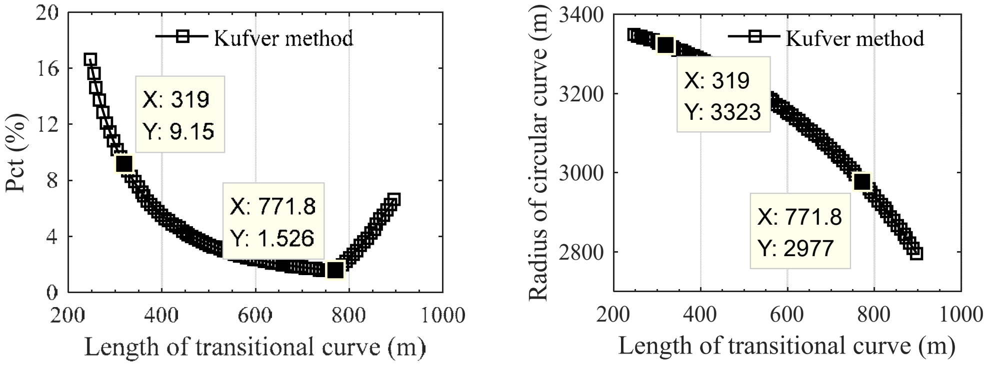

(a) L_t-P_{CT}

(b) L_t-R

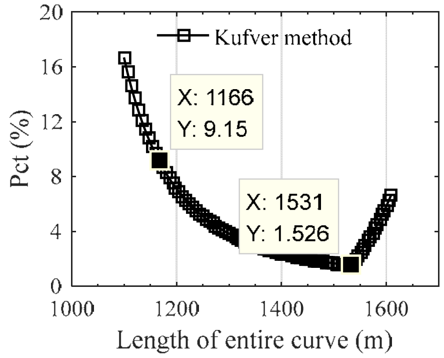

(c) L_{total}-P_{CT}

Figure 6.7 The optimal solution based on the Kufver's method

As described in Section 6.2.3.1, the Kufver's method aims to improve the existing curve to obtain the best comfort level P_{CT}, in which a setting-out point is required to be pre-fixed to constrain the alignment parameters (see Equation (6.9b)). The setting-out point is now pre-fixed at the center (P_C) of the existing curve, where the distance $L_{P_C P_I}$ between the point P_I and P_C is calculated as 27.70 m. The optimal solution calculated based on the Kufver's method is shown in Figure 6.7. It can be seen from Figures 6.7(a) and 6.7(b) that with the setting-out point pre-fixed, there is an optimal solution for the minimum value of P_{CT} of 1.53%, in which R is 2977 m, L_t is 772 m, and L_{total} is 1531 m (see Figure 6.7(c)). Clearly, the length of the entire curved track is much longer than that in the existing SML (1213 m). It can be therefore concluded that the Kufver's method could offer the optimal solution for the minimum value of P_{CT}, which is much smaller than that of the existing curve, but the length of the entire curved track (construction cost) is greatly increased.

Moreover, another solution satisfying the boundary condition of Equation (6.9b) can be found and marked in Figure 6.7 in terms of the comfort level P_{CT} of 9.14% provided by the SML, in which the alignment parameters R, L_t, D, and C_d are 3323m, 319m, 12° and 1.64°, respectively. As shown in Figure 6.7(c), this solution can provide a comparable comfort level P_{CT} of 9.15% with the length of the entire curved track of 1166 m, which is shortened by 47 m compared with the length of the actual curved track (1213 m).

6.3.3 Optimal solution based on the present method

In this subsection, the same comfort level P_{CT} of 9.14% is used as the minimum value of satisfaction of the comfort level (P_{CT0} in Eq. (6.10)) to calculate the optimal solution using the proposed method, and the results are plotted in Figure 6.8.

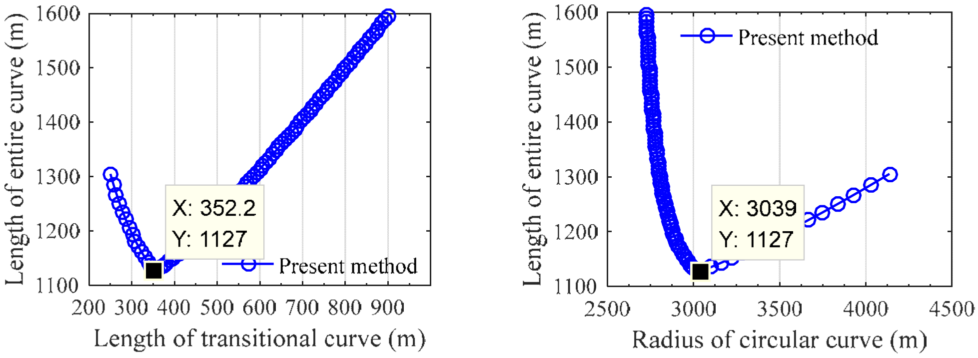

(a) L_t-L_{total} (b) R-L_{total}

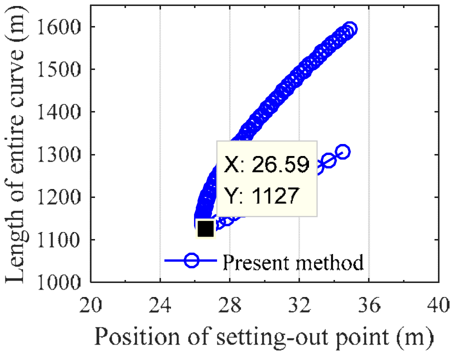

(c) $L_{P_l P_C} - L_{total}$

Figure 6.8 The optimal results based on the present method

Figure 6.8(a) shows that in the case of the given comfort level P_{CT0} of 9.14%, the minimum length of the entire curved track L_{total} is 1127 m, which is shorter than that of the actual curved track in the SML by 86 m and much shorter than the optimal solution offered by the Kufver's method (1531 m). The associated alignment parameters R and L_t are, respectively, 3039 m (see Figure 6.8(b)) and 352 m (see Figure 6.8(a)). The optimal cant and cant deficiency are, respectively, 12° and 1.41°.

In summary, the alignment parameters R, L_t, D, and C_d of the optimal solution offered by the proposed method are 3039 m, 352 m, 12° and 1.41° respectively, while these parameters in the actual curved track are 3300 m, 372 m, 12° and 0°. The comparison of these two sets of alignment parameters shows that the optimal solution is realized by duly reducing the radius of the circular track and the length of the transitional track but increasing the cant deficiency. In addition, to obtain the global minimum length of the entire curved track, the position of the setting-out point (P_C) is accordingly optimized and the distance $L_{P_I P_C}$ between the point P_I and P_C is 26.59 m (see Figure 6.8(c)), while it is 27.70 m in the actual curved track of the SML.

Moreover, by comparing Figure 6.8 with Figure 6.7, it can be also found that even in the case of the same comfort level of 9.14%, the length of the entire curved track L_{total} of the optimal solution (1127 m) from the proposed method is shorter than that of the Kufver's solution (1166 m).

6.4 Dynamic Model of a Coupled Maglev Train and Curved Viaduct System

As described in Section 6.2, both the current and new optimization methods are based on the assumption that the three intermediate quantities in the P_{CT} formula are predominated by the curved track-induced responses while the effect of the vehicle's motion-induced responses is simply considered by the introduction of a dynamic coefficient. Moreover, the effect of dynamic response of curved viaduct on the ride quality of the passengers is not considered. Therefore, a realistic dynamic model of a coupled maglev train-curved viaduct system should be numerically established and experimentally validated. The validated dynamic model can be then explicitly used to compute the responses of the train and viaduct subsystems to assess the accuracy of the optimal solution from the new optimization method.

6.4.1 Vehicle model

The vehicle model is established based on ones used in the Shanghai maglev train system and shown in Figure 6.9. Each vehicle component is modelled as rigid body, and their connections are simulated by spring-dashpot elements. Each car (vehicle) body is modelled by five DOFs, i.e. the lateral, vertical, rolling, pitching and yawing. Each bogie has six DOFs: the lateral, vertical, rolling of the front C-shaped frame, rolling of the rear C-shaped frame, pitching and yawing. Each rocker is assigned one DOF to indicate its rolling motion only and their other DOFs are the same as the DOFs of the bogie. Each levitation magnet is assigned with two DOFs for the vertical and pitching displacement. Similarly, each guidance magnet is also modeled by two DOFs for the lateral and yawing displacement. The total number of DOFs for each maglev vehicle is 101. The detailed modelling and parameters of the vehicle can be found in the Chapters 4 and 5.

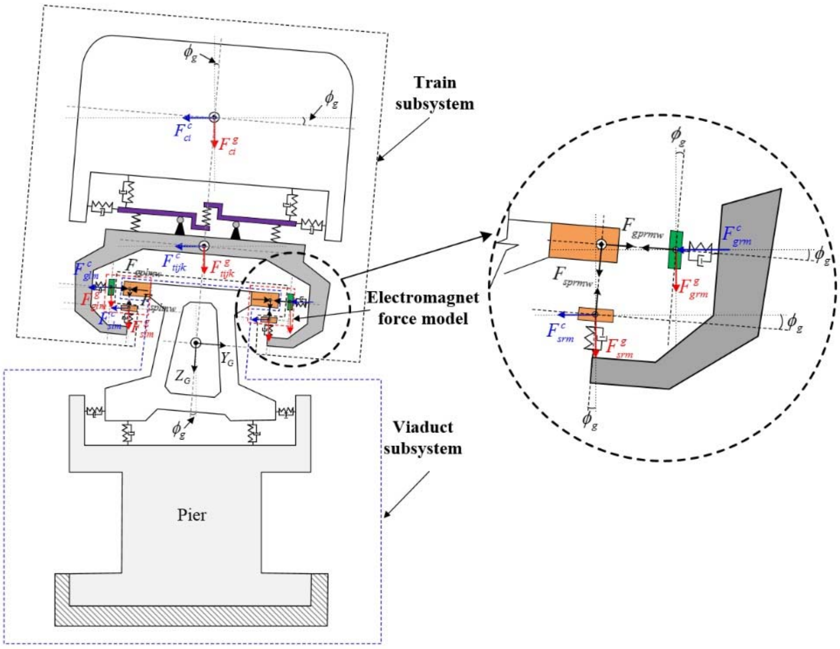

(a) Cross section of the model of the coupled maglev train and viaduct system

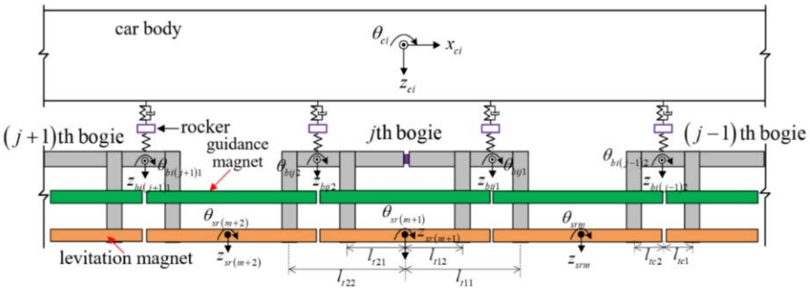

(b) Vertical plan of the train subsystem model

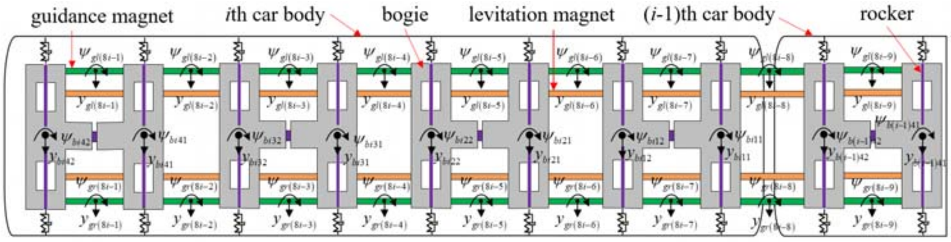

(c) Top plan of the train subsystem model

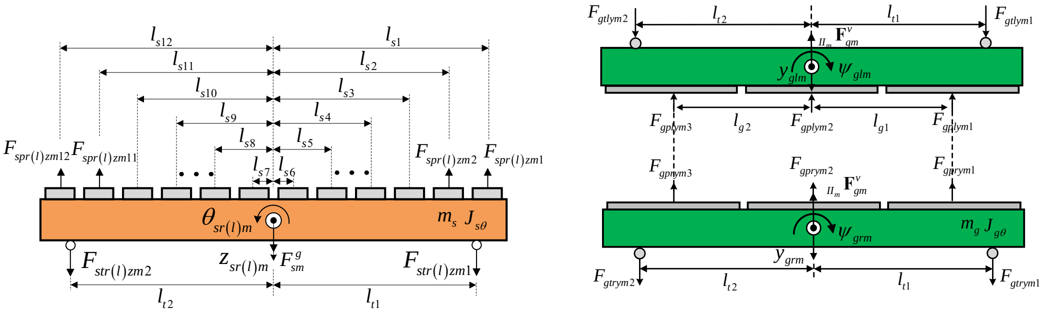

(d) Force diagram of the levitation magnet

(e) Force diagram of the guidance magnet

Figure 6.9 Schematic diagram of the maglev train subsystem

6.4.2 Curved viaduct model

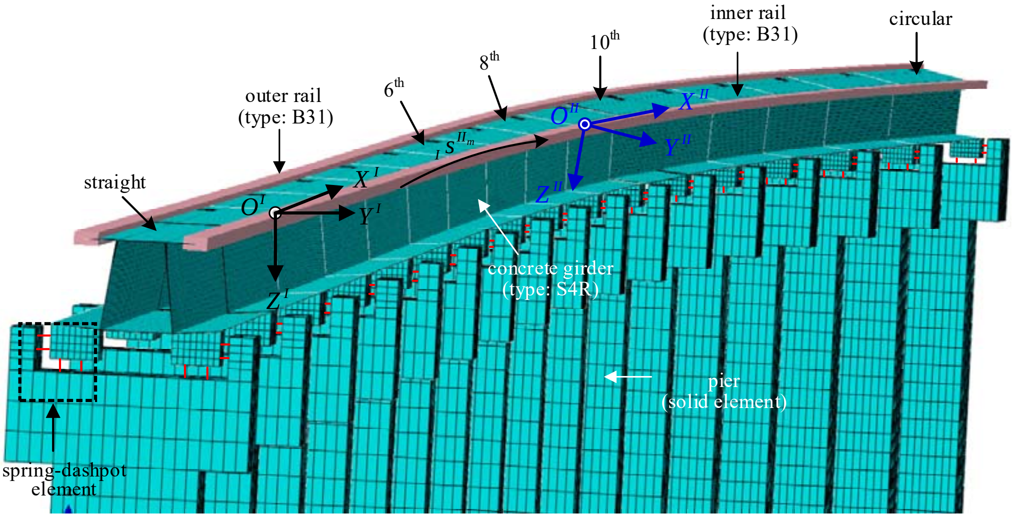

Figure 6.10 Finite element model of the curved viaduct subsystem

The curved viaduct model is established for the real curved viaduct used in the SML and shown in Figure 6.10. The rails are modeled by three dimensional 2-node linear beam elements, and the girders by 4-node shell elements. Each pier is modeled by 8-node solid elements. Six DOFs for each node of the above elements are considered, which include three translational DOFs and three rotational DOFs. The influence of pile foundation and soil on the pier is ignored and the bottom of the piers is assumed to be fixed (Malveiro et al., 2014; Su et al., 2010). The tie constraint is implemented to simulate the connections between the rails and girders. Besides, 4 linear spring-damper elements parameterized by the equivalent stiffness of the bearing are employed to represent the bearing connecting the girder to the single-column pier in both the vertical and lateral directions. More specifically, the stiffness of each spring-damper element in the vertical and lateral direction is assigned with 4×10^{10} N/m and 1.25×10^{10} N/m, respectively (Su et al., 2010). The damping coefficient of each spring-damper element in the vertical and lateral direction is assigned with 1.2×10^{5} N·sec/m and 6×10^{4} N·sec/m, respectively (Su et al., 2010). More information about the curved viaduct modelling can be referred to the Chapters 4 and 5.

6.4.3 Global equations of motion and solution method

A series of trajectory coordinate systems are employed to define the motion of the train subsystem moving on the curved track (Dimitrakopoulos & Zeng, 2015; Zeng et al., 2016; Zeng & Dimitrakopoulos, 2016). The equation of motion of each rigid body (car bodies, rockers, bogies, levitation magnets and guidance magnets) moving on the curved track is first established. Then, by combining the equation of motion of each rigid body, the equations of motion of all the vehicle components are assembled to form the equation of motion of the train subsystem as shown in the first equation in Eq. (6.17). The second equation in Eq. (6.17) is the equation of motion of the curved viaduct subsystem. The detailed procedure for the formation of Eq. (6.17) can be found in the Chapter 4 and Chapter 5, in which the equations of motion for the coupled maglev train-transitional viaduct system are expressed as

$$\begin{bmatrix} {}_{II}\mathbf{M}_V & \mathbf{0} \\ \mathbf{0} & {}_{I}\mathbf{M}_G \end{bmatrix}\begin{bmatrix} {}_{II}\ddot{\mathbf{U}}_V \\ {}_{I}\ddot{\mathbf{U}}_G \end{bmatrix}+\begin{bmatrix} {}_{II}\mathbf{C}_V & \mathbf{0} \\ \mathbf{0} & {}_{I}\mathbf{C}_G \end{bmatrix}\begin{bmatrix} {}_{II}\dot{\mathbf{U}}_V \\ {}_{I}\dot{\mathbf{U}}_G \end{bmatrix}+\begin{bmatrix} {}_{II}\mathbf{K}_V & \mathbf{0} \\ \mathbf{0} & {}_{I}\mathbf{K}_G \end{bmatrix}\begin{bmatrix} {}_{II}\mathbf{U}_V \\ {}_{I}\mathbf{U}_G \end{bmatrix}=\begin{bmatrix} {}_{II}\mathbf{F}_V^{e}+{}_{II}\mathbf{F}_V^{v}+{}_{II}\mathbf{F}_V^{G\to V} \\ {}_{I}\mathbf{F}_G^{e}+{}_{I}\mathbf{F}_G^{V\to G} \end{bmatrix} \quad (6.17)$$

where the vectors in the first equation are for the train subsystem, defined in the generalized trajectory coordinates (*II*); ${}_{II}\mathbf{M}_V$, ${}_{II}\mathbf{K}_V$ and ${}_{II}\mathbf{C}_V$ are the mass, stiffness and damping matrices, respectively, of the train subsystem; ${}_{II}\mathbf{U}_V$, ${}_{II}\dot{\mathbf{U}}_V$, and ${}_{II}\ddot{\mathbf{U}}_V$ are the displacement, velocity, and acceleration vectors, respectively, of the train subsystem; ${}_{II}\mathbf{F}_V^e$ is the external force vector, including the gravity forces, seismic loads or wind loads, acting on the train subsystem; and ${}_{II}\mathbf{F}_V^v$ is the inertial force vector, including the centrifugal force and Coriolis force, of the train subsystem. The vectors in the second equation are for the curved viaduct subsystem, defined in the global coordinates (*I*); ${}_{I}\mathbf{U}_G$, ${}_{I}\dot{\mathbf{U}}_G$ and ${}_{I}\ddot{\mathbf{U}}_G$ are the displacement, velocity and acceleration vectors of the viaduct subsystem; ${}_{I}\mathbf{F}_G^e$ is the external force vector, including the gravity force, seismic loads, and wind loads, acting on the viaduct subsystem. The interaction between the two subsystems is realized by the two force vectors ${}_{II}\mathbf{F}_V^{G\to V}$ and ${}_{I}\mathbf{F}_V^{V\to G}$. ${}_{II}\mathbf{F}_V^{G\to V}$ is the external resultant forces acting on all of the DOFs of the train subsystem. The nonzero entries of ${}_{II}\mathbf{F}_V^{G\to V}$ are associated with the levitation and guidance magnets only, and they are summed over the interactive electromagnet forces ${}_{II}\mathbf{F}\left(i_w^t,h_w^t\right)$ of each magnet. Meanwhile, the calculated electromagnet forces ${}_{II}\mathbf{F}\left(i_w^t,h_w^t\right)$ in the trajectory coordinate system are transformed to the global coordinate system by $\left({}_{I}\mathbf{R}^{II_m\to I}\right)^T {}_{II}\mathbf{F}\left(i_w^t,h_w^t\right)$ to form the nonzero entries in the vector ${}_{I}\mathbf{F}_V^{V\to G}$. More information about the formulation and solution method can be referred to the Chapter 5.

6.4.4 Validation of the dynamic model

To validate the accuracy of the dynamic model, an experimental study on the maglev train moving over the SML was conducted. The concerned viaduct subsystem in the SML is of a total length of 412.06 m (17×24.768 m), which includes one straight span for entrance, one circular curved span for departure, and 15 transitional spans (L_t =371.52 m) in the middle.

6.4.4.1 Comparison of vehicle responses

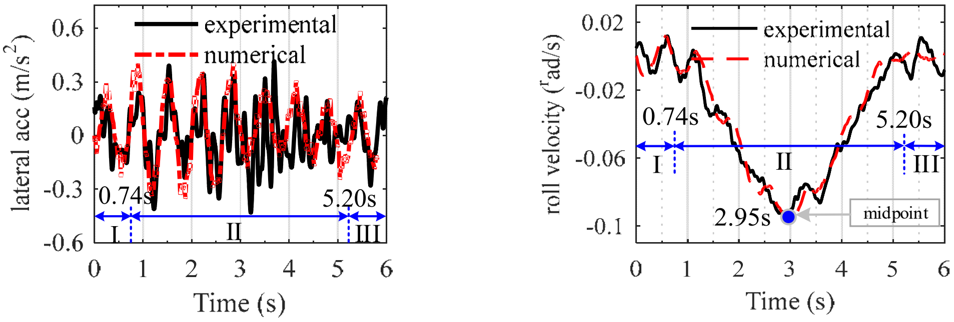

(a) lateral acceleration (b) roll velocity

Figure 6.11 Computed and measured dynamic responses of the 2ed vehicle in the maglev train of the SML.

Figure 6.11 shows the computed and measured lateral acceleration and roll velocity of the 2ed vehicle in the maglev train moving over the curved track. The comparison results show that the computed results well match with the measurement data. According to the location of the mass center of the 2ed vehicle moving on the curved track, the graphs in Figure 6.11 can be divided into three segments. The first segment refers to the period I (0~0.74s) when the mass center of the 2ed vehicle body is moving on the straight span. The second segment corresponds to the period II (0.74s~5.20s) when the 2nd vehicle body is moving on the transitional curved spans, while the 3rd segment conforms the period III, during which the 2nd vehicle body is moving on the circular curved span. Because the guidance forces generated by the vehicle moving over the transitional spans are slightly larger than those over the straight span and circular span, the lateral acceleration response of the vehicle in the period II is slightly larger than that in the period I and period III (see Figure 6.11a). However, the vehicle angular velocity of the vehicle in the period II is much larger than that of the vehicle in the period I and III. The reason is that the vehicle angular velocity is mainly induced by the rate of change of high difference (RHD) of the track. The maximum value of the vehicle angular velocity appears when the peak RHD occurs.

6.4.4.2 Comparison of one-second averages and intermediate quantities

The three one-second averages of the computed and measured lateral acceleration, lateral jerk, and roll velocity of the 2nd vehicle are calculated by using Eq. (6.5), and the intermediate quantities in the P_{CT} formula are also calculated as the maximum value of the three one-second averages. The comparative results are shown in Figure 6.12.

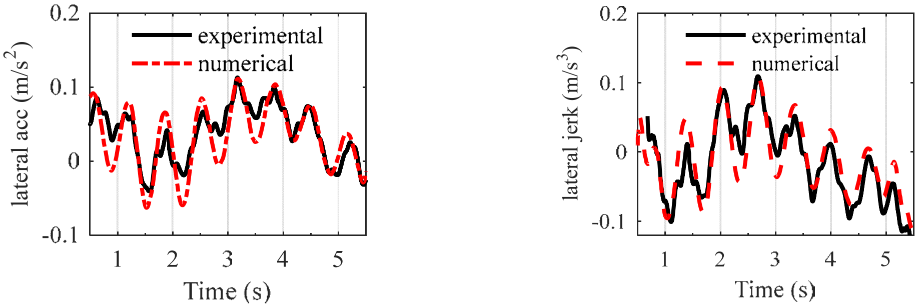

(a) lateral acceleration

(b) lateral jerk

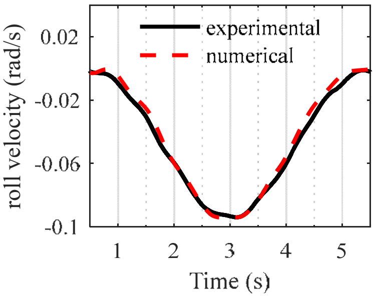

(c) roll velocity

Figure 6.12 One-second averages of the perceived responses within the 2^ed vehicle from the experimental and numerical studies.

First, by comparing Figure 6.12 with Figure 6.11, one may observe that through the low-pass filter and one-second window average, both the computed and measured responses are substantially smoothed. It can also be seen that the one-second averages of the numerical results can match the experimental ones, particularly for roll velocity. Moreover, the maximum values of the one-second averages, that is, intermediate quantities, of the computed and measured responses are almost the same, with the lateral acceleration around 0.111 m/s^2, the lateral jerk around 0.106 m/s^3, and the roll velocity around 0.097 rad/s. By substituting the computed and measured intermediate quantities into Eq. (6.4), the computed and measured P_{CT} values are equal to 9.29%, slightly higher than the value of 9.14% which is calculated based on the simplified method in Section 6.3.1. Besides, since the P_{CT1} is 0% and the P_{CT2} is 9.29%, it can be further concluded that the comfort level P_{CT} induced by the train moving on the curved track of the SML is controlled by P_{CT2}. That is, the comfort level is mainly controlled by the roll velocity of the vehicle.

In summary, the computed responses, intermediate quantities and P_{CT} value match the measurement results quite well. The proposed dynamic model can be used to predict and assess the comfort level of the vehicle moving over curved track and to further verify the accuracy of the optimal solution from the proposed optimization method.

6.5 Verification of Optimal Solution Based on Dynamic Model

As discussed in Section 6.3, the Kufver's optimization method does not take the minimum length of the entire curved track as the objective function. Therefore, the optimal solution from this method will not be further discussed in this subsection. Instead, the accuracy of the optimal solution offered by the proposed optimization method is verified based on the validated dynamic model. It is recalled that the alignment parameters R, L_t, D, and C_d of the real curved track concerned in the SML is 3300m, 372m, 12°, 0°, while the optimal solution from the proposed method yields 3039 m, 352 m, 12° and 1.41°, respectively. The total length of the real curved track concerned in the SML is 1213 m, while it is 1127 m as the optimal solution from the proposed method. Clearly, the optimal solution does give the minimum length to reduce the construction cost. Nevertheless, the optimal solution provided by the proposed method shall be validated using the dynamic model of the coupled maglev train-curved viaduct system because the proposed method involves some assumptions and simplifications. In this regard, by using the two sets of alignment parameters from the real SML and the optimal solution, the dynamic responses and comfort level of the maglev vehicle running on the curved viaduct are assessed in terms of the dynamic model established in Section 6.4.

6.5.1 Comparison of vehicle responses

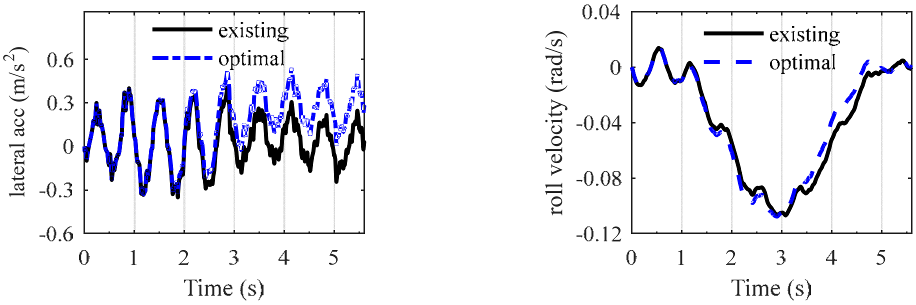

(a) lateral acceleration (b) roll velocity

Figure 6.13 Comparison of dynamic responses of the 2^{ed} vehicle

Figure 6.13 shows the comparison of the dynamic responses of the 2^{ed} vehicle, calculated using the validated dynamic model and the two sets of alignment parameters. It can be seen from Figure 6.13(a) that the maximum lateral acceleration (0.51 m/s^2) of the vehicle obtained using the optimal alignment parameters is larger than that (0.40 m/s^2) using the actual alignment parameters of the SML. This difference is mainly caused by the presence of a cant deficiency in the track because the lateral acceleration increases with the value of C_d (see Eq. (6.7a)). The comparison of the two sets of alignment parameters show that both R and L_t of the actual curved track (3300 m and 372 m) are decreased in the optimal solution of 3057 m and 352 m, respectively, but the cant deficiency C_d is increased from 0° of the actual curved track to 1.41° of the optimal solution. It is noted from Eq. (6.7c) that the maximum rolling velocity is respectively of inverse proportion to the three alignment parameters, namely, R, L_t, and C_d. As a result, due to the coordination of the three parameters, the maximum of roll velocity remains almost unchanged, if comparing 0.102 rad/s with 0.103 rad/s, as shown in Figure 6.13(b).

6.5.2 Comparison of one-second averages and intermediate quantities

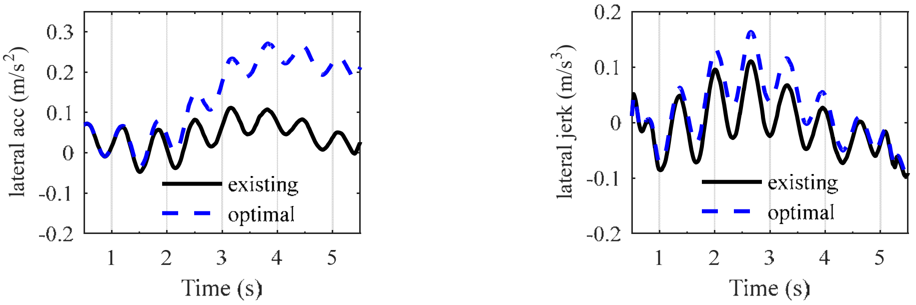

(a) lateral acceleration (b) lateral jerk

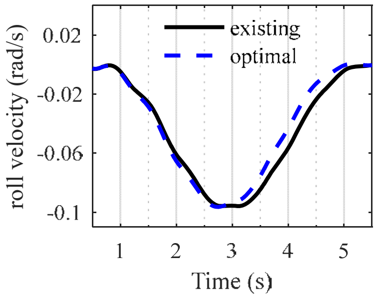

(c) roll velocity

Figure 6.14 Comparison of one-second averages of the 2ed vehicle.

The three one-second averages are also calculated by using Eq. (6.5) and the computed responses shown in Figure 6.13. By comparing Figure 6.13 with Figure 6.14, it can be observed that through the low-pass filter and one-second window average, the one-second averaged responses are substantially smoothed. However, the differences in the one-second averaged lateral acceleration and lateral jerk between the two cases appear to be enlarged (see Figure 6.14a and Figure 6.14b). The maximum value of the one-second average of the lateral acceleration from the optimal solution is 0.271 m/s^2, which is considerably larger than 0.111 m/s^2 from the actual curved track. Besides, the intermediate quantity of the lateral jerk from the optimal solution is 0.168 m/s^3, which is also higher than that of the existing one (0.106 m/s^3). However, by comparing Figure 6.14c with Figure 6.13b, one may observe that the change of roll velocity from the computed responses to the intermediate quantities is moderate, and only the relatively high-frequency vibration is smoothed and the low-frequency vibration remains unchanged. As a result, the intermediate quantities of roll velocity of the two cases are almost the same, 0.968 rad/s against 0.966 rad/s.

6.5.3 Comparison with the proposed optimization method

By substituting the two sets of the alignment parameters of the existing track and the optimal solution into Equation (6.7) and Equation (6.4), the intermediate quantities and the P_{CT} values can be calculated, and the results are shown in Table 6.2. Besides, the intermediate quantities calculated based on the dynamic analysis model (see Section 6.5.2) as well as the P_{CT} values are also summarized in Table 6.2.

Table 6.2 Comparison of the intermediate quantities and P_{CT} values calculated based on the proposed optimization method and the dynamic analysis model.

Intermediate quantity	Existing solution 3300 m-372 m-12°-0°		Optimal solution 3039 m-352m-12°-1.41°	
	Proposed method	Dynamic model	Proposed method	Dynamic model
$\lvert\ddot{y}_{1s}\rvert_{\max}$ (m/s^2)	0.062	0.111	0.289	0.271
$\lvert\dddot{y}_{1s}\rvert_{\max}$ (m/s^3)	0.028	0.106	0.138	0.168
$\lvert\dot{\varphi}_{1s}\rvert_{\max}$ (rad/s)	0.0964	0.0968	0.0963	0.0966
P_{CT1} (-)	0.00%	0.00%	0.03%	0.11%
P_{CT2} (-)	9.14%	9.24%	9.11%	9.19%
P_{CT} (-)	9.14%	9.24%	9.14%	9.30%

It can be seen from Table 6.2 that the calculated intermediate quantities based on the dynamic analysis model are generally larger than those based on the proposed optimization method so that the P_{CT} values based on the dynamic model are also relatively higher than those from the proposed optimization method. If having a closer look, it can be observed that the roll velocities predicted by the proposed optimization method can well match those calculated based on the dynamic model. As a result, the related values P_{CT2} are also very close. Because this case study is dominated by the roll velocity and the value P_{CT2}, the total values P_{CT} from the optimization method and the dynamic model are similar. It is also noted that due to the decrease of the parameters R, L_t and D and the increase of C_d, relatively larger lateral acceleration and lateral jerk are produced by using the optimal parameters compared with those using the parameters of the existing track. Nevertheless, the values P_{CT1} remain zero or very small, so that there is a little effect on the total values P_{CT}. Nonetheless, the length of the entire curved track is considerably shortened by using the optimal solution.

In summary, the accuracy of the optimal solution from the proposed optimization method is validated through the comparison with the results from the dynamic model. Under the same comfort level P_{CT} offered, the optimal solution is superior to the existing one by offering a shorter length of the entire curved track.

6.6 Optimal Solution via Vehicle Speed

The optimal solution for the alignment of horizontally curved track in a high-speed maglev line depends on design vehicle speed. The optimal solutions corresponding to different vehicle speeds are therefore computed and listed in Table 6.3, in which the comfort level of passengers is set by the same value of 9.14% and the intersection angle of two straight tracks remains constant of 0.255 rad.

Table 6.3 The optimal solutions for different vehicle speeds

v (km/h)	R/m	L_t/m	v^2/R	v/L_t	D/°	C_d/°	L_{total}/m	P_{CT}
200	1345	236	29.74	0.847	12	1.415	579	9.14%
250	2100	296	29.76	0.844	12	1.424	832	9.14%
300	3039	352	29.62	0.852	12	1.413	1127	9.14%
350	4117	414	29.75	0.845	12	1.424	1464	9.14%
400	5380	472	29.74	0.847	12	1.416	1844	9.14%
450	6805	530	29.76	0.849	12	1.424	2268	9.14%
500	8405	592	29.74	0.845	12	1.418	2734	9.14%

The results from Table 6.3 show that with the increase of vehicle speed, the radius of the circular track, R, the arc length of the entire transitional track, L_t, and the total length of the entire curved track, L_{total}, all increase. It is noted from the fourth and fifth columns of Table 6.3 that no matter what vehicle speed (v) is, the value of v^2/R and the value of v/L_t only slightly vary around a constant value of 29.74 and 0.85, respectively. Therefore, the optimal radius of the circular track (R) is linearly proportional to the square of the vehicle speed (v), while the optimal transitional length (L_t) is linearly proportional to the vehicle speed (v). As a result, the increasing rate of the optimal radius of the circular track is much higher than that of the optimal transitional length and higher than the total length of the entire curved track. Moreover, since the optimal cant deficiency (C_d) is determined by the value of v/L_t (see Equation (6.14)), the optimal cant deficiencies (C_d) also varies slightly around a constant value of 1.42°, as shown in the seventh column of Table 6.3. The constant cant deficiencies can ensure that the intermediate quantities of lateral acceleration and lateral jerk (see Equations (6.7a) and (6.7b)) remain constant so that P_{CT1} and its impact on the comfort level P_{CT} is almost zero. The optimal cants (D) also remain at the upper limit of the cant (12°).

6.7 Summary

A new optimization method has been proposed in this study for the alignment design of horizontally curved track in a high-speed maglev line. The optimal solution from the proposed method has been compared with the optimal solution from the current (Kufver's) method and the existing solution for the actual curved track in the SML. To validate the accuracy of the optimal solution from the proposed method, the dynamic model of a coupled maglev train and curved viaduct system has been numerically established and experimentally validated. The validated dynamic model has been then explicitly used to compute the responses of the train and viaduct subsystems to assess the accuracy of the optimal solution. Main conclusions from this study can be drawn as follows:

(1) Due to different objective functions considered in the proposed method and the Kufver's method, different optimization results are achieved. The optimal solution from the proposed method provides the minimum length of the entire curved track with a satisfaction of comfort level, while the Kufver's optimal solution offers the best comfort level without considering the minimum length of curved track.

(2) Nevertheless, under the same comfort level, the optimal solution from the proposed method can offer a shorter length of the curved track than the Kufver's method and the existing solution in the SML. This is realized by the optimal solution from the

proposed method through the duly reduction of the radius and the length of the transitional track but the increase of the cant deficiency.

(3) Since the computed responses, intermediate quantities, and P_{CT} valued match the measurement results quite well, the proposed dynamic model can be used to predict and assess the comfort level of the vehicle moving over the curved track and to further verify the accuracy of the optimal solution from the proposed optimization method.

(4) The intermediate quantity of roll velocity predicted by the proposed optimization method can well match that calculated based on the dynamic model so that the value P_{CT2} and the value P_{CT} from the dynamic model are very close to those from the proposed optimization method.

(5) Because of the reduction of R, L_t, and D and the increase of C_d, relatively larger intermediate quantities of lateral acceleration and lateral jerk are produced by using the optimal solution compared with the existing one. Nevertheless, the value of P_{CT1} still remains zero or a very small value so that there is a little effect on the total value P_{CT}.

(6) With the increase of the vehicle speed, both the radius of the circular track and the length of the transitional track increase. However, the cant remains constant at its upper limit value and the cant deficiency varies slightly around a constant value.

In summary, the accuracy of the optimal solution from the proposed optimization method is validated through the comparison with the results from the dynamic model. The optimal solution provided by this study can be used for the initial alignment design of horizontally curved track in a high-speed maglev line.

CHAPTER 7

CONCLUSIONS AND RECOMMENDATIONS

7.1 Conclusions

This thesis focuses on accurate dynamic analysis and alignment design of high-speed maglev trains that run on straight, circular, and transitional viaducts. The originality of this study is attributed to the following: (1) the establishment of a realistic high-speed maglev train-viaduct interaction model with detailed simulation of the magnets in the train and modular function units in the viaduct; (2) the development of a trajectory coordinate-based framework for the analysis of the high-speed maglev train running on the circular curved track; (3) the extension of the trajectory coordinate-based analysis approach to the analysis of the maglev train running on a transitional curved viaduct; (4) the conduction of the measurements on the SML to validate the proposed model; and (5) the development of a minimum length-based optimization method for the alignment design of a horizontally curved track in a high-speed maglev line. The major contributions and conclusions of this thesis can be summarized as follows.

1. A realistic and detailed high-speed maglev train-viaduct interaction model is proposed in this thesis. The proper modeling with detailed simulation of the magnets and modular function units of viaducts can duly account for the dynamic interaction between the train and viaduct systems. The computed acceleration and displacement time histories of the girder at its midspan agree with the measured acceleration and displacement time histories. The characteristic frequencies identified from the simulation result are consistent with those from the measured ones. The identified characteristic frequencies and spectral analyses manifest that the appropriate modeling of the levitation magnets and the pole pitch is important because they are two key contributors to the dynamic response of the viaduct subsystem. Given the flexibility of elastic bearings and high column piers introduced in the proposed coupled train-viaduct system, the vertical displacement response of the girder increases, whereas the vertical acceleration response of the girder decreases. The effect of flexibility of the pier on the girder response is relatively weaker, and more contributions are induced by

the flexibilities of elastic bearings. The proper modeling of the rails and bracket supports is also important, which not only influences the response of the rails and magnets but also affects the riding comfort of the train, particularly in the roll acceleration.

2. An interaction model of the high-speed maglev train and circular curved viaduct is developed by introducing the trajectory coordinate systems. By applying the proposed framework to the SML, the dynamic behaviors of the maglev train are experimentally and numerically investigated with good agreement. The responses of the maglev train moving over curved viaducts of balanced radii and cant angles are almost identical to those of straight viaducts. In addition, cant deficiency is quite significant for the curved viaduct where the increase of deficient cant angle causes a sharp increase in the responses of the radial and rotational directions. For the maglev train moving with an initial equilibrium state, track irregularities are the main excitations for the vehicle responses in the radial and rotational directions but not for the vertical. Moreover, a sufficiently long spiral entry is a must for the maglev train to move from the straight to the circular curved track. Otherwise, issues, such as ride comfort and operational safety of the vehicle, will become extremely serious.

3. A framework for accurate dynamic analysis of high-speed maglev trains running over transitional curved viaducts is presented in this thesis. By applying this framework to the SML, the dynamic characteristics and responses of the maglev vehicles and the transitional curved viaduct are investigated. When the vehicle runs on a transitional curved track, the levitation forces applied on the outer rail keep pace with the RHD, and the maximum levitation force occurs at the location of the maximum RHD. The rolling displacement and velocity of the vehicle are highly related to the HD and RHD of the track because the air gap between the magnet of the vehicle and the rail of the viaduct is controlled to approach an ideal value. The maximum value of the vehicle angular velocity appears when the peak RHD occurs. Moreover, the differences in the vertical displacement responses of the outer and inner rails occur, and the maximum value of such difference appears at the middle section of the transitional track. A similar phenomenon occurs in the rotational displacement response of the viaduct. Moreover, the parametric studies show that the length of

transitional viaduct significantly affects all types of vehicle responses. A short transitional length indicates a high vehicle response. The transitional length also affects the lateral and rotational responses of the viaduct, whereas its effect on the vertical response is moderate. The increase of deficient cant angle causes a sharp increase in the responses of the transitional curved viaduct in the radial and rotational directions. In addition, the cant deficiency considerably affects the angular velocity response of the vehicle moving on the transitional curved viaduct.

4. A new optimization method is proposed in this study for the alignment design of horizontally curved track in a high-speed maglev line. A comparison of with the solution of Kufver's method and the existing solution in the SML shows that the optimal solution from the proposed method provides the minimum length of the entire curved track with a satisfaction of comfort level. This result is realized by the optimal solution from the proposed method through the proper reduction of the radius and the length of the transitional track but the increase in cant deficiency. By using the proposed coupled high-speed maglev train and curved viaduct system, the intermediate quantity of roll velocity predicated by the proposed optimization method can well match the value calculated based on the dynamic model, such that the P_{CT2} and P_{CT} values from the dynamic model are extremely close to those from the proposed optimization method. However, because of the reduction of R and L_t and the increase of C_d, relatively larger intermediate quantities of lateral acceleration and lateral jerk are produced by using the optimal solution compared with the existing one. Nevertheless, the value of P_{CT1} remains zero or an extremely small value, such that it has minimal effect on the total value P_{CT}. With the increase of the vehicle speed, both the radius of the circular track and the length of the transitional track increase. However, the cant remains constant at its upper limit value and the cant deficiency varies slightly around a constant value. In summary, the accuracy of the optimal solution from the proposed optimization method is validated through the comparison with the results from the dynamic model. The optimal solution provided by this study can be used for the initial alignment design of a horizontally curved track in a high-speed maglev line.

7.2 Recommendations for Future Studies

Although progress has been made in these studies in the development of the high-speed train that moves on the straight, circular, and transitional viaducts, several important issues require further investigations.

1. An experimental study was conducted on a train running on the SML to validate the proposed framework and computed results. Only simple measurements on the vehicle response were conducted because the operation of the high-speed maglev train must not be interrupted. For throughout validation, additional comprehensive field measurements (e.g., measurements on vehicle responses at different locations of the carriage and experimental investigation of viaduct response at the circular transitional curved track sections) shall be conducted in the future. The full-scale measurements for the evaluation of the discomfort level with the high-speed maglev train moving on the transitional curved track shall also be conducted.

2. The Chuo Shinkansen Line with the design speed of 500 km/h has been under construction since 2014. The maglev train system with a design speed of 600 km/h has also been in the research and development in China, and its test operation is expected by 2020. Additional maglev lines with higher operating speeds will be constructed in the future. Accordingly, some new dynamic characteristics of vehicles and viaducts may be induced, such as high-frequency vibration and noise, resonance phenomenon, stability of train-viaduct interaction, and derailment. The further studies on even higher speed maglev trains running on slender viaducts are required.

3. Serious issues of curving ride quality of the train may be enhanced by the increase of train speeds, which will also affect the safety performance of the viaducts. As a result, the dynamic analysis and alignment design of a horizontally curved track subjected to the maglev train operating at a high speed shall be conducted in the future. The effectiveness and applibility of the sinusoidal-formed transitional curve should be examined, and the curves with high smoothness order must be explored.

4. With increased train speed, the effectiveness and applicability of the proposed

electromagnet force-air gap model with a PD controller shall be further examined or validated through experimental studies. The control algorithms used in previous studies [e.g., proportional-integral (PI), proportional-integral-derivative (PID), and linear-quadratic regulator (LQR)] must be further examined to serve the interaction modeling between the high-speed maglev train and viaduct stably and efficiently.

5. The moving speed of the train along the entire track (straight + transitional + circular track) is assumed constant in the case studies of this thesis. In practice, the acceleration and deceleration of the maglev train speed can reach an extremely high value of 1.5 m/s^2. Thus, the dynamic interaction effect between the vehicle and viaduct in the longitudinal direction (moving direction of the train), which is induced by the acceleration and deceleration of train speed, is considerable and shall be discussed in the future.

6. Moreover, when the train is moving on a transitional curved track, train speed reduction is often used to counteract the decrease in curve radius-induced centrifugal forces acting on the vehicle. Accordingly, the dynamic issues of the ride quality of the train and dynamic performance of the viaduct in the longitudinal direction (moving direction of the train) induced by the train braking deceleration will be encountered and shall be examined in the future.

7. To simply establish the train-viaduct interaction model, the behaviors of the coupled system are assumed to be linear-elastic. In practice, the train and viaduct systems are sizable and complicated. Furthermore, when the train is moving on the transitional curved track, some structural nonlinearity may occur in the train and viaduct system due to the rapid increase of the levitation forces between the magnets and outer rail. Such structural nonlinearity shall be considered further.

APPENDIX A

THE DETAILED EXPRESSIONS OF ELEMENT MATRICES IN EQUATION (3.5).

The sub-stiffness matrix of the car body of the i^{th} vehicle is

$$\mathbf{K}_{cci} = \begin{bmatrix} 16k_{cty} & 0 & -16k_{cty}v_c & 0 & 0 \\ 0 & 16k_{ctz} & 0 & 0 & 0 \\ -16k_{cty}v_c & 0 & 16k_{cty}v_c^2 + 16k_{ctz}h_c^2 & 0 & 0 \\ 0 & 0 & 0 & 2k_{ctz}\sum_{j=1}^{4}\sum_{k=1}^{2} l_{cjk}^2 & 0 \\ 0 & 0 & 0 & 0 & 2k_{cty}\sum_{j=1}^{4}\sum_{k=1}^{2} l_{cjk}^2 \end{bmatrix}_{5\times5} \tag{A.1}$$

The sub-stiffness matrix of the rockers of the i^{th} vehicle is

$$\mathbf{K}_{tti} = \operatorname{diag}\begin{bmatrix} \mathbf{K}_{tti11} & \mathbf{K}_{tti21} & \cdots & \mathbf{K}_{ttijk} & \cdots & \mathbf{K}_{tti41} & \mathbf{K}_{tti42} \end{bmatrix} \tag{A.2a}$$

where the submatrix of each element in Equation (A.2a) is

$$\mathbf{K}_{ttijk} = \begin{bmatrix} k_{az}h_{tr2}^2 + k_{ctz}h_{tr1}^2 + k_{ttz}h_{tr3}^2 & k_{ttz}h_{tr3}^2 \\ k_{ttz}h_{tl3}^2 & k_{arz}h_{tl2}^2 + k_{ctz}h_{tl1}^2 + k_{ttz}h_{tl3}^2 \end{bmatrix}_{2\times2} \tag{A.2b}$$

The sub-stiffness matrix of the bogies of the i^{th} vehicle is

$$\mathbf{K}_{bbi} = \operatorname{diag}\begin{bmatrix} \mathbf{K}_{bbi1} & \mathbf{K}_{bbi2} & \mathbf{K}_{bbi3} & \mathbf{K}_{bbi4} \end{bmatrix} \tag{A.3a}$$

where the submatrix of each element in Equation (A.3a) is

$$\mathbf{K}_{bbij} = \begin{bmatrix} 4k_{cty} + 8(6)k_{bgy} & & & & & \text{sym} \\ 0 & 4k_{ctz} + 8(6)k_{bsz} & & & & \\ 2k_{cty}v_{b1} - 4(2)k_{bgy}v_{b2} & 0 & K_{bb\phi1ij} & & & \\ 2k_{cty}v_{b1} - 4(2)k_{bgy}v_{b2} & 0 & -k_{bbij} & K_{bb\phi2ij} & & \\ 0 & (-2k_{bsz}l_{b22}) & 0 & 0 & K_{bb\theta ij} & \\ 0 & 0 & K_{bb\phi1\psi ij} & K_{bb\phi2\psi ij} & 0 & K_{bb\psi ij} \end{bmatrix}_{6\times6} \tag{A.3b}$$

in which the elements $K_{bb\phi 1ij}$, $K_{bb\phi 2ij}$, $K_{bb\theta ij}$, $K_{bb\psi ij}$, $K_{bb\phi 1\psi ij}$,and $K_{bb\phi 2\psi ij}$ in Equation (A.3b) are expressed as follows:

$$K_{bb\phi 1ij} = 2k_{ctz}h_{tl1}^2 + 4(2)k_{bsz}h_{bl3}^2 + 2k_{cty}v_{b1}^2 + 4(2)k_{bgy}v_{b2}^2 + k_{bb} \tag{A.3c}$$

$$K_{bb\phi 2ij} = 2k_{ctz}h_{tl1}^2 + 4(2)k_{bsz}h_{bl3}^2 + 2k_{cty}v_{b1}^2 + 4(2)k_{bgy}v_{b2}^2 + k_{bb} \tag{A.3d}$$

$$K_{bb\theta ij} = 4k_{ctz}l_{tl1}^2 + 2k_{bsz}\sum_{k=1}^{2}\sum_{n=1(2)}^{2(1)} l_{bkn}^2 \tag{A.3e}$$

$$K_{bb\psi ij} = 4k_{cty}l_{tl1}^2 + 2k_{bgy}\sum_{k=1}^{2}\sum_{n=1(2)}^{2(1)} l_{bkn}^2 \tag{A.3f}$$

$$K_{bb\phi 1\psi ij} = 2k_{cty}l_{t1}v_{b1} - 2k_{bgy}v_{b2}\sum_{n=1(2)}^{2} l_{b1n} \tag{A.3g}$$

$$K_{bb\phi 2\psi ij} = 2k_{cty}l_{t2}v_{b1} - 2k_{bgy}v_{b2}\sum_{n=1}^{2(1)} l_{b2n} \tag{A.3h}$$

The sub-stiffness matrix of the mth levitation magnet to the vehicle is

$$\mathbf{K}_{ssm} = \mathrm{diag}\begin{bmatrix} 2k_{bsz} & 2k_{bsz}l_{b1}^2 & 2k_{bsz} & 2k_{bsz}l_{b1}^2 \end{bmatrix} \tag{A.4}$$

The sub-stiffness matrix of the mth guidance magnet to the vehicle is

$$\mathbf{K}_{ggm} = \mathrm{diag}\begin{bmatrix} 2k_{bgy} & 2k_{bgy}l_{b1}^2 & 2k_{bgy} & 2k_{bgy}l_{b1}^2 \end{bmatrix} \tag{A.5}$$

The sub-stiffness matrix between the car body and 16 sets of rockers of the ith vehicle is

$$\mathbf{K}_{cti} = \mathbf{K}_{tci}{}^{\mathrm{T}} = \begin{bmatrix} 0 & 0 & \cdots & 0 & 0 \\ -k_{ctz}h_{tl1} & -k_{ctz}h_{tr1} & \cdots & -k_{ctz}h_{tl1} & -k_{ctz}h_{tr1} \\ -k_{ctz}h_{tl1}h_{cl} & -k_{ctz}h_{tr1}h_{cr} & \cdots & -k_{ctz}h_{tl1}h_{cl} & -k_{ctz}h_{tr1}h_{cr} \\ k_{ctz}h_{tl1}l_{c11} & k_{ctz}h_{tr1}l_{c11} & \cdots & k_{ctz}h_{tl1}l_{c42} & k_{ctz}h_{tr1}l_{c42} \\ 0 & 0 & \cdots & 0 & 0 \end{bmatrix}_{5\times 16} \tag{A.6}$$

The sub-stiffness matrix generated between the car body and 4 bogies of the ith vehicle is

$$\mathbf{K}_{cbi} = \begin{bmatrix} \mathbf{K}_{cbi1} & \mathbf{K}_{cbi2} & \mathbf{K}_{cbi3} & \mathbf{K}_{cbi4} \end{bmatrix} \tag{A.7a}$$

where the submatrix of each element in Equation (A.7a) is

$$\mathbf{K}_{cbij} = \begin{bmatrix} -4k_{cty} & 0 & -2k_{cty}v_{b1} & -2k_{cty}v_{b1} & 0 & 0 \\ 0 & -4k_{ctz} & 0 & 0 & 0 & 0 \\ 4k_{cty}v_c & 0 & 2h_{tl1}h_{cl}k_{ctz} + 2k_{cty}v_c v_{b1} & 2h_{tl1}h_{cl}k_{ctz} + 2k_{cty}v_c v_{b1} & 0 & 0 \\ 0 & 2k_{ctz}\sum_{k=1}^{2} l_{cjk} & 0 & 0 & -2k_{ctz}\sum_{k=1}^{2} l_{cjk}l_{tk} & 0 \\ -2k_{cty}\sum_{k=1}^{2} l_{cjk} & 0 & -2k_{cty}l_{cj1}v_{b1} & -2k_{cty}v_{b1}l_{cj2} & 0 & -2k_{cty}\sum_{k=1}^{2} l_{cjk}l_{tk} \end{bmatrix} \tag{A.7b}$$

The sub-stiffness matrix generated between the bogies and rockers of the i^{th} vehicle is

$$\mathbf{K}_{bti} = \mathbf{diag}\begin{bmatrix} \mathbf{K}_{bti1} & \mathbf{K}_{bti2} & \mathbf{K}_{bti3} & \mathbf{K}_{bti4} \end{bmatrix} \tag{A.8a}$$

where the submatrix of each element in Equation (A.8a) is

$$\mathbf{K}_{tbij} = \mathbf{K}_{btij}{}^{\mathrm{T}} = \begin{bmatrix} 0 & h_{tl1}k_{ctz} & h_{tl1}^2 k_{ctz} & 0 & -h_{tl1}l_{t1}k_{ctz} & 0 \\ 0 & h_{tr1}k_{ctz} & h_{tr1}^2 k_{ctz} & 0 & -h_{tr1}l_{t1}k_{ctz} & 0 \\ 0 & h_{tl1}k_{ctz} & 0 & h_{tl1}^2 k_{ctz} & -h_{tl1}l_{t2}k_{ctz} & 0 \\ 0 & h_{tr1}k_{ctz} & 0 & h_{tr1}^2 k_{ctz} & -h_{tr1}l_{t2}k_{ctz} & 0 \end{bmatrix}_{4\times 6} \tag{A.8b}$$

The sub-stiffness matrix generated between the bogie and electromagnets is

$$\mathbf{K}_{(sb,gb)i} = \begin{bmatrix} \mathbf{K}_{(sb,gb)i1} & \mathbf{K}_{(sb,gb)i2} & \mathbf{K}_{(sb,gb)i3} & \mathbf{K}_{(sb,gb)i4} \end{bmatrix} \tag{A.9a}$$

In the case of $m \notin [m_0, m_0 + 2]$, where $m_0 = 8(i-1) + 2(j-1)$, the elements of $\mathbf{K}_{(sb,gb)im}$ will be **0**. Otherwise, it will be determined by the following equations:

$$\mathbf{K}_{(sb,gb)ij} = \begin{bmatrix} \mathbf{0} & \mathbf{K}_{(sb,gb)ijm_0} & \mathbf{K}_{(sb,gb)ij(m_0+1)} & \mathbf{K}_{(sb,gb)ij(m_0+2)} & \mathbf{0} \end{bmatrix}^{\mathbf{T}} \tag{A.9b}$$

where $\mathbf{K}_{(sb,gb)ijm_0}$, $\mathbf{K}_{(sb,gb)ij(m_0+1)}$ and $\mathbf{K}_{(sb,gb)ij(m_0+2)}$ are the nonzero matrix, calculated by

$$\mathbf{K}_{sbijm_0} = \begin{bmatrix} 0 & -k_{bsz} & -h_{bl1}k_{bsz} & 0 & l_{b11}k_{bsz} & 0 \\ 0 & l_{b2}k_{bsz} & h_{bl1}l_{b2}k_{bsz} & 0 & l_{b11}l_{b1}k_{bsz} & 0 \\ 0 & -k_{bsz} & -h_{br1}k_{bsz} & 0 & l_{b11}k_{bsz} & 0 \\ 0 & l_{b2}k_{bsz} & h_{br1}l_{b2}k_{bsz} & 0 & -l_{b11}l_{b2}k_{bsz} & 0 \end{bmatrix}_{4\times 6} \tag{A.9c}$$

$$\mathbf{K}_{sbij(m_0+1)} = \begin{bmatrix} 0 & -2k_{bsz} & -h_{bl1}k_{bsz} & -h_{bl1}k_{bsz} & 0 & 0 \\ 0 & 0 & h_{bl1}l_{b1}k_{bsz} & h_{bl1}l_{b2}k_{bsz} & -2l_{b1}{}^{2}k_{bsz} & 0 \\ 0 & -2k_{bsz} & -h_{br1}k_{bsz} & -h_{br1}k_{bsz} & 0 & 0 \\ 0 & 0 & h_{br1}l_{b1}k_{bsz} & h_{br1}l_{b2}k_{bsz} & -2l_{b1}{}^{2}k_{bsz} & 0 \end{bmatrix}_{4\times6} \tag{A.9d}$$

$$\mathbf{K}_{sbij(m_0+2)} = \begin{bmatrix} 0 & -k_{bsz} & 0 & -h_{bl1}k_{bsz} & l_{b22}k_{bsz} & 0 \\ 0 & l_{b1}k_{bsz} & 0 & h_{bl1}l_{b1}k_{bsz} & -l_{b22}l_{b1}k_{bsz} & 0 \\ 0 & -k_{bsz} & 0 & -h_{br1}k_{bsz} & l_{b22}k_{bsz} & 0 \\ 0 & l_{b1}k_{bsz} & 0 & h_{br1}l_{b1}k_{bsz} & -l_{b22}l_{b1}k_{bsz} & 0 \end{bmatrix}_{4\times6} \tag{A.9f}$$

$$\mathbf{K}_{gbijm_0} = \begin{bmatrix} -k_{bgy} & 0 & v_{b2}k_{bgy} & 0 & 0 & -l_{b11}k_{bgy} \\ -l_{b2}k_{bgy} & 0 & l_{b2}v_{b2}k_{bgy} & 0 & 0 & -l_{b2}l_{b11}k_{bgy} \\ -k_{bgy} & 0 & v_{b2}k_{bgy} & 0 & 0 & -l_{b11}k_{bgy} \\ -l_{b2}k_{bgy} & 0 & l_{b2}v_{b2}k_{bgy} & 0 & 0 & -l_{b2}l_{b11}k_{bgy} \end{bmatrix}_{4\times6} \tag{A.9g}$$

$$\mathbf{K}_{gbij(m_0+1)} = \begin{bmatrix} -2k_{bgy} & 0 & v_{b2}k_{bgy} & v_{b2}k_{bgy} & 0 & 0 \\ 0 & 0 & l_{b1}v_{b2}k_{bgy} & l_{b2}v_{b2}k_{bgy} & 0 & -2l_{b1}{}^{2}k_{bgy} \\ -2k_{bgy} & 0 & v_{b2}k_{bgy} & v_{b2}k_{bgy} & 0 & 0 \\ 0 & 0 & l_{b1}v_{b2}k_{bgy} & l_{b2}v_{b2}k_{bgy} & 0 & -2l_{b1}{}^{2}k_{bgy} \end{bmatrix}_{4\times6} \tag{A.9h}$$

$$\mathbf{K}_{gtij(m_0+2)} = \begin{bmatrix} -k_{tgy} & 0 & 0 & v_{t2}k_{tgy} & 0 & -l_{t22}k_{tgy} \\ -l_{t1}k_{tgy} & 0 & 0 & l_{t1}v_{t2}k_{tgy} & 0 & -l_{t1}l_{t22}k_{tgy} \\ -k_{tgy} & 0 & 0 & v_{t2}k_{tgy} & 0 & -l_{t22}k_{tgy} \\ -l_{t1}k_{tgy} & 0 & 0 & l_{t1}v_{t2}k_{tgy} & 0 & -l_{t1}l_{t22}k_{tgy} \end{bmatrix}_{4\times6} \tag{A.9i}$$

The sub-damping matrix **C** can be obtained by simply replacing “k” by “c” in the above equations.

APPENDIX B

PARAMETERS USED IN THE CASE STUDY

Table B.1 Dynamic properties of SMT used in the coupled system

Terms		Symbol	Unit	Value
Car body mass		m_c	kg	3.90×10^4
Car body inertial moment	Rolling	$J_{c\phi}$	$\mathrm{kg}\cdot\mathrm{m}^2$	6.46×10^4
	Pitching	$J_{c\theta}$	$\mathrm{kg}\cdot\mathrm{m}^2$	1.75×10^6
	Yawing	$J_{c\psi}$	$\mathrm{kg}\cdot\mathrm{m}^2$	1.76×10^6
Bogie mass		m_b	kg	1.32×10^3
Bogie inertial moment	Rolling	$J_{b\phi}$	$\mathrm{kg}\cdot\mathrm{m}^2$	5.80×10^2
	Pitching	$J_{b\theta}$	$\mathrm{kg}\cdot\mathrm{m}^2$	2.20×10^2
	Yawing	$J_{b\psi}$	$\mathrm{kg}\cdot\mathrm{m}^2$	1.10×10^3
Rocker mass		m_t	kg	80
Rocker inertial moment	Rolling	$J_{t\phi}$	$\mathrm{kg}\cdot\mathrm{m}^2$	10
Levitation magnet mass		m_s	kg	603
Levitation magnet inertial moment	Pitching	$J_{s\theta}$	$\mathrm{kg}\cdot\mathrm{m}^2$	434
Guidance magnet mass		m_g	kg	387
Guidance magnet inertial moment	Yawing	$J_{g\psi}$	$\mathrm{kg}\cdot\mathrm{m}^2$	187
Car body-rocker vertical spring		k_{ctz}	N/m	2.0×10^6
Car body-rocker vertical damper		c_{ctz}	N·s/m	5.0×10^3
Car body-rocker lateral spring		k_{cty}	N/m	2.0×10^6
Car body-rocker lateral damper		c_{cty}	N·s/m	2.0×10^3
Rocker -rocker vertical spring		k_{ttz}	N/m	2.0×10^5
Air spring		k_{az}	N/m	1.9×10^6
Bogie anti-rolling spring		$k_{bb\phi}$	N/m/rad	1.0×10^6
Bogie-levitation magnet vertical spring		k_{bsz}	N/m	2.0×10^7
Bogie-levitation magnet vertical damper		c_{bsz}	N·s/m	5.0×10^3
Bogie-guidance magnet lateral spring		k_{bgy}	N/m	2.8×10^7
Bogie-guidance magnet lateral damper		c_{bgy}	N·s/m	500

Table B.2 Dimensions of SMT used in the coupled system

Terms	Direction	Symbol	Unit	Value
Car body	Lateral	$h_{cr}, -h_{cl}$	m	1.520
	Vertical	v_c	m	0.911
	Longitudinal	$l_{c11}\ -l_{c42}$	m	10.836
	Longitudinal	$l_{c12}, -l_{c41}$	m	7.74
	Longitudinal	$l_{c21}, -l_{c32}$	m	4.644
	Longitudinal	$l_{c22}, -l_{c31}$	m	1.548
Bogie	Lateral	$h_{br1}, -h_{bl1}$	m	1.400
	Vertical	v_{b1}	m	-0.25
	Vertical	v_{b2}	m	0.476
	Vertical	v_{b3}	m	0.976
	Longitudinal	$l_{b11}, -l_{b22}$	m	2.0015
	Longitudinal	$l_{b12}, -l_{b21}$	m	1.0945
	Longitudinal	$l_{b1}, -l_{b2}$	m	1.548
	Longitudinal	$l_{bc1}, -l_{bc2}$	m	0.22675
Rocker	Lateral	$h_{tr1}, -h_{tl1}$	m	0.950
	Lateral	$h_{tr2}, -h_{tl2}$	m	0.570
	Lateral	$-h_{tr3}, h_{tl3}$	m	0.540
Levitation magnet	Longitudinal	$l_{s1}, -l_{s12}$	m	1.419
	Longitudinal	$l_{s2}, -l_{s11}$	m	1.161
	Longitudinal	$l_{s3}, -l_{s10}$	m	0.903
	Longitudinal	$l_{s4}, -l_{s9}$	m	0.645
	Longitudinal	$l_{s5}, -l_{s8}$	m	0.387
	Longitudinal	$l_{s6}, -l_{s7}$	m	0.129

Table B.3 The material properties of viaduct in SML used in the coupled system

Terms	Description	Symbol	Unit	Value
Rail track	Linear gravity	G_{track}	kN/m	1.75
	Elastic modulus	E_{track}	$\mathrm{N/mm^2}$	2.06×10^5
	Damping ratio	D_{track}		0.02
Concrete girders piers bent-caps foundations	Volume density	ρ_{girder}	kg/m	2551
	Elastic modulus	E_{girder}	$\mathrm{N/mm^2}$	3.9×10^4
	Shear modulus	G_{girder}	$\mathrm{N/mm^2}$	1.625×10^4
	Damping ratio	D_{girder}		0.02

Table B.4 The parameters used for electromagnetic force model

μ_0 (H/m)	N_m	A_w (m^2)	h_0 (m)	K_0	P_0 (N)	K_d	K_p	R_0 (Ω)	i_0 (A)
$4\pi\times10^{-7}$	270	0.04	0.001	9.161×10^{-4}	2809.7	4000	-2000	1	17.51

APPENDIX C

THE DETAILED EXPRESSIONS OF ELEMENT MATRICES IN EQUATION (4.5).

The parameters for determining the location and orientation of the m^{th} trajectory coordinate system with respect to the global coordinate system can be deduced as

$$\begin{cases} {}_I s^{II_m} = {}_I s_0^{II_m} + vt \\ {}_I \psi^{II_m} = {}_I s^{II_m} / R \\ {}_I \theta^{II_m} = 0 \\ {}_I \phi^{II_m} = \phi_g \end{cases} \tag{C.1}$$

where ${}_I s_0^{II_m}$ is the initial position of the origin of the m^{th} trajectory coordinate system defined in the global coordinate system for time $t = 0$.

With the parameters given by Eq. (C.1), the transformation matrix ${}_I \mathbf{R}^{II_m \to I}$ can be given as:

$${}_I \mathbf{R}^{II_m \to I} = \left[{}_I \mathbf{i}^{II_m} \quad {}_I \mathbf{j}^{II_m} \quad {}_I \mathbf{k}^{II_m} \right] = \begin{bmatrix} \cos\left({}_I\psi^{II_m}\right) & -\sin\left({}_I\psi^{II_m}\right)\cos\phi_g & \sin\left({}_I\psi^{II_m}\right)\sin\phi_g \\ \sin\left({}_I\psi^{II_m}\right) & \cos\left({}_I\psi^{II_m}\right)\cos\phi_g & -\cos\left({}_I\psi^{II_m}\right)\sin\phi_g \\ 0 & \sin\phi_g & \cos\phi_g \end{bmatrix} \tag{C.2}$$

The coefficient matrix ${}_I \mathbf{L}^{II_m}$ in Eq. (4.7) can be written as

$${}_I \mathbf{L}^{II_m} = \left[\begin{array}{cccc} \dfrac{\mathrm{c}\,{}_I\psi^{II_m}}{R}\left(R - {}_{II_m}y^{III_i}\,\mathrm{c}\phi_g + {}_{II_m}z^{III_i}\,\mathrm{s}\phi_g\right) & -\mathrm{c}\phi_g\,\mathrm{s}\,{}_I\psi^{II_m} & \mathrm{s}\phi_g\,\mathrm{s}\,{}_I\psi^{II_m} & \\ \dfrac{\mathrm{s}\,{}_I\psi^{II_m}}{R}\left(R - {}_{II_m}y^{III_i}\,\mathrm{c}\phi_g + {}_{II_m}z^{III_i}\,\mathrm{s}\phi_g\right) & \mathrm{c}\phi_g\,\mathrm{c}\,{}_I\psi^{II_m} & -\mathrm{s}\phi_g\,\mathrm{c}\,{}_I\psi^{II_m} & \mathbf{0}_{3\times3} \\ 0 & \mathrm{s}\phi_g & \mathrm{c}\phi_g & \end{array} \right] \tag{C.3}$$

The translational motions of the origin of the i^{th} body defined in the m^{th} trajectory coordinate system, ${}_{II_m}y^{III_i}$ and ${}_{II_m}z^{III_i}$, are much smaller than the radius R. Eq. (C.3) can be further simplified as

$$ {}_{I}\mathbf{L}^{II_m} = \begin{bmatrix} \cos\left({}_{I}\psi^{II_m}\right) & -\cos\left(\phi_g\right)\sin\left({}_{I}\psi^{II_m}\right) & \sin\left(\phi_g\right)\sin\left({}_{I}\psi^{II_m}\right) & \\ \sin\left({}_{I}\psi^{II_m}\right) & \cos\left(\phi_g\right)\cos\left({}_{I}\psi^{II_m}\right) & -\sin\left(\phi_g\right)\cos\left({}_{I}\psi^{II_m}\right) & \mathbf{0}_{3\times3} \\ 0 & \sin\left(\phi_g\right) & \cos\left(\phi_g\right) & \end{bmatrix} \tag{C.4} $$

The vector $\left({}_{I}\mathbf{L}^{II_m}\right)^T {}_{I}\boldsymbol{\gamma}_R^{II_m\to I}$ used in Eq. (4.7) can be subsequently obtained as

$$ \left({}_{I}\mathbf{L}^{II_m}\right)^T {}_{I}\boldsymbol{\gamma}_R^{II_m\to I} = \frac{v^2}{R}\begin{bmatrix} 0 \\ \cos\phi_g + \dfrac{\left(-{}_{II_m}y^{III_i}\cos^2\phi_g + {}_{II_m}z^{III_i}\cos\phi_g\sin\phi_g\right)}{R} \\ -\sin\phi_g - \dfrac{\left(-{}_{II_m}y^{III_i}\cos\phi_g\sin\phi_g + {}_{II_m}z^{III_i}\sin^2\phi_g\right)}{R} \\ \mathbf{0}_{3\times1} \end{bmatrix} \approx \frac{v^2}{R}\begin{bmatrix} 0 \\ \cos\phi_g \\ -\sin\phi_g \\ \mathbf{0}_{3\times1} \end{bmatrix} \tag{C.5} $$

Furthermore, the matrix ${}_{III_i}\mathbf{H}^{II_m}$ used in Eq. (4.7) is parameterized as

$$ {}_{III_i}\mathbf{H}^{II_m} = \left[\begin{bmatrix} -{}_{II_m}\theta^{III_i}\cos\phi_g + {}_{II_m}\psi^{III_i}\sin\phi_g \\ \sin\phi_g + {}_{II_m}\phi^{III_i}\cos\phi_g \\ \cos\phi_g - {}_{II_m}\phi^{III_i}\sin\phi_g \end{bmatrix}\frac{1}{R} \quad \mathbf{0}_{3\times1} \quad \mathbf{0}_{3\times1} \quad \begin{bmatrix} 1 & {}_{II_m}\theta^{III_i}\,{}_{II_m}\phi^{III_i} + {}_{II_m}\psi^{III_i} & -2\,{}_{II_m}\theta^{III_i} + {}_{II_m}\phi^{III_i}\,{}_{II_m}\psi^{III_i} \\ -{}_{II_m}\psi^{III_i} & 1-\left({}_{II_m}\phi^{III_i}\right)^2 & 2\,{}_{II_m}\phi^{III_i} + {}_{II_m}\theta^{III_i}\,{}_{II_m}\psi^{III_i} \\ {}_{II_m}\theta^{III_i} & -2\,{}_{II_m}\phi^{III_i} & 1-\left({}_{II_m}\theta^{III_i}\right)^2-\left({}_{II_m}\phi^{III_i}\right)^2 \end{bmatrix}\right] \tag{C.6} $$

The angular velocity of the i^{th} vehicle body defined in its body coordinate system is then expressed as

$$ {}_{III_i}\boldsymbol{\omega}_i = {}_{III_i}\mathbf{H}^{II_m}\,{}_{II_m}\dot{\mathbf{U}}_i \tag{C.7} $$

The vector ${}_{III_i}\boldsymbol{\gamma}_{\boldsymbol{\theta}}^{I\to III_i}$ in Eq. (4.7) can be expanded as

$$ {}_{III_i}\boldsymbol{\gamma}_{\boldsymbol{\theta}}^{I\to III_i} = \begin{bmatrix} \frac{v}{R}\left({}_{II_m}\theta^{III_i}\sin\phi_g + {}_{II_m}\psi^{III_i}\cos\phi_g\right) & -\frac{v}{R}\cos\phi_g + {}_{II_m}\theta^{III_i}\,{}_{II_m}\dot{\phi}^{III_i} & \frac{v}{R}\sin\phi_g - {}_{II_m}\dot{\theta}^{III_i} + {}_{II_m}\psi^{III_i}\,{}_{II_m}\dot{\phi}^{III_i} \\ \frac{v}{R}\left(\cos\phi_g - {}_{II_m}\phi^{III_i}\sin\phi_g\right) & \frac{v}{R}\cos\phi_g\,{}_{II_m}\psi^{III_i} - {}_{II_m}\phi^{III_i}\,{}_{II_m}\dot{\phi}^{III_i} & -\frac{v}{R}\sin\phi_g\,{}_{II_m}\psi^{III_i} + {}_{II_m}\dot{\phi}^{III_i} + {}_{II_m}\psi^{III_i}\,{}_{II_m}\dot{\theta}^{III_i} \\ \frac{v}{R}\left(-\sin\phi_g - {}_{II_m}\phi^{III_i}\cos\phi_g\right) & -\frac{v}{R}\cos\phi_g\,{}_{II_m}\theta^{III_i} - {}_{II_m}\dot{\phi}^{III_i} & \frac{v}{R}\sin\phi_g\,{}_{II_m}\theta^{III_i} - {}_{II_m}\theta^{III_i}\,{}_{II_m}\dot{\theta}^{III_i} - {}_{II_m}\phi^{III_i}\,{}_{II_m}\dot{\phi}^{III_i} \end{bmatrix}\begin{bmatrix} {}_{II_m}\dot{\phi}^{III_i} \\ {}_{II_m}\dot{\theta}^{III_i} \\ {}_{II_m}\dot{\psi}^{III_i} \end{bmatrix} \tag{C.8} $$

APPENDIX D

THE DETAILED EXPRESSIONS OF ELEMENT MATRICES IN EQUATION (5.5).

The vectors ${}_{I}\mathbf{L}^{II_m}$, ${}_{III_i}\mathbf{H}^{II_m}$, ${}_{III_i}\boldsymbol{\gamma}_{\boldsymbol{\theta}}^{I\rightarrow III_i}$ and ${}_{III_i}\boldsymbol{\omega}_i$ used in Eq. (5.5) can be calculated by the following equations.

$$
{}_{I}\mathbf{R}^{II_m\rightarrow I}=\begin{bmatrix}\cos\left({}_{I}\psi^{II_m}\right) & -\sin\left({}_{I}\psi^{II_m}\right)\cos\left({}_{I}\phi^{II_m}\right) & \sin\left({}_{I}\psi^{II_m}\right)\sin\left({}_{I}\phi^{II_m}\right)\\ \sin\left({}_{I}\psi^{II_m}\right) & \cos\left({}_{I}\psi^{II_m}\right)\cos\left({}_{I}\phi^{II_m}\right) & -\cos\left({}_{I}\psi^{II_m}\right)\sin\left({}_{I}\phi^{II_m}\right)\\ 0 & \sin\left({}_{I}\phi^{II_m}\right) & \cos\left({}_{I}\phi^{II_m}\right)\end{bmatrix} \tag{D.1}
$$

The coefficient matrix ${}_{I}\mathbf{L}^{II_m}$ can be written as

$$
{}_{I}\mathbf{L}^{II_m}=\left[\begin{array}{cccc}\mathrm{c}\left({}_{I}\psi^{II_m}\right)\cdot\left\{1-k\cdot{}_{II_m}y^{III_i}\cdot\mathrm{c}\left({}_{I}\phi^{II_m}\right)+k\cdot{}_{II_m}z^{III_i}\cdot\mathrm{s}\left({}_{I}\phi^{II_m}\right)\right\} & -\mathrm{c}\left({}_{I}\phi^{II_m}\right)\cdot\mathrm{s}\left({}_{I}\psi^{II_m}\right) & \mathrm{s}\left({}_{I}\phi^{II_m}\right)\cdot\mathrm{s}\left({}_{I}\psi^{II_m}\right) & \\ \mathrm{s}\left({}_{I}\psi^{II_m}\right)\cdot\left\{1-k\cdot{}_{II_m}y^{III_i}\cdot\mathrm{c}\left({}_{I}\phi^{II_m}\right)+k\cdot{}_{II_m}z^{III_i}\cdot\mathrm{s}\left({}_{I}\phi^{II_m}\right)\right\} & \mathrm{c}\left({}_{I}\phi^{II_m}\right)\cdot\mathrm{c}\left({}_{I}\psi^{II_m}\right) & -\mathrm{s}\left({}_{I}\phi^{II_m}\right)\cdot\mathrm{c}\left({}_{I}\psi^{II_m}\right) & \mathbf{0}_{3\times3}\\ 0 & \mathrm{s}\left({}_{I}\phi^{II_m}\right) & \mathrm{c}\left({}_{I}\phi^{II_m}\right) & \end{array}\right] \tag{D.2}
$$

The coefficient matrix ${}_{III_i}\mathbf{H}^{II_m}$ is parameterized as

$$
{}_{III_i}\mathbf{H}^{II_m}=\left[\begin{bmatrix}-{}_{II_m}\theta^{III_i}\cdot\mathrm{c}\left({}_{I}\phi^{II_m}\right)+{}_{II_m}\psi^{III_i}\cdot s\left({}_{I}\phi^{II_m}\right)\\ s\left({}_{I}\phi^{II_m}\right)+{}_{II_m}\phi^{III_i}\cdot\mathrm{c}\left({}_{I}\phi^{II_m}\right)\\ \mathrm{c}\left({}_{I}\phi^{II_m}\right)-{}_{II_m}\phi^{III_i}\cdot s\left({}_{I}\phi^{II_m}\right)\end{bmatrix}\cdot k(s)\quad\mathbf{0}_{3\times1}\quad\mathbf{0}_{3\times1}\quad\begin{bmatrix}1 & {}_{II_m}\theta^{III_i}\cdot{}_{II_m}\phi^{III_i}+{}_{II_m}\psi^{III_i} & -2\,{}_{II_m}\theta^{III_i}+{}_{II_m}\phi^{III_i}\cdot{}_{II_m}\psi^{III_i}\\ -{}_{II_m}\psi^{III_i} & 1-\left({}_{II_m}\phi^{III_i}\right)^2 & 2\,{}_{II_m}\phi^{III_i}+{}_{II_m}\theta^{III_i}\cdot{}_{II_m}\psi^{III_i}\\ {}_{II_m}\theta^{III_i} & -2\,{}_{II_m}\phi^{III_i} & 1-\left({}_{II_m}\theta^{III_i}\right)^2-\left({}_{II_m}\phi^{III_i}\right)^2\end{bmatrix}\right] \tag{D.3}
$$

The angular velocity of the i^{th} vehicle body defined in its body coordinate system is then expressed as

$$
{}_{III_i}\boldsymbol{\omega}_i={}_{III_i}\mathbf{H}^{II_m}\,{}_{II_m}\dot{\mathbf{U}}_i \tag{D.4}
$$

The vector ${}_{III_i}\boldsymbol{\gamma}_{\boldsymbol{\theta}}^{I\rightarrow III_i}$ can be expanded as

$$
{}_{III_i}\boldsymbol{\gamma}_{\boldsymbol{\theta}}^{I\rightarrow III_i}=\begin{bmatrix}k\cdot v\cdot\left\{{}_{II_m}\theta^{III_i}\cdot\mathrm{s}\left({}_{I}\phi^{II_m}\right)+{}_{II_m}\psi^{III_i}\,\mathrm{c}\left({}_{I}\phi^{II_m}\right)\right\} & -k\cdot v\cdot\mathrm{c}\left({}_{I}\phi^{II_m}\right)+{}_{II_m}\theta^{III_i}\cdot{}_{II_m}\dot{\phi}^{III_i} & k\cdot v\cdot\mathrm{s}\left({}_{I}\phi^{II_m}\right)-{}_{II_m}\dot{\theta}^{III_i}+{}_{II_m}\psi^{III_i}\cdot{}_{II_m}\dot{\phi}^{III_i}\\ k\cdot v\cdot\left\{\mathrm{c}\left({}_{I}\phi^{II_m}\right)-{}_{II_m}\phi^{III_i}\cdot\mathrm{s}\left({}_{I}\phi^{II_m}\right)\right\} & k\cdot v\cdot\mathrm{c}\left({}_{I}\phi^{II_m}\right)\cdot{}_{II_m}\psi^{III_i}-{}_{II_m}\phi^{III_i}\cdot{}_{II_m}\dot{\phi}^{III_i} & -k\cdot v\cdot\mathrm{s}\left({}_{I}\phi^{II_m}\right)\cdot{}_{II_m}\psi^{III_i}+{}_{II_m}\dot{\phi}^{III_i}+{}_{II_m}\psi^{III_i}\cdot{}_{II_m}\dot{\theta}^{III_i}\\ k\cdot v\cdot\left\{-\mathrm{s}\left({}_{I}\phi^{II_m}\right)-{}_{II_m}\phi^{III_i}\,\mathrm{c}\left({}_{I}\phi^{II_m}\right)\right\} & -k\cdot v\cdot\mathrm{c}\left({}_{I}\phi^{II_m}\right)\cdot{}_{II_m}\theta^{III_i}-{}_{II_m}\dot{\phi}^{III_i} & k\cdot v\cdot\mathrm{s}\left({}_{I}\phi^{II_m}\right)\cdot{}_{II_m}\theta^{III_i}-{}_{II_m}\theta^{III_i}\cdot{}_{II_m}\dot{\theta}^{III_i}-{}_{II_m}\phi^{III_i}\cdot{}_{II_m}\dot{\phi}^{III_i}\end{bmatrix}\begin{bmatrix}{}_{II_m}\dot{\phi}^{III_i}\\ {}_{II_m}\dot{\theta}^{III_i}\\ {}_{II_m}\dot{\psi}^{III_i}\end{bmatrix} \tag{D.5}
$$

REFERENCES

Adasooriya, N.D. (2016). Fatigue reliability assessment of ageing railway truss bridges : Rationality of probabilistic stress-life approach. *Case Studies in Structural Engineering 6*: 1–10.

Au, F.T.K., Cheng, Y.S. & Cheung, Y.K. (2001). Vibration analysis of bridges under moving vehicles and trains: an overview. *Progress in Structural Engineering and Materials 3*(3): 299–304.

Baidu: Chinese Maglev http://www.gov.cn/zhengce/content/2016-12/19/content5150090.htm

Beskhyroun, S., Wegner, L.D. & Sparling, B.F. (2011). New methodology for the application of vibration-based damage detection techniques. *Structural Control and Health Monitoring 19*(1): 88–106.

British Standard EN 12299:2009. (2009). Railway applications — Ride comfort for passengers — Measurement and evaluation. European Committee for Standardization.

Cai, Y. & Chen, S.S. (1996). Vehicle / Guideway Dynamic Interaction in Maglev Systems. *Journal of Dynamic Systems, Measurement, and Control 118*: 526–530.

Cai, Y., Chen, S.S., M., R.D. & T, C.H. (1996). Vehicle / Guideway Dynamic Interaction in Maglev Systems. *Journal of Dynamic Systems, Measurement, and Control 118*(September 1996): 526–530.

Cai, Y., Chen, S.S., Rote, D.M. & Coffey, H.. (1993a). Vehicle/Guideway Interaction and Ride Comfort in Maglev Systems. *International conference on speed technology for railway and maglev vehicles* 22–25.

Cai, Y., Chen, S.S., Rote, D.M. & Coffey, H.T. (1993b). Dynamics, stability, and control of maglev systems.

Cai, Y., Chen, S.S., Rote, D.M. & Coffey, H.T. (1994). Vehicle/guideway Interaction For High Speed Vehicles On A Flexible Guideway. *Journal of Sound and Vibration*.

CEN. (2010). Railway applications - Track - Track alignment design parameters - Track gauges 1435 mm and wider - Part 1: Plain line. European Standard.

Chandra, S. & Agarwal, M.M. (2007). *Railway engineering*. New Delhi: Oxford University Press.

Chen, Y.-H. & Li, C.-Y. (2000). DYNAMIC RESPONSE OF ELEVATED HIGH-SPEED RAILWAY. *Journal of Bridge Engineering 5*(May): 124–130.

Chu, B.K., Asce, F., Garg, V.K. & Asce, F. (1985). Imapact in truss bridge due to frequent trains. *Journal of Engineering Mechanics 111*(2): 159–174.

Chu, K.H., Garg, V.K. & Wiriyachai, A. (1980). Dynamic Interaction of Railway Train and Bridges. *Vehicle System Dynamics 9*(4): 207–236.

Ciotlaus, M. (2015). C60 International Conference , November 2013 TRANSITION CURVES FOR HIGH SPEED RAILWAYS. In *C60 International Conference, November 2013*.

Crandall, C.L. (1893). *The transition curve by offsets and by deflection angles*. New York: John Wiley & Sons.

Dai, H. (2005). Dynamic behavior of maglev vehicle/guideway system with control.

Dimitrakopoulos, E.G. & Zeng, Q. (2015). A three-dimensional dynamic analysis scheme for the interaction between trains and curved railway bridges. *Computers & Structures 149*: 43–60.

Dinh, V.N., Kim, K. Du & Warnitchai, P. (2009). Dynamic analysis of three-dimensional bridge-high-speed train interactions using a wheel-rail contact model. *Engineering Structures 31*(12): 3090–3106.

Droździel, J. & Sowiński, B. (2006). Railway car dynamic response to track transition curve and single standard turnout. *WIT Transactions on the Built Environment 88*: 849–858.

Eurocode. (2003). *Actions on structures-Part 2: Traffic loads on bridges*.

Goodall, R. (1985). The theory of electromagnetic levitation. *Physics in Technology 16*(5): 207–213.

Guo, W.H. & Xu, Y.L. (2001). Fully Computerized Approach To Study Cable-Stayed Bridge–Vehicle Interaction. *Journal of Sound and Vibration 248*(4): 745–761.

Haigermoser, A., Luber, B., Rauh, J. & Gräfe, G. (2015). Road and track irregularities: measurement, assessment and simulation. *Vehicle System Dynamics 53*(7): 878–957.

Han, H.-S. & Kim, D.-S. (2016). *Magnetic levitation：Maglev Technology and Applications*. *Springer Tracts on Transportation and Traffic* (Vol. 13). New York, USA: Springer Tracts on Transportation and Traffic.

Han, H.S., Yim, B.H., Lee, N.J., Hur, Y.C. & Kim, S.S. (2009). Effects of the guideway's vibrational characteristics on the dynamics of a Maglev vehicle. *Vehicle System Dynamics 47*(3): 309–324.

He, J.L., Rote, D.M. & Coffey, H.T. (1994). *Study of Japanese electrodynamic-suspension maglev system*.

He, X., Kawatani, M., Hayashikawa, T. & Matsumoto, T. (2011). Numerical analysis on seismic response of Shinkansen bridge-train interaction system under moderate earthquakes. *Earthquake Engineering and Engineering Vibration*

10(1): 85–97.

Higgins, A.L. (1922). *The transition spiral and its introduction to railway curves with field exercises in construction and alignment*. New York: Van Nostrand.

Hodas, S. (2014). Design of Railway Track for Speed and High-speed Railways. *Procedia Engineering 91*(TFoCE): 256–261.

JB161-2012, Code for design of high-speed maglev transportation (draft), Shanghai urban and rural construction and transportation committee, 2012.

Ju, S.H., Ho, Y.S. & Leong, C.C. (2012). A finite element method for analysis of vibration induced by maglev trains. *Journal of Sound and Vibration 331*(16): 3751–3761.

Ju, S.H., Leong, C.C. & Ho, Y.S. (2014). Safety of Maglev Trains Moving on Bridges Subject to Foundation Settlements and Earthquakes. *Journal of Bridge Engineering 19*(1): 91–100.

Ju, S.H., Liao, J.R. & Ye, Y.L. (2010). Behavior of ground vibrations induced by trains moving on embankments with rail roughness. *Soil Dynamics and Earthquake Engineering 30*(11): 1237–1249.

Ju, S.H. & Lin, H.T. (2003). Resonance characteristics of high-speed trains passing simply supported bridges. *Journal of Sound and Vibration 267*(5): 1127–1141.

Ju, S.H., Lin, H.T. & Huang, J.Y. (2009). Dominant frequencies of train-induced vibrations. *Journal of Sound and Vibration 319*(1–2): 247–259.

Katz, R.M., Nene, V.D., Ravera, R.J. & Skalski, C.A. (1974). Performance of Magnetic Suspensions for High Speed Vehicles Operating Over Flexible Guideways. *Journal of Dynamic Systems, Measurement, and Control 96*(2): 204–212.

Kim, K.-J., Han, J.-B., Han, H.-S. & Yang, S.-J. (2015). Coupled vibration analysis of Maglev vehicle-guideway while standing still or moving at low speeds. *Vehicle System Dynamics 53*(4): 587–601.

Klasztorny, M. & Langer, J. (1990). Dynamic response of single-span beam bridges to a series of moving loads. *Earthquake Engineering & Structural Dynamics 19*(8): 1107–1124.

Kobry, A. (2017). *Transition Curves for Highway Geometric Design*. New York, USA: Springer Tracts on Transportation and Traffic Andrzej.

Kufver, B. (1997). *Optimisation of single horizontal curves in railway alignments*. Swedish.

Kufver, B. (2000a). *Optimisation of single horizontal railway curves procedures involving evalution of vehicle reactions*. Swedish National Road and Transport Research Institute.

Kufver, B. (2000b). *Optimisation of horizontal aligments for railways - Procedures involving evaluation of dynamic vehicle response*. Swedish NationalRoad and Transpart Research Institute.

Kufver, B. & Andersson, E. (1998). Optimisation of length of transition curves with vehicle reaction taken into consideration. *WIT Transactions on The Built Environment 34*: 34–42.

KufVer, B. & Andersson, E. (1998). Optimisation of length of transition curves with vehicle reaction taken into consideration. *Transactions on the Built Environment 34*: 33–42.

Kwon, S.D., Lee, J.S., Moon, J.W. & Kim, M.Y. (2008). Dynamic interaction analysis of urban transit maglev vehicle and guideway suspension bridge subjected to gusty wind. *Engineering Structures 30*(12): 3445–3456.

Lauriks, G., Evans, J., Forstberg, J., Balli, M. & Angoiti, I. De. (2003). *UIC comfort* *tests-Investigation of ride comfort and comfort disturbance on transition and circular curves*.

Lever, H. (1998). *Technical Assessment of Maglev System Concepts, Final Report by the Government Maglev System Assessment Team. US Army Corpss of Engineers*.

Li, G.Q., Wang, Z.L., Chen, S.. & Xu, Y.L. (2015). Field measurements and analyses of environmental vibrations induced by high-speed Maglev. *Science of the Total Environment* 1–13.

Li, X., Wang, D., Liu, D., Xin, L. & Zhang, X. (2018). Dynamic analysis of the interactions between a low-to-medium-speed maglev train and a bridge: Field test results of two typical bridges. *Proceedings of the Institution of Mechanical Engineers, Part F: Journal of Rail and Rapid Transit 0*(0): 095440971875850.

Li, X., Zhang, Z. & Zhang, X. (2016). Using elastic bridge bearings to reduce train-induced ground vibrations : An experimental and numerical study. *Soil Dynamics and Earthquake Engineering 85*(June): 78–90.

Lindahl, M. (2001). *Track geometry for high-speed railways- a literature survey and simulation of dynamic vehicle response*. Stockholm.

Ling, L., Deng, Y., Guan, Q. & Jin, X. (2017). Effect of track irregularities on the dynamic behavior of a tram vehicle. *Journal of Advances in Vehicle Engineering 3*(1): 29–39.

Link1. https://en.wikipedia.org/wiki/Incheon_Airport_Maglev

Link2. https://en.wikipedia.org/wiki/Changsha_Maglev_Express

Link3. https://en.wikipedia.org/wiki/Shanghai_maglev_train

Link4. https://en.wikipedia.org/wiki/Transrapid

Link5. https://en.wikipedia.org/wiki/Linimo

Link6. https://en.wikipedia.org/wiki/S1_line_(Beijing_Subway)

Liu, Z., Long, Z. & Li, X. (2015). Maglev Trains：Key Underlying Technologies. Springer Tracts in Mechanical Engineering. Springer Tracts in Mechanical Engineering.

Long, X. (2008). *Study on dynamic effect of alignment parameter on train running quality and its optimization for high-speed railway*. Beijing Jiaotong University.

Long, X. & Wei, Q. (2010). Dynamic analysis of railway transition curves. *Journal of Rail and Rapid Transit 224*(1): 1–14.

Majka, M. & Hartnett, M. (2008). Effects of speed , load and damping on the dynamic response of railway bridges and vehicles. *Computers & Structures 86*(6): 556–572.

Malveiro, J., Ribeiro, D., Calçada, R. & Delgado, R. (2014). Updating and validation of the dynamic model of a railway viaduct with precast deck. *Structure and Infrastructure Engineering 10*(11): 1484–1509.

Naeimi, M., Tatari, M. & Esmaeilzadeh, A. (2015). Dynamic interaction of the monorail – bridge system using a combined finite element multibody-based model. *Journal of Multi-body Dynamics 229*(2): 132–151.

Nagurka, M.. & Wang, S.K. (1997). A Superconducting Maglev Vehicle / Guideway System With Preview Control : Part I — Vehicle, Guideway, and Magnet Modelling. *Journal of Dynamic Systems, Measurement, and Control 119*(4): 638–643.

Ning, J., Lin, J. & Zhang, B. (2016). Time-frequency processing of track irregularities in high-speed train. *Mechanical Systems and Signal Processing 66–67*: 339–348.

Perrin, G., Soize, C., Duhamel, D. & Funfschilling, C. (2013). Track irregularities stochastic modeling. *Probabilistic Engineering Mechanics 34*: 123–130.

Pirti, A., Yücel, M.A. & Ocalan, T. (2016). Transrapid and the transition curve as sinusoid. *Tehnicki vjesnik - Technical Gazette 23*(1): 315–320.

Reitz, J.R. (1970). Forces on moving magnets due to Eddy currents. *Journal of Applied Physics 41*(5): 2067–2071.

Ren, S. (2008). *Dynamic Simulation of the Maglev Guideway Design*. the Delft University of Technology.

Sadeghi, J., Khajehdezfuly, A., Esmaeili, M. & Poorveis, D. (2016). Investigation of rail irregularity effects on wheel/rail dynamic force in slab track: Comparison of two and three dimensional models. *Journal of Sound and Vibration 374*: 228–244.

Sadeghi, J. & Shoja, H. (2013). Impact of superelevation deficiencies on the loading pattern of railway sleepers. *Proceedings of the Institution of Mechanical Engineers, Part F: Journal of Rail and Rapid Transit 227*(3): 286–295.

Shabana, A.A., Zaazaa, K.E. & Sugiyama, H. (2008). *Railroad vehicle dynamics: a computational approach*. CRC Press.

Shi, J., Fang, W., Wang, Y. & Zhao, Y. (2014). Measurements and analysis of track irregularities on high speed maglev lines. *Journal of Zhejiang University SCIENCE A 15*(6): 385–394.

Shi, J. & Wang, Y.J. (2011). Dynamic response analysis of single-span guideway caused by high speed maglev train. *Latin American Journal of Solids and Structures 8*(3): 213–228.

Shi, J., Wei, Q. & Zhao, Y. (2007). Analysis of dynamic response of the high-speed EMS maglev vehicle/guideway coupling system with random irregularity.

Vehicle System Dynamics 45(12): 1077–1095.

Shu, J., Zhang, Z., Gonzalez, I. & Karoumi, R. (2013). The application of a damage detection method using Artificial Neural Network and train-induced vibrations on a simplified railway bridge model. *Engineering Structures 52*: 408–421.

Sinha, P. (1987). *Electromagnetic suspension-dynamics and control*. IEE.

Smith M. ABAQUS/Standard User's Manual, Version 6.9. Providence, RI: Simulia, 2009.

Song, M.-K. & Fujino, Y. (2008). Dynamic analysis of guideway structures by considering ultra high-speed Maglev train-guideway interaction. *Structural Engineering and Mechanics 29*(4): 355–380.

Song, M.-K., Noh, H.-C. & Choi, C.-K. (2003). A new three-dimensional finite element analysis model of high-speed train–bridge interactions. *Engineering Structures 25*(13): 1611–1626.

Su, D., Fujino, Y., Nagayama, T. & Jr, J.Y.H. (2010). Vibration of reinforced concrete viaducts under high-speed train passage : measurement and prediction including train – viaduct interaction. *Structure and Infrastructure Engineering 2479*(August 2017).

Talukdar, R.P. & Talukdar, S. (2016). Dynamic Analysis of High-Speed MAGLEV Vehicle-Guideway System: An Approach in Block Diagram Environment. *Urban Rail Transit 2*(2): 71–84.

Tari, E. & Baykal, O. (2005). A new transition curve with enhanced properties *3*: 913–923.

TB10621. (2014). Code for design of high speed railway. National Railway Administration of China.

Teng, Y.F. (2008). *The study of vibration of high speed maglev guideway interaction* *with vehicle (In Chinese)*. Shanghai Jiaotong University.

Tsuchiya, M. & Ohsaki, H. (2000). Characteristics of electromagnetic force of EMS-type maglev vehicle using bulk superconductors. *IEEE Transactions on Magnetics 36*(5 I): 3683–3685.

Um, J.-H., Choi, I.-Y. & Lee, J.S. (2015). Evaluation of Optimal Horizontal Alignment Considering Ride Comfort in. *JOURNAL OF THE KOREAN SOCIETY FOR RAILWAY 18*(5): 457–465.

Um, J.H., Choi, I.Y., Yang, S.C. & Kim, M.C. (2010). Optimization of alignment considering ride comfort for superimposition of vertical and horizontal curves *225*: 649–662.

Wang, S.K. & Nagurka, M.L. (1997). A Superconducting Maglev Vehicle-Guideway System With Preview ControlPart II-Controller Design and System Behavior.pdf. *Journal of Dynamic Systems, Measurement, and Control 119*(4): 644–649.

Wang, T., Garg, V.K. & Chu, K. (1991). Railway bridge/vehicle interaction studies with new vehicle model. *Journal of Structural Engineering 117*(7): 2099–2116.

Wang, Z.L., Xu, Y.L., Li, G.Q., Chen, S.W. & Zhang, X.L. (2018). Dynamic Analysis of a Coupled System of High-Speed Maglev Train and Curved Viaduct. *International Journal of Structural Stability and Dynamics 18*(11): 1–32.

Wang, Z.L., Xu, Y.L., Li, G.Q., Yang, Y.B., Chen, S.W. & Zhang, X.L. (2017). Dynamic Interaction of High - Speed Maglev Train and Viaduct: Modeling and Validation. *Engineering Structures on* 1–41 (Under review).

Wang, Z.L., Xu, Y.L., Li, G.Q., Yang, Y.B., Chen, S.W. & Zhang, X.L. (2018). Modeling and validation of coupled high-speed maglev train-and-viaduct systems considering support flexibility. *Vehicle System Dynamics* (January).

Wilkie, D.F. (1972). Dynamics, control and ride quality of a magnetically levitated high speed ground vehicle. *Transportation Research 6*(1971): 343–369.

Wikipedia: maglev https://en.wikipedia.org/wiki/Maglev

Wikipedia: Chūō Shinkansen https://en.wikipedia.org/wiki/Ch%C5%AB%C5%8D_ Shinkansen

Wilson, J.R. & Womack, W.C. (2004). *Urban Maglev Technology Development Program assumes Colorado Maglev Project (final report).*

Woźnica, P. (2014). Optimisation of Railway Polynomial Transition Curves with Different Number of Terms. *Logistics & Transport 2*(22): 57–65.

Wu, X. (2003a). *Maglev Train*. Shanghai: Shanghai Science and Technology Press.

Wu, X. (2003b). *Maglev Train*. Shanghai Science and Technology Press.

Wu, Y.S. & Yang, Y. Bin. (2003). Steady-state response and riding comfort of trains moving over a series of simply supported bridges. *Engineering Structures 25*(2): 251–265.

Xia, H., Guo, W.W., Wu, X., Pi, Y.L. & Bradford, M.A. (2008). Lateral dynamic interaction analysis of a train-girder-pier system. *Journal of Sound and Vibration 318*(4–5): 927–942.

Xia, H., Han, Y., Zhang, N. & Guo, W. (2006a). Dynamic analysis of train–bridge system subjected to non-uniform seismic excitations. *EARTHQUAKE ENGINEERING AND STRUCTURAL DYNAMICS 35*(12): 1563–1579.

Xia, H., Han, Y., Zhang, N. & Guo, W. (2006b). Dynamic analysis of train–bridge system subjected to non-uniform seismic excitations. *EARTHQUAKE ENGINEERING AND STRUCTURAL DYNAMICS 35*(12): 1563–1579.

Xia, H., Noda, Y., Hayashikawa, T., Kawatani, M. & Matsumoto, T. (2011). An analytical approach to coupled vibration of curved rationalized girder bridges and running vehicles. *Procedia Engineering 14*: 2906–2915.

Xia, H., Xu, Y.L. & Chan, T.H.T. (2000a). Dynamic interaction of long suspension bridges with running trains. *Journal of Sound and Vibration 237*(2): 263–280.

Xia, H., Xu, Y.L. & Chan, T.H.T. (2000b). Dynamic interaction of long suspension bridges with running trains. *Journal of Sound and Vibration 237*(2): 263–280.

Xia, H., Xu, Y.L. & Chan, T.H. (2000). Dynamic Interaction of Long Suspension Bridges With Running Trains. *Journal of Sound and Vibration 237*(2): 263–280.

Xia, H. & Zhang, N. (2005). Dynamic analysis of railway bridge under high-speed trains. *Computers & Structures 83*(23–24): 1891–1901.

Xia, H., Zhang, N. & De Roeck, G. (2003). Dynamic analysis of high speed railway bridge under articulated trains. *Computers and Structures 81*(26–27): 2467–2478.

Xia, H., Zhang, N. & Guo, W.W. (2006). Analysis of resonance mechanism and conditions of train-bridge system. *Journal of Sound and Vibration 297*(3–5): 810–822.

Xu, L. & Zhai, W. (2017). A novel model for determining the amplitude-wavelength limits of track irregularities accompanied by a reliability assessment in railway vehicle-track dynamics. *Mechanical Systems and Signal Processing 86*(September 2016): 260–277.

Xu, Y.-L. (2013). *Wind Effects on Cable-Supported Cable-Supported Bridges*. John Wiley & Sons, Incorporated.

Xu, Y.L. & Guo, W.H. (2004). Effects of bridge motion and crosswind on ride comfort of road vehicles. *Journal of Wind Engineering and Industrial*

Aerodynamics 92: 641–662.

Xu, Y.L., Li, Q., Wu, D.J. & Chen, Z.W. (2010). Stress and acceleration analysis of coupled vehicle and long-span bridge systems using the mode superposition method. *Engineering Structures 32*(5): 1356–1368.

Xu, Y.L., Xia, H. & Yan, Q.S. (2003). Dynamic response of suspension bridge to high wind and running train. *Journal of Bridge Engineering 8*(1): 46–55.

Xu, Y.L., Zhang, N. & Xia, H. (2004). Vibration of coupled train and cable-stayed bridge systems in cross winds. *Engineering Structures 26*(10): 1389–1406.

Yaghoubi, H. & Rezvani, M.A. (2011). Development of Maglev Guideway Loading Model. *Journal of Transportation Engineering 137*(3): 201–213.

Yang, Y. Bin & Wu, Y.S. (2001). A versatile element for analyzing vehicle-bridge interaction response. *Engineering Structures 23*(5): 452–469.

Yang, X., Gu, S., Zhou, S., Yang, J., Zhou, Y. & Lian, S. (2015). Effect of track irregularity on the dynamic response of a slab track under a high-speed train based on the composite track element method. *Applied Acoustics 99*: 72–84.

Yang, Y.-B., Chang, C.-H. & Yau, J.-D. (1999). An element for analysing vehicle–bridge systems considering vehicle's pitching effect. *International Journal for Numerical Methods in Engineering 46*(March): 1031–1047.

Yang, Y.-B., Liao, S.-S. & Lin, B.-H. (1995). Impact Formulas for Vehicles Moving over Simple and Continuous Beams. *Journal of Structural Engineering 121*(11): 1644–1650.

Yang, Y.-B. & Lin, B.-H. (1995). Vehicle-bridge interaction analysis by dynamic condensation method. *Journal of Structural Engineering 121*(11): 1636–1643.

Yang, Y.-B., Lin, C.W. & Yau, J.D. (2004). Extracting bridge frequencies from the dynamic response of a passing vehicle. *Journal of Sound and Vibration 272*(3–

5): 471–493.

Yang, Y.-B. & Yau, J.-D. (1997). Vehicle-bridge interaction element for dynamic analysis. *Journal of Structural Engineering 123*(11): 1512–1518.

Yang, Y.-B., Yau, J.-D. & Hsu, L.-C. (1997). Vibration of simple beams due to trains moving at high speeds. *Engineering Structures 19*(11): 936–944.

Yang, Y., Yau, J. & Wu, Y. (2004). *Vehicle-bridge interaction dynamics With Applications to High-Speed Railways*. World Scientific.

Yang, Y.B., Cheng, M.C. & Chang, K.C. (2013). Frequency Variation in Vehicle–Bridge Interaction Systems. *International Journal of Structural Stability and Dynamics 13*(02): 1350019.

Yang, Y.B., Lin, C.L., Yau, J.D. & Chang, D.W. (2004). Mechanism of resonance and cancellation for train-induced vibrations on bridges with elastic bearings. *Journal of Sound and Vibration 269*(1–2): 345–360.

Yang, Y.B., Wu, C.M. & Yau, J.D. (2001). Dynamic Response of a Horizontally Curved Beam Subjected To Vertical and Horizontal Moving Loads. *Journal of Sound and Vibration 242*(3): 519–537.

Yang, Y.B. & Yau, J.D. (2011). An iterative interacting method for dynamic analysis of the maglev train-guideway/foundation-soil system. *Engineering Structures 33*(3): 1013–1024.

Yau, J.-D., Wu, Y.-S. & Yang, Y.-B. (2001). Impact Response of Bridges With Elastic Bearings To Moving Loads. *Journal of Sound and Vibration 248*(1): 9–30.

Yau, J.-D., Yang, Y.-B. & Kuo, S.-R. (1999). Impact response of high speed rail bridges and riding comfort of rail cars. *Engineering Structures 21*(9): 836–844.

Yau, J.D. (2001). Resonance of continuous bridges due to high speed trains. *Journal* *of Marine Science and Technology 9*(1): 14–20.

Yau, J.D. (2009a). Response of a maglev vehicle moving on a series of guideways with differential settlement. *Journal of Sound and Vibration 324*(3–5): 816–831.

Yau, J.D. (2009b). Aerodynamic Response of an Ems-Type Maglev Vehicle Running on Flexible Guideways. In *10th Interactional Conference on Fluid Control, Measurement, and Visualization*. Moscow, Russia.

Yau, J.D. (2009c). Response of a maglev vehicle moving on a series of guideways with differential settlement. *Journal of Sound and Vibration 324*(3–5): 816–831.

Yau, J.D. (2010a). Interaction response of maglev masses moving on a suspended beam shaken by horizontal ground motion. *Journal of Sound and Vibration 329*(2): 171–188.

Yau, J.D. (2010b). Aerodynamic vibrations of a maglev vehicle running on flexible guideways under oncoming wind actions. *Journal of Sound and Vibration 329*(10): 1743–1759.

Yau, J.D. & Frýba, L. (2007). Response of suspended beams due to moving loads and vertical seismic ground excitations. *Engineering Structures 29*(12): 3255–3262.

Yi, S. (2017). *Dynamic Analysis of High-Speed Railway Alignment Theory and Practice*. Southwest Jiaotong University Press.

Yim, B.H., Han, H.S., Lee, J.K. & Kim, S.S. (2009). Curving performance simulation of an EMS-type Maglev vehicle. *Vehicle System Dynamics 47*(10): 1287–1304.

Yu, Z. & Mao, J. (2017). Probability analysis of train-track-bridge interactions using a random wheel/rail contact model. *Engineering Structures 144*: 120–138.

Yuting, W., Qin, Y. & Wei, X. (2012). Track irregularities estimation based on acceleration measurement. In *International Conference on Measurement, Information and Control*.

Zboifiski, K. (1998). Dynamical investigation of railway vehicles on a curved track. *European Journal of Mechanics - A/Solids 17*: 1001–1020.

Zboinski, K. & Woznica, P. (2017). Optimization of polynomial transition curves from the viewpoint of jerk value. *Archives of Civil Engineering 63*(1): 181–199.

Zboinski, K. & Woznica, P. (2018). Combined use of dynamical simulation and optimisation to form railway transition curves. *Vehicle System Dynamics 3114*: 1–57.

Zeng, Q. & Dimitrakopoulos, E.G. (2016). Seismic response analysis of an interacting curved bridge–train system under frequent earthquakes. *Earthquake Engineering & Structural Dynamics*. 45(7): 1129–1148.

Zeng, Q., Yang, Y.B. & Dimitrakopoulos, E.G. (2016). Dynamic response of high speed vehicles and sustaining curved bridges under conditions of resonance. *Engineering Structures*. 114: 61–74.

Zhai, W.M., Zhao, C.F. (2015). Dynamics of maglev vehicle/guideway system (I)-magnet/rail interaction and system stability. *Chinese Journal of Mechanical Engineering*. 41(7): 1-10.

Zhai, W.M., Zhao, C.F. (2015). Dynamics of maglev vehicle/guideway system (II)-modeling and simulation. *Chinese Journal of Mechanical Engineering*. 41(8): 163-175.

Zhai, W.M., Wang, S., Zhang, N. & Gao, M. (2013). High-speed train – track – bridge dynamic interactions – Part II : experimental validation and engineering application. *International Journal of Rail Transportation 1*(2): 25–41.

Zhai, W., Xia, H., Cai, C. & Gao, M. (2013). International Journal of Rail High-speed train – track – bridge dynamic interactions – Part I : theoretical model and numerical simulation. *International Journal of Rail Transportation* 1(2): 3–24.

Zhai, W.M. Cai, S.Z. Guo, C.B. (1996), Coupling model of vertical and lateral vehicle/track interactions,*Vehicle System Dynamics*, 26(1):61-79

Zhai, W.M., Cai, C.B. and Wang, K.Y. (2004), Numerical simulation and field experiment of high-speed train-track-bridge system dynamics,*Vehicle System Dynamics*. 41:677-686

Zhai, W.M. and True, H. (2000) Vehicle-track dynamics on a ramp and on the bridge: Simulation and measurements,*Vehicle System Dynamics*, 33: 604-615

Zhai, W.M. and Wang, K.Y.(2006) Lateral interactions of trains and tracks on small-radius curves: simulation and experiment,*Vehicle System Dynamics*, 44: 520-530

Zhai, W.M., He, Z.X. and Song, X.L. (2010), Prediction of high-speed train induced ground vibration based on train-track-ground system model, *Earthquake Engineering and Engineering Vibration*, 9(4):545-554

Zhang, G., Li, J. & Yang, Z. (2011). Estimation of power spectrum density track irregularities of low-speed Maglev railway lines (In Chinese). *Journal of the China Railway Socity 33*(10).

Zhang, N., Tian, Y. & Xia, H. (2016). A Train-Bridge Dynamic Interaction Analysis Method and Its Experimental Validation. *Engineering 2*(4): 528–536.

Zhang, N., Xia, H. & Guo, W. (2008). Vehicle-bridge interaction analysis under high-speed trains. *Journal of Sound and Vibration 309*(3–5): 407–425.

Zhang, N., Xia, H., Guo, W.W., Roeck, G.D.E. & Leuven, K.U. (2010). A vehicle-bridge linear interaction model and its validation. *International Journal of Structural Stability and Dynamics 10*(2): 335–361.

Zhang, Q., Vrouwenvelder, A. & Wardenier, J. (2001). Numerical simulation of train-bridge interactive dynamics. *Computers & Structures 79*(10): 1059–1075.

Zhao, C. & Zhai, W. (2002). Maglev Vehicle/Guideway Vertical Random Response and Ride Quality. *Vehicle System Dynamics 38*(3): 185–210.

Zhao, G. & Zeng, S. (1995). Effect of curve radius and off-balance superelevation on side wear of high rail on curved track. *China Railway Science 16*(3): 90–96.

Zhao, Y. (2009). *Study on dynamic characteristics of high-speed maglev transportation track beam considering pier vibration*. Beijing Jiaotong University.

Ziyaeifar, M. (2005). Interaction study of train–bridge–track systems using Maxwell model. *Vehicle System Dynamics 43*(11): 771–794.